Faculty of Science and Engineering

WASM: Minerals, Energy and Chemical Engineering

Department of Petroleum Engineering

Experimental Evaluation of Variation in Petrophysical Properties during CO_2 Injection in Carbonate Rocks: Effective Mechanisms

Mohamed Bashir J. Khather

This thesis is presented for the Degree of

Doctor of Philosophy

of

Curtin University

October 2018

Declaration

To the best of my knowledge and belief this thesis contains no material previously published by any other person except where due acknowledgment has been made.

This thesis contains no material which has been accepted for the award of any other degree or diploma in any university.

Signature: ……

Date: 12/10/2018

Publication List

Parts of this thesis have been published in the following articles:

1. Khather, Mohamed, Ali Saeedi, Reza Rezaee, Ryan RP Noble, and David Gray. 2017. Experimental Investigation of Changes in Petrophysical Properties during CO_2 Injection into Dolomite-Rich Rocks. International Journal of Greenhouse Gas Control 59: 74-90.
2. Khather, M., Saeedi, A., Rezaee, R., Noble, R.R.P., 2018. Experimental evaluation of carbonated brine-limestone interactions under reservoir conditions-emphasis on the effect of core scale heterogeneities. International Journal of Greenhouse Gas Control, 68: 128-145.
3. Khather, M., Saeedi, A. Experimental investigations of change in petrophysical properties during CO_2 injection into chalk reservoirs (proceeding). One Curtin International Postgraduate Conference (OCPC) 2017
4. Khather, Mohamed, Ali Saeedi, Matthew B. Myers, and Michael Verrall. 2019. An Experimental Study for Carbonate Reservoirs on the Impact of CO_2-EOR on Petrophysics and Oil Recovery. Fuel 235: 1019-1038. doi: https://doi.org/10.1016/j.fuel.2018.08.094.

Executive Summary

Geo-sequestration is considered to have a measurable global potential for reducing the anthropogenic greenhouse gas emissions, in particular CO_2. During the geo-sequestration process, CO_2 may be injected on its own or via other methods such as carbonated water injection into deep geological media where it may be trapped permanently. The injection or in-situ generation of special fluid mixtures may trigger a series of chemical reactions between the fluids and the rock formation. While these reactions are generally well-characterised from a qualitative perspective, the extent to which they may impact on the petrophysical properties of the target formation requires a detailed evaluation on a case-by-case basis.

With the presence of highly reactive minerals in their composition, carbonate rocks may undergo alternations to their properties in a larger extent compared with their sandstone counterparts. Such possible alternations may be induced by a number of mechanisms such as mineral dissolution, mineral precipitation, mechanical/physical compaction and fines migration. Furthermore, if crude oil is present, CO_2 injection may destabilise the asphaltene content of the crude triggering asphaltene precipitation as another mechanism that may affect some of the rock's petrophysical properties.

This research evaluates the changes in the petrophysical properties of a number of carbonate samples (limestone, dolostone and chalk), after undergoing carbonated brine flooding or CO_2 enhanced oil recovery (CO_2-EOR) processes under in-situ reservoir conditions in the laboratory. The main emphasis of such an investigation is on the identification and characterisation of the effects of the earlier mentioned mechanisms. To achieve this primary objective, the core-flood experiments are complemented by porosity, permeability and NMR (nuclear magnetic resonance) measurements, X-ray CT (computed tomography) and SEM (scanning electron microscopy) imaging, XRD (X-ray Diffraction) analysis and finally chemical analysis of the produced brine and the crude oil used in some experiments. There are a few related studies of limited scope performed before by other researchers previously. However, the aim of current research is to provide a comprehensive picture of the problem at hand using an integrated approach. In other words, the active mechanisms and their influencing factors are evaluated all together to identify and characterise interdependencies too. Furthermore, this study uses new innovative sample configurations leading to the generation of more solid and insightful evidence in support of the arguments presented about the results.

The research results show various degrees of change in the petrophysical properties of the samples such as different levels of increase or decrease in their permeability. The extent and direction (i.e. positive or negative) of change to rock properties are found to be a function of the occurrence and dominance of the earlier mentioned mechanisms. For instance, an increase in permeability is attributed to the dominance of the mineral dissolution mechanism while a decrease in this property may reveal that one or several of other mechanisms (i.e. physical compaction, mineral or asphaltene precipitation and fines migration) control the properties of a post-flood sample. The earlier mentioned auxiliary techniques applied are found to be insightful in detecting the occurrence and degree of dominance of these mechanisms. For example, in samples with high degree of change to their permeability, X-ray CT and SEM images reveal signs of significant mineral dissolution with the X-ray images clearly showing the establishment of dissolution fingers and wormhole(s) along the length of some samples.

It is generally observed that physical compaction, mineral precipitation and fines migration mechanisms become active and their influence detectable if the dissolution mechanism was of significant degree. For example, mechanical compaction would occur only if the mineral dissolution manages to weaken a rock sample adequately resulting in the deformation of the sample under the experimental confining pressure. Also, the extent of the effect of these mechanisms are found to be largely controlled by the mineralogy of a sample as well as the original textural features and core-scale heterogeneities (e.g. fractures, preferential flow paths, etc.) present in the pre-flood sample. Furthermore, the degree and nature of changes in the petrophysical properties of rock samples are seen to be dependent on the distance from the injection point where carbonated water/CO_2 would enter a rock sample. For example, the dissolution mechanism and the subsequent mechanical compaction are detected to be more active close to the inlet of the sample while mineral dissolution and fines migration would often control post-flood sample properties towards its outlet.

In addition to the earlier discussed mechanisms, asphaltene precipitation is found to play a key role in deciding the post-flood properties of the samples subjected to CO_2-EOR. This mechanism is found to have effects very similar to those of fines migration and mineral precipitation. The EOR experiments were conducted under either continuous CO_2 injection or the Water Alternating Gas (WAG) flooding scheme where formation water and CO_2 were injected as alternating slugs. Although asphaltene precipitation is found to be the absolute dominant during continuous CO_2 injection, the WAG technique found to also give rise to the

dissolution mechanism to the extent that some wormholes with limited length are generated in the inlet region of some samples.

Acknowledgement

In the name of Allah, the Most Gracious and the Most Merciful

Alhamdulillah, all praises to Allah for the strengths and His blessing in completing this thesis. Special appreciation goes to my supervisor, ***Dr. Ali Saeedi***, for his supervision and constant support. His invaluable help of constructive comments and suggestions has been instrumental in the success of this research. I would also like to give special thanks and appreciation to ***Curtin University*** and ***academic staff*** in the Department of Petroleum Engineering for their support.

My deepest gratitude goes to my beloved ***parents***. However my father Mr. Bashir J.Khather passed away while I was studying may Allah mercy him. I would like to dedicate it to both him and my mother Fawzia Mustafa. Also, not forgetting ***my wife***, ***my aunt***, ***my beloved brothers, sister and sons***, Mrs. Monera, Salha, Ali, Abdo, Ahmad, Ennas, Omar, Alla and Yusif for their endless love, prayers encouragement and care. To those who indirectly contributed to this research, your kindness means a lot to me. Thank you very much.

Mohamed Khather

Table of Contents

Publication List II
Executive Summary III
1. Introduction and Objectives 1
1.1. Underground CO_2 storage 3
1.2. Research Objectives 7
1.3. Organisation of Thesis 8
2. Background: In-situ Interactions and Active Mechanisms 9
2.1. Thermo-physical properties of fluids 12
2.1.1. Pure CO_2 12
2.1.2. Pure water (H_2O) 14
2.1.3. In-situ fluid mixtures 15
CO_2 solubility in crude oil 17
Oil viscosity reduction 17
Oil swelling 17
Interfacial tension reduction 17
Asphaltene precipitation 18
2.2. Fluid-fluid and fluid-rock interactions 19
2.2.1. Trapping mechanisms 19
2.2.2. Effects on characteristics of fluid-rock system 25
2.3. Reservoir heterogeneity and lithology 29
2.4. Effective stresses acting on the reservoir rock 30
2.5. Previous related experimental work 31
3. Experimental Apparatus, Material and Procedures 38
3.1. Core-flooding Apparatus 38
3.1.1. The injection system 40
3.1.2. The core holder 41
3.1.3. The data collection and monitoring system 43
3.2. The Experimental Conditions and Material 44
3.2.1. P-T conditions 44
3.2.2. Fluids 44
3.2.3. Core samples 45
3.3. Experimental procedures 52
3.3.1. Sample perpetration and preliminary measurements 52
3.3.2. Medical X-ray CT imaging 54

3.3.3. X-ray Diffraction (XRD) analysis 55
3.3.4. Scanning Electron Microscopy (SEM) 56
3.3.5. Nuclear magnetic resonance (NMR) 56
3.3.6. CO_2-saturated brine (live brine) preparation 60
3.3.7. The Core-flooding procedures 61
4. Experimental results 66
4.1. X-ray Diffraction (XRD) analysis 66
4.2. Basic sample property measurements 66
4.2.1. Live brine flooding 66
4.2.2. Continuous CO_2-EOR flooding 68
4.2.3. Water-Alternating-Gas (WAG) flooding 69
4.3. Medical X-ray CT imaging 69
4.3.1. Live brine flooding 70
4.3.2. Continuous CO_2-EOR flooding 90
4.3.3. Water-Alternating-Gas (WAG) flooding 98
4.4. Nuclear magnetic resonance (NMR) measurements 101
4.4.1. Live brine flooding 102
4.4.2. Continuous CO_2-EOR flooding 115
4.4.3. Water-Alternating-Gas (WAG) flooding 121
4.5. Scanning Electron Microscopy (SEM) 124
4.5.1. Live brine flooding 125
4.5.2. CO_2-EOR flooding 128
4.6. Effluent fluid chemistry analysis 130
4.6.1. Effluent brine samples 131
4.6.2. Crude oil samples 132
5. Interpretations and Discussions 133
5.1. Live brine flooding 134
5.1.1. Sample group 1 (limestone cores) 134
5.1.2. Sample group 2 (dolostone cores) 141
5.1.3. Sample group 3 (chalk cores) 147
5.1.4. Sample group 4 (manufactured hetergeneous Indiana Limestone sample) 149
5.2. Continuous CO_2-EOR flooding 150
5.3. Water-Alternating-Gas (WAG) flooding 155
5.3.1. Samples VS-2 and INL-11 (limestone) 155
5.3.2. Sample GD-11 (dolostone) 158

6. Summary, conclusions and recommendations 159
6.1. Summary 159
6.2. Conclusions 160
6.2.1. Live brine flooding 160
6.2.2. Continuous CO_2 and WAG flooding 161
6.3. Recommendations 162
Nomenclature 164
References 171

List of Figures

Figure 1. 1. Current carbon dioxide concentrations in May 2016 (data taken from Scripps CO_2 Program UCSD / Scripps Institution of Oceanography). 2
Figure 1. 2. The process of carbon capture and storage (CCS). 2
Figure 1. 3. Various types of CO_2 storage sites. 3
Figure 1. 4. CO_2 density increases with depth (Data taken from IEA 2008). 5
Figure 2. 1. One-dimensional single-phase fluid flow through a porous medium. 10
Figure 2. 2. Phase diagram for pure CO_2 (data were taken from IPCC, 2005). 13
Figure 2. 3. Pure CO_2 viscosity at various P-T conditions (Data were taken from NIST, 2010). 13
Figure 2. 4. Density of pure CO_2 as a function of temperature and pressure (data were taken from Bachu, 2008). 14
Figure 2. 5. The phase diagram of pure water. 15
Figure 2. 6. Stratigraphic or structural trapping: (1) CO_2 is trapped between two impermeable layers, (2) CO_2 is trapped by a fold in the geological layers and (3) CO_2 is trapped by a sealing fault. 21
Figure 2. 7. Residual trapping of CO_2. 22
Figure 2. 8. Solubility trapping processes CO_2 enhanced by the so called convective mixing (sinking of denser carbonated water). 23
Figure 2. 9. The time-scale and level of security of CO_2 trapping mechanisms. 24
Figure 2. 10. Dissolution and precipitation processes during CO_2 injection. 26
Figure 2. 11. Dissolution processes in the fractured carbonate rocks during CO_2 injection. 27
Figure 2. 12. Contact angle (θ) as a measure of wettability. 29
Figure 2. 13. Effect of wettability on fluids distribution for an oil-water fluid system. 29
Figure 2. 14. 3D X-ray images of the inlet region of samples before and after flooding (black and gray areas represent pores and grain solids, respectively) (after Luquot and Gouze, 2009). 32
Figure 2. 15. Post-flood X-ray CT image illustrating the dissolution patterns formed in a dolomite-rich homogeneous sample (after Smith et al. 2013). 33
Figure 2. 16. X-ray CT images (a) before and (b) after flooding for a vuggy limestone sample illustrating the formation of wormholes (after Smith et al. 2013). 34
Figure 2. 17. Differential pressure profiles for all the vuggy limestone samples (after Smith et al. 2013). 34

Figure 2. 18. X-ray CT images showing the generation of dissolution patterns during core-floods conducted under different flow rates: (a) 1 ml/min, (b) 0.1 ml/min and (c) 0.01 ml/min (after Luhmann et al. 2014). 35
Figure 2. 19. SEM image obtained before and after flooding for Sample E-S4 (after Zekri, Shedid and Almehaideb 2009). 36
Figure 2. 20. . Pre- and post-flood permeability of a composite core versus the distance from the inlet (at So = 79%) (after (Zekri et al. 2013). 37
Figure 2. 21. Pre- and post-flood permeability of a composite core versus the distance from the inlet (at So = 30%) (after Zekri et al. 2013). 37
Figure 3.1. A photo of the core-flooding apparatus used in this experimental study. 39
Figure 3.2. A general schematic diagram of the core flooding apparatus used in the experiments. 39
Figure 3.3. The four injection pumps and associated electronic devices. 40
Figure 3.4. The three fluid sample bottles and associated connections. 41
Figure 3.5. The general schematic diagram of the core-holder used during the experiments (after Saeedi, 2011). 42
Figure 3.6. A photo of the core-holder used during the experiments. 42
Figure 3.7. The two computer connected to the apparatus for data-logging and monitoring. 43
Figure 3.8. The five limestone core samples included in Group 1. 46
Figure 3.9. The four dolostone samples included in Group 2. 47
Figure 3.10. Chalk core plugs (one composite core sample) of Group 3. 48
Figure 3.11. Manufactured heterogeneous core sample included in Group 4. 49
Figure 3.12. Carbonate core samples (limestone and dolostone) included in Group 5. 50
Figure 3.13. Carbonate core samples (limestone and dolostone) included in Group 6. 51
Figure 3.14. The Dean-Stark apparatus. 53
Figure 3.15. The AP-608 Automated porosi-permeameter apparatus. 54
Figure 3.16. The X-ray CT scanner (Siemense SOMATOM) (image taken from www.healthcare.siemens.com.au). 55
Figure 3.17. The Bruker D4 XRD apparatus (image taken from www.bpress.nc). 55
Figure 3.18. The nuclear magnetic resonance (NMR) apparatus. 57
Figure 3.19. The high-pressure saturation cells. 58
Figure 3.20. The ProspaRCA software main menu window. 59
Figure 3.21.The T2 analysis window. 59

Figure 3.22. The stirred high-pressure, high-temperature Parr reactor.....60
Figure 3.23. The sample with the combination layers of heating shrink Teflon, conventional Viton rubber sleeve, fixed end plug and adjustable floating end plug. 62
Figure 4.1. CT Value distribution and X-ray cross-sectional images for sample VS-1 before and after flooding. The CT number profiles and cross-sectional images show signs of massive mineral dissolution along the sample. 71
Figure 4.2. CT Value distribution and X-ray cross-sectional images for sample SC-2 before and after flooding. The CT number profiles and cross-sectional images show signs of dissolution along the length of the sample. From the CT profiles, the sample seems to have become less dense due to mineral dissolution. 72
Figure 4.3. CT Value distribution and X-ray cross-sectional images for sample TC-2 before and after flooding. The CT number profile shows obvious signs of dissolution in the sample, where the sample becomes less dense. The dissolution is obvious at 15.6 mm from the sample inlet, possibly due to the effect of the fracture serving as a preferential flow path through which chemical reactions can occur. 73
Figure 4.4. CT Value distribution and X-ray cross-sectional images for sample VC-2 before and after flooding. The CT number profile shows an increase (mineral precipitation and compaction) and decrease (mineral dissolution) at certain locations, which is attributed to the minerals distribution within the sample. 74
Figure 4.5. CT Value distribution and X-ray cross-sectional images for sample SC-1 inlet part of the composite core before and after flooding. The CT number profiles and cross-sectional images show signs of excessive dissolution close to the inlet of the sample. Then, the CT value increased due to a combination of mineral precipitation and mechanical compaction; the compaction is obvious at 14.4 mm from the core inlet (see red arrows).....75
Figure 4.6. CT Value distribution and X-ray cross-sectional images for sample SC-1 outlet part of the composite core before and after flooding. The CT number profiles and cross-sectional images show signs of reduction in permeability after undergoing the flooding process. The reduction may be attributed to the mineral precipitation and mechanical compaction.....76
Figure 4.7. CT Value distribution and X-ray cross-sectional images for sample CH-1 inlet part of the composite core before and after flooding. The CT number profiles and cross-sectional images show signs of dissolution along the length of the sample. The sample seems to have become less dense due to mineral dissolution. 77

Figure 4.8. CT Value distribution and X-ray cross-sectional images for sample CH-1 outlet part of the composite. The CT number profiles and cross-sectional images show signs of dissolution close to the inlet after undergoing the flooding process. 78
Figure 4.9. CT Value distribution and X-ray cross-sectional images for sample IL-1 part of the composite (two halves). The CT number profiles and cross-sectional images show signs of dissolution after undergoing the flooding process. 79
Figure 4.10. CT Value distribution and X-ray cross-sectional images for sample IL-2 part of the composite (two halves). The CT number profiles and cross-sectional images show almost no change after undergoing the flooding process. 80
Figure 4.11. CT Value distribution and X-ray cross-sectional images for sample VS-3 before and after flooding. The CT number profiles and cross-sectional images show signs of moderate mineral dissolution close to the inlet of the sample. 81
Figure 4.12. CT Value distribution and X-ray cross-sectional images for sample VS-4 before and after flooding. The CT number profiles and cross-sectional images show signs of dissolution close to the inlet of the sample. From the CT profiles, the outlet region of the sample seems to have become denser due to mineral precipitation and mechanical compaction. 82
Figure 4.13. CT Value distribution and X-ray cross-sectional images for sample VC-3 before and after flooding. The CT number profiles and cross-sectional images show signs of excessive dissolution close to the inlet of the sample. From the CT profiles, the outlet region of the sample seems to have become denser due to mineral precipitation and mechanical compaction. 83
Figure 4.14. CT Value distribution and X-ray cross-sectional images for sample TC-1 before and after flooding. The CT number profiles, in particular, show obvious signs of dissolution in the sample, with the sample becoming less dense. This change is evenly distributed throughout the sample, possibly due to the effect of the fracture serving as a preferential flow path through which chemical reactions can occur. 84
Figure 4.15. 2D and 3D images for Sample VS-1 to evaluate the changes. The images show the creation of wormholes along the length of the sample, due to the massive dissolution of calcite minerals. 85
Figure 4.16. 2D and 3D images for sample SC-2 to evaluate the changes. The images show the creation of wormholes along the length of the sample, due to the massive dissolution of calcite minerals. 85

Figure 4.17. 2D and 3D images for sample TC-2 to evaluate the changes. The images show the dissolution of minerals, resulting in the formation of a wormhole, along the path of the pre-existing fracture. 86
Figure 4.18. 2D and 3D images for sample SC-1 inlet part of the composite core to evaluate the changes. The images show the creation of wormholes along the length of the sample due to massive dissolution. However, the collapse of the sample under overburden pressure, which mitigated the dissolution effect, was observed from the visual image (blue circle). 86
Figure 4.19. 2D and 3D images for sample SC-1 outlet part of the composite core to evaluate the changes. The images show that some pores have disappeared along the length of the sample after flooding, which causes a reduction in overall permeability. The reduction may be caused by the precipitation of minerals dissolved from the inlet plug. 87
Figure 4.20. 2D and 3D images for sample CH-1 inlet part of the composite core. The images show the creation of wormholes along the length of the sample, due to massive dissolution. 87
Figure 4.21. The 3D image for sample CH-1 outlet part of the composite core. The image shows dissolution fingers close to the inlet, only after undergoing the flooding process. 88
Figure 4.22. 2D and 3D images for sample IL-1 part of the composite core (two halves). The images show dissolution fingers close to the inlet, only after undergoing the flooding process. 88
Figure 4.23. 2D view of 3D X-ray images and a photo of the inlet for sample VS-3. Both show signs of dissolution in the inlet region of the sample. Wormholes can be seen in the post-flood X-ray image. 89
Figure 4.24. 2D view of 3D X-ray images and a photo of the inlet for sample VS-4. Signs of dissolution are apparent from both evidence. Wormholes can be seen in the post-flood X-ray image. 89
Figure 4.25. 2D view of 3D X-ray images and a photo of the inlet for sample VC-3. Both evidence show excessive dissolution in the inlet region of the sample. 90
Figure 4.26. 2D X-ray images for sample TC-1, showing the location of the natural fractures before and after flooding. 90
Figure 4.27. CT Value distribution and X-ray cross-sectional images for sample SD-1 inlet part of the composite core before and after flooding. The CT number profiles

and cross-sectional images show signs of dissolution close to the inlet. Then, the CT profiles seem to have become denser due to asphaltene precipitation, resulting in a decrease of overall sample permeability. 91
Figure 4.28. CT Value distribution and X-ray cross-sectional images for sample SD-1 outlet part of the composite core before and after flooding. The CT number profiles and cross-sectional images show almost no change in the first half of the sample. However, the CT profiles seem to have become denser at the end of the core sample. The change might be due to asphaltene and mineral precipitation, resulting in a slight decrease in sample permeability. 92
Figure 4.29. CT Value distribution and X-ray cross-sectional images for sample INL-2 inlet part of the composite core before and after flooding. The CT number profiles and cross-sectional images show signs of asphaltene precipitation along the length of the sample, as CT profiles seem to have become denser, resulting in a reduction in sample permeability. 93
Figure 4.30. CT Value distribution and X-ray cross-sectional images for sample INL-2 outlet part of the composite core before and after flooding. The CT number profiles and cross-sectional images show signs of asphaltene precipitation along the length of the sample, as CT profiles seem to have become denser, resulting in a reduction in overall sample permeability. 94
Figure 4.31. CT Value distribution and X-ray cross-sectional images for sample GD-1 before and after flooding. The CT number profile increased (asphaltene precipitation) and decreased (mineral dissolution) at certain locations. This fluctuation may be attributed to the minerals distribution within the sample. 95
Figure 4 32. CT Value distribution and X-ray cross-sectional images for sample INL-1 before and after flooding. The CT number profiles and cross-sectional images show signs of asphaltene precipitation along the length of the sample, as CT profiles seem to have become denser, resulting in a reduction in overall sample permeability. 96
Figure 4.33. 2D and 3D images for sample INL-1 to evaluate the changes. The images show that some pores have disappeared as the image become denser showing more lighter coloured areas especially close to the sample inlet after flooding, which causes a reduction in overall permeability. The reduction may be caused by asphaltene precipitation. 97
Figure 4.34. 3D images for the sample SD-1 inlet part of the composite core to evaluate the changes. The images show that some pores have disappeared along the length of

the sample after flooding as the image become denser showing more lighter coloured areas, which causes a reduction in overall permeability. The reduction may be caused by asphaltene precipitation. 97
Figure 4.35. CT Value distribution and X-ray cross-sectional images for sample VS-2 before and after flooding. The CT number profiles and cross-sectional images show signs of dissolution in the first half of the sample. The CT profiles seem to have become denser due to asphaltene and mineral precipitation. 98
Figure 4.36. CT Value distribution and X-ray cross-sectional images for sample GD-11 before and after flooding. The CT number profiles and cross-sectional images show signs of asphaltene precipitation along the length of the sample, as the CT profiles seem to have become denser, resulting in a reduction in overall sample permeability. 99
Figure 4.37. CT Value distribution and X-ray cross-sectional images for Sample INL-11 before and after flooding. The CT number profiles and cross-sectional images show signs of dissolution along the length of the sample. The CT profiles seem to have become less dense due to mineral dissolution. 100
Figure 4.38. 3D images for sample VS-2 before and after flooding. The images show the creation of wormholes along the length of the sample due to the massive dissolution of carbonate minerals. 101
Figure 4.39. 3D images for sample INL-11 before and after flooding. The images show the creation of dissolution fingers due to mineral dissolution. 101
Figure 4.40. Change in the cumulative porosity (top) and incremental NMR T2 distribution (bottom) of Sample VS-1 before and after flooding. The overall NMR porosity of the sample decreased. Its NMR T2 distribution shifted to the left, indicating that the sample's pore sizes have become smaller after flooding. 102
Figure 4.41. Change in the cumulative porosity (top) and incremental NMR T2 distribution (bottom) of Sample SC-2 before and after flooding. The overall NMR porosity of the sample decreased. Its NMR T2 distribution shifted to the left, indicating that the sample's pore sizes have become smaller after flooding. 103
Figure 4.42. Change in the cumulative porosity (top) and incremental NMR T2 distribution (bottom) of Sample TC-2 before and after flooding. The overall NMR porosity of the sample decreased. Its NMR T2 distribution shifted to the left, indicating that the sample's pore sizes have become smaller after flooding. 104
Figure 4.43. Change in the cumulative porosity (top) and incremental NMR T2 distribution (bottom) of Sample VC-2 before and after flooding. The overall NMR

porosity of the sample decreased. Its NMR T2 distribution shifted to the left, indicating that the sample's pore sizes have become smaller after flooding. 105
Figure 4.44. Change in the cumulative porosity (top) and incremental NMR T2 distribution (bottom) of Sample SC-1 inlet part before and after flooding. The NMR porosity of the sample decreased slightly. Its NMR T2 distribution shifted to the left, indicating that the sample's pore sizes have become smaller after flooding. 106
Figure 4.45. Change in the cumulative porosity (top) and incremental NMR T2 distribution (bottom) of Sample SC-1 outlet part before and after flooding. The NMR porosity of the sample decreased slightly. Its NMR T2 distribution shifted to the left, indicating that the sample's pore sizes have become smaller after flooding. 107
Figure 4.46. Change in the cumulative porosity (top) and incremental NMR T2 distribution (bottom) of Sample CH-1 inlet part before and after flooding. The overall NMR porosity of the sample decreased. Its NMR T2 distribution shifted to the left, indicating that the sample's pore sizes have become smaller after flooding. 108
Figure 4.47. Change in the cumulative porosity (top) and incremental NMR T2 distribution (bottom) of Sample CH-1 outlet part before and after flooding. The overall NMR porosity of the sample decreased. Its NMR T2 distribution shifted to the left, indicating that the sample's pore sizes have become smaller after flooding. 109
Figure 4.48. Change in the cumulative porosity (top) and incremental NMR T2 distribution (bottom) of half Sample IL-1 before and after flooding. The overall NMR porosity of the sample increased. Its NMR T2 distribution shows almost no change, indicating that the sample's pore sizes remained the same after flooding. 110
Figure 4.49. Change in the cumulative porosity (top) and incremental NMR T2 distribution (bottom) of half Sample IL-2 before and after flooding. The overall NMR porosity of the sample decreased. Its NMR T2 distribution shifted to the left, indicating that the sample's pore sizes have become smaller after flooding. 111
Figure 4.50. Change in the cumulative and incremental NMR T2 distribution of Sample VS-3 before and after flooding. While the overall NMR porosity of the sample increased, its NMR T2 distribution shifted to the left, indicating that the sample's pore sizes have become smaller after flooding. 112
Figure 4.51. Change in the cumulative and incremental NMR T2 distribution of Sample VS-4 after flooding. While the overall NMR porosity of the sample increased, its NMR T2 distribution shifted to the left, indicating that the sample's pore sizes have become smaller after flooding. 113

Figure 4.52. Change in the cumulative and incremental NMR T2 distribution of Sample VC-3 after flooding. The overall NMR porosity of the sample decreased. Its NMR T2 distribution showed a moderate shift to the left, indicating that the sample's pore sizes have become smaller after flooding. 114
Figure 4.53. Change in the cumulative and incremental NMR T2 distribution of Sample TC-1 after flooding. While the overall NMR porosity of the sample increased, its NMR T2 distribution did not show any obvious signs of change in its pore sizes.....115
Figure 4.54. Change in the cumulative porosity (top) and incremental NMR T2 distribution (bottom) of Sample SD-1 inlet part before and after flooding. The overall NMR porosity of the sample decreased. Its NMR T2 distribution shifted to the left, indicating that the sample's pore sizes have become smaller after flooding. 116
Figure 4.55. Change in the cumulative porosity (top) and incremental NMR T2 distribution (bottom) of Sample SD-1 outlet part before and after flooding. The overall NMR porosity of the sample decreased. Its NMR T2 distribution shifted to the left, indicating that the sample's pore sizes have become smaller after flooding.....117
Figure 4.56. Change in the cumulative porosity (top) and incremental NMR T2 distribution (bottom) of Sample INL-2 inlet part before and after flooding. The overall NMR porosity of the sample decreased. Its NMR T2 distribution shifted to the left, indicating that the sample's pore sizes have become smaller after flooding.....118
Figure 4.57. Change in the cumulative porosity (top) and incremental NMR T2 distribution (bottom) of Sample INL-2 outlet part before and after flooding. The overall NMR porosity of the sample decreased. Its NMR T2 distribution shifted to the left, indicating that the sample's pore sizes have become smaller after flooding. Due to the similarities between this sample and Sample INL-2 inlet part (e.g. same sample type, mineralogy, etc.), the NMR data show very similar initial trends and then almost identical subsequent alterations for the two samples. 119
Figure 4.58. Change in the cumulative porosity (top) and incremental NMR T2 distribution (bottom) of Sample GD-1 before and after flooding. The overall NMR porosity of the sample decreased. Its NMR T2 distribution shifted to the left, indicating that the sample's pore sizes have become smaller after flooding. 120
Figure 4.59. Change in the cumulative porosity (top) and incremental NMR T2 distribution (bottom) of Sample INL-1 before and after flooding. The NMR porosity of the sample decreased slightly. Its NMR T2 distribution shifted slightly to the left, indicating that the sample's pore sizes have become smaller after flooding. 121

Figure 4.60. Change in the cumulative porosity (top) and incremental NMR T2 distribution (bottom) of Sample VS-2 before and after flooding. The NMR porosity of the sample decreased. Its NMR T2 distribution shifted slightly to the left, indicating that the sample's pore sizes have become smaller after flooding. 122
Figure 4.61. Change in the cumulative porosity (top) and incremental NMR T2 distribution (bottom) of Sample GD-11 before and after flooding. The NMR porosity of the sample decreased. Its NMR T2 distribution shifted slightly to the left, indicating that the sample's pore sizes have become smaller after flooding. 123
Figure 4.62. Change in the cumulative porosity (top) and incremental NMR T2 distribution (bottom) of Sample INL-11 before and after flooding. The NMR porosity of the sample showed almost no change. Its NMR T2 distribution shifted slightly to the left, indicating that the sample's pore sizes have become smaller after flooding. 124
Figure 4.63. SEM images on sample VS-1 at the inlet of the core: (a) before flooding and (b) after flooding show signs of excessive dissolution of carbonate minerals, resulting in highly profound alterations to the pore structure of the the post-flood rock sample... 125
Figure 4.64. SEM images on sample SC-2 at the outlet of the core: (a) before flooding and (b) after flooding show destructive damage caused by the massive dissolution of carbonate minerals, resulting in highly profound alterations to the pore structure of the post-flooding that show signs of mineral precipitation. 126
Figure 4.65. SEM images on sample SC-2 at the outlet of the core: (a) before flooding and (b) after flooding show massive dissolution of carbonate minerals, which cause changes in the pore structure of the post-flood rock sample. 126
Figure 4.66. SEM images on sample TC-2 at the inlet of the core: (a) before flooding and (b) after flooding show signs of dissolution of carbonate minerals at the fracture location and its vicinity, altering the pore-scale structures and the entire surface of the fracture of the post-flood rock sample. 127
Figure 4.67. SEM images on sample SC-1 at the middle of the core: (a) before flooding and (b) after flooding show signs of mineral precipitation and possible migration of carbonate fines. 127
Figure 4.68. SEM images on sample SC-1 at the middle of the core: (a) before flooding and (b) after flooding show signs of mineral precipitation and possible migration of carbonate fines. 128

Figure 4.69. SEM images on sample CH-1 at the middle of the core: (a) before flooding and (b) after flooding show massive dissolution of carbonate minerals, which cause changes in the pore structure of the post-flood rock sample. 128
Figure 4.70. SEM images taken from a thin disk of Sample SD-1: (a) before flooding and (b) after flooding, showing evidence of mineral precipitation and traces of asphaltene deposition. 129
Figure 4.71. SEM images taken from a thin disk of Sample SD-1: (a) before cold toluene cleaning and (b) after cold toluene cleaning clearly showing signs of asphaltene precipitation. 129
Figure 4.72. SEM images taken from a thin disk of Sample INL-2: (a) before cold toluene cleaning and (b) after cold toluene cleaning showing signs of asphaltene precipitation. 130
Figure 4.73. SEM images of sample SD-1 showing dark precipitates that are insoluble in cold toluene. A comparison of the EDS results obtained for these dark areas (points 1 to 3) with the background dolomite on which they sit, showing that the precipitates are mostly carbon and oxygen. 130
Figure 5.1. The evolution of differential pressure across Sample VS-1 during the flooding. The differential pressure decreases as the sample permeability increases under the effect of mineral dissolution. 135
Figure 5.2. 2D view of the 3D X-ray images and a photo of the inlet face of Sample VC-2. Both show signs of significant dissolution in the sample. The overall texture of the sample seems to have been distorted in the post-flood X-ray image under the effect of dissolution and compaction mechanisms. 136
Figure 5.3. Sample SC-1 consisting of two short plugs of SC-1 (inlet part) and SC-1 (outlet part) and a thin disk. 139
Figure 5.5. The evolution of the differential pressure across Sample VS-3 during live brine flooding. Continuous decrease in the differential pressure is a sign of minerals being dissolved from the sample resulting in improved permeability. 143
Figure 5.9. X-ray CT scan vertical and horizontal section images of sample IL-1: (a) before flooding and (b) after flooding. The images clearly show that the live brine tends to follow the large pores and establish new paths. 150
Figure 5.10. Oil recovery verses pore volume injected (PVI) for Sample SD-1. 153
Figure 5.11. Oil recovery versus pore volume injected (PVI) for Sample GD-1. 154
Figure 5.12. Oil recovery versus pore volume injected (PVI) for Sample INL-2. 154

Figure 5.13. Oil recovery versus pore volume injected (PVI) for Sample INL-1. 155
Figure 5.14. Oil recovery versus pore volume injected (PVI) for Sample VS-2.....157
Figure 5.15. Oil recovery versus pore volume injected (PVI) for sample INL-11.....157
Figure 5.16. Oil recovery versus pore volume injected (PVI) for sample GD-11.....158

List of Tables

Table 1. 1. Advantages and disadvantages of the various geological media (data taken from Sally Benson 2011). 4
Table 2. 1. Basic physical properties of pure CO_2 (data taken from IPCC, 2005). 12
Table 2. 2. Some physical constants of pour water (after Wagner and Pruss, 2002). 14
Table 2.3. Measurements CO_2 solubility in aqueous NaCl solutions (after Mao el al.2013). 16
Table 2. 4. Porosity, permeability and minerals compositions of the samples tested by Smith et al. (2013)..... 33
Table 3. 1. Reservoir P–T conditions during the core flooding experiments. 44
Table 3. 2. The composition of the synthetic brine used. 44
Table 3. 3. The composition of the crude oil used in the experiments. 45
Table 3. 4. Characteristics of samples in Group 1. 46
Table 3. 5. Characteristics of the samples in Group 2. 47
Table 3. 6. Characteristics of Group 3 samples. 48
Table 3. 7. Characteristics of Group 4 samples. 49
Table 3. 8. Characteristics of the samples included in Group 5. 51
Table 3. 9. Characteristics of samples included in Group 6. 52
Table 3. 10. NMR acquisition parameters used. 57
Table 3. 11. The common parameters used during the NMR measurements. 57
Table 4. 1. The results of the XRD tests performed on all samples. 67
Table 4. 2. The results of the basic rock property measurements conducted on Group 1 (Limestone) samples tested under flooding Scenario 1 (L: length, OD: outside diameter). 67
Table 4. 3. The results of the basic rock property measurements conducted on Group 2 (Dolostone) samples tested under flooding Scenario 1 (L: length, OD: outside diameter). 68
Table 4. 4. The results of the basic rock property measurements conducted on Group 3 (Chalk) samples tested under flooding Scenario 1 (L: length, OD: outside diameter). 68
Table 4. 5. The results of the basic rock property measurements conducted on Group 4 (manufactured radially heterogeneous limestone) samples tested under flooding Scenario 1 (L: length, OD: outside diameter). 68
Table 4. 6. The results of the basic rock property measurements conducted on Group 5 samples tested under flooding Scenario 2 (L: length, OD: outside diameter). 69

Table 4. 7. The results of the basic rock property measurements conducted on Group 6 samples tested under flooding Scenario 3 (L: length, OD: outside diameter). 69
Table 4. 8. Results of the effluent brine analysis (Ca and Mg) collected during live brine flooding conducted on samples VS-1, SC-1 and TC-2. 131
Table 4. 9. Results of the effluent brine analysis (Ca, Mg and S) collected during live brine flooding conducted on samples VS-3, VS-4 and TC-1. 131
Table 4. 10. Results of the effluent brine analysis (Ca and Mg) collected during WAG flooding conducted on samples VS-2, GD-11 and INL-11 132
Table 4. 11. Wax, resin and asphaltene concentrations in original and effluent oil samples.....132
Table 5. 1. The molar increase of Ca, Mg and S in the effluent brine samples related to the net dissolution of minerals and associated ratios (Ca:Mg molar ratio for dissolution of dolomite =1, Ca:S molar ratio for dissolution of anhydrite =1). 142

Chapter 1

1. Introduction and Objectives

Carbon dioxide (CO_2) is an inorganic matter made up of one carbon and two oxygen atoms. Humans inhale oxygen and exhale CO_2, while plants absorb CO_2 and release oxygen through a process known as photosynthesis. CO_2 is found almost everywhere in the nature, such as in the air, underground geological settings (e.g. petroleum gas or natural CO_2 reservoirs), oceans and seas around the world (USCSC 2009).

Along with a few other gases such as CH_4 and water vapour, CO_2 is a greenhouse gas whose existence in the Earth's atmosphere is essential to keep the Earth habitably warm. In fact, CO_2 accounts for over 60% of the greenhouse gases and much of it is released from burning fossil fuels (Halmann et al. 1998a). However, an excessive increase in the concentration of the greenhouse gases in the atmosphere can cause an unusual increase in the Earth's surface temperature and give rise to the global warming phenomenon (UNFCCC 2002). Global warming is often associated with very complex climatic and ecological problems that the world is facing today (UNFCCC 2002).

Carbon is the main component of many fuels, including crude oil, natural gas and coal burning of which results in the release of significant CO_2 emissions worldwide every day. Indeed, over 85% of the world's energy needs are provided by fossil fuels, and the U.S. Department of Energy (DOE) predicts that fossil fuel demand will remain unchanged until 2030 (USCSC 2009). For instance, the majority of the global electricity output comes from the combustion of fossil fuels. Furthermore, the world is experiencing rapid growth in population and economic boom in many industrial sectors, all of which would lead to further increase in energy consumption (Bachu 2008b). A study by the University of New South Wales (UNSW) has revealed that CO_2 emissions from power stations in Australia is expected to increase by about 40% from about 200 Mt in 2004 to about 280 Mt by 2020.

The world's most updated record for atmospheric CO_2 concentrations, measured at the Mauna Loa Observatory in Hawaii, shows that the atmospheric concentration of carbon dioxide has risen from less than 316 ppm in 1958 to almost 408 ppm in May 2016 (Figure 1.1). This data indicates an increase of 2.1 ppm per year, for the fifteen years leading to 2015, compared to the 1.5 ppm yearly increase between 1990 and 2000 (Scripps Institution of Oceanography 2015). As mentioned earlier, it is a known fact that such increases in the greenhouse-gas

concentrations in the atmosphere is the main drive behind the global warming phenomenon and the subsequent climate change (Halmann et al. 1998b).

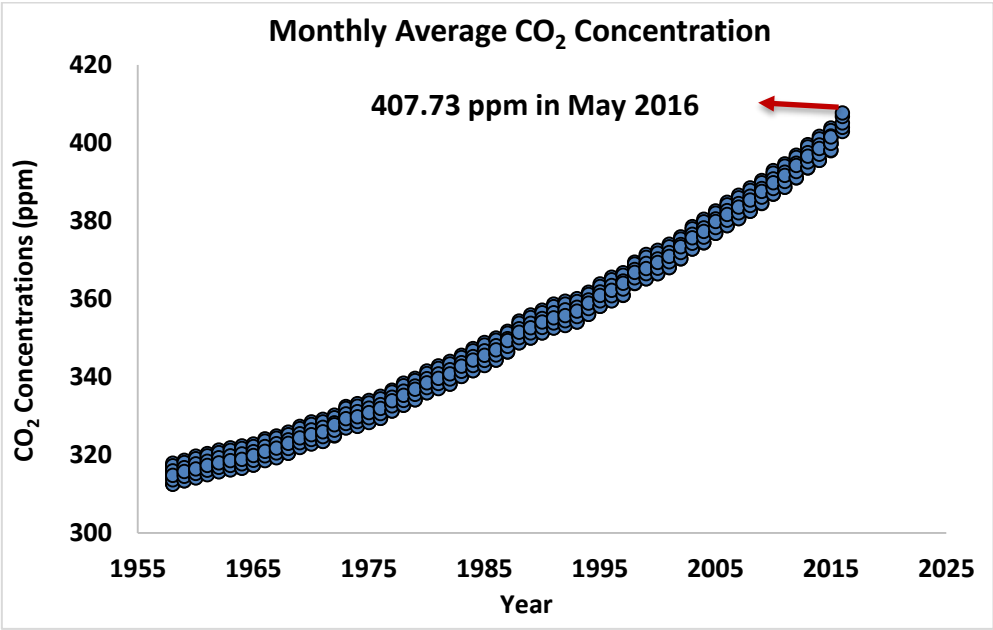

Figure 1. 1. Current carbon dioxide concentrations in May 2016 (data taken from Scripps CO_2 Program UCSD / Scripps Institution of Oceanography).

In order to mitigate climate change and the risks associated with it, a number of countries have committed themselves to reduce the amount of CO_2 released into the atmosphere. In order to help the cause, scientists have been searching for effective solutions to limit the amount of CO_2 entering the atmosphere. Carbon capture and storage (CCS) has been found to be a long-term option for reducing the CO_2 emissions originating from human activities. The CCS involves the capture of the unwanted gas at its sources (e.g. power stations) and then, its subsequent transportation through pipelines to a suitable storage location, where it could be compressed and injected into an underground geological formation or the ocean bed (Figure 1.2).

Figure 1. 2. The process of carbon capture and storage (CCS).

By volume, ocean beds provide the largest storage capacity among all possible storage media. However, there are many complex issues and uncertainties associated with storing CO_2 in the oceans, including the environmental impacts (IPCC 2005), which need to be addressed before

their utilisation. On the other hand, CO_2 injection and storage in underground geological formations (i.e. mature or depleted oil and gas reservoirs, aquifers and unmineable coalbeds) is an immediate option, which presents less environmental complexities and provides storage capacity for large amounts of CO_2 (Figure 1.3).

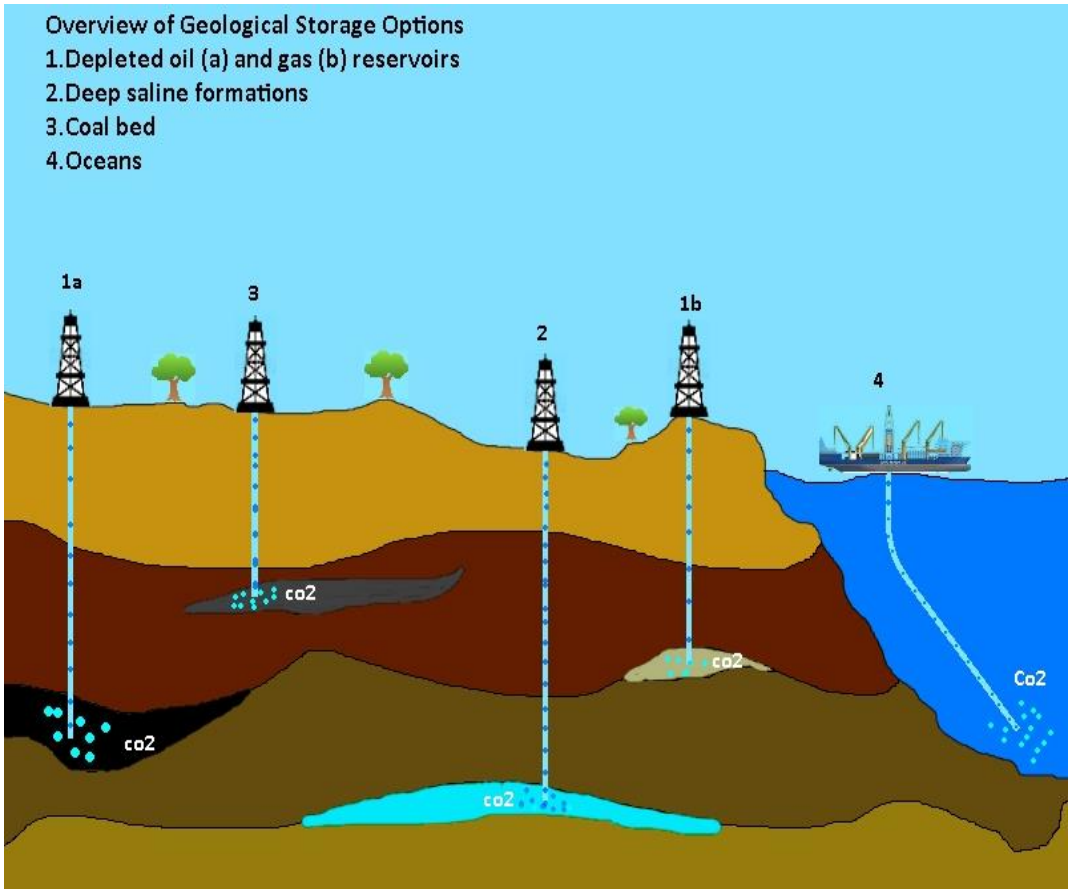

Figure 1. 3. Various types of CO_2 storage sites.

1.1. Underground CO_2 storage

Presented in Table 1.1 are the advantages and disadvantages of various geological media that can be used for CO_2 storage. Among the candidate media, deep saline aquifers and depleted hydrocarbon reservoirs are very often regarded as the most viable options. Furthermore, the saline formations are more often named as the preferred option because of their very large storage capacity and widespread availability around the globe. In addition, this type of medium is available for immediate utilisation and their effectiveness has been demonstrated by almost a 100 years of natural gas storage in the United States and Europe. However, in general, a saline aquifer needs to be overlaid by a seal or caprock to prevent the upwards flow of any mobile CO_2 reaching the top of the aquifer into the overlaying formations, which for example, may contain important natural resources such as potable water (Bachu 2008a; Benson et al. 2008; IPCC 2005).

Table 1. 1. Advantages and disadvantages of the various geological media (data taken from Sally Benson 2011).

Storage site	**Advantages**	**Disadvantages**
Oil and Gas Reservoirs	• Well-characterised volume • Known seal • Potential enhanced recovery to offset cost	• Smallest capacity (~25 gigatons of carbon) • Limited in number • Requires infrastructure to transport CO_2
Deep saline aquifers	• Large capacity (~250 to 900 gigatons of carbon) • Widespread availability	• Poorly characterised • Greatest geological uncertainty • Unknown seal effectiveness
Unmineable Coal Beds	• Adjacent to many large power plants (CO_2 source) • Potential gas (methane) recovery to offset cost	• Poorly characterised • Difficult to define "unmineable" coal • Potential coal resources may be rendered unusable

As the other viable type of CO_2 storage site, depleted hydrocarbon reservoirs have a unique and important advantage, which is proven containment and storage integrity. These reservoirs have already held hydrocarbons in place for millions of years. Even CO_2 itself can be found in deep reservoirs, where it has been safely stored for thousands or millions of years (USCSC 2009). Furthermore, CO_2 injection has been widely used for enhanced oil recovery (EOR) in such media with different types of lithology (sandstone and carbonate) and a wide range of crude oils (light to heavy). Depending on the in-situ conditions of pressure and temperature, as well as the crude oil characteristics, the injection of CO_2 may be applied in either miscible or immiscible modes (Gale et al. 2011; Zekri et al. 2013; Zekri et al. 2009). However, regardless of the mode employed, a relatively high additional oil recovery may be achieved. This extra oil recovery can offset the cost of the CO_2 injection.

Compared against a depleted oil reservoir, an identical depleted gas reservoir has the potential to hold a larger amount of CO_2 because, in general, a gas reservoir yields a higher recovery factor (RF), thus creating more space available for the CO_2 to occupy. Also, any residually trapped or bypassed natural gas is less dense and highly compressible (Benson 2004; Class et al. 2009; Seo et al. 2003). Another benefit of using hydrocarbon reservoirs to store CO_2 is that they may have the infrastructure needed for CO_2 injection available on site already. While storing CO_2 in hydrocarbon bearing media offers some benefits, it may also suffer from a number of drawbacks. Most of the likely uncertainties are associated with the presence of

hydrocarbon in their pore space, such as reduced injectivity and the complex phase behaviour of the in-situ created fluid mixtures (Oldenburg et al. 2011; Saeedi et al. 2012).

An important suitability criterion for any geological CO_2 storage site is its depth. It is widely argued that CO_2 needs to be stored in its supercritical state, as its density is the highest when supercritical under the elevated temperatures encountered in deep geological structures (Figure 1.4) (IEA 2008; Bennion et al. 2005; Benson et al. 2008). The dense supercritical CO_2 takes up less space and therefore, increases the storage capacity of a site. The favourable conditions for the supercritical state to occur can be achieved in most underground geological formations below the depth of 800m, corresponding to the pressure and temperature of about 7.38 MPa and 31.95˚C, respectively (IEA 2008; Span et al. 1996).

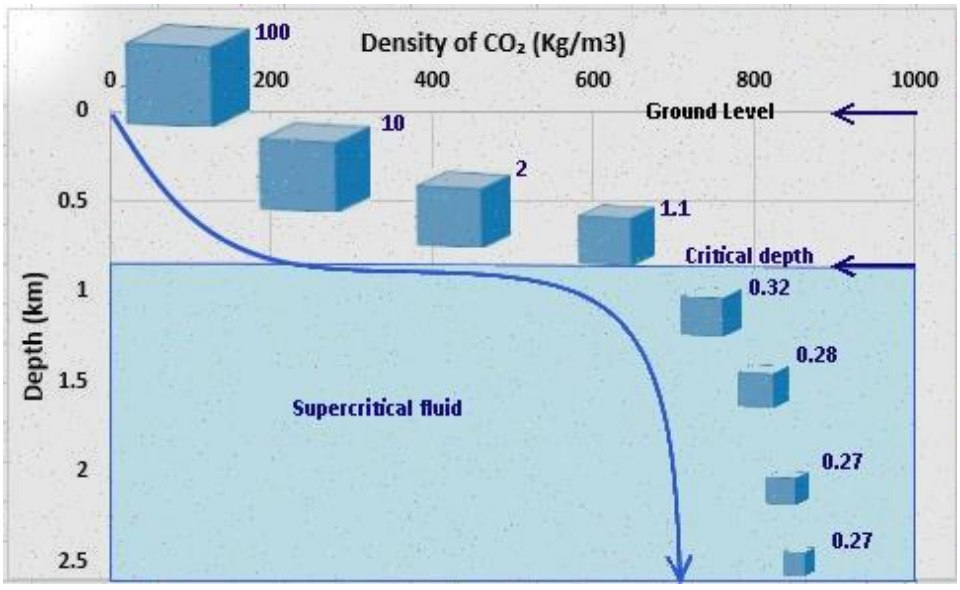

Figure 1. 4. CO_2 density increases with depth (Data taken from IEA 2008).

The injection of CO_2 into subsurface geological formations was first undertaken in Texas, USA, in the early 1970s, as part of the CO_2 enhanced oil recovery (CO_2-EOR) projects and has been ongoing there and many other locations ever since. Carbon dioxide injection for enhanced oil recovery has been implemented in Canada too. The first successful application of CO_2-EOR in Western Canada began in 1984 at the Joffre Field in southern Alberta (Sally Benson 2011; Burrowes et al. 2001). Currently, apart from EOR applications, there are a number of pilot and commercial CO_2 storage projects either ongoing or being proposed. One large-scale commercial injection site is the Sleipner Project operated by Statoil, where more than 17 Mt of CO_2 has been injected into a deep offshore saline formation since 1996 in the North Sea, Norway. At the In Salah project in Algeria, operated by Sonatrack, BP and Statoil, CO_2 was removed from the natural gas and injected into a depleted gas reservoir outside the boundaries

of the main gas fields being produced. In this project, from 2004 to 2011, about 1.2 Mt of CO_2 was injected per year into the depleted gas reservoir (IEA 2008; Wright et al. 2009).

Regardless of the type of the geological medium used for CO_2 storage, the injection process and the subsequent interactions between the various elements of the underground CO_2-brine-rock system is expected to result in the occurrence of a variety of complex chemical and physical mechanisms which could then introduce uncertainties into how the injection and storage process may proceed over intermediate to long term. Therefore, the likelihood of occurrence, exact nature and implications of these mechanisms have to be evaluated and understood before the commencement of any CCS project (Izgec et al. 2008; Saeedi 2012). In preparation to outline the particular objectives set for this research work, a more detailed overview of the physical and chemical mechanisms/processes referred to above and their end effects are provided below.

- *Fluid-rock and fluid-fluid interactions*

  Upon injection, CO_2 would dissolve into the in-situ residnet fluids (mostly brine) forming a reactive solution (carbonic acid) that can then intercat with the formation rock and, for example, cause mineral dissolution. The degree of such interactions strongly depends on the in-situ pressure and temperature, type of minerals present in the rock and the mineral surface area that is available for the reactions to take place (Luhmann et al. 2014). Subsequnetly, any generated chemical species in the solution may be transported further into the rock formation away from the injection point and/or begin to precipitate in the pore space of the rock formation in the form of new minerals (Egermann et al. 2005). The dissoltion of minerals may also weaken the sructural strength of the rock resulting in its micro- and marco-scale deformation/compaction. Furthermore, the above fluid-rock intercations may result in the release of fine particles from the matrix of the rock that could also be transported further downstream of the flow and bridge and/or plug pore-throats. In addition, in the case of CO_2-EOR, in-situ interactions of CO_2 with the crude oil may result in the destabilisation and then precipitation of some crude oil's heady fractions such as asphaltenes.

- *Change in petrophysical properties of the rock formation*

  The earlier mentioned intercations/mechanisms (e.g. mineral dissolution and precipitation, mechnical compaction, fines migration and asphaletene precipitation), depending on their intensity, could lead to changes in the petrophysical properties (permeability, pore size distribution, porosity, etc.) of the rock formation and

subsequnetly alter the storage capacity, injectivity and generally, the multiphase flow characteristics of the formation (Egermann et al. 2005; Izgec et al. 2005; Luquot et al. 2009). It is also worth noting that seme of these mechanisms may also result in other more localised complication such as those associated with wellbore intergrity and stability.

1.2. Research Objectives

Carbonate formations constitute more than half of the world's petroleum reservoirs, making them likely candidates for CO_2 injection for the both purposes of storage and EOR. Furthermore, given the high proportions of highly reactive minerals (e.g. calcite, dolomite, anhydrite, etc.) in their composition, the interactions between carbonate rock formations and the in-situ created or injected fluid mixtures involving CO_2 are expected to be much more pronounced in such formations than their sandstone counterparts.

Taking into account the above important points and the discussion present in the previous section of this chapter around possible fluid-fluid and fluid-rock interactions and their impacts, the ultimate goal of this research is to conduct a collection of various laboratory tests to obtain a better understanding of the possible effects that the introduction of CO_2 into the deep subsurface environment may have on the characteristics of some typical carbonate formations. Towards achieving the above stated ultimate goal, the following objectives have been pursued:

I. To perform a number of core-flooding experiments exposing carbonate rock samples (limestone and dolostone) to CO_2 and/or carbonated brine under elevated pressure and temperature.
II. To use a collection of diagnostic laboratory techniques and tools that can be used to characterise the rock samples before and after flooding and determine any alterations to the petrophysical properties of the samples.
III. To pinpoint and understand the mechanisms behind any observed changes in the samples and, where possible, relate them to the original sample properties/features, as well as the experimental conditions.
IV. To investigate the effect of the three laboratory injection schemes of continuous carbonated brine flooding, continuous CO_2 injection and water-alternating-gas (WAG) flooding on the results obtained in pursuing objectives I-III.

1.3. Organisation of Thesis

This thesis is divided into six individual but interrelated chapters. The current chapter (Chapter 1) is to set the scene and provide a brief description of the problem at hand and how this research may fit into the bigger picture. Initially, it presents a general introduction to the global warming phenomenon. Then, it discusses the CCS as a potential remedial technique to reduce CO_2 emissions into the atmosphere. Presented in the end of the chapter is the ultimate goal of this study and a full list of its objectives.

The second chapter focuses on providing a detailed background behind this work as that would form the foundation for the rest of the chapters which cover and discuss the particulars of the experimental work conducted in this research program. Most parts of this chapter provide a compreheisive background to the fluid-fluid and fluid-rock interactions that may occur with the introduction of CO_2 into deep geological media and rock changing mechanisms that may subsequently take place. At the end of this chapter, a review is done on a number of related previous studies with the main aim of demonstrating the importance of the points discussed early on in the chapter.

Chapter 3 can be divided into two major parts. The first part presents in details the experimental setups used to carry out the laboratory works. In the second part, the experimental procedures and steps involved in conducting various experiments are outlined and discussed. The fourth chapter includes a comprehenisve coverage of the results obtained from all experimental works. Subsequnetly, Chapter 5 presents a comprehensive discussion on the results obtained as presented previously in Chapter 4.

Finally, Chapter 6 includes a short summary and main conclusions that can be drawn from this research. It also provides recommendations for further research built upon the findings of this work.

Chapter 2

2. Background: In-situ Interactions and Active Mechanisms

The underground geological media often have a very complex nature at all scales (i.e. pore-, core- and field-sacle). This complexity combined with other factors such as multiphase nature of the fluid system, fluid-rock intercations, phase behaviour of the fluid system etc., would influence the fluid flow in these media making its quantitive description uncertaine and difficult to acheive. The simplest form of fluid flow in the porous media, known as the linear steady-state type, can be described as the one-dimensional flow of a single fluid, under a constant pressure gradient measured in the direction of the flow (Figure 2.1). Due to simplicity, this type of flow can be quantified using the empirical relationship (Eq. 2.1) developed by Henry Darcy in 1856 (Tiab et al. 2004; Whitaker 1986). However, the application of this equation in real life subsurface fluid flow processes is only valid under three main assumption as outlined and described below.

- *Flow is laminar (i.e. fixed flow paths or streamlines)*:
  This is a reasonable assumption in reservoir-scale as the typical flowrates during underground fluid flow processes are too low to promote turbulence. However, turbulent flow can occur around a wellbore where fluids flow at high velocity resulting the so called Non-Darcy flow (Saeedi 2012; Tiab et al. 2004). The net-effect of any turbulence may be analytically modelled using techniques such as that developed by Forchheimer (1901) where he incorporated the effect of turbulence into the Darcy equation as an additional flowrate-dependent pressure drop (Eq. 2.2).

- *No chemical reactions occur between the fluid and reservoir rock*:
  This assumption is often valid under normal circumstances however, would not hold if there is a change (e.g. clay swelling, mineral dissolution, etc.) induced by the fluid to the porous medium.

- *One phase is present at 100% saturation*:
  Multiple phases (e.g. CO_2, water, oil, natural gas, etc.) are commonly involved in underground fluid flow processes. Therefore, the Darcy equation in its simple original form (Eq. 2.1) is inadequate to describe the fluid flow nature of such processes. However, as depicted by Eq. 2.3, the origianl Darcy equation can be readily amended

to account for multiphase flow using the concept of relative permeability (Whitaker 1986; Tiab et al. 2004; Saeedi 2012).

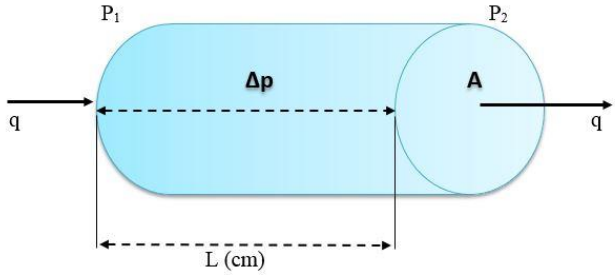

Figure 2. 1. One-dimensional single-phase fluid flow through a porous medium.

$$q = -\left(\frac{k}{\mu}\right)\left(\frac{A}{L}\right)\Delta p \qquad \text{Eq. 2.1}$$

where: q = rate of fluid flow *($cm^3.s^{-1}$)*

A = cross-sectional area open to flow *(cm^2)*

μ = dynamic viscosity of flowing fluid *(cp)*

Δp = pressure drop across porous medium *(atm)*

L = length of porous medium *(cm)*

k = permeability *(Darcy)*

$$-\frac{dp}{dL} = \left(\frac{\mu}{k}\right)v + \beta\rho v^2 \qquad \text{Eq. 2.2}$$

where:

$\frac{dp}{dL}$ = pressure grident measured in the direction of the flood *($atm.cm^{-1}$)*

v = Darcy veocity *($cm.s^{-1}$)*

ρ = fluid density *($gr.cm^{-3}$)*

β = emprically driven inertial factor *(cm^{-1})*

The rest of the parameters included in Eq. 2.2 have the same meaning as those included in Eq. 2.1.

$$q_f = -\left(\frac{kk_{rf}}{\mu_f}\right)\left(\frac{A}{L}\right)\Delta p_f \qquad \text{Eq: 2.3}$$

where: f = refer to the individual fluids that flow in a multiphase flow system

k_{rf} = reletive prmeability of fluid f (i.e. effective permeablity of fluid to absolute permeability (k) of the porous medium)

The rest of the parameters included in Eq. 2.3 have the same meaning as those included in Eq. 2.1.

As discussed above, any deviation from the first and third assumptions that underpin the Darcy's Law can be taken care of by some sort of mathematical/analytical amendment to the original Darcy equation. However, no similar remedy may be proposed in the case of any deviation from the second assumption. That is becuase the nature of the effects that such deviation may impose on the fluid flow chracteristics of a fluid-rock system are highly case-dependent and may vary (qualitatively and quantitativly) substantially from one case to another. Due to the highly reactive nature of the fluid mixtures created during CO_2 injection into deep rock formations and/or the possible complex intercations between CO_2 and in-situ crude oil (in the case of CO_2 injection into oil reservoirs), the degree of deviation from the second assumption during such underground processes could be potentially high. It is worth noting that any deviation from this assumption could impact on a number of important near wellbore- and field-scale fcators such as the injectivity, storage capacity, residual saturations, relative permeabilities, flood sweep efficiency, wellbore integrity/stability, etc.

Following on from the above introductory section, the purpose of this chapter is two-fold. Initially, a detailed description of a number of factors that are expcetd to influnce multiphase flow during CO_2 injection/flooding in deep underground rock formations is provided. This description will be presented primarily in the context of the above paragraph and the objectives put forth for this research in Chapter 1. The second part of this chapter provides a review of a few closely related studies. It is worth noting that the purpose of the second part is not to provide a comprehensive review of the relevant literature. Instead, it is to demonstrate the effects of the mechnisms and factors introduced and discussed in the first part of this chapter using the results obtained in some example studies conducted by other researchers previously. Further review of the relevant litreture would be presented throughout Chapter 5 where the results of this study would be interpreted and discussed in details.

2.1. Thermo-physical properties of fluids

As explicitly demonstrated by the Darcy's Law (Eq. 2.1), fluid flow in the porous media is directly influenced by the thermo-physical properties of the fluids involved. Furthermore, as indicated earlier, multiphase flow in underground reservoirs, especially when it involves CO_2, may be associated with complex processes and mechanisms controlled by the intercations between the fluids themselves or the fluids and the host rock formation. The degree of such intercations in turn is a function of the thermophysical properties and kinetics of the in-situ fluid system (e.g. CO_2-brine, CO_2-crude oil) as well as the prevailing underground conditions (e.g. pressure (P), temperature (T), salinity, etc.). For instace, P, T, salinity and the general phase behaviour of the CO_2-brine system would control CO_2 solubility into brine, brine pH, fluids viscosity and density some of which, for example, impact heavily on the kinetics of any geochemical reactions to occur. Therefore, given the particular objctives of this study, the primary purpose of this section is to present a short overview of the basic thermophysical properties of each fluid phase (e.g. pure CO_2, brine and aqueous solutions) inolved during CO_2 injection/flooding.

2.1.1. Pure CO_2

Some basic physical properties and phase diagram of pure CO_2 are provided in Table 2.1 and Figure 2.2, respectively. Although CO_2 exists as a gaseous phase under standard conditions, as can be deduced from its phase diagram (Figure 2.2), under the in-situ conditions of interest for CO_2 storage (depth>800m) and almost for all potential candidate reservoirs for CO_2-EOR around the globe, CO_2 would exist in its supercritical state (Müller 2011). One major advantage of storing CO_2 in its supercritical state is its high density enabling the storage of a high mass of CO_2 per unit volume of the rock pore space (Saeedi 2011). Supecritical CO_2 has a viscosity close to that of its gaseous phase but a density close to that of its liquid phase (IPCC 2005). Figures 2.3 and 2.4 show variation in the viscosity and density of pure CO_2 at various P-T conditions, respectively.

Table 2. 1. Basic physical properties of pure CO_2 (data taken from IPCC, 2005).

Property	Value
Molecular weight *(gr/mol)*	44.01
Critical temperature *(°C)*	31.1
Critical pressure *(MPa)*	7.39
Critical density *(kg m^{-3})*	467
Triple point temperature (°C)	-56.5
Triple point pressure (MPa)	0.518
Boiling (sublimation) point (101.3 KPa) (°C)	-78.5

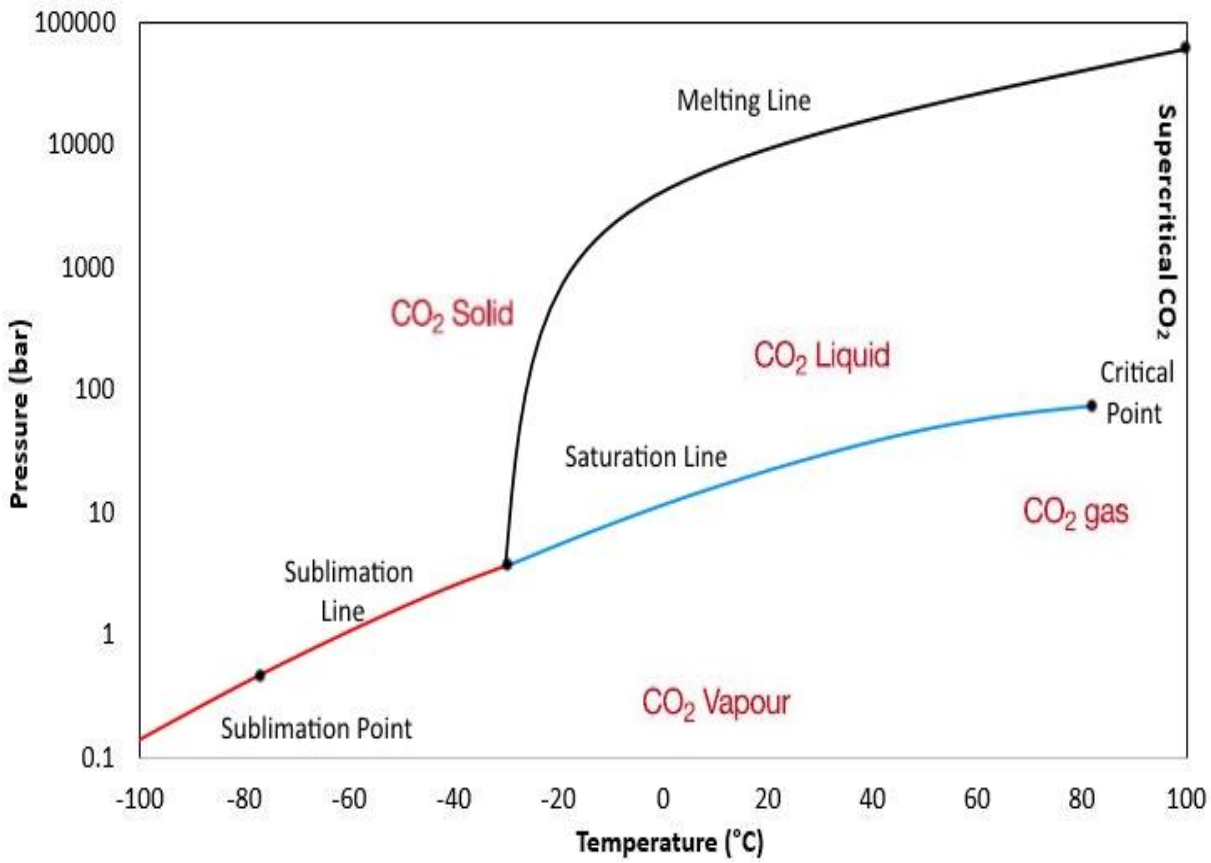

Figure 2. 2. Phase diagram for pure CO_2 (data were taken from IPCC, 2005).

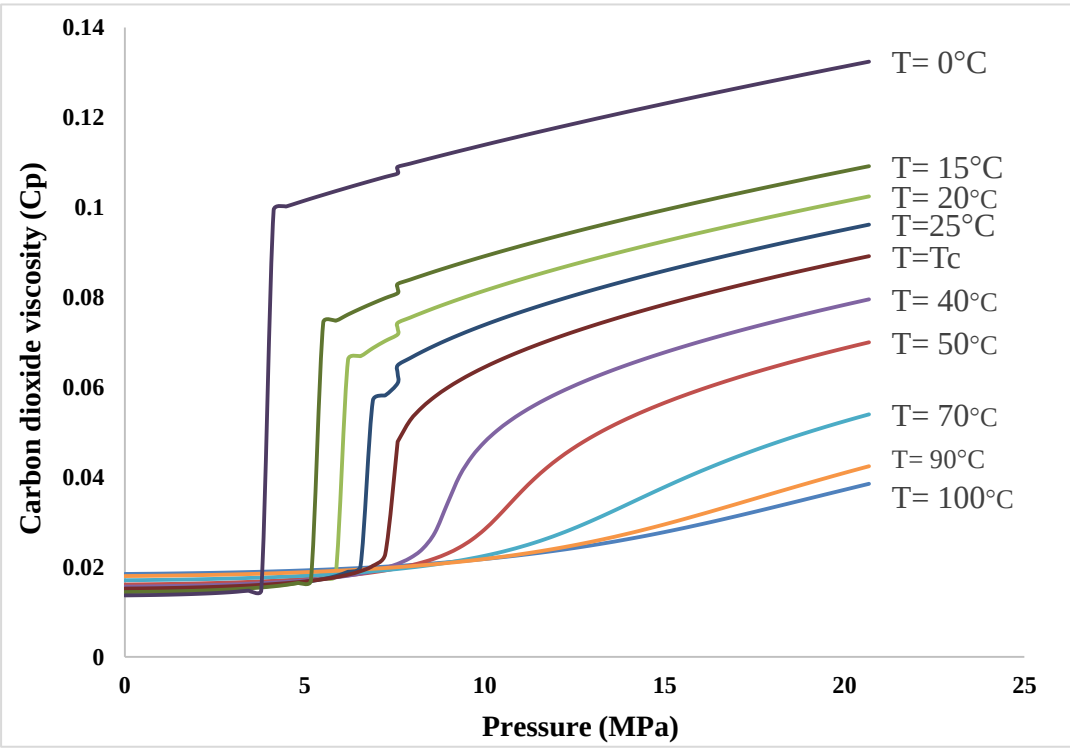

Figure 2. 3. Pure CO_2 viscosity at various P-T conditions (Data were taken from NIST, 2010).

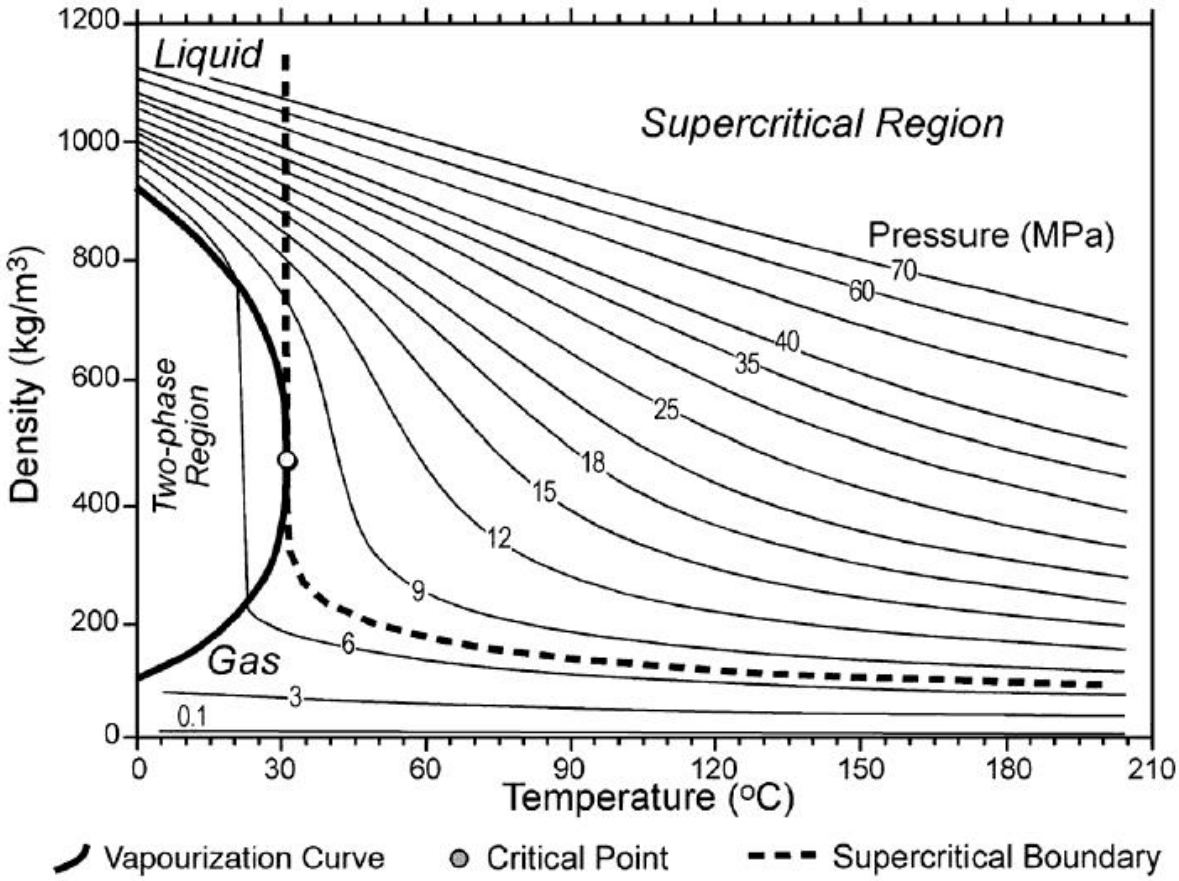

Figure 2. 4. Density of pure CO_2 as a function of temperature and pressure (data were taken from Bachu, 2008).

2.1.2. Pure water (H_2O)

Pure water (H_2O) is a substance whose phase behaviour and thermophysical properties have been very well charactrised much of it is owed to the effortless research conducted by International Association for the properties of Water and Steam (IAPWS) to date (Wagner et al. 1993). The phase diagram and some basic thermophysical propeties of pure water are presented in Table 2.2 and Figure 2.5. Pure water has a nutral pH that can change with the disolution of various substances (e.g. CO_2) in it.

Table 2. 2. Some physical constants of pour water (after Wagner and Pruss, 2002).

Property	***Value***
Molar mass, M *(gr/mol)*	18.015
Specific gas constant, R *(kJkg $^{-1}$ k^{-1}))*	0.461
Critical density, ρ_c *(kg/m^3)*	322
Triple point liquid density, ρ_t (kg/m^3)	999.793
Triple point vapour density, ρ_t (kg/m^3))	0.597

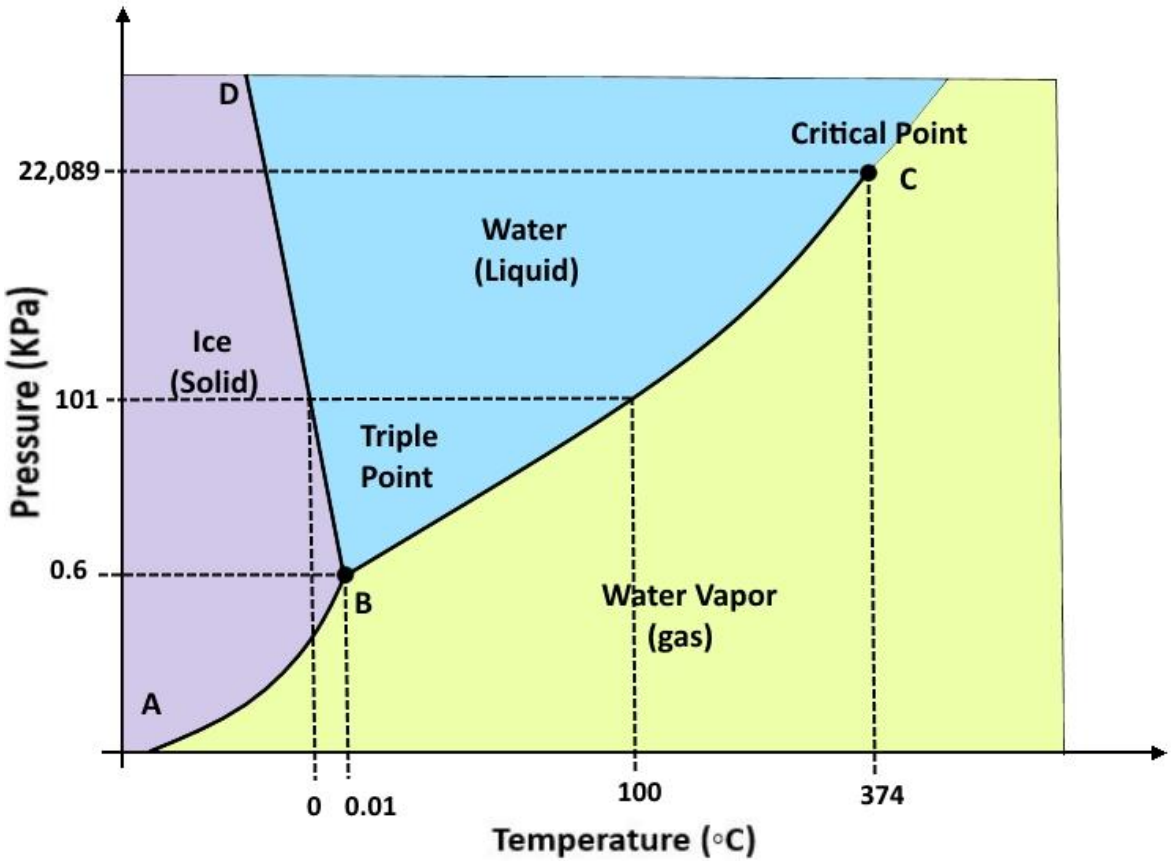

Figure 2. 5. The phase diagram of pure water.

2.1.3. In-situ fluid mixtures

Depending on the type of the underground geological medium (e.g. saline aquifer, hydrocarbon reservoir, etc.) that CO_2 may be injected into, there may be a range of in-situ reactions occurring between the injected CO_2 and the resident fluids and then, possibly, between the resultant fluid mixtures/solutions and the host rock formation. For instance, during CO_2 injection into a saline aquifer, CO_2 comes into contact with the formation brine and begins dissolving in it creating a reactive acidic solution (Enick et al. 1990; Hangx 2005) which then can react with some of formation's constituent minerals. In order to predict and better understand the possible interactions between the various elements of the pertinent underground fluid-rock systems and the possible consequences of such interactions, it is essential to review and understand the thermodynamic properties and phase behaviour of the suspect fluid mixtures and related geochemical processes (Jindrová et al. 2015).

2.1.3.1 CO_2-brine system

As indicated earlier, upon injection, CO_2 would begin dissolving into the residence formation water. In fact, for the case of CO_2 geological storage, as will be discussed in greater details later, the dissolution of CO_2 into brine is looked into as one of the four possible CO_2 trapping

mechanisms. The solubility of CO_2 in a formation water increases with increase in pressure but decreases with increase in temperature and brine salinity. As mentioned earlier and will be discussed in further details later, with the dissolution of CO_2 into the formation water its pH would decrease turning it into a reactive solution (Müller 2011; Pruess et al. 2001). Furthermore, the CO_2 dissolution would make the brine denser causing it to sink to the bottom of the storage formation at a rate influenced by other factors such as viscosity, formation vertical permeability, degree of formation heterogeneity, etc. Table 2.3 presents a comprehensive list of the research work in which CO_2 solubility in aqueous NaCl solutions have been experimentally measured.

Table 2.3. Measurements CO_2 solubility in aqueous NaCl solutions (after Mao el al.2013).

References	T (C˚)	P (bar)	m_{NaCl} (mol kg^{-1})	Nd
Burmakina et al. (1982)	25	1	0–0.201	9
Cramer (1982)	23.6 – 238.6	8–62	0–1.95	20
Gehrig et al. (1986)	141.85–509.85	30–2717	1.09–4.28	64
Nighswander et al. (1989)	80.5–200.5	20.4–102.1	0–0.18	67
He and Morse (1993)	0–90	0.07–1.0	0.1–6.14	31
Rumpf et al. (1994)	39.99–159.97	1.51–96.37	0–5.999	76
Vázquez et al. (1994a)	24.95	1.045	0–2.91	5
Vázquez et al. (1994b)	19.95–34.95	1.04–1.07	0.692–2.903	16
Zheng et al. (1997)	5–64.98	0.69–0.95	0.68–3.32	18
Gu (1998)	30–50	17.73–58.96	0.5–2.0	60
Schmidt and Bodnar (2000)	275–650	450–3500	1.09–11.41	42
Kiepe et al. (2002)	40.23–79.92	0.98–101	0.52–4.34	64
Bando et al. (2003)	30–60	100–200	0.18–0.56	36
Koschel et al. (2006)	49.95–99.95	50–202.4	1–3	14
Ferrentino et al. (2010)	39.85	100–150	0.18	2
Liu et al. (2011)	45	21–158.3	1.93–1.98	8
Yan et al. (2011)	50.05–140.05	50–400	0–5	54

Note: Nd is a number of measurements.

2.1.3.2 CO_2-crude oil system

Although investigating the performance of CO_2-EOR is not a primary focus of this research work, as will be discussed in further details in chapters 3-5, some of the experiments conducted here involved crude oil as one of the fluids present in the pore space of some of the rock samples. This was to address the fourth objective specified for this research in Chapter 1. Therefore, a brief overview of the reactions that may occur between the crude oil and injected CO_2 is presented in this section of this chapter.

The process of CO_2-EOR can be broadly classified into two major types of miscible and immiscible. The miscibility of the injected CO_2 depends on many factors such as the in-situ

pressure and temperature and the phase behaviour of the crude oil system (Mosavat et al. 2014; Hawez et al. 2014; Emera et al. 2006; Simon et al. 1965). The miscible displacement occurs at a pressure above the Minimum Miscibility Pressure (MMP) of the oil (Babadagli 2006; Hawez et al. 2014) and, therefore, in-situ pressures less than MMP would yield an immiscible displacement. For the purpose of EOR, CO_2 may be injected continuously or as part of a Water Alternating Gas (WAG) process. The WAG injection scheme has the potential to improve the sweep efficiency of the injected CO_2, by supressing the gas mobility and improving the conformance of the flood (Jiang et al. 2010; Cârcoană 1992).

When CO_2 is dissolved in the crude during EOR processes, a number of physical and chemical processes may take place (e.g. viscosity reduction, oil swelling, asphaltene precipitation, interfacial tension (IFT) reduction, etc.) that can potentially affect the performance of the recovery process and the phase behaviour of the system (Li 2013; Mosavat et al. 2014).

CO_2 solubility in crude oil

The dissolution of CO_2 into crude oil could result in complex phase behavioural phenomena such as asphaltene precipitation (Nguele et al. 2016; Chung et al. 1991; Hirschberg et al. 1984). The dissolution of CO_2 into the crude oil is also the root cause of the other effcetive recovery enhancing mechanisms (e.g. viscosity reduction, oil swelling, IFT reduction, etc.) during CO_2-EOR.

Oil viscosity reduction

Oil viscosity decreases dramatically with increasing CO_2 content in the oil and consequently leading to improved mobility and increase in the oil recovery (Emera et al. 2006; Li 2013). Viscosity reduction is higher in magnitude for heavy oils (initially more viscous) as compared to light oils (Holm et al. 1974; Li 2013). Pressure and temperature play a significant role in dictating the viscosity of the CO_2-Oil mixture.

Oil swelling

Similar to viscosity reduction, oil swelling is considered as another effective mechanisms of oil recovery during CO_2-EOR. The swelling of the oil would disturb the saturation distribution of the fluids present in the pore space of a rock (i.e. oil and water) resulting in the mobilisation of the otherwise trapped residual oil. The degree of oil swelling during CO_2 injection is controlled by pressure, temperature and crude oil compositions (Li 2013).

Interfacial tension reduction

When CO_2 is injected into an oil reservoir, the IFT of in-situ fluid system may be reduced, minimising the significance of the capillary forces responsible for the entrapment of the oil

phase resulting in the mobilisation of the trapped residual oil (Li 2013; Sun et al. 2005; Mangalsingh et al. 1996; Jha 1986).

Asphaltene precipitation

Asphaltenes are molecular substances that are naturally present in the crude oil in a range percentages (typically 1-20%). Asphaltenes have the highest molecular weight among hydrocarbon susbtances and a complex chemical composition mainly consisting of carbon, hydrogen, oxygen, nitrogen, sulfur and a low percentage of nickel (Ancheyta 2010; Demirbas 2016). As a way of indentification, asphaltenes are known to be insoluble in n-heptane (C_7H_{16}) but soluble in toluene (Demirbas 2016).

One of the potential major problems associated with CO_2 flooding during EOR processes is asphaltene deposition. Under initial reservoir conditions, the asphaltenes are in suspension in the crude oil in what scientists know as the colloidal state in the pseudo-equilibrium condition. However, the injected CO_2 may influence this equilibrium resulting in their precipitation (Nguele et al. 2016; Chung et al. 1991; Hirschberg et al. 1984). The drop out of the asphaltenes in the pore space of the reservoir rock may have negative effects on the properties of the in-situ fluid-rock system such as variation in porosity, permeability and wettability (Nguele et al. 2016). For instance, asphaltene particles may be transported in suspension downstream of the flood specially around the production wellbore, blocking small pores and pore throats causing permeability reduction and formation damage (Bagheri et al. 2011). A number of researchers have studied the effects of asphaltene precipitation on the petrophysical properties of reservoir rocks during CO_2 flooding. Jafari Behbahani et al. (2012) investigated asphaltene deposition during CO_2 injection into a long core containing a live crude oil. In their experiment, they found the CO_2 injection to cause a significant increase in the pressure drop measured across the core sample. This increase in pressure drop was attributed by the resarchers to asphaltene precipitation. Similar results were observed by Bagheri et al. (Bagheri et al. 2011) who experimentally investigated the severity of the asphaltene precipitation phenomenon during CO_2 and natural gas injection or volumetric deleption for fluid-rock system representing an oil reservoir in Iran. Takahashi et al. (2003) conducted CO_2 flood tests above the MMP of their crude oil in both sandstone and carbonate cores. However, depsite of the significant precipitation of asphaltene in their experiments, their carbonate cores did not not reveal appreciable decraese in their permeability. The researchers attributed this behaviour to the permeability enhancing effects of the dissolution of the rock minerals that may occur during CO_2 injection working against negative effects of asphaletene precipitation or the possibility that the asphaltene particle sizes were too small to cause any permeability reduction (Takahashi

et al. 2003). In another experimental work, Srivastava et al. (1997) conducted core flood experiments to examine the effect of asphaltene precipitation in the Weyburn Reservoir in Canada using core samples collected from different zones of the reservoir (marly, vuggy and high-grain-size). The researchers found the severity of asphaltene precipitation in their experiments to be a function of the initial permeability of the cores used. In other words, the asphaltene precipitation was found to be more pronounced in high permeability (high-grain-size) than in those with lower permeability (marly and normal vuggy) (Srivastava et al. 1997). Zekri et al. (2013) conducted an experimental study in which they performed CO_2 injection in a number of tight limestone cores using a light crude oil (31.67 ˚API) with an asphaltene concentration of 0.20 wt% from an oil field in Abu Dhabi, UAE. The results obtained by these researchers indicated a reduction in the porosity and permeability and wettability alteration in the core samples all attributed to the asphaltene precipitation (Zekri et al. 2013).

2.2. Fluid-fluid and fluid-rock interactions

As discussed to some extent earlier, the injected CO_2 into deep geological formations is expected to interact with the in-situ fluids resulting in the generation of fluid mixtures that can subsequently intercat with the host rock formation in various forms. Such iteractions may alter the characteristics of the fluid-rock system impacting on the general mulitphase phase flow behaviour (e.g. injectivity, storage capcity, sweep efficiency, etc.) of the underground systsem. In an attempt to address the significance and consequences of the fluid-fluid and fluid-rock interactions that occur during CO_2 injection, this section of this chapter initially provides an overview of the main CO_2 trapping mechanisms as they are closely tied together with the above mentioend interactions. Then, the second part provides a detailed background into how these interactions may impact on the characteristics of the underground fluid-rock system. It is worth noting that asphaltene precipitation is regraded in this study as another major mechanism responsible for changing rock's petrophysical properties. However, since this mechanism was reviewed and its effects were adequately discussed in Section 2.1.3.2, no further background discussions would be presented about it in this section. This mechanism will be briefly touched upon later only in the context of wettability alteration that may occur to rock formations.

2.2.1. Trapping mechanisms

When it comes to the storage capacity at the large reservoir-scale, the major topic of interest to the scientific community is the way CO_2 may be trapped underground by the known trapping mechanisms. Therefore, it is critical to understand the nature of the relationship between the fluid-fluid or fluid-rock interactions and these trapping mechanisms.

A geological trap is a special stratigraphical setting of rocks suitable for containing fluids. Conventionally, a hydrocarbon trap is sealed by a relatively impermeable formation by which the upwards migration of the hydrocarbon is brought to a halt. For the case of CO_2 storage however, the unwanted gas may be held in place in a storage formation by up to four basic trapping mechanisms (Saeedi 2012), namely stratigraphic or structural trapping, residual or capillary trapping, solubility trapping and mineral trapping. The presence and contribution of each individual mechanism depend on the local geology, lithology of the target formation and the in-situ conditions of the fluid-rock system (IEA 2008; IPCC 2005; Benson et al. 2008; Benson 2004; Sally Benson 2011; Saeedi 2012; Izgec et al. 2006).

2.2.1.1. Stratigraphic trapping

Generally, it is believed that the dominant CO_2 trapping mechanism in majority of storage sites is the stratigraphic trapping which is also known as the structural trapping (IEA 2008). This mechanism involves the physical entrapment of CO_2 below a low permeability seal (caprock), such as a shale layer or salt bed. In other words, under the effect of bouyancy forces, the less dense CO_2 in the form of a plume would migrate upwards through the porous storage rocks until it reaches the top of the formation where it may be trapped by the impermeable seal layer (Benson et al. 2008; IPCC 2005; Sally Benson 2011). The sealing effect of some traps may be provided by sealing faults that can act as permeability barriers. Although, in some environments faults can also act as preferential pathways for fluid flow (Sally Benson 2011; IPCC 2005). Figure 2.6 illustrates different types of structural trapping according to the sealing mechanism in place. The amount of CO_2 required to be stored over long term by this trapping mechanism in particular depends on the effectiveness of the other three trapping mechanisms as will be discussed in details below.

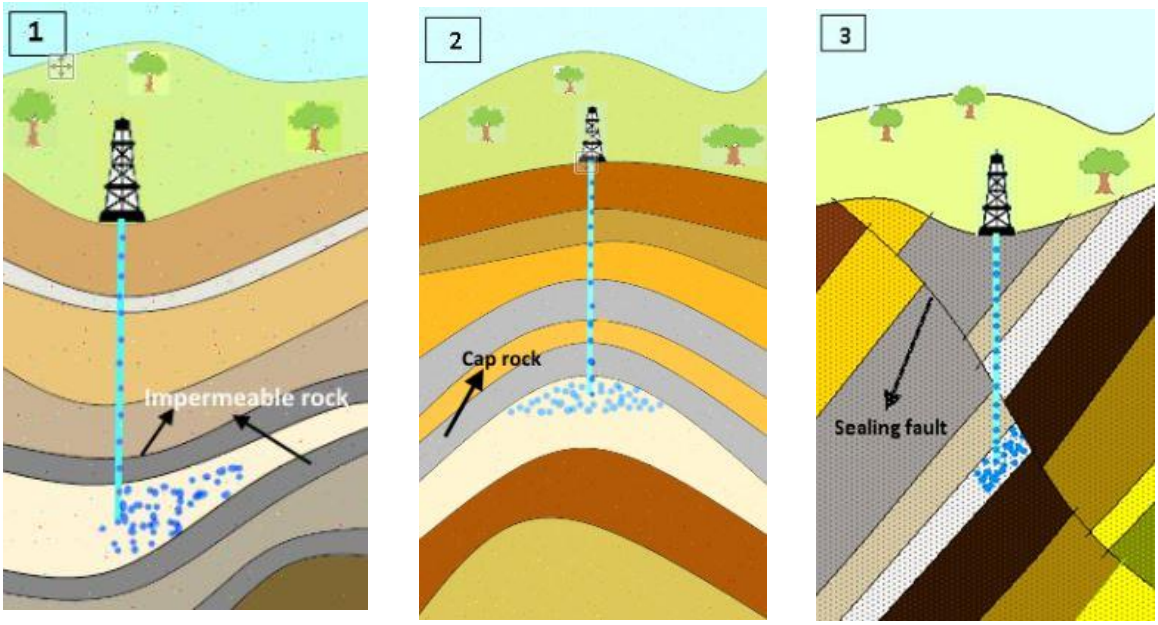

Figure 2. 6. Stratigraphic or structural trapping: (1) CO_2 is trapped between two impermeable layers, (2) CO_2 is trapped by a fold in the geological layers and (3) CO_2 is trapped by a sealing fault.

2.2.1.2. Residual Trapping

Resuidal trapping which is also known as capillary trapping takes place relatively fast in the pore space of the storage rock (Sally Benson 2011). Once the injection stage stops, the CO_2 present in the pore space of the rock would be displaced by the water flowing in from neighbouring rocks or the injection wells (if water is injected in alternation with CO_2). During this process, the invading water cannot remove and displace all of the CO_2 as the capillary forces result in the entrapment of CO_2 in the form of disconnected and immobilised blobs, ganglia and clusters (IPCC 2005; Niu et al. 2014). Figure 2.7 shows the process of the residual trapping of CO_2. This mechanism may be relied upon as the primary trapping mechanism in saline aquifers that do not have a dedicated closed/sealed trap.

Since capillary forces are reponsible for entrapment of CO_2 in the residual form, any change in the pore network and pore morphology (pore and pore-throat sizes, pore size distribution, pore shapes, etc.) of the host rock may then impact on the capacity of the rock to residually trap CO_2. Therefore, fluid-fluid interactions and any subsequent interactions between the generated fluid mixtures and the rock may alter the significance and contribution of capillary trapping for a fluid-rock system.

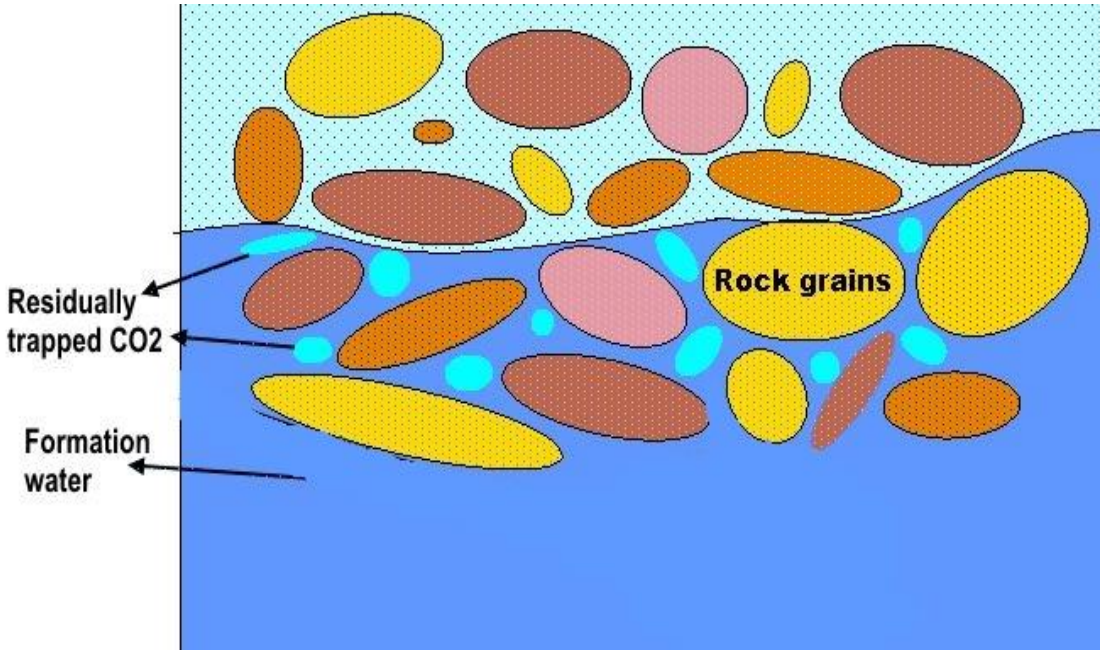

Figure 2. 7. Residual trapping of CO_2.

2.2.1.3. Solubility Trapping

Upon injection CO_2 begins to dissolve in the resident formation water giving rise to a process commonly known as the solubility trapping (Benson et al. 2008). As indicated earlier in this chapter, the solubility of CO_2 in water increases with increase in pressure and decreases with increase in temperature and water salinity (Benson et al. 2008). The solubility trapping may be enhanced by the so called convective mixing (Figure 2.8) resulted from the rise in formation water density as it dissolves CO_2 causing the solution to sink to the bottom of the storage formation (IEA 2008; IPCC 2005; Sally Benson 2011). The dissolution of CO_2 in the formation water occurs through the following chemical reactions (Sally Benson 2011; Gaus 2010; Egermann et al. 2005).

$$CO_2 + H_2O \leftrightarrow H_2CO_3 \leftrightarrow HCO_3^- + H^+ \leftrightarrow (CO_3)_2^- + 2H^+ \qquad \text{Eq: 2.4}$$

$$CO_2 + H_2O \leftrightarrow H_2CO_3 \leftrightarrow H^+ + HCO_3^- \qquad \text{Eq: 2.5}$$

As easily deduced from its title, this trapping mechanism is directly controlled by the level of in-situ fluid-fluid interactions as they control how much of the injected CO_2 may dissolve in the resident fluids. What is more, as revealed by the above two chemical reactions and will be discussed in further details later, the dissolution of CO_2 in the in-situ water and formation of carbonic acid is the main cause of the in-situ geochemical reactions. Therefore, this trapping mechanism may also indirectly influence the two trapping mechanisms of capillary and mineral trapping.

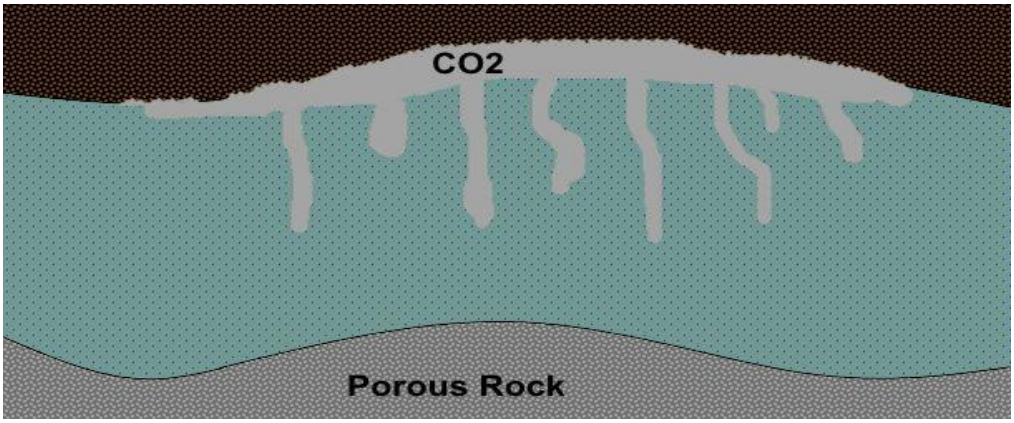

Figure 2. 8. Solubility trapping processes CO_2 enhanced by the so called convective mixing (sinking of denser carbonated water).

2.2.1.4. Minerals trapping

In terms of the time-scale it requires to take place, the mineral trapping may be considered as the final phase of CO_2 entrapment. It may be initiated once the solubility trapping has already taken place. As referred to earlier, the dissolution of CO_2 in the formation water (initially at thermodynamic equilibrium with the rock minerals) leads to a decrease in pH (Luquot et al. 2009). The main consequence of the decreased pH is the dissolution of primarily carbonate minerals (e.g. dolomite $CaMg(CO_3)_2$, calcite ($CaCO_3$) and anhydrite ($CaSO_4$)) along with increased alkalinity (i.e. generation of HCO_3^-) via the following chemical reactions (Salem et al. 2013).

$2H^+ + CaMg(CO_3)_2 \leftrightarrow Mg^{2+} + Ca^{2+} + 2\,HCO_3^-$ or, Eq: 2.6

$CaMg(CO_3)_2 + 2H_2CO_3 \leftrightarrow Ca^{2+} + Mg^{2+} + 4\,HCO_3^-$ Eq: 2.7

$CaCO_3 + CO_2 + H2O \leftrightarrow Ca^{2+} + 2\,HCO_3^-$, and/or Eq: 2.8

$H^+ + CaCO_3 \leftrightarrow Ca^{2+} + HCO_3^-$ or, Eq: 2.9

$CaCO_3 + H2CO_3 \leftrightarrow Ca^{2+} + 2\,HCO_3^-$ Eq: 2.10

$CaSO_4 + CO_2 + H_2O \leftrightarrow CaCO_3 + H_2SO_4$ Eq: 2.11

As a final end product of these reactions, certain carbonate minerals can form and precipitate causing the permanent entrapment of CO_2 in the most stable possible form (Gunter et al. 1993; Xu et al. 2001; Bachu et al. 1994). Equations 2.12-2.16 present some important examples of the reactions through which mineral precipitation may occur during CO_2 injection (Izgec et al. 2008; Saeedi 2012) (Oelkers et al. 2008; Bachu et al. 1994).

$Mg^{2+} + HCO^-_3 \leftrightarrow H^+ + MgCO_3$ Eq: 2.12

$Ca^{2+} + HCO^-_3 \leftrightarrow H^+ + CaCO_3$ Eq: 2.13

$Fe^{2+} + HCO^{-}_{3} \leftrightarrow H^{+} + FeCO_3$ Eq: 2.14

$Mg_2SiO_4 + 2CO_2 \leftrightarrow 2MgCO_3 + SiO_2$ Eq: 2.15

$CaAl_2SiO_8 + CO_2 + 2\,H_2O \leftrightarrow CaCO_3 + Al_2Si_2O_5(OH)_4$ Eq: 2.16

Under the reservoir conditions, the reaction of minerals with CO_2 and in-situ created or injected carbonated water (as depicted by the above chemical reactions) are thermodynamically favoured but, in general, may proceed at a slow rate. They may be initiated in a matter of days in the case of some carbonate minerals, but take hundreds to thousands of years to take place in the case of the silicate minerals (e.g. Quartz-Feldspar-Mica). In general, the rate of the reactions depends on the rock and formaton water compositions, the temperature and pressure of the reservoir, the water/rock contact area as well as the flow rate of the fluid flowing through the rock (Oelkers et al. 2008). Although carbonate minerals have high reaction rates in general, a closer evaluation indicates that the reaction rate constant of anhydrite is higher than that of calcite and much higher than the reaction rate constant of dolomite (Stumm 1992; Wellman et al. 2003; Mohamed et al. 2010).

Generally, the efficiency and security of CO_2 storage in a particular site would depend on respective contributions from both physical and geochemical trapping mechanisms as reviewed above. As depicted by Figure 2.9, each of the trapping processes takes place over different time-scales (from 1 day to 1000 years) at different rates and provide various levels of storage security (Benson et al. 2008; IEA 2008; IPCC 2005).

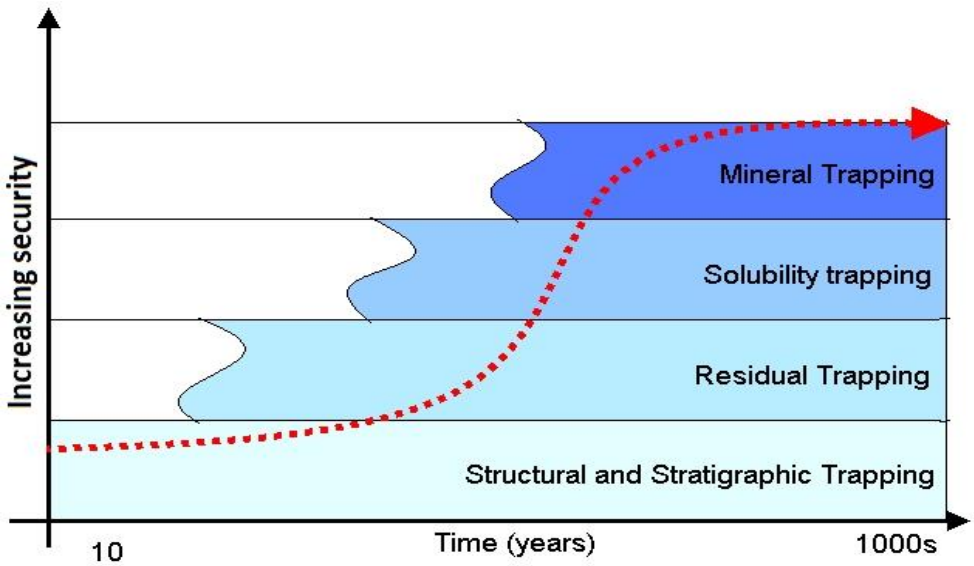

Figure 2. 9. The time-scale and level of security of CO_2 trapping mechanisms.

2.2.2. Effects on characteristics of fluid-rock system

As discussed earlier, any interaction of the injected CO_2 with the rock minerals may result in their dissolution and then possible later precipitation of new minerals contributing towards the permanent entrapment of CO_2. On the other hand, the mineral dissolution and precipitation are also considered as two main mechanisms that may alter the petrophysical properties of the rock (Oomole et al. 1983; Izgec et al. 2005; Moghadasi et al. 2004). As briefly discussed in Chapter 1, the dissolution may also result in the occurrence of another mechanism referred to as mechanical/physical compaction (Detwiler 2008; Kono et al. 2014) This third mechanism takes place due to the weakening of the mechanical/physical strength of the rock by mineral dissolution. The occurrence and extent of the effects of these three mechanisms depends on a number of factors such as the mineral composition and distribution of the rock, the degree of heterogeneity and the original textural features of the geological formation of interest (Oomole et al. 1983) as well as the in-situ conditions of pressure and temperature.

Although the dissolution of rock minerals may increase the rock permeability, the precipitation mechanism can work against it leading to an eventual reduction in permeability and effective porosity (Izgec et al. 2005). Such effects have been observed by a number of researchers in core-flood experiments (Oomole et al. 1983; Izgec et al. 2005). As reported by these researchers, mineral precipitation would be greatly influenced by the pressure drop generated across the rock samples during the flooding process; the larger the pressure drop, the more the intensity of the mineral precipitation and the reduction in the permeability of the rock (Oomole et al. 1983). Also, it has been argued in the literature that the attraction forces between the particles transported and the surfaces of the pores inside the rock may increase the precipitation rate (Izgec et al. 2006). When it comes to the laboratory core-flood experiments, as illustrated in Figure 2.10, the flow direction could also be a contributing factor in how the rock properties might change along the length of the rock sample. Figure 2.10 illustrates the process of dissolution and subsequent deposition of carbonate minerals in a carbonate rock subjected to carbonated brine injection. The permeability decline caused by mineral precipitation in the downstream pores can reach up to 90% of the rock's initial permeability; such level of reduction, among other factors, may be controlled by the initial permeability itself, as well as the flow rate and duration of the injection (Moghadasi et al. 2004).

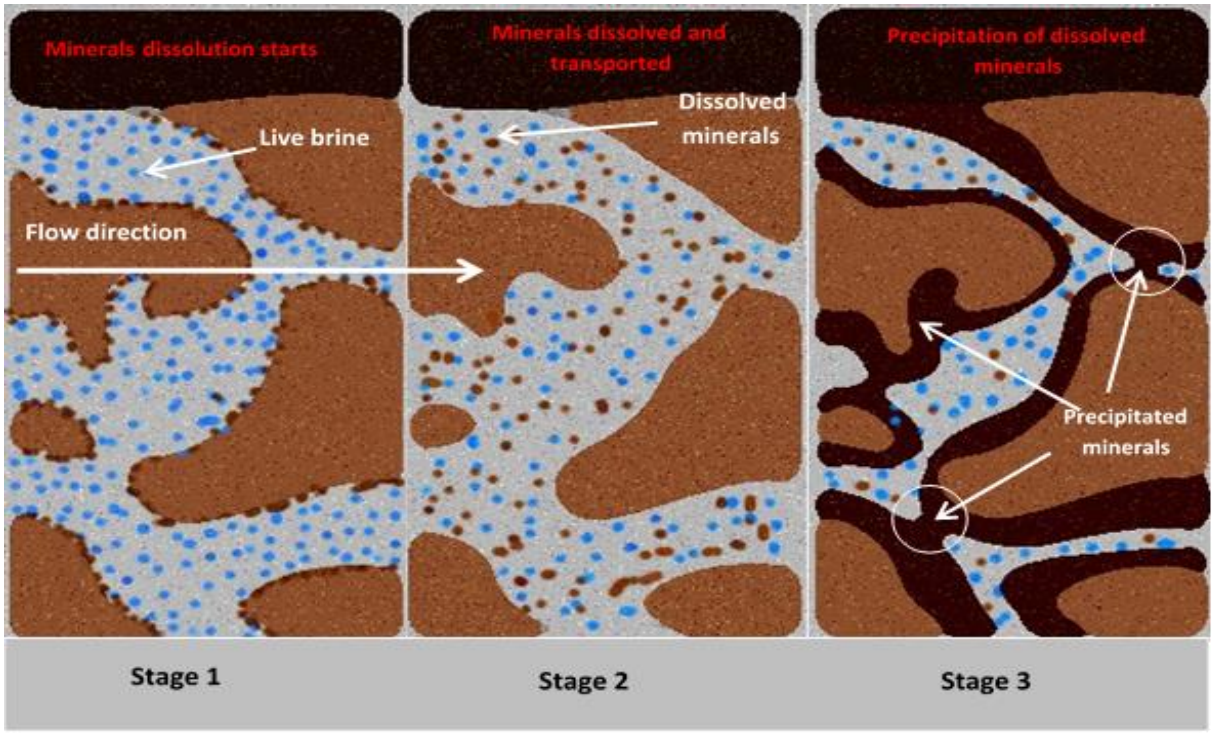

Figure 2. 10. Dissolution and precipitation processes during CO_2 injection.

During flooding, at the injection point where CO_2-saturated brine comes in contact with the rock first, the brine begins to establish flow path(s) through possible pre-existing high permeability channels/streaks in the rock (Tutolo et al. 2014). As one may expect, this kind of behaviour is more pronounced in highly heterogeneous media. Should this be the case, the high flow rate of highly reactive carbonated brine would begin to react with the rock minerals within the established flow channels at a high rate. Subsequently, the rock (especially carbonate minerals such as calcite and dolomite (if any)) would begin to dissolve in the brine, leading to a further increase in the permeability along the established flow path, resulting in the formation of what is known as the wormhole (Egermann et al. 2005; Izgec et al. 2006). Clay minerals (if present) may also react with carbonic acid quite rapidly, which can lead to pore space geometry changes in a relatively short time (Izgec et al. 2008). Due to the special geometry of fractures, the way chemical reactions occur during CO_2 injection into fractured rocks and change their properties could be to some extent different from what may occur in non-fractured rocks. In fractured formations, the geochemical reactions (mineral dissolution) are likely to occur within the fractures and their close vicinity, as they provide preferential flow paths for the reactive fluids to pass through (similar to the effect of high permeability streaks discussed earlier). During this process, the alteration to the fracture surface asperities may subsequently change their mechanical properties, leading to the possible deformation of the fracture aperture (Elkhoury et al. 2013). Depending on the exact nature of such alterations and subsequent

events, the fracture aperture may become wider or narrower. Generally, fracture permeability may increase as the fast-flow channels are etched or may decrease as asperities dissolve bringing the fracture walls closer under the effect of the overburden pressure (Polak et al. 2004). Figure 2.11 shows, schematically, one possible way of permeability change in a fractured carbonate reservoir. The relative rates of dissolution and then transport of dissolved minerals by fluid flowing through the fracture would control the dissolution process within the fracture and any ensuing change to the fracture porosity and permeability (Detwiler et al. 2007).

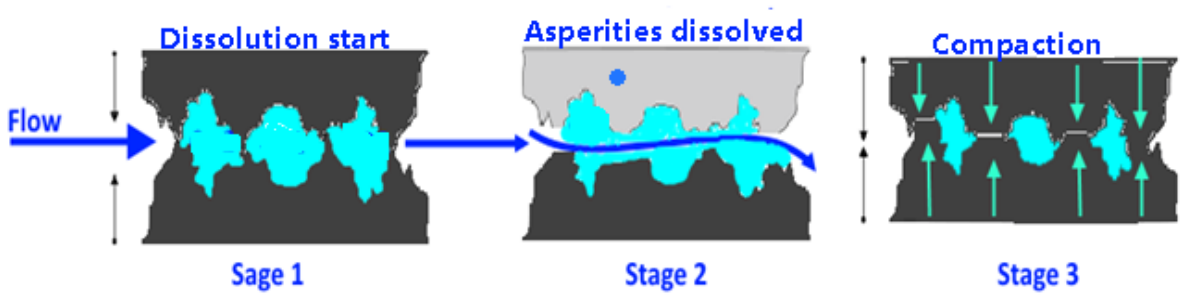

Figure 2. 11. Dissolution processes in the fractured carbonate rocks during CO_2 injection.

2.2.2.1. Other mechanism

In addition to the mechanisms discussed already (i.e. mineral dissolution, mineral precipitation, mechanical/physical compaction and asphaltene precipitation), although not as common, there may be other mechanisms induced by the injection and presence of CO_2 in an underground geological structure that could influence the petrophysical and fluid flow characteristics of the subsurface system. Two of such mechanisms whose occurrence and consequential effects are discussed here are fines migration and wettability alteration.

The fines migration is a well characterised phenomenon during subsurface fluid flow processes in which, usually, clay fines may be dislodged from the pore space of the rock formation resulting in formation damage around injection/production wells (Wilson et al. 2014; Lemon et al. 2011; Bennion 1992; Priisholm et al. 1987). Although the type of fines that are the subject of discussion here (i.e. predominantly carbonate fines) and their release mechanisms may not be necessarily the same as the clay fines referred to above, their end effect may be quite similar. In other words, the transport/migration of these fines may result in, primarily, permeability reduction and formation damage. As discussed earlier, mineral dissolution may commence as soon as the injected and/or in-situ created carbonated water comes in contact with reactive mineral that may be present in the composition of the host rock formation. This mineral dissolution may reduce the rock's structural strength resulting in its mechanical compaction under the effect of overburden stress. During this process, some small sized mineral fragments or 'fines' may break off from the rock matrix and be released into the pore space of the rock.

These fines may then be transported downstream of the flow resulting in the blockage/bridging of the pore-throats and hence the permeability reduction or local change in porosity.

The second not very common but important mechanism referred to and briefly discussed here is the wettability alteration. Wettability is an important factor controling fluid flow in the porous media. It is a measure of the attraction between the fluids and the internal surface of a porous medium with the wetting fluid being the most attracted to the surface (Donaldson 2008; Anderson 1986; Abdallah et al. 2007). Wettability influences critical subsurface factors such as injectivity, fluids distribution, relative permeability, residual saturations, etc. (Anderson 1986; Chalbaud et al. 2007; Yang et al. 2008; Farokhpoor et al. 2013; Saeedi et al. 2011; Donaldson 2008). Wettability is characterised using the concept of contact angle (θ). As demonstrated Figure 2.12 for an oil-water fluid system, as measured through the water phase, a θ less than $90°$ reveals a water-wet rock while a θ greater than $90°$ means the rock is oil-wet. The effect of wettability on fluids distribution is also demonstrated in Figure 2.13.

The importance of the phase behavior of fluids as well as the in-situ fluid-fluid and fluid-rock interactions and their impacts on the characteristics of the deep fluid-rock systems were discussed previously in this chapter. However, in general, in subsurface fluid-rock systems, the gas (if present) is considered to be the non-wetting phase but under the storage/injection conditions, CO_2 would most likely exist in its supercritical state (Chalbaud et al. 2007) which tends to make prediction of the wettability state of a rock formation uncertain when brought in contact with CO_2. More importantly and as the primary purpose of the present discussion, the expected fluid-fluid and fluid-rock interactions induced by CO_2 injection may lead to wettability alterations. The wettability alteration may be caused by a reduction in the pH of the formation water and/or precipitation of heavy fractions out of the crude oil (if present) within the pore space of the rock. The possible mechanisms behind the above two phenomena (pH change and precipitation of heavy fractions) have already been discussed in details in earlier sections of this chapter.

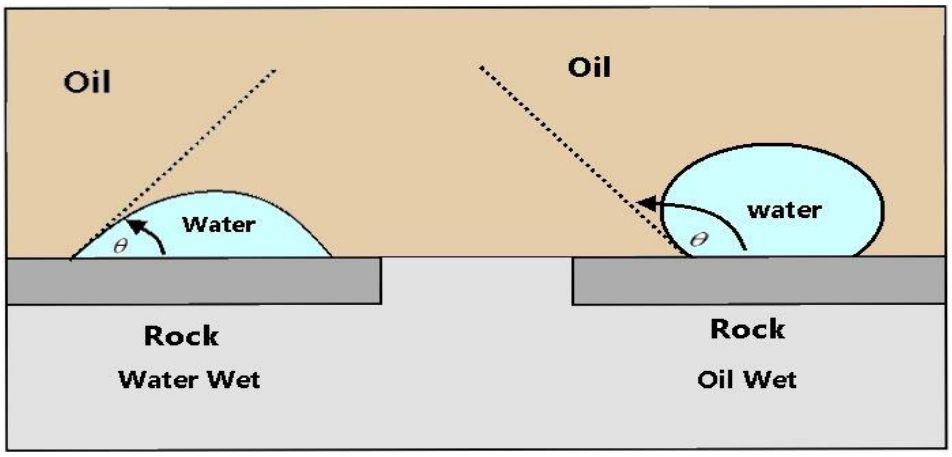

Figure 2. 12. Contact angle (θ) as a measure of wettability.

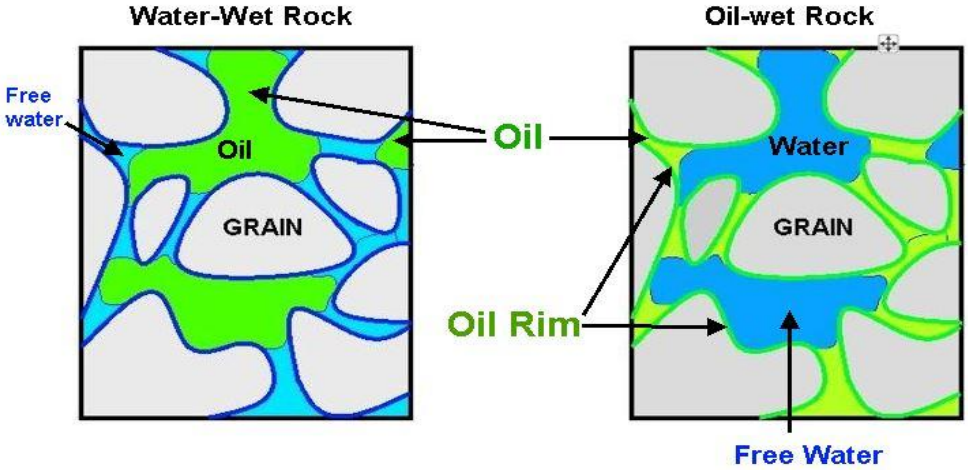

Figure 2. 13. Effect of wettability on fluids distribution for an oil-water fluid system.

2.3. Reservoir heterogeneity and lithology

It is widely acknowledged by the scientific and technical community that heterogeneities at any scale (from meter to kilometre scale) can strongly influence multiphase flow characteristics of an underground fluid-rock system by, for instance, presenting flow barriers, reducing transmissibility across the reservoir sections/layers, influencing sweep efficiency, etc. Furthermore, the lithology of the reservoir rock can also control multiphase flow by influencing parameters such as fluid-rock interactions, wettability, etc. In general, carbonate reservoirs, compared with their sandstone counterparts, present a much more complex system to characterise when evaluating the influence of heterogeneity and lithological features on their fluid flow characteristics.

Carbonate reservoirs represent about fifty percent of the oil and gas production around the world (Mazzullo 2004). However, CO_2 storage/EOR in these reservoirs is more challenging due to their extreme heterogeneous nature. These reservoirs are often highly heterogeneous in

terms of their porosity and permeability distribution and rock typing. In addition, they suffer from difficult to evaluate and often variable wettability, complex natural fracture netwroks and many other rock textural features (Agar et al. 2014; Asghari et al. 2004; Kadhim et al. 2014; Jonoud et al. 2013) As discussed previously, prominent minerals present in the composition of carbonate rocks (e.g. calcite and dolomite) have high surface reaction rates which when combined with the heterogeneous and complex nature of such rock formations can lead to the highly complex and non-uniform fluid-rock interactions (Egermann et al. 2005). As discussed in details previously, the degree and nature of such intercations then control the occurrence of important mechanisms such mineral dissolution and precipitation and possible mechanical compaction of the reservoir rock (Zekri et al. 2009).

2.4. Effective stresses acting on the reservoir rock

For subsurface geological systems, the effective stress is defined as the difference between the overburden and reservoir pore pressures. The overburden pressure applied to a reservoir stems from the weight of the rock layers (and their saturating fluids) overlaying the reservoir. The reservoir pore or fluid pressure is controlled by the prevailing pressure regime of the aquifer underneath the reservoir. The overburden pressure is often assumed to increase by the widely accepted gradient of 1 psi/ft while for a normally pressured reservoir, the pore pressure could be calculated for the depth of the reservoir using normal hydrostatic pressure equation that incorporates the prevailing water pressure gradient (e.g. 0.43 psi/ft).

The petrophysical properties of the reservoir rock such as porosity, permeability and relative prmeability may be strongly influenced by the effective stresses acting on the rock (Al-Quraishi et al. 2005; Lucia 2007). Dpending on their level of complexity in lithological and rock textural features and heterogeneous nature, in carbonate reservoirs, the effective stress may have a significant effect on the rock properties and in general reservoir quality (Lucia 2007). For instance, the degree of permeability reduction due to increase in effecive stress is highly pronounced in carbonate rocks with micro vuggy porosity and micropore structures (Shafiee et al. 2009). The impotance of the effective stress is further realised knowning that subsurface processes such as withdrawal and injection of fluids have a direct impact on the effective stress, due to pore pressure alteration (Al-Quraishi et al. 2005; Saeedi 2012; Berryman 1992). Furthermore, in-situ fluid-rock intercations such as mineral dissolution (which are expected to be more pronounced in carbonate reservoirs) could intensify the potential effects of any change in in-situ effective stress.

2.5. Previous related experimental work

As stated in Chapter 1, the primary purpose of this research is to experimentally evaluate the effects of potential fluid-rock intercations occuring during CO_2 injection into carbonate rock formations on their petrophsyical propeties. There has been a limited number of experimental studies carried out investigating such effects in carbonate reservoirs. In this part of Chapter 2, a review of a few selected studies is presented with the main purpose of demonstrating the effects of some of the factors and mechanisms discussed earlier in this chapter.

Izgec et al. (2005) experimentally investigated the effect of CO_2 injection into carbonate rock samples in order to evaluate the changes in their porosity and permeability caused by fluid-rock interactions. Carbonate plugs were cored from Midyat Formation located in South East of Turkey. The Midyat Formation is heterogeneous and vuggy with almost 95% calcite. The experiments were conducted at different flow rates, water salinities and temperatures while the pore and confining pressures were kept constant. The results obtained by the researchers showed that when a core sample was vertically oriented its permeability increased and then decreased after a certain pore volume of CO_2 injection. On the other hand, an oevrall decrease in the permeability was observed for the horizontally oriented cores. A slight increase in the porosity was observed for both cases. Izgec et al. (2005) attributed the difference in the permeability changes between the vertical and horzontal oriented samples to the effect of gravitational forces acting on the injected CO_2. It has been argued that, in the case of vertically-oriented experiments, due to the gravitational forces, the injected CO_2 would tend to channel through and evolve faster towards the top of the sample. Therefore, the chemical reactions would be more pronounced near the inlet where CO_2 is more spread and the generated carbonic acid comes in contact with a larger pore surfce and therefore would dissolved carbonate minerals resulting in an increase in the sample permeability at the inlet initially. However, the transportation of the dissolved minerals would block the smaller pores downstream/top of the sample causing a later reduction in the permeability. On the other hand, for horizontally designed experiments, with the absence of bouyancy forces in horizontal direction, the injected CO_2 would move slowly towards the outlet of the core sample. Although due to the mineral dissolution porosity would increase near the inlet, the dissolved calcite particles would precipitate in the flow path along the length of the sample with higher intensity at its outlet where the pore pressure also decreases resulting in a decrease in the permeability (Izgec et al. 2005).

Similar to Izgec et al. (2005), Luquot and Gouze (2009) also investigated the variations in the porosity and permeability of carbonate samples during CO_2 injection. The four samples used

in this study were taken from an oolitic limestone from Mondeville of the middle Jurassic age (Paris Basin, France). The experiments were carried out under in-situ reservoir conditions (T = 100 ˚C and P = 12 MPa) using four different CO_2-saturated brines whose composition was varied slightly. Three dimensional X-ray micro-tomography (μCT) measurements were performed on the samples before and after flooding. The μCT images and effluent fluid analysis confirmed highly pronounced dissolution in the sample inlets, which resulted in the creation of wormholes close to this region (Figure 2.14) causing an increase in the porosity and permeability of the samples . Also, based on their results, they stated that the shape and length of the created wormholes would be controlled by the initial petrophysical properties and pore structure of the rock samples. Mineral precipitation was also observed in one sample. The mineral precipitation was verfied using SEM imaging and chemical analysis of the effluent brine (Luquot et al. 2009).

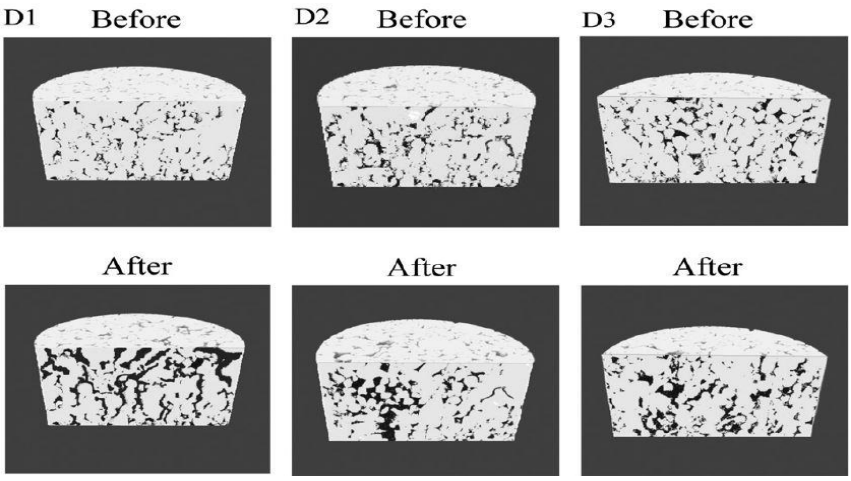

Figure 2. 14. 3D X-ray images of the inlet region of samples before and after flooding (black and gray areas represent pores and grain solids, respectively) (after Luquot and Gouze, 2009).

Smith et al. (2013) conducted a number of core-flooding experiments on dolomite-rich (Marly dolostone) and limestone (vuggy) samples collected from the Weyburn-Midale field (Canada). The porosity, permeability and average mineral composition of their samples are reported in Table 2.4. Their experiments were performed using brine (pre-equilibrated with CO_2 at various pressures) to investigate the effect of heterogeneity and rock-fluid interactions on the evolution of porosity and permeability during the flooding process. All experiments were performed at 60˚C, a confining pressure of 24.8 MPa, and a back pressure of 12.4 MPa. As reported by the researchers, homogeneous dolomite-rich samples showed a relatively even mineral dissolution front. The uniform dissolution was pronounced within the first few millimetres from the inlet of the samples, causing an increase in the porosity in this area (Figure 2.15). Some dissolution

fingers were observed for Sample M-1 which were attributed to the special mineralogy of this sample as it consisted of the highest proportion of calcite compared to the other samples (Smith et al. 2013).

Table 2. 4. Porosity, permeability and minerals compositions of the samples tested by Smith et al. (2013).

Sample ID	Calcite	Dolomite	Anhydrite	Porosity	Permeability
	% of total core volume			(%)	(mD)
M-3	19	45	0	36	1.7
M-2	7.7	61	0	31	1.2
M-1	20	49	0	31	0.92
M-0	14	52	0	35	1.7
V-3	59	26	0	15	0.032
V-3	35	26	0	39	N/a
V-2	55	27	Trace	16	0.032
V-2	52	27	0	20	N/a
V-1	63	24	Trace	13	0.024
V-1	62	23	0	15	N/a
V-0.5	56	29	Trace	15	0.0091
V-0.5	49	29	0	22	N/a

Note: in the sample IDs, letters M and V stand for Marly dolostones and Vuggy limestone respectively. The numbers in the sample IDs represent the pressures at which brine was pre-equilibrated with CO_2.

In the sample set testd by Smith et al. (2013), compared with the homogeneous dolostones, the vuggy limestone samples presented greater heterogeneity with respect to their pore space geometry and mineral composition. As a result, the flooding experiments conducted on these samples caused highly pronounced and non-uniform dissolution of calcite mineral resulting in the creation of channels or wormholes along the length of each sample (Figure 2.16). Therefore, a large increase in the permeability was observred in all of their post-flood samples. The gradual increase in the sample permeabilities also caused a decrease in the differential pressure recorded across the samples during the experiments (Figure 2.17).

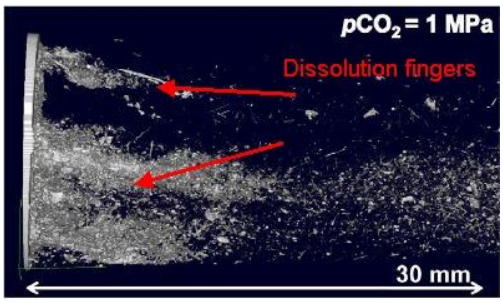

Figure 2. 15. Post-flood X-ray CT image illustrating the dissolution patterns formed in a dolomite-rich homogeneous sample (after Smith et al. 2013).

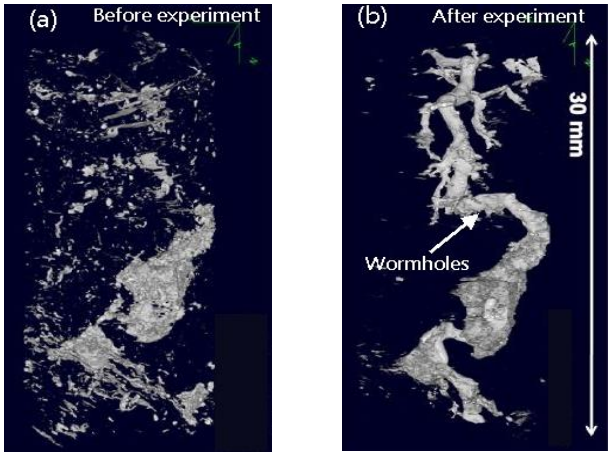

Figure 2. 16. X-ray CT images (a) before and (b) after flooding for a vuggy limestone sample illustrating the formation of wormholes (after Smith et al. 2013).

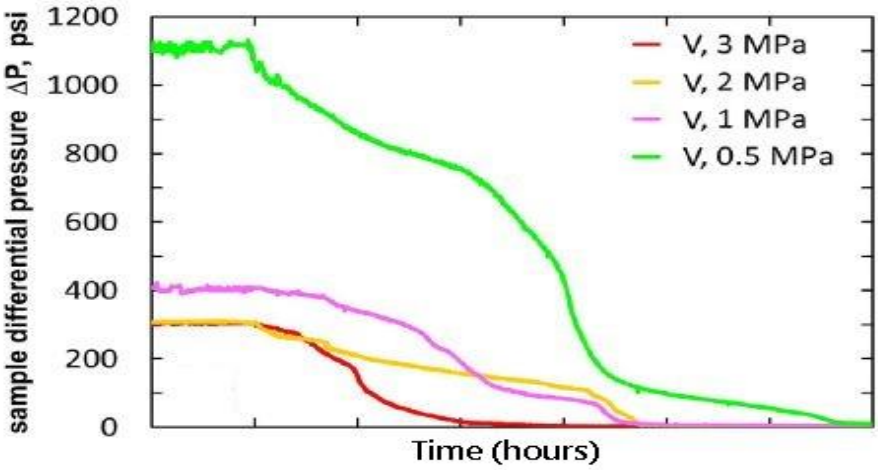

Figure 2. 17. Differential pressure profiles for all the vuggy limestone samples (after Smith et al. 2013).

Another core flooding study was conducted by Luhmann et al. (2014) to examine the fluid-rock interactions in dolomite-rich rocks to evaluate possible variations in their porosity and permeability under high pressure and high temperature conditions. Nine samples were flooded using CO_2-saturated brine at 100˚C and 15 MPa using different injection flow rates of 0.01, 0.1 and 1 ml/min. The X-ray CT images generated in the study showed the formation of different dissolution patterns in the samples causing significant increases in their post-flood permeability. As apparent from Figure 2.18, the different injection flow rates used by Luhmann et al. (2014) also resulted in the formation of different dissolution patterns.

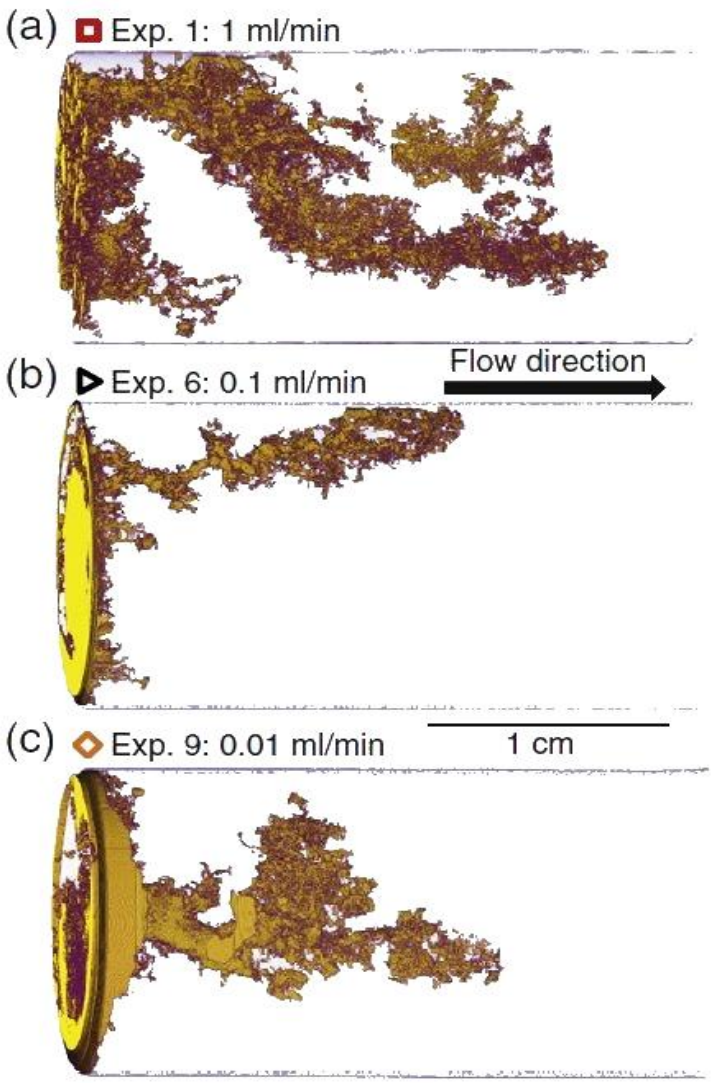

Figure 2. 18. X-ray CT images showing the generation of dissolution patterns during core-floods conducted under different flow rates: (a) 1 ml/min, (b) 0.1 ml/min and (c) 0.01 ml/min (after Luhmann et al. 2014).

Zekri et al. (2009) performed an experimental study to evluate the potential of asphaltene precipitation and mineral dissolution during the CO_2-EOR processes in carbonate formations. The experiments were carried out at reservoir conditions (27.58 MPa and 121˚C). Ten limestone core samples whose permeability and porosity varied between 0.17 and 170 mD and 19 to 29%, respectively, were used in their study. To achieve the objectives of their study, they employed two different experimental procedures. In the their first set of experiments, CO_2 was injected into samples saturated with brine only. The results obtained from this set showed different levels of both increase and decrease in the permeability of the samples flooded. The further analysis performed by Zekri et al. (2009) confirmed that the dissolution of carbonate minerals resulted in an increase in the permeability and porosity of some samples, whereas a later precipitation of dissolved minerals caused a reduction in the permeability of others. As

the second set of their experiments, CO_2 was injected into oil staurated samples to study the effect of the possible interactions between CO_2, oil and rock on their experimental results. The crude oil used by the researchers contained 0.2 wt% asphaltene. The results obtained from the second set of experiments showed moderate to significant reductions in the permeability of all samples but one. The observed reductions in sample permeabilities were attributed by the researchers to the asphaltene precipitation phenomenon with the reduction being more pronounced in the case of high permeability cores. Figure 2.19 compares the SEM images obtainbed by Zekri et al. (2009) for one of the cores before and after the CO_2 flooding, which revealed signs of asphaltene deposition on the pore surfaces of the rock. They also suggested that the deposition of asphaltene would depend on the mineralogical composition and distribution within the samples tested.

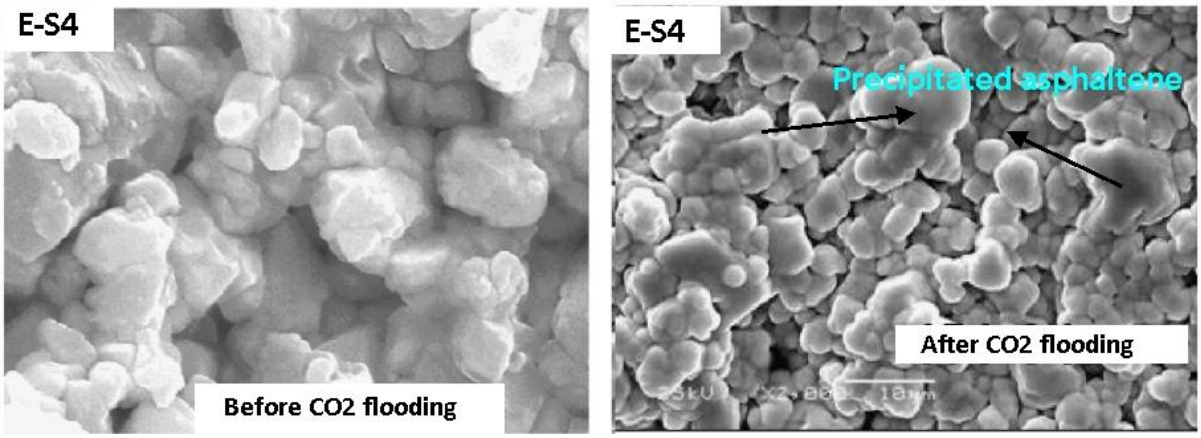

Figure 2. 19. SEM image obtained before and after flooding for Sample E-S4 (after Zekri, Shedid and Almehaideb 2009).

Zekri et al. (2013) conducted another experimental study to investigate the changes in the petrophysical properties of heterogeneous, low permeability limestone reservoir plugs subjected to CO_2 flooding under reservoir conditions (27.58 MPa and 121˚C). The researchers used three composite samples with each sample consisting of four individual plugs arranged in the descending order of their permeability values in the flow direction. In their experiments, before CO_2 flooding each core was prepared in a way that it would contain a cerian level of oil saturation (0.79, 0.5 and 0.3%). The Crude oil used was a light oil of 31.67 ˚API with 0.2 wt% asphaltene sourced from a field in Abu Dhabi, UAE. Similar to their previous study, the researchers detected asphaltene precipitation induced by CO_2 flooding in their experiments. They found the negative effect of asphaltene precipitation on sample permeabilities to counteract any enhancing effects of mineral dissolution. The balance between the two phenomena was found to control how porosity and permeability would change along the length

of the composite cores (Figures 2.20 and 2.21). The initial level of oil saturation before CO_2 flooding was also found to influnece the results obtained (Figures 2.20 and 2.21) (Zekri et al. 2013).

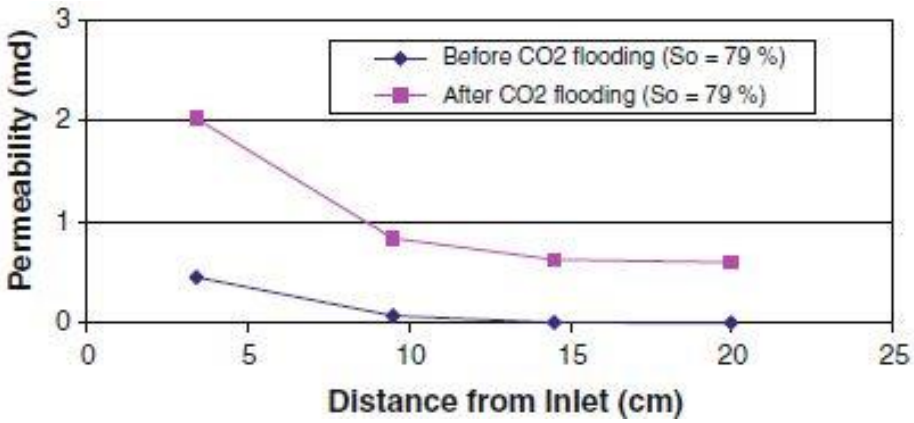

Figure 2. 20. . Pre- and post-flood permeability of a composite core versus the distance from the inlet (at So = 79%) (after (Zekri et al. 2013).

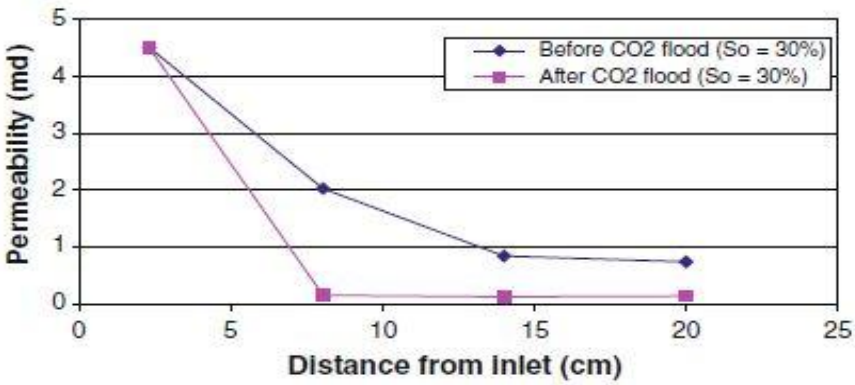

Figure 2. 21. Pre- and post-flood permeability of a composite core versus the distance from the inlet (at So = 30%) (after Zekri et al. 2013).

Chapter 3

3. Experimental Apparatus, Material and Procedures

To achieve the objectives of this study as outlined in Chapter 1, a specially designed experimental program was designed and carried out that included core-flood experiments complemented by a collection of laboratory analysis including X-ray CT and SEM imaging, porosity-permeability measurements, XRD analysis, NMR measurements, etc. The laboratory work were performed on 19 carbonate samples using the Curtin Department of Petroleum Engineering's in-house facilities (e.g. a high pressures-high temperature three-phase steady-state core flooding apparatus) as well as a number equipment belonging to CSIRO-Kensington in Western Australia.

Various sections of this chapter provide a full description of the experimental apparatus and materials used and the procedures followed in conducting different experimental work planned for this study.

3.1. Core-flooding Apparatus

Figures 3.1 and 3.2 provide, respectively, a photo and a schematic of the core flooding apparatus used in this study. The apparatus is designed to handle experiments with pressures and temperatures up to 100 MPa and 200 °C, respectively. The core-holder, fluid accumulators and flow-lines carrying the experimental fluids are located in a fan forced oven to keep the temperature constant during the experiments. A controller module is used to regulate the oven temperature with an accuracy of ±0.2 °C. The injection pumps are of syringe type making the fluid injections pulsation-free. During the experiments, pressure, volume and flow rate can be controlled and recorded with the accuracies of ±14 KPa, ±0.05 cc and ±0.05 cc/h, respectively. All wetted parts of the apparatus are made from hastelloy, super duplex stainless steel or titanium to minimise any fluid contamination or damages caused by corrosion when exposed to highly corrosive materials (e.g. carbonated water or high salinity brine) under high pressures and temperatures for prolonged period of time.

Overall, the apparatus consists of four main parts, including the injection, separation and collection (not used in this research), and controlling and monitoring systems. Presented in the following section of this chapter is a detailed description of those systems that were utilised in this study.

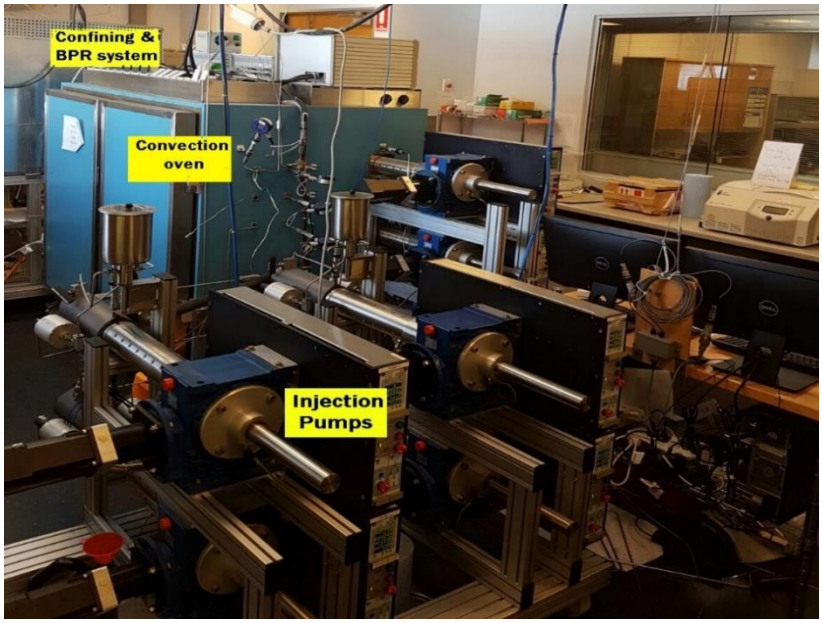

Figure 3.1. A photo of the core-flooding apparatus used in this experimental study.

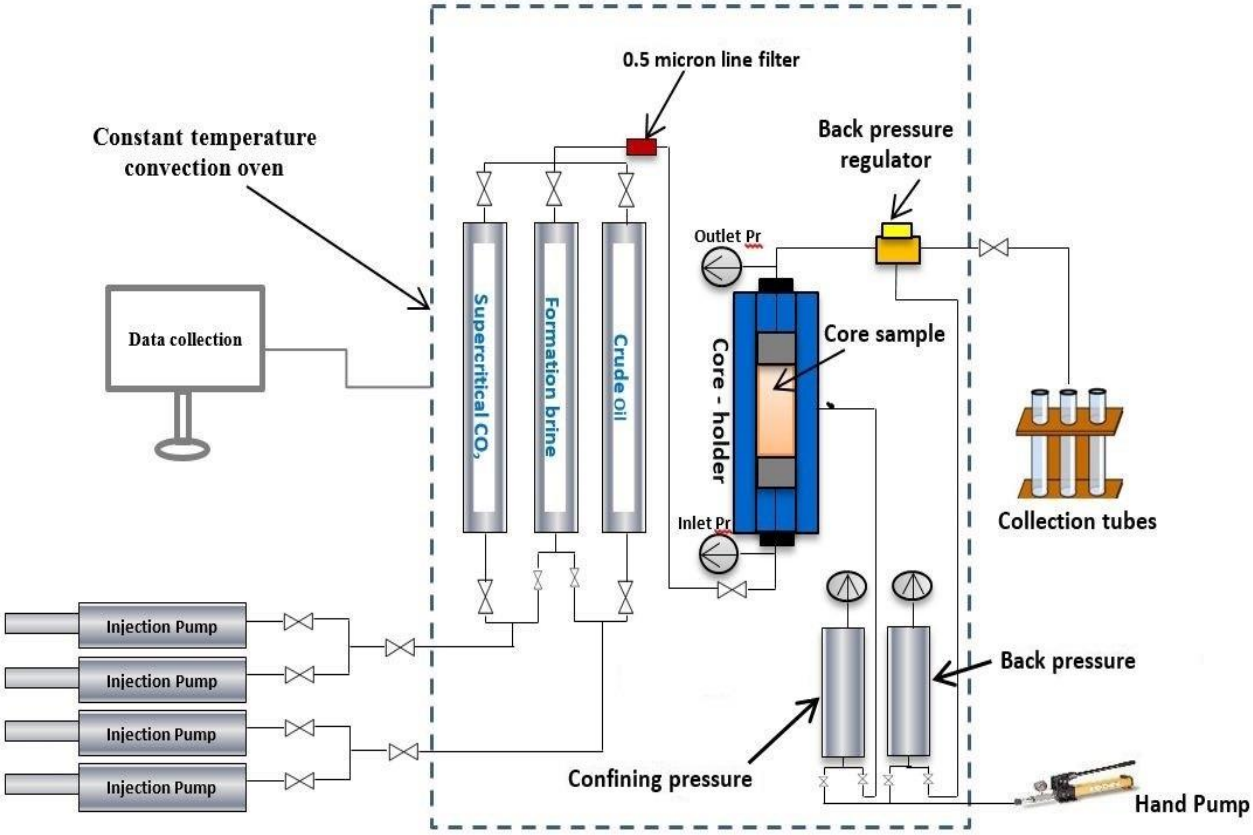

Figure 3.2. A general schematic diagram of the core flooding apparatus used in the experiments.

3.1.1. The injection system

Overall, the injection system consists of two parts. The first part includes four injection pumps that are connected to their dedicated electronically controlled pneumatic valves to control the flow direction and/or isolate a pump when needed (Figure 3.3). Each pump can inject up to 300 cc of fluids in one run. Furthermore, the pumps can be operated under various injection modes of constant pressure and constant flow-rate, as well as constant pressure with different pressure ramps or a setting to reach a desired injection volume. Injection pressure and flow-rate can be controlled independently for each pump through a number of controller modules that can be operated directly using dedicated keypads or using a software package installed on two computer machines.

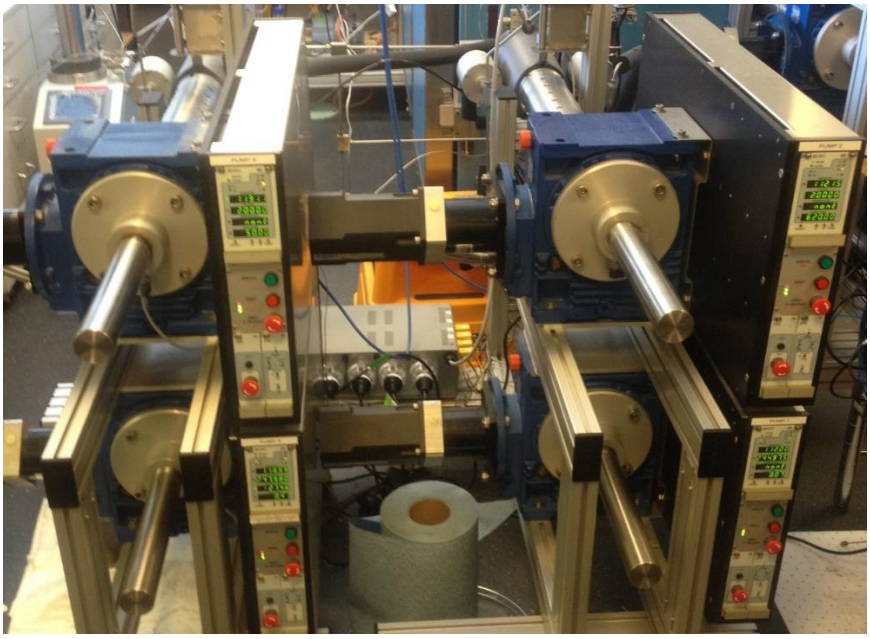

Figure 3.3. The four injection pumps and associated electronic devices.

The second part of the injection system mainly includes three high pressure accumulators to hold various injection fluids (e.g. oil, brine and CO_2) as needed (Figure 3.4). Each bottle has a capacity of 1500 cc, which allows for the non-stop pumping of a relatively large number of fluid pore volumes. Although each injection pump has a 300cc capacity only, they can be operated in two synchronised pairs allowing for continuous injection of larger volume of the fluids when required. All three bottles are vertically oriented and connected to the injection pumps from the bottom. They all have a floating piston inside to separate the hydraulic oil injected by the pumps from the injection fluids.

Figure 3.4. The three fluid sample bottles and associated connections.

3.1.2. The core holder

A schematic diagram of the core-holder used in this study is shown in Figure 3.5. The core-holder is a Core Laboratories' HCH series standard biaxial core-holder in which a common radial and axial pressure is applied on the core sample. The radial pressure (or the confining pressure) is applied using the annular space between the core sample and the inner diameter along the length of the core-holder while the axial pressure is applied using a floating end plug attached to the outlet side of the core-holder. The confining pressure is applied by first filling the above annular space with water and then increasing the pressure using a manual high pressure pump (Figure 3.6). The adjustable/floating outlet end plug of the core-holder also allows for different core-sample lengths to be used for the experiments. Finally, there are two connection ports at each end of the core-holder for fluid injection/production and recording of the differential pressure across the sample. The core-holder can be oriented in vertical or horizontal directions by attaching a specially designed stand to it.

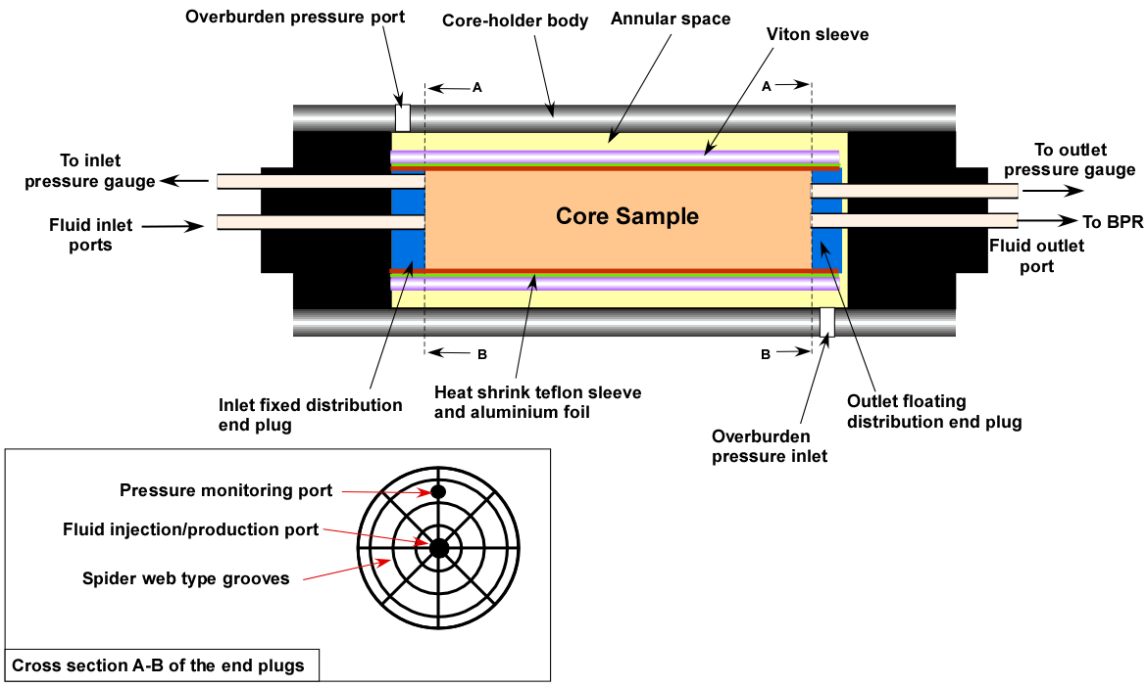

Figure 3.5. The general schematic diagram of the core-holder used during the experiments (after Saeedi, 2011).

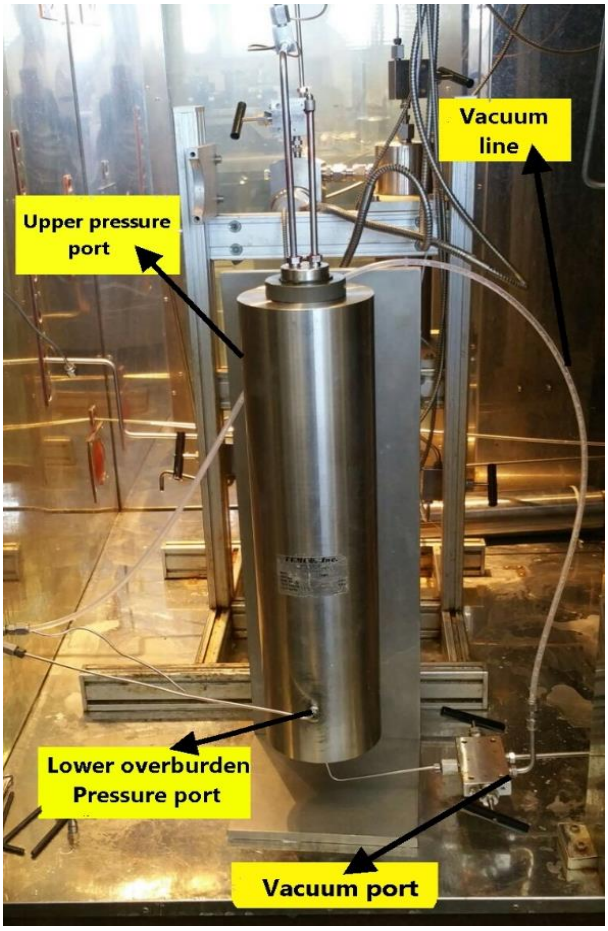

Figure 3.6. A photo of the core-holder used during the experiments.

The end faces of the inlet and outlet end plugs of the core-holder (Figure 3.5) feature a spider-web-type groove pattern to ensure even distribution of the fluids as they enter or exit the core-sample. To prevent the outwards diffusion of CO_2 from the core sample, it is necessary to use a special multilayered sleeve during the experiments. The CO_2 diffusion would damage ordinary rubber sleeves undermining the integrity of the core-holder assembly as it would allow the overburden fluid to communicate with the pore fluids resulting in the immediate termination of the experiment. The CO_2-proof sleeve is made of several layers including heat-shrink Teflon, aluminium foil and Viton rubber (Figure 3.5).

As seen from Figure 3.2, another minor component of the system attached to the outlet of the core-holder is a dome-type back-pressure-regulator (BPR). The BPR is to maintain a constant and steady pore pressure inside the core sample and also to keep the fluid flow one-directional during the experiments. The pilot pressure to the BPR and overburden line are provided by two vertically oriented intermediate cylinders (Figure 3.2) with a small cushion of an inert gas (e.g. N_2) on top of them. The gas cushion is to minimise the effect of any temperature fluctuations on the stability of the pressures applied. Although, both cylinders are placed inside a constant temperature fan forced oven to effectively eliminate any temperature variations.

3.1.3. The data collection and monitoring system

All parts of the apparatus (e.g. sensors, electronic interfaces, pneumatic valves, injection and collection pumps and controller modules) are connected to two high-performance computer machines. Appropriate data logging and monitoring software are installed on both computers allowing for experimental data to be recorded with time steps as short as one second (Figure 3.7).

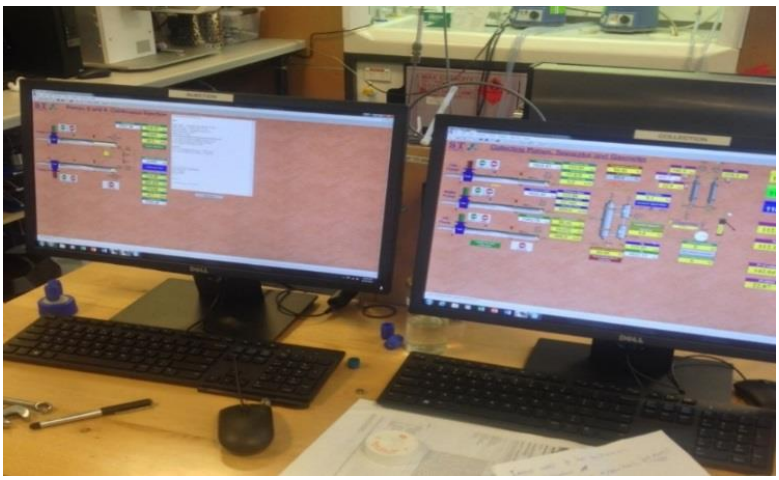

Figure 3.7. The two computer connected to the apparatus for data-logging and monitoring.

3.2. The Experimental Conditions and Material

3.2.1. P-T conditions

Table 3.1 presents pressure and temperature values applied in the core-flood experiments. While the same overburden pressure and temperature were used in all the experiments, two pore pressures of 14 and 20 MPa were applied during CO_2-EOR and live brine flooding experiments, respectively.

Table 3. 1. Reservoir P–T conditions during the core flooding experiments.

Reservoir parameter	Value
Pore pressure (MPa)	14 or 20
Overburden pressure (MPa)	27
Reservoir temperature (°C)	65

3.2.2. Fluids

The fluids used in this study included the dead formation brine, live brine (brine saturated with CO_2 at the in-situ pressure and temperature), supercritical CO_2 and crude oil. The brine was prepared using distilled water and appropriate amounts of different analytical grade salts supplied by Sigma-Aldrich. Table 3.2 presents the composition of the brine used. This composition was chosen based on the data available for an actual deep rock formation from which some of the samples were sourced.

Table 3. 2. The composition of the synthetic brine used.

Chemical compound	Weight per Litre mg/L
Sodium chloride (NaCl)	30,172
Potassium chloride (KCl)	494
Calcium chloride ($CaCl_2.2H_2O$)	8,686
Magnesium chloride ($MgCl_2.6H_2O$)	2,442
Total Dissolved Solids	**38,366**

The live brine was prepared in a stirred high-pressure and high-temperature Parr reactor using high purity CO_2 (99.99 wt%) and the above-mentioned synthetically prepared brine. Live brine was prepared at experimental conditions (pressure and temperature) and then displaced from the reactor vessel into one of the core-flooding setup's fluid accumulators kept under the experiment conditions. Water vapour saturated-CO_2 was stored in another fluid bottle. The crude oil used in some of the experiments was obtained from an oil field in the Middle East. The chemical composition of the crude oil is presented in Table 3.3. As can be seen, the oil is very light (38˚API) and has a low concentration of wax, resin and asphaltene (9.945%).

Table 3. 3. The composition of the crude oil used in the experiments.

Component	Mol %	Component	Mol %	Component	Mol %	Component	Mol %
C2	0.21	C10	7.12	C20	1.995	C30	0.687
C3	1.155	C11	5.835	C21	1.768	C31	0.625
iC4	0.543	C12	4.953	C22	1.566	C32	0.579
nC4	2.64	C13	4.587	C23	1.375	C33	0.493
iC5	1.773	C14	4.025	C24	1.214	C34	0.461
nC5	3.467	C15	3.984	C25	1.056	C35	0.426
C6	6.253	C16	3.16	C26	0.984	-	-
C7	7.056	C17	3.258	C27	0.876	-	-
C8	8.211	C18	2.687	C28	0.834	-	-
C9	7.563	C19	1.983	C29	0.784	-	-

3.2.3. Core samples

A range of carbonate core samples (chalk, dolomite and limestone) were used. The cores had a common standard diameter of about 3.8 cm (1.5”) but with different lengths. They were sourced from several hydrocarbon reservoirs in the Middle East and some were drilled from quarried blocks. The selected core samples covered a wide range of permeabilities and porosities from very low to relatively high. Various experimental scenarios were performed on the core samples for different objectives, which required the division of the core samples into six groups based on the rock type (e.g. limestone or dolomite), permeability, porosity, any special hetergeneity features (e.g. fracture) and, finaly, the objective persued.

The first sample group consisted of five limestone cores (Figure 3.8). Table 3.4 presents the original pre-flood petrophysical properties of the core samples included in this group.

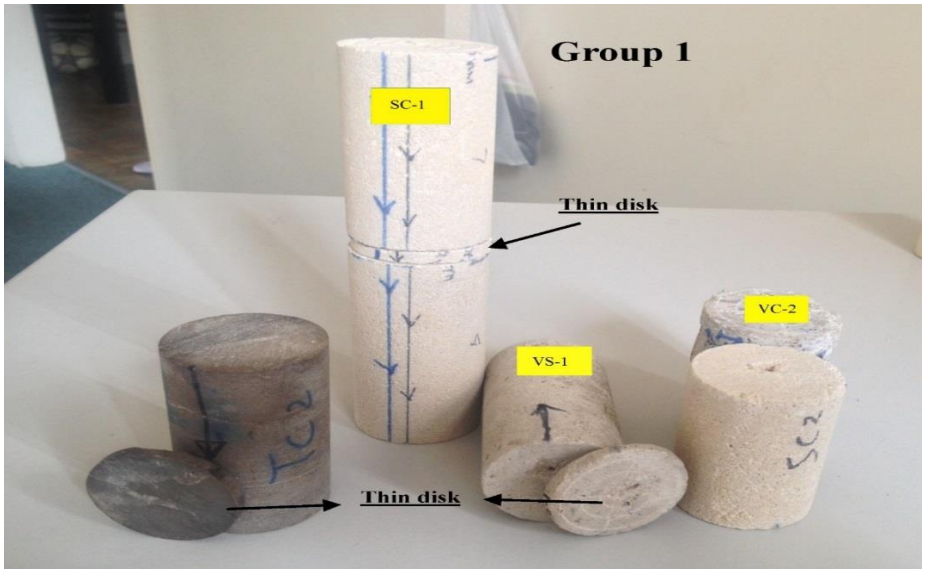

Figure 3.8. The five limestone core samples included in Group 1.

Table 3. 4. Characteristics of samples in Group 1.

Sample ID	Length (cm)	Diameter (cm)	Lithology	Porosity (%)	Permeability (mD)
VS-1	6.88	3.71	Limestone	21.40	22.01
SC-1 Inlet	6.98	3.81	Limestone	31.123	46.803
SC-1 Outlet	8.31	3.81	Limestone	31	37.53
SC-2	5.79	3.81	Limestone	32.57	54.91
TC-2	6.90	3.72	Fractured limestone	9.10	0.41
VC-2	5.95	3.84	Vuggy limestone	24.00	288.84

Sample SC-1 was a composite core consisting of two pieces of core plugs (SC-1 inlet and SC-1 outlet) cut from an initially long single piece. The reason for cutting the initial single piece into two individual plugs was to investigate the effect of fluid flow direction on the potential changes in the petrophysical properties of the plugs during the core-flood experiments. As an novel feature of this research compared to those done previously, a thin (thickness $\approx 5\ mm$) disk was also cut from some of the core-plugs tested (Samples SC-1, SC-2, TC-2 and VS-1) (Figure 3.8). These thin disks would undergo SEM scans before and after the core-floods to reveal any microstructural changes, which the samples might undergo due to the flooding procedure. The disks were polished on both end faces so that high quality and detailed enough SEM images could be generated. Furthermore, the thin disks were placed at different locations (inlet, outlet and middle of the samples), in order to evaluate the changes that might happen along the length of the core samples after the core-flooding experiments. With the use of the thin disks, the same exact spot could be scanned via SEM before and after flooding making the

comparison between the pre- and post-flood state of the rock more accurate. Further information about the use of the disks will be presented in chapters 4 and 5.

The second sample group included four dolostone cores (Figure 3.9). These samples also covered a range of permeabilities, from low to intermediate. Table 3.5 presents the original pre-flood petrophysical properties of these core samples.

Table 3. 5. Characteristics of the samples in Group 2.

Sample ID	Length (cm)	Diameter (cm)	Lithology	Porosity (%)	Permeability (mD)
VS-3	4.77	3.83	Tight Dolostone	11.97	2.82
VS-4	4.55	3.84	Tight Dolostone	11.62	1.44
VC-3	6.95	3.76	Vuggy Dolostone	40.98	528.14
TC-1	4.56	3.79	Fractured Dolostone	6.45	0.11

Figure 3.9. The four dolostone samples included in Group 2.

The third group consisted of two chalk cores (to be included in one composite sample) (Figure 3.10). The original pre-flood petrophysical properties of these two samples are provided in Table 3.6. Similar to some samples in Group 1 for the same objective explained before, a thin disk was cut from one of the cores and placed in the middle, as illustrated in Figure 3.10.

Table 3. 6. Characteristics of Group 3 samples.

Sample ID	Length (cm)	Diameter (cm)	Lithology	Porosity (%)	Permeability (mD)
CH-1 Inlet	7.61	3.71	Chalk	30.51	38.49
CH-1 Outlet	6.28	3.71	Chalk	27.88	29.77

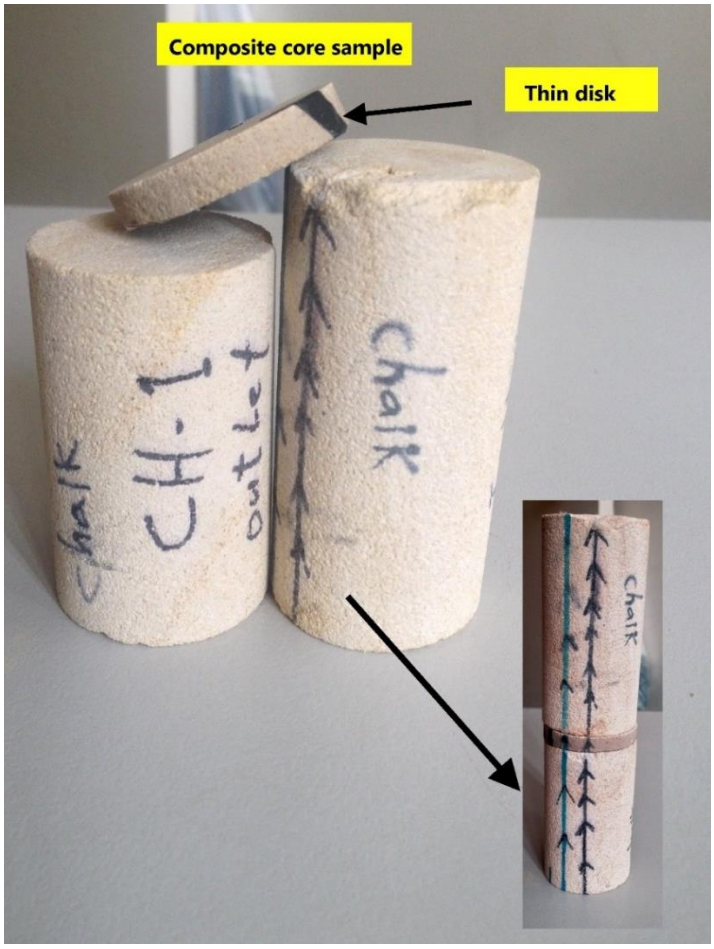

Figure 3.10. Chalk core plugs (one composite core sample) of Group 3.

The fourth group included a single manufactured radially heterogeneous sample consisting of two half-cores each cut from a different Indiana Limestone sample, namely IL-1 and IL-2 (Figure 3.11). Samples IL-1 and IL-2 were each cut from a different block of Indiana Limestone rock (purchased from the U.S.), one (IL-1) with a relatively moderate and another (IL-2) with a relatively low permeability (Table 3.7). The two half-cores were cleaned and their cut surfaces carefully polished so the two halves would make a near perfect single core (Figure 3.11). The main purpose behind the manufacture of this core assembly was to evaluate the

effect of heterogeneity on the results of the core-flooding experiments and compare the results with those obtained for other naturally homogeneous cores tested.

Table 3. 7. Characteristics of Group 4 samples.

Sample ID	Length (cm)	Radius (r) (cm)	Lithology	Porosity (%)	Permeability (mD)
IL-1	7.63	1.87	Indiana limestone	16.96	229.17
IL-2	7.63	1.87	Indiana limestone	11.86	3.42

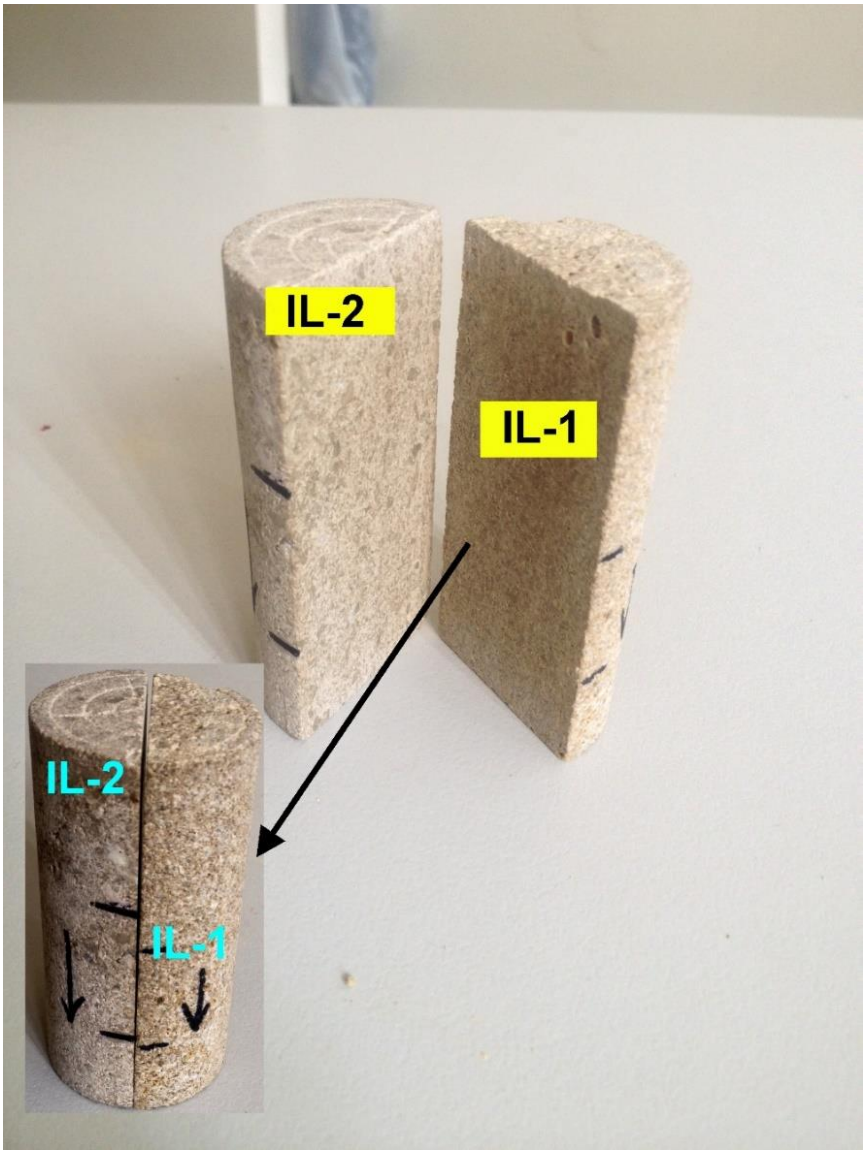

Figure 3.11. Manufactured heterogeneous core sample included in Group 4.

Four other carbonate (Indiana Limestone, Guelph Dolomite and Silurian Dolomite) samples were included in the fifth group of cores tested (Figure 3.12). The reason for including these samples in a separate group was that, instead of deep hydrocarbon reservoirs, they were cut

from quarried rock blocks purchased from the U.S these samples were tested using a continous CO_2-EOR flooding procedure (i.e. CO_2 injected continously for EOR purposes). The selected samples covered a wide range of permeabilities, from very low to relatively high. Table 3.8 presents the original pre-flood petrophysical properties of the samples. As can be seen from Figure 3.12, two of the samples were composite cores with a thin disk included in their sample assemblies.

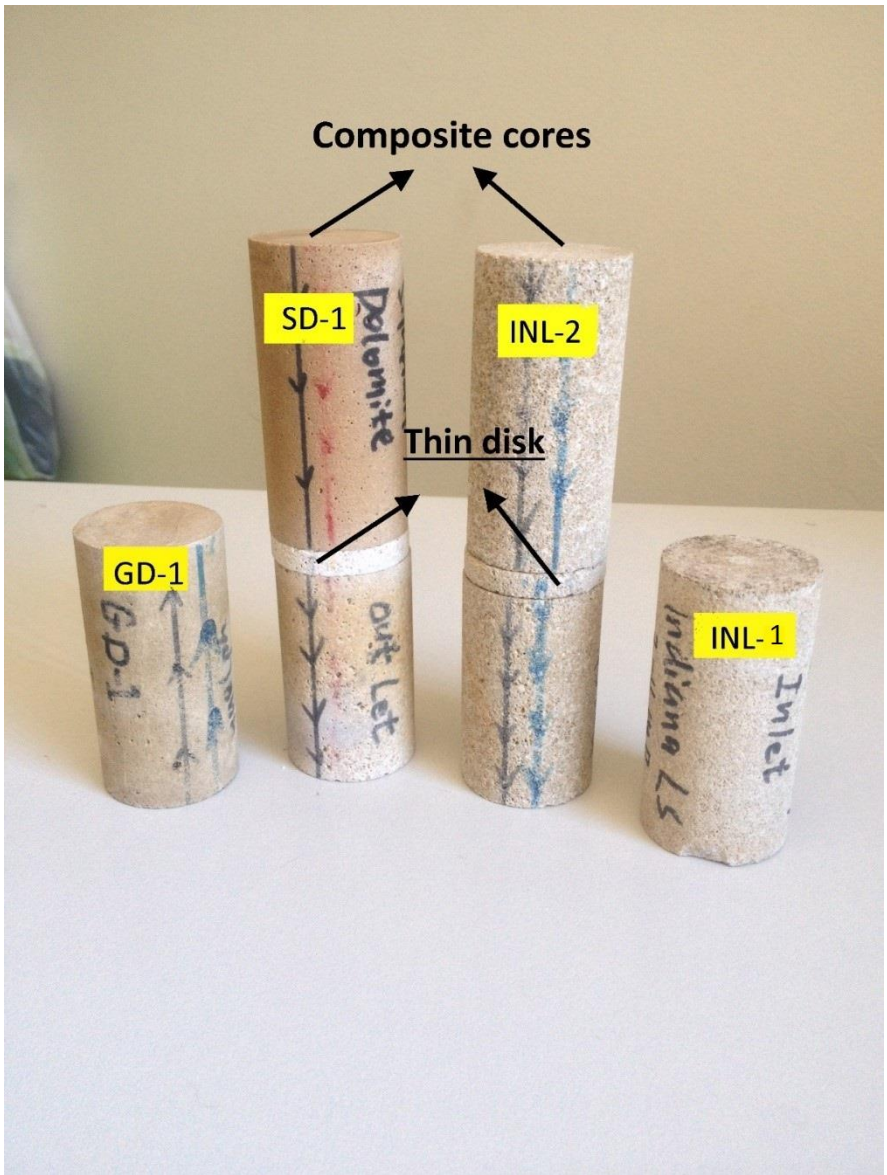

Figure 3.12. Carbonate core samples (limestone and dolostone) included in Group 5.

Table 3. 8. Characteristics of the samples included in Group 5.

	Sample ID	Length (cm)	Diameter (cm)	Lithology	Porosity (%)	Permeability (mD)
Composite core	SD-1 Inlet	7.61	3.8	Silurian dolomite	11.34	18
	SD-1 Outlet	6.35	3.8	Silurian dolomite	10.44	24.47
Composite core	INL-2 Inlet	7.58	3.73	Indiana limestone	16.78	324.54
	INL-2 Outlet	6.31	3.77	Indiana limestone	16.77	290.21
	GD-1	7.58	3.76	Guelph dolomite	13.16	8.59
	INL-1	7.6	3.81	Indiana limestone	15.47	6.72

The core samples in group six (Figure 3.13) included three carbonate samples. These samples were used for CO_2 WAG flooding (CO_2 injected in alternation with formation water) and this is the reason behind including them in a separate group. Sample VS-2 is a limestone core sample obtained from a carbonate reservoirs in the Middle East. Samples GD-11 and INL-11 are Guelph Dolomite and Indiana Limestone, respectively, which were purchased from the U.S. These samples covered a range of permeabilities, from very low to intermediate. Table 3.9 presents the original pre-flood petrophysical properties of the core samples in this group.

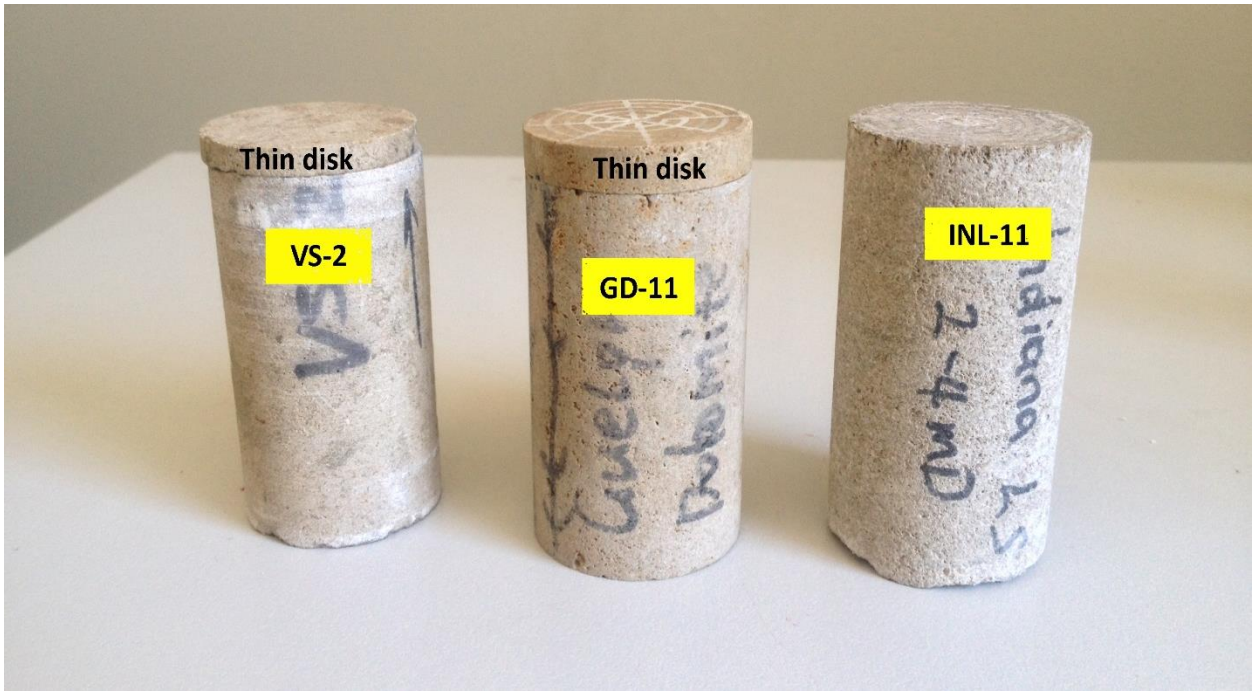

Figure 3.13. Carbonate core samples (limestone and dolostone) included in Group 6.

For SEM analysis, thin disks ($\sim 5\ mm$) was cut from samples VS-1 and GD-11 and attached to the samples during the experiments.

Table 3. 9. Characteristics of samples included in Group 6.

Sample ID	Length (cm)	Diameter (cm)	Lithology	Porosity (%)	Permeability (mD)
VS-2	6.3	3.55	Limestone	12.74	1.45
GD-11	6.28	3.76	Guelph dolomite	16.61	69
INL-11	6.97	3.76	Indiana limestone	15.7	11.1

3.3. Experimental procedures

As indicated earlier in this chapter, as a major component of this work, a series of core-flooding experiments was carried out on the different groups of samples outlined earlier following a number of flooding procedures. To detremine how the flooding procedures may alter the characteristics of the rock samples and characterise the possible mechanisms behind any changes, a set of carefully selected auxiliary measurements were also conducted on the pre- and post-flood core samples to obtain various sets of necessary data and information.

Apart from the standard porosity, permeability and XRD measurements, NMR T2 measurements were performed on fully brine saturated samples, to reveal their pore size distribution and the potential changes to this distribution after the core-flood experiments. Furthermore, X-ray CT images were generated for each rock sample using a medical CT scanner. The X-ray images would reveal the degree of heterogeneity inside each sample, as well as the potential changes to the core-scale and, to some extent, the pore-scale features in each sample due to the flooding procedures. Scanning Electron Microscopy (SEM) was also performed on the previously described thin disks to pinpoint any possible microstructural alterations to the post-flood samples.

Presented in the following section of this chapter is a detailed description of the various experimental analysis whose brief outlines were provided above.

3.3.1. Sample perpetration and preliminary measurements

All the core plugs were cut dry using a coring bit from either the whole-cores recovered from hydrocarbon wells or quarried rock blocks and then trimmed and polished using appropriate tools and then cleaned of dust using a fine brush and compressed air. Before conducting any of the earlier mentioned laboratory analysis, the cores and their offcuts were cleaned of any possible hydrocarbons and salt residues in a temperature controlled Dean-Stark apparatus (Figure 3.14), using warm methanol and toluene in turn and then dried in a vented oven at 65°C for different periods of time (12 to 72 hours), depending on their permeability. The samples remained in the oven until their weights stabilised indicating that they were completely dry. They were then removed from the oven and cooled down in a desiccator to room temperature,

before any measurements could be performed on them starting with the measurement of the samples' dimensions (i.e. length and diameter) and dry weights.

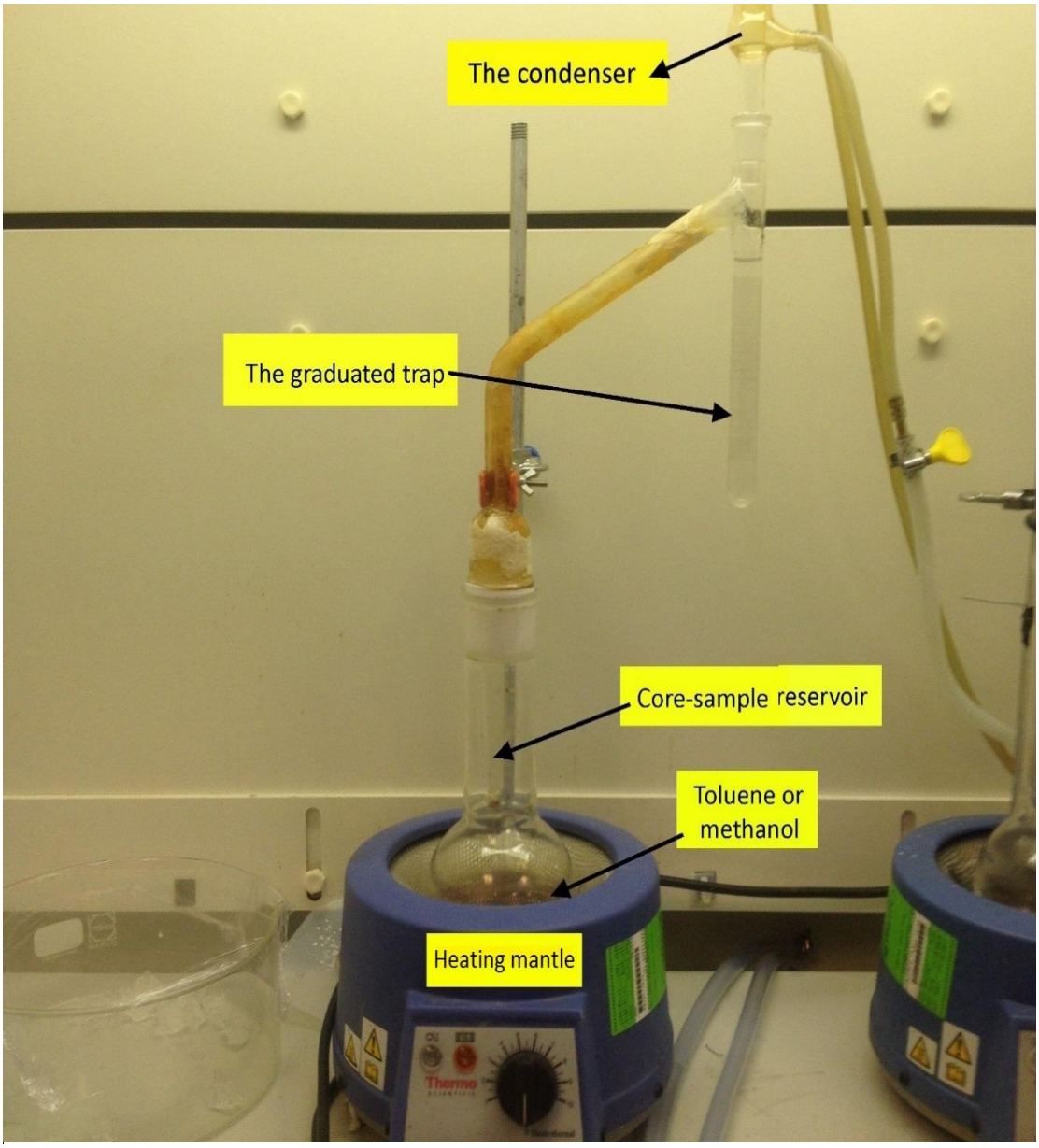

Figure 3.14. The Dean-Stark apparatus.

Porosity and permeability measurements were conducted on the cleaned and dried samples under in-situ net-effective stress using an automated helium porosi-permeameter (AP-608 instrument, Coretest Systems Inc.) (Figure 3.15). This instrument measures porosity and pore volume via a technique based on the Boyle's Law. It also uses an unsteady-state pulse decay technique to measure permeability.

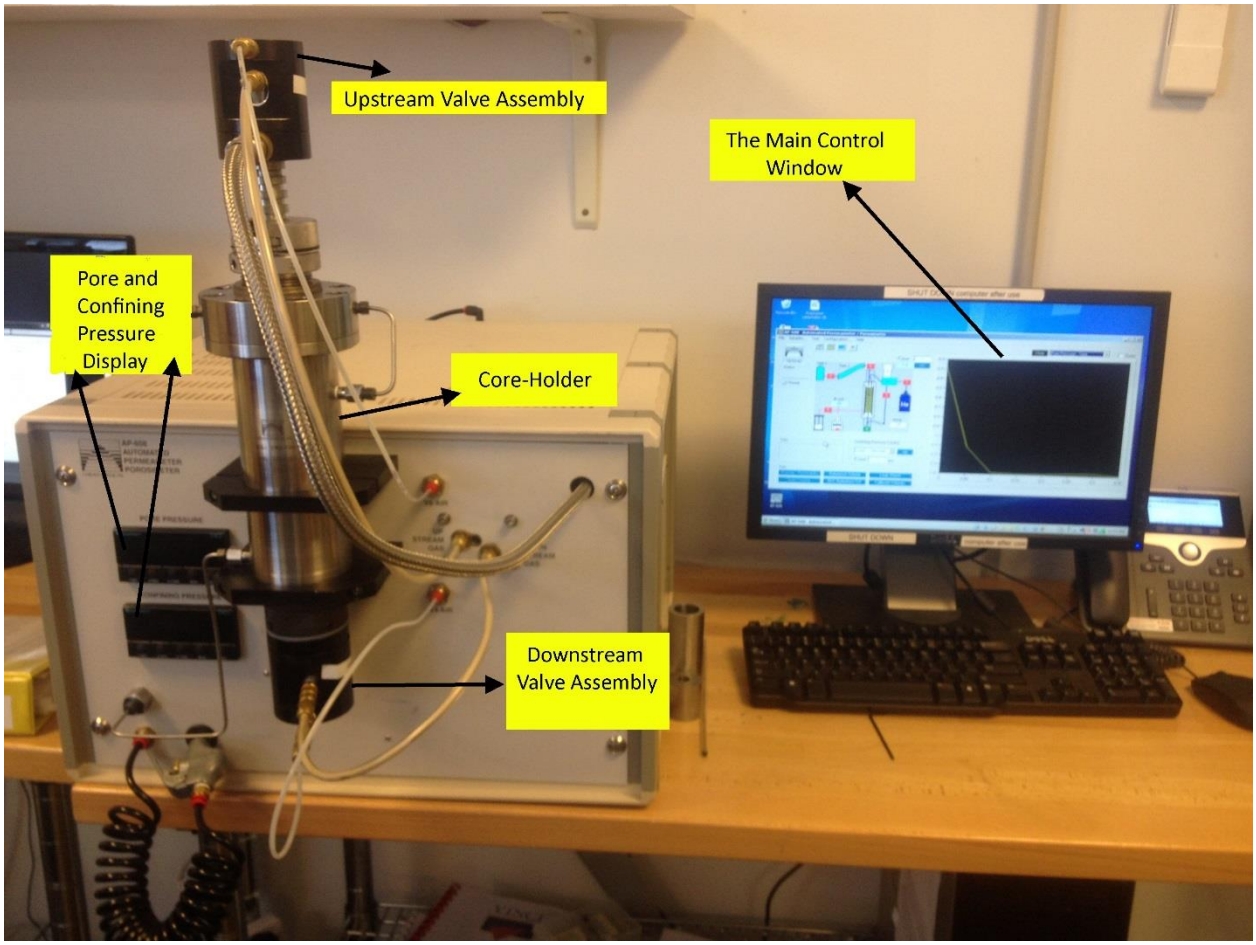

Figure 3.15. The AP-608 Automated porosi-permeameter apparatus.

3.3.2. Medical X-ray CT imaging

X-ray CT scans were done on all samples using a dual energy medical X-ray scanner (Siemense SOMATOM) (Figure 3.16). This imaging technique is generally suitable for the visualization from metre to millimetre scale and often achieves a voxel resolution around 100 µm3. In this study, an energy beam of 140 kV/500mAs was applied to acquire high-resolution transversal images every 400 µm along the Z axis (aligned parallel to the length of the samples) and 100 µm in the X and Y axes (perpendicular to the length of the samples). The ImageJ software was used to process the X-ray data and generate 2D and 3D views and reveal any special structures and features within the samples before and after the flooding.

Figure 3.16. The X-ray CT scanner (Siemense SOMATOM) (image taken from www.healthcare.siemens.com.au).

3.3.3. X-ray Diffraction (XRD) analysis

The XRD analyses were performed using a Bruker D4 XRD instrument (Figure 3.17) fitted with a Co tube, Fe filter and a Lynxeye position sensitive detector using a 2-theta range of 5 – 90°, step size of 0.02° and a divergence slit of 1°. The XRD end results were calculated using the Rietveld method in the software program, Siroquant. These measurements were performed on the cleaned offcuts of the samples, after turning them into powder form using mortar and pestle.

Figure 3.17. The Bruker D4 XRD apparatus (image taken from www.bpress.nc).

3.3.4. Scanning Electron Microscopy (SEM)

The SEM analysis used was a Philips XL40 controlled pressure in instrument fitted with a Bruker energy dispersing X-ray spectrometer (EDS). For these measurements, before flooding, to protect the samples from contamination, they were not coated by a carbon layer which is often applied in conducting such analysis. The SEM instrument was operated with an accelerating voltage of 30 kV in the controlled pressure mode, with a chamber pressure of 0.5 mBar, to prevent the charging of nonconductive materials and eliminate the need for the conductive coating of the sample. The images were collected with a back scattered electron detector which shows atomic number contrast (low atomic numbered materials such as Carbon appear black and high atomic numbered materials such as Lead appear white). The Bruker EDS was used to collect and analyse spectra from selected points. The spectrum collected were used for the identification of the elements present in the minerals without quantification.

A Tescan Mira3 field emission scanning electron microscope (FESEM) was used to collect high-resolution and stitched images of the entire end face of the sample disks. For samples prior to the core flooding, the FEGSEM was operated at 25 kV and $3x10^{-11}$ A, with a chamber pressure of 20 Pa, to prevent the charging of nonconductive materials and eliminate the need for the conductive coating of the sample. After the core flooding, the samples were carbon coated and examined in the SEM again using 25 kV and $3x10^{-9}$ A with a chamber pressure of $1x10^{-3}$ Pa.

3.3.5. Nuclear magnetic resonance (NMR)

The NMR T2 relaxation time spectrum of a rock sample recorded using an NMR test conducted on the brine saturated sample can be used to calculate its porosity and evaluate its pore size distribution (Coates et al. 1999; Dunn et al. 2002). The T2 value of a single pore is proportional to the surface-to-volume ratio of the pore, which is directly related to the porosity and pore size distribution of the rock (Coates, Xiao and Prammer 1999). In this work, NMR analyses were conducted on all core samples before and after the flooding experiments using a 2MHz low field NMR instrument (Magritek Ltd), with a Magritek Q-Switched P54 Probe, which provides high-performance measurements on cores with diameters of up to 3.8 cm (1.5") (Figure 3.18). The list of the NMR acquisition parameters and their values are provided in Table 3.10. In addition to the acquisition parameters, the common parameters and system components are also presented in Table 3.11.

Table 3. 10. NMR acquisition parameters used.

Inter-expt. Delay (ms)	Dummy Scans	Number of echoes	Tau (µs)	Point per echo	Echo shift (µs)	Dwell Time (µs)
15000	10	60000	75	12	15	0.5

Table 3. 11. The common parameters used during the NMR measurements.

Parameter Name	Value
B1 Frequency (MHz)	2.00479
90 Dgree Pluse Amplitude (dB)	-12
180 Dgree Pluse Amplitude (dB)	-6.5
Pulse Length (µs)	20
Damping Time (µs)	15
Receiver Gain (dB)	40
Minimum SNR	200

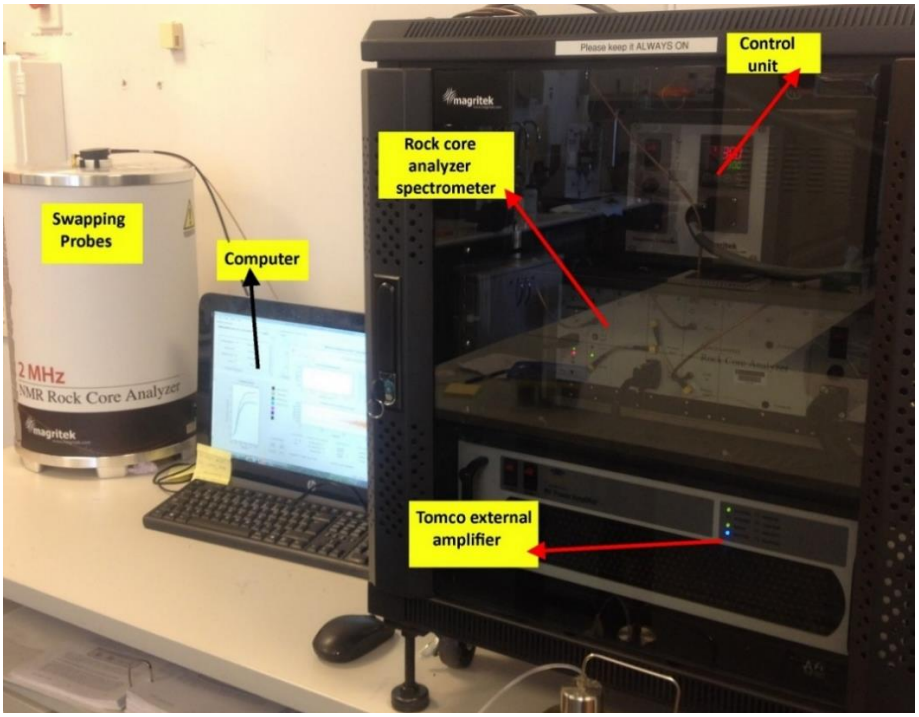

Figure 3.18. The nuclear magnetic resonance (NMR) apparatus.

In preparation for the NMR measurements, all samples were pressure-saturated with the previously prepared deaerated brine using the high-pressure cells shown in Figure 3.19. The samples were loaded into the cells and then connected to a vacuum pump to evacuate any trapped air in their pore space for 24 hours. Subsequently, formation brine was injected into the cells using a syringe pump to a total pressure of 17.3 MPa. The full saturation of the samples was achieved by operating the pump under constant pressure mode until the pump's volume

reading remained constant. It is also worth noting that, to be able to calculate the porosity of a sample, the NMR signal was calibrated by running an experiment on a glass vial containing a known volume of the formation brine. The procedure followed for every NMR test is summarised below:

1. Run a calibration sample using a brine sample of known volume (i.e. 20 ml). The brine sample used in the calibration was the same brine used to saturate the rock samples.
2. Run a calibration to collect the background signal from a cling wrap used to cover the samples to prevent evaporation of the saturating water during the tests and thereby increase the accuracy of the results obtained from the main NMR test.
3. Pressure saturate the samples with formation brine using high-pressure cells.
4. Remove the samples from the high-pressure cells and weigh them. The exterior of the samples were wiped from excess brine and then quickly covered with the cling wrap referred to before.
5. Insert the warped sample into the probe (P54) to start the test.
6. Run the data acquisition software (ProspaRCA) from the control computer machine (Figure 3.20). Enter the required data/information about the rock sample and then follow a series of steps and processes in the software to measure and extract the T2 data (Figure 3.21).
7. After the T2 experiment has finished, analyse the T2 results using the 'Analyse' button to define the relaxation spectrum (Figure 3.21).

Figure 3.19. The high-pressure saturation cells.

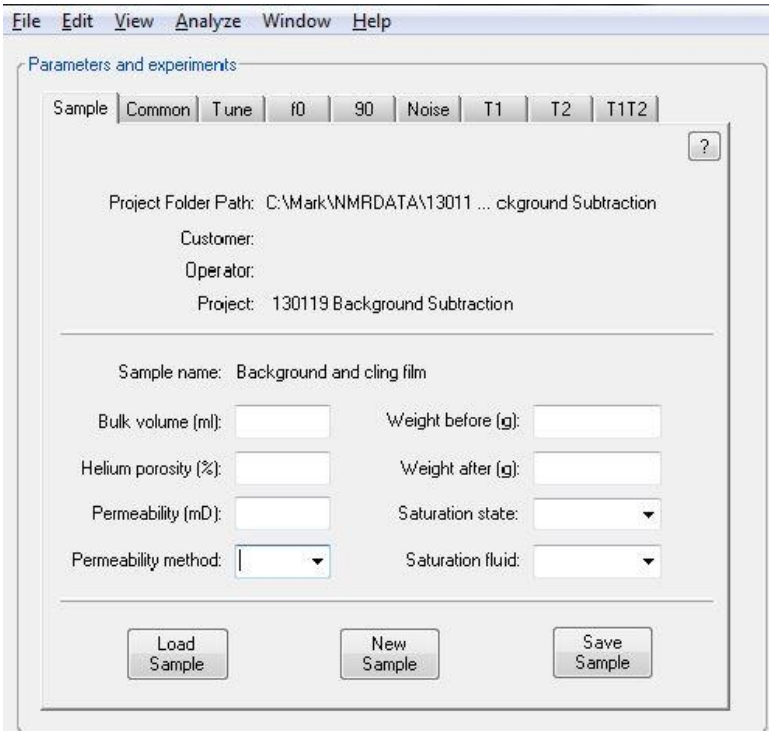

Figure 3.20. The ProspaRCA software main menu window.

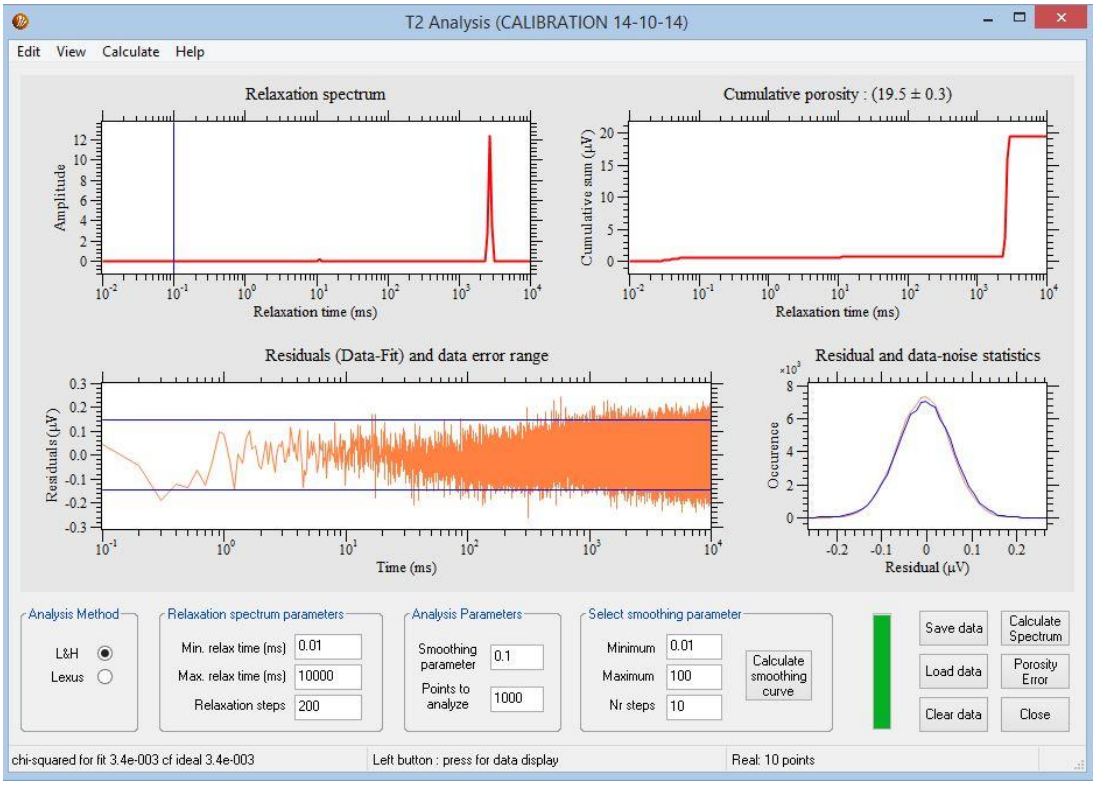

Figure 3.21.The T2 analysis window.

3.3.6. CO_2-saturated brine (live brine) preparation

For the core flooding experiments, the injection brine was fully saturated with CO_2 under reservoir conditions before being injected through the rock samples. This was to enhance fluid-rock interaction during the flooding and simulate the actual conditions encountered during CO_2 geo-storage where CO_2 would dissolve in the in-situ brine and begin reacting with the hosting rock formation. Also, for some of the flooding experiments, CO_2 was injected at some stage to displace the brine or crude oil. For these experiments, the CO_2 and brine were pre-equilibrated with each other to prevent mass transfer between the two phases.

As mentioned earlier, the live brine (CO_2-saturated brine) was prepared in a stirred high-pressure and high-temperature Parr reactor (Figure 3.22). Initially about 400 cc brine was injected to the bottom of the reactor vessel and then CO_2 was introduced into the vessel and pressurised to the desired experimental pressure while it was also heated to reach the required temperature. Subsequently, the reactor's stirring device was used to agitate and circulate CO_2 through the brine while the vessel pressure was maintained using a CO_2 charged syringe pump connected to it. The stirring continued until the pump's volume reading remained constant and steady. Then, the prepared live brine was displaced into the core-flooding apparatus's brine accumulator under constant pressure by injecting CO_2 into the top of the reactor vessel. Water vapour-saturated CO_2 was also prepared using a similar approach.

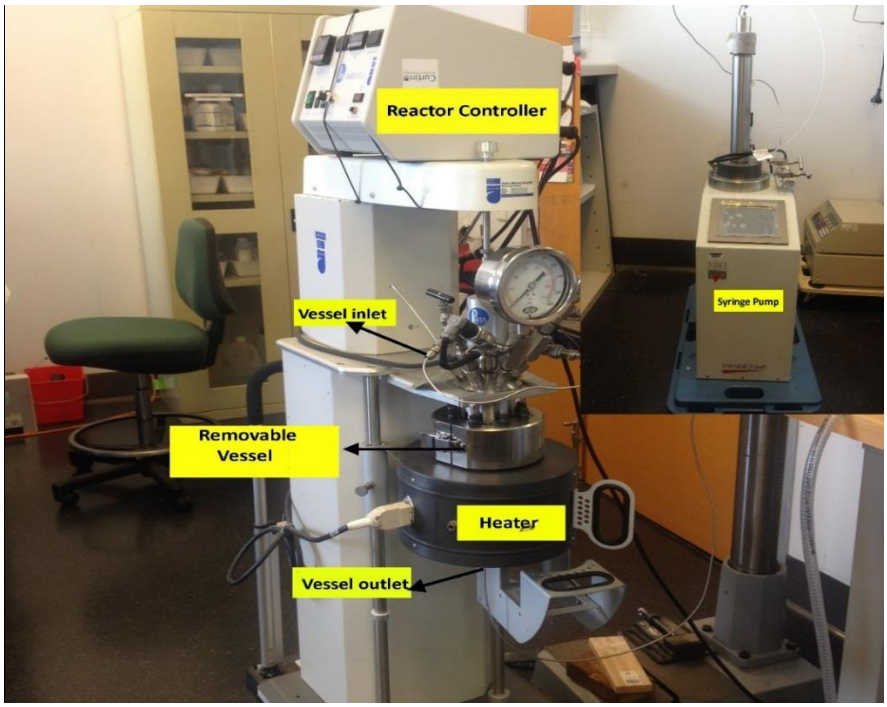

Figure 3.22. The stirred high-pressure, high-temperature Parr reactor.

3.3.7. The Core-flooding procedures

To achieve the predefined objectives of this study, three sets of core-flooding experiments were conducted each following its own specific flooding procedure. The flooding scenarios included: (1) Live brine flooding to evaluate the effect of fluid-rock interactions on petrophysical properties of rock samples during CO_2 strage in carbonate aquifers, (2) Evaluating the same factors as Scenario 1 plus EOR potential during continuous CO_2 injection into carbonate hydrocarbon reservoirs (CO_2-EOR) and, (3) Evaluating the same factors as Scenario 2 when CO_2 is injected in alternation with brine (WAG flooding scheme). The remainder of this chapter will cover the detailed procedures followed in conducting each of the above flooding schenrios.

3.3.7.1. Scenario 1: live brine flooding

Under this scenario, four sample sets including five limestone, four dolostone, two chalk and a manufactured radially heterogeneous Indiana Limestone sample (prepared using two separate plugs) were flooded with live brine under reservoir conditions. Upon the completion of all the earlier mentioned preliminary measurements, the core-flood experiments were carried out using the following procedure.

1. Loading the core-sample into the core-holder:

1.1. For every core-flood experiment, a clean and dry core sample was loaded into the multilayered combination sleeve referred to earlier. Then, placed on the fixed core-holder's inlet plug (Figure 3.23).

1.2. The inlet plug with the sample were inserted into the core-holder body and the inlet end cap was screwed into place. Then, the core-holder was oriented vertically and the support stand was attached to it to keep the core-holder stand safe.

1.3. Subsequently, the adjustable outlet plug was slowly and carefully inserted into the other end of the core-holder until it firmly rested at the outlet face of the core plug. Then, the end cap was screwed and tightened in place (Figure 3.23).

1.4. The overburden annular space of the core-holder was then filled slowly with water and pressurised to the full net-effective stress using a high-pressure hand-pump. The overburden fluid was initially injected from the lower overburden pressure port located at the bottom of the core-holder while the upper port was left open so the air would be displaced and expelled from the annular space (Figure 3.6). The absence of air would help with achieving a better initial seal around the sample. The reason behind using water as the overburden fluid was that, compared with hydraulic oil, it was less damaging to the sample in the case of a leakage. After

inspecting the core-holder for any possible leaks, the inlet and outlet of the core-holder were connected to appropriate flow-lines.

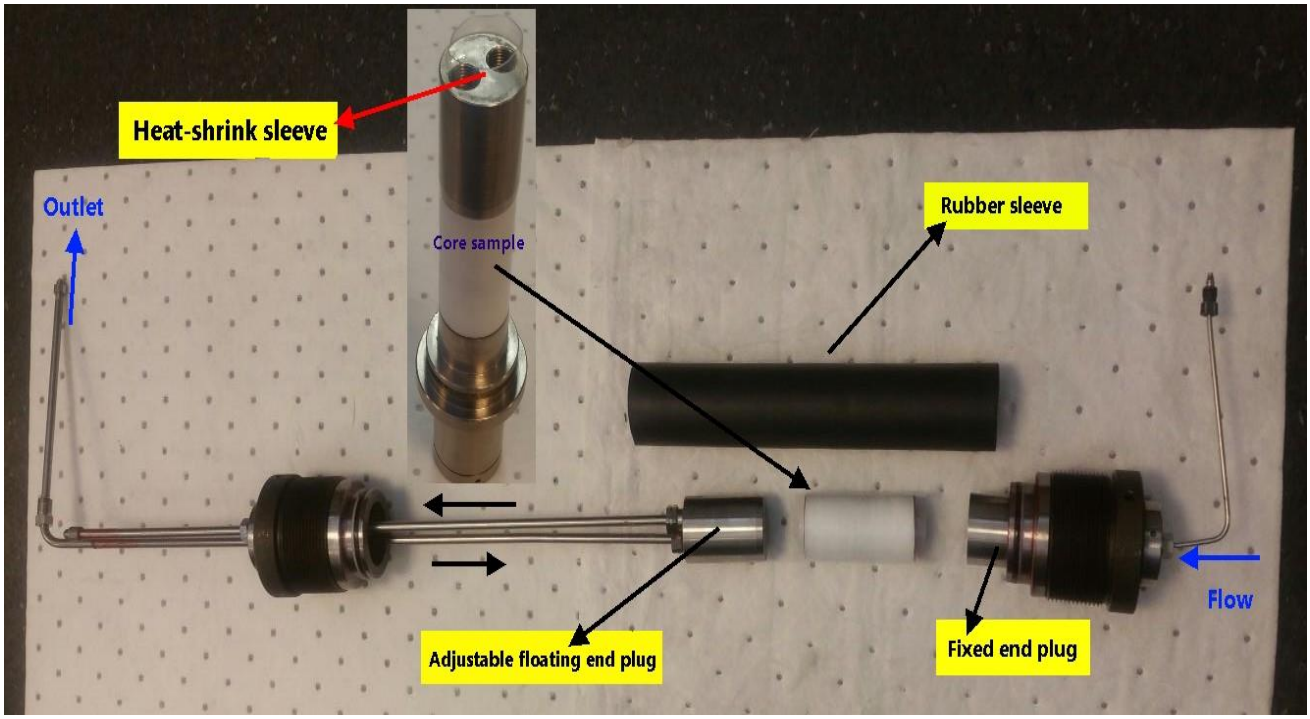

Figure 3.23. The sample with the combination layers of heating shrink Teflon, conventional Viton rubber sleeve, fixed end plug and adjustable floating end plug.

2. Vacuuming the system (sample and flow-lines):
   2.1. A vacuum pump was connected to the core-holder assembly and via an incorporated vacuum line (Figure 3.6). The core-holder was placed under vacuum between 12 and 24 hours, depending on the permeability of the sample, until the pressure reading on the inlet and outlet of the sample decreased and then remained stable.
   2.2. Once the vacuum period ended, the vacuum line was isolated, the vacuum pump turned off and the vacuum port was capped.
3. Saturating the sample with dead brine:
   3.1. The pore pressure was increased gradually using deaerated dead formation brine injection with a syringe pump. The injection was started at a low flow rate while monitoring the pore pressure as it would start to increase. In the meantime, the overburden pressure was also increased at the same rate as the pore pressure, until it reached the desired in-situ value. This kept the overburden pressure higher than the pore pressure, else it could lead to a failure in the experiment.

3.2. The core sample was left under reservoir condition in contact with the brine for a period of time (12-24 hours) to fully saturate the core and achieve adsorption equilibrium. The full saturation was verified by monitoring the volume of the injection syringe pump (operating under constant pressure mode) for stability.

4. Injection of live brine:

4.1. After the initial brine saturation, the sample was ready for flooding. The live brine was injected at the constant flow-rate of 30 cc/hr for all samples. A total of 600 cc live brine was injected through every sample.

4.2. A few effluent brine samples were collected during the some experiment to evaluate the fluid-rock chemical reactions that may occur while flooding the sample.

4.3. At the completion of the experiment, the confining and pore pressures were released gradually and the core sample was carefully removed from the core-holder.

After unloading the sample, it was subjected to the Dean-Stark extraction again using warm methanol to remove the water and salt residues from the sample. Subsequently, the sample was dried using the previously described procedure and post-flood sample characterisation was carried out as outlined earlier in this chapter.

3.3.7.2. Scenario 2: Continuous CO_2 injection for CO_2-EOR

Under the second scenario, four samples (two Indiana Limestone, one Silurian Dolomite and one Guelph Dolomite) were flooded using brine, crude oil and CO_2 in turn. The initial part of the flooding procedure was identical to the first three steps carried out under Scenario 1. Then, the following steps were followed in a chronological order.

1. Establishing the residual water saturation:

   By opening the relevant valves, crude oil injection into the sample was started at a constant flow-rate. The injection continued until no more formation brine could be produced. The produced fluids (oil and brine) were collected in small graduated tubes to accurately measure their volume so residual water saturation (S_{wr}) inside the sample (or the initial oil saturation (S_{oi})) could be calculated.

2. Water flooding (EOR):

   The injection of formation brine was started at a constant flow rate. The produced fluids were collected against time in small graduated tubes so oil production profile could be obtained accurately. The brine injection was continued until no more crude oil was produced.

3. Continuous CO_2 flooding (EOR):
   3.1. A total volume of 600 cc of CO_2 was injected through the core sample at constant flow-rate. The reason behind the injection of such a large volume of CO_2 was to recover as much oil as possible and to keep the core sample in contact with freshly injected CO_2 for a relatively long time and promote alteration to the petrophysical properties of the sample (if any).
   3.2. The produced fluids (brine and crude oil) were collected in small graduated tubes so the volume of any incremental oil recovered could be determined against time.
   3.3. At the completion of each experiment, the confining pressure and pore pressure were released gradually and the core sample was removed from the core-holder.
   3.4. After unloading the sample, it was washed using cold toluene. The cold toluene would remove any remaining oil but any precipitated asphaltene during the test would be preserved for further evaluation.

Similar to Scenario 1, the sample was then dried using the previously described procedure and post-flood sample characterisation was carried out as outlined earlier in this chapter.

3.3.7.3. Scenario 3: Water-Alternating-Gas (WAG) experiments

Three samples (two Indiana Limestone and one Guelph Dolomite) were subjected to Water Alternating Gas (WAG) flooding where formation water and CO_2 were injected through the samples in alternation after the establishment of the residual oil by the initial water flood. Similar to Scenario 2 experiments, the initial part of the flooding procedure was identical to the first three steps carried out under Scenario 1. Then, the following steps were followed in a chronological order.

1. Water-Alternating-Gas (WAG) flooding:
   1.1. Carbon dioxide and brine were injected alternately at constant flow-rate with injection cycles of half a sample pore-volume.
   1.2. The produced liquids were collected in small graduated tubes to keep track of the oil recovery profile against time accurately. The injection was continued long after no more crude oil was produced, to give the injected fluids a relatively long time to interact with the rock sample and promote alteration to its petrophysical properties (if any).
   1.3. At the completion of the experiment, the confining and pore pressures were released gradually and the core sample was removed from the core-holder.
   1.4. Similar to Scenario 2 experiments, after unloading the sample, in pursuing the same objective as stated earlier, the sample was washed using cold toluene only.

Similar to the previous two scenarios, the sample was dried using the previously described procedure and post-flood sample characterisation was carried out as outlined earlier in this chapter.

It is worth noting that during the core-flooding experiments, all parameters (i.e. flow rate, volumes, pore pressure, confining pressure, as well as inlet and outlet pressures of the core-holder) were recorded against time at adequate time intervals.

Chapter 4

4. Experimental results

This chapter is to present the results of the various experimental measurements whose detailed procedures were provided in Chapter 3. As indicated before, three sets of core-flooding experiments were conducted each following its own specific procedure. As discussed in details in the previous chapter, to evaluate any changes that the samples may undergo, a set of experimental tools and techniques including porosity-permeability measurements, X-ray CT scanning, NMR T2 measurements and SEM imaging, were used to test the pre- and post-flood samples. For each of the above measurement techniques, the results are categorised and presented according to the three core-flooding procedures followed. It is worth noting that a detailed discussion of the results obtained and observations made as included in this chapter will be presented later in Chapter 5.

4.1. X-ray Diffraction (XRD) analysis

Many of the events that may occur during the core-flooding experiments and their eventual net effects on the samples' properties would strongly depend on the mineralogy of the rock samples used. Therefore, X-ray Diffraction (XRD) measurements were performed on all samples to reveal their detailed composition. The XRD results for all samples are presented in Table 4.1. These measurements were performed on the sample powders prepared using the clean offcuts of the core plugs.

4.2. Basic sample property measurements

As indicated in Chapter 3, the porosity, permeability, dry weight and dimensions of every sample were measured before and after subjecting them to any of the flooding procedures. The data measured for the post-flood samples show some degree of alteration when compared to their pre-flood values. As will be discussed in detail in the next chapter, such alterations are believed to be the result of one or a combination of the mineral dissolution, mineral precipitation, fines migration, mechanical/physical compaction and/or asphaltene precipitation mechanisms.

4.2.1. Live brine flooding

As mentioned earlier, the samples flooded with this flooding procedure covered all three rock types of limestone, dolostone and chalk. The sample included eight single intact core plugs, two composite samples and one radially heterogeneous sample (made up of two half-cores prepared by splitting two separate whole plugs axially in half). Tables 4.2 - 4.5 present the

results of the pre- and post-flood measurements conducted on various sample groups outlined in Chapter 3.

Table 4. 1. The results of the XRD tests performed on all samples.

Sample ID	Dolomite wt%	Anhydrite wt%	Quartz wt%	Calcite wt%	Halite wt%	Albite wt%	Ankerite wt%
SC1	0.30	0.00	0.40	97.70	0.00	1.00	0.50
SC2	0.30	0.00	0.40	97.40	0.30	<1	0.60
VS1	3.70	0.00	0.60	93.70	0.50	<1	0.70
VC2	0.50	0.00	0.20	96.90	0.90	<1	0.50
TC2	6.00	0.00	0.70	91.70	0.30	<1	0.20
VS-3	87.90	9.60	0.40	0.20	0.60	<1	0.50
VS-4	57.90	38.00	0.90	0.20	0.60	2.00	0.40
VC-3	98.80	0.00	0.40	0.80	0.00	<1	0.00
TC-1	75.70	20.70	0.40	0.00	0.40	<1	1.90
CH-1	0.70	0.00	0.40	98.90	0.00	0.00	0.00
IL-1	1.90	0.00	1.10	97.00	0.00	0.00	0.00
IL-2	1.50	0.00	1.20	97.30	0.00	0.00	0.00
VS-2	13.10	0.00	0.50	82.20	0.60	1.00	2.20
GD-11	98.20	0.00	0.00	0.00	0.00	1.70	0
INL-11	0.00	0.00	0.70	99.30	0.00	0.00	0
SD-1	97.90	0.00	0.30	0.00	0.00	1.70	0.00
INL-2	1.40	0.00	0.70	97.90	0.00	0.00	0.00
GD-1	98.20	0.00	0.00	0.00	0.00	1.70	0.00
INL-1	0.00	0.00	0.70	99.30	0.00	0.00	0.00

Table 4. 2. The results of the basic rock property measurements conducted on Group 1 (Limestone) samples tested under flooding Scenario 1 (L: length, OD: outside diameter).

Sample ID	Before flooding						After flooding					
	NMR ϕ	Gas ϕ	K	L	OD	Dry wt.	NMR ϕ	Gas ϕ	K	L	OD cm	Dry wt.
	%	%	mD	cm	Cm	gr	%	%	mD	cm	cm	gr
VS-1	22.21	21.4	22.01	6.88	3.71	162	21.93	20.4	2004.4	6.88	3.64	158.65
SC-1 Inlet part	31.65	31.12	46.8	6.98	3.81	148	31.46	30.57	71.28	6.96	3.69	147.14
SC-1 Outlet part	31.65	31	37.53	8.31	3.81	176.2	31.41	30.38	32.86	8.31	3.81	178.2
SC-2	32.96	32.57	54.91	5.79	3.81	124.5	32.93	31.67	13034.67	5.73	3.74	117.72
TC-2	9.47	9.1	0.41	6.9	3.72	180.47	9.13	9	9215.2	6.88	3.72	179.24
VC-2	21.84	24	288.84	5.95	3.84	132.1	20.46	23.67	4820.4	5.95	3.79	131.23

Table 4. 3. The results of the basic rock property measurements conducted on Group 2 (Dolostone) samples tested under flooding Scenario 1 (L: length, OD: outside diameter).

Sample ID	Before flooding						After flooding					
	NMR ϕ	Gas ϕ	K	L	OD	Dry wt.	NMR ϕ	Gas ϕ	K	L	OD	Dry wt.
	%	%	mD	cm	cm	gr	%	%	mD	cm	cm	gr
VS-3	14.41	11.97	2.82	4.77	3.83	137.2	15.78	13.73	5	4.77	3.83	134.3
VS-4	13.57	11.62	1.44	4.55	3.84	131.11	14.7	12.89	1.39	4.45	3.84	126.3
VC-3	41.6	40.98	528.14	6.95	3.76	128.3	36.02	35.99	224.93	6.84	3.71	N/A
TC-1	8	6.45	0.11	4.56	3.79	136	8.77	7.51	0.68	4.47	3.79	132.6

Table 4. 4. The results of the basic rock property measurements conducted on Group 3 (Chalk) samples tested under flooding Scenario 1 (L: length, OD: outside diameter).

Sample ID	Before flooding						After flooding					
	NMR ϕ	Gas ϕ	K	L	OD	Dry wt.	NMR ϕ	Gas ϕ	K	L	OD	Dry wt.
	%	%	mD	Cm	cm	gr	%	%	mD	Cm	cm	gr
CH-1 Inlet	30	30.51	38.49	7.61	3.71	150.178	28.79	29.42	6408.52	7.51	3.71	149.102
CH-1 Outlet	27.55	27.88	29.77	6.28	3.71	130.842	26.47	27.1	28.67	6.28	3.71	131.562

Table 4. 5. The results of the basic rock property measurements conducted on Group 4 (manufactured radially heterogeneous limestone) samples tested under flooding Scenario 1 (L: length, OD: outside diameter).

Sample ID	Before flooding						After flooding					
	NMR ϕ	Gas ϕ	K	L	OD	Dry wt.	NMR ϕ	Gas ϕ	K	L	OD	Dry wt.
	%	%	mD	cm	cm	gr	%	%	mD	cm	cm	gr
IL-1	16.73	16.96	229.17	7.63	3.74	92.39	17.52	16	210.12	7.57	3.62	91.05
IL-2	11.79	11.86	3.42	7.63	3.74	101.02	11.26	10.85	3.00	7.63	3.70	101.02

4.2.2. Continuous CO_2-EOR flooding

The samples tested using this flooding scenario (Scenario 2) covered an Indiana Limestone, a Guelph Dolomite and a Silurian Dolomite as included in Group 5 of samples. The results of basic rock property measurements conducted on the pre- and post-flood samples are presented in Table 4.6.

Table 4. 6. The results of the basic rock property measurements conducted on Group 5 samples tested under flooding Scenario 2 (L: length, OD: outside diameter).

Sample ID	Before Flooding						After Flooding					
	NMR ϕ	Gas ϕ	K	L	OD	Dry wt.	NMR ϕ	Gas ϕ	K	L	OD	Dry wt.
	%	%	mD	cm	cm	gr	%	%	mD	cm	cm	gr
SD-1 Inlet	12.28	11.34	18	7.61	3.8	212.57	9.23	10.47	7.52	7.59	3.78	213.1
SD-1 Outlet	12.79	10.44	24.47	6.35	3.8	177.09	9.80	10.50	21.11	6.34	3.79	177.2
INL-2 Inlet	16.72	16.78	324.54	7.58	3.73	182.34	12.14	15.91	187.30	7.57	3.73	183.12
INL-2 Outlet	15.76	16.77	290.21	6.31	3.77	156.4	12.14	15.88	235.23	6.30	3.77	157.2
GD-1	13.27	13.16	8.59	7.58	3.76	208.06	10.72	12.45	6.06	7.58	3.75	208.35
INL-1	15.10	15.47	6.72	7.6	3.81	195	14.72	14.58	5.86	7.59	3.81	195.9

4.2.3. Water-Alternating-Gas (WAG) flooding

Two limestone and one dolostone sample were flooded using the WAG flooding procedure (Scenario 3). The results of basic rock property measurements conducted on the pre- and post-flood samples are presented in Table 4.7.

Table 4. 7. The results of the basic rock property measurements conducted on Group 6 samples tested under flooding Scenario 3 (L: length, OD: outside diameter).

Sample ID	Before Flooding						After Flooding					
	NMR ϕ	Gas ϕ	K	L	OD	Dry wt.	NMR ϕ	Gas ϕ	K	L	OD	Dry wt.
	%	%	mD	cm	cm	gr	%	%	mD	cm	cm	gr
VS-2	12.94	12.74	1.45	6.30	3.55	148.22	10.24	12.1	16	6.23	3.55	148.3
GD-11	16.40	16.61	69	6.28	3.76	164.36	14.21	16.13	37.42	6.28	3.72	164.96
INL-11	15.36	15.70	11.10	6.97	3.76	174.29	15.50	15.10	24.69	6.97	3.76	174.3

4.3. Medical X-ray CT imaging

As indicated earlier, X-ray CT imaging was used as a visualising technique to detect and qualitatively analyse possible spatial changes to the petrophysical properties of the samples due to different mechanisms (e.g. dissolution, precipitation, physical compaction, and to a lesser extent fines migration and asphaltene precipitation) that might have become active during various flooding scenarios conducted. To achieve this objective, X-ray CT scanning was performed on all the samples in their pre- and post-flood dry states. The resulting data were used to generate a number of 2D and 3D images for some of the core samples, to also

evaluate the development of any possible wormhole or dissolution features due to flooding. Furthermore, CT-value profiles were extracted from the X-ray images at different locations along the axis of every sample (resolution of 0.4 mm). This data can be used as an indicator of how the bulk density might vary along the length of a sample. The CT images are presented with dark or black colours representing low CT-value and light or white colours representing high CT values. In other words, the dark regions in the images show the low-density areas (pores), while the regions of relatively light colour show the high-density rock grains (Otani 2004). In this work, the comparison between the pre- and post-flood CT value profiles along with the selected cross-sectional images, were used to evaluate the variability of any flooding-induced alterations in the samples against the distance from their inlet faces. It is worth noting that in generating the X-ray images for different samples, different colour coding and colour combinations are used. In choosing the colours it has always been tried to make the images as clear as possible with respect to the pre- and post-flood features detectable for different samples.

In general, using the X-ray images and the associated information, different observations could be made for different sample groups flooded. For example, while the post-flood permeability increased in some samples, it decrease in others. Also, although some samples had undergone excessive dissolution as apparent by the formation of wormholes, others were less affected. A detailed discussion of these results will be presented in the next chapter.

4.3.1. Live brine flooding

The average CT value profiles and selected cross-sectional images along the length of samples VS-1, SC-2, TC-2, VC-2, SC-1, CH-1, IL-1 & IL-2 (two half-cores), VS-3, VS-4, VC-3 and TC-1 are shown in figures 4.1-4.14, respectively. Furthermore, 2D view of the 3D X-ray images for some samples along with some photos taken from various spots on the samples are shown in figures 4.15-4.26. These figures present clear evidences of the presence of wormholes and exessive mineral dissolution in some samples.

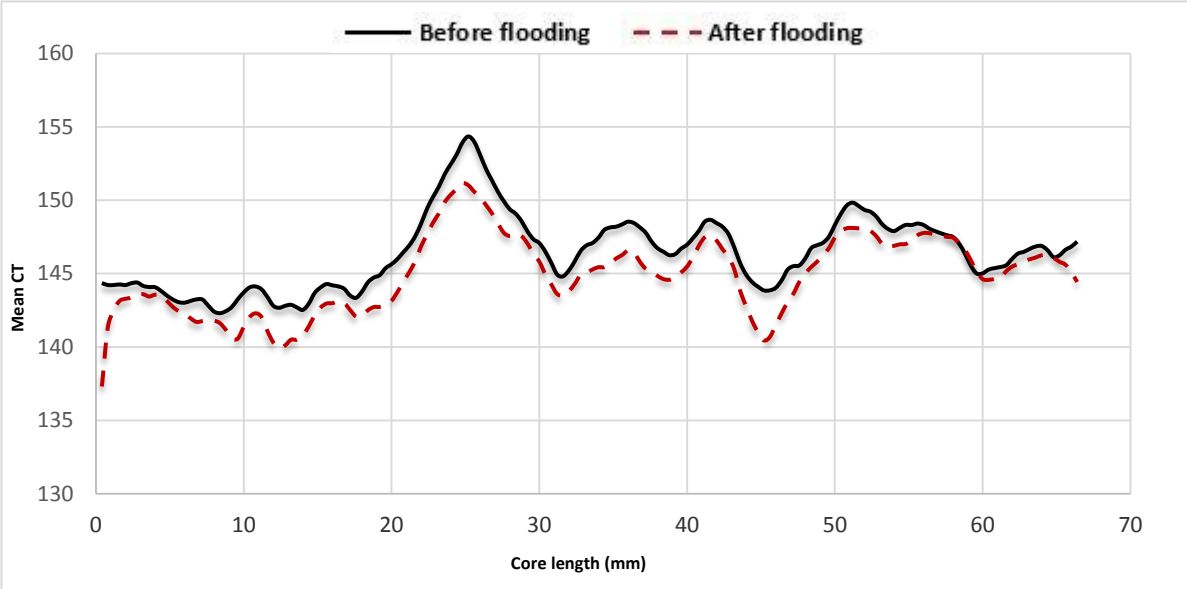

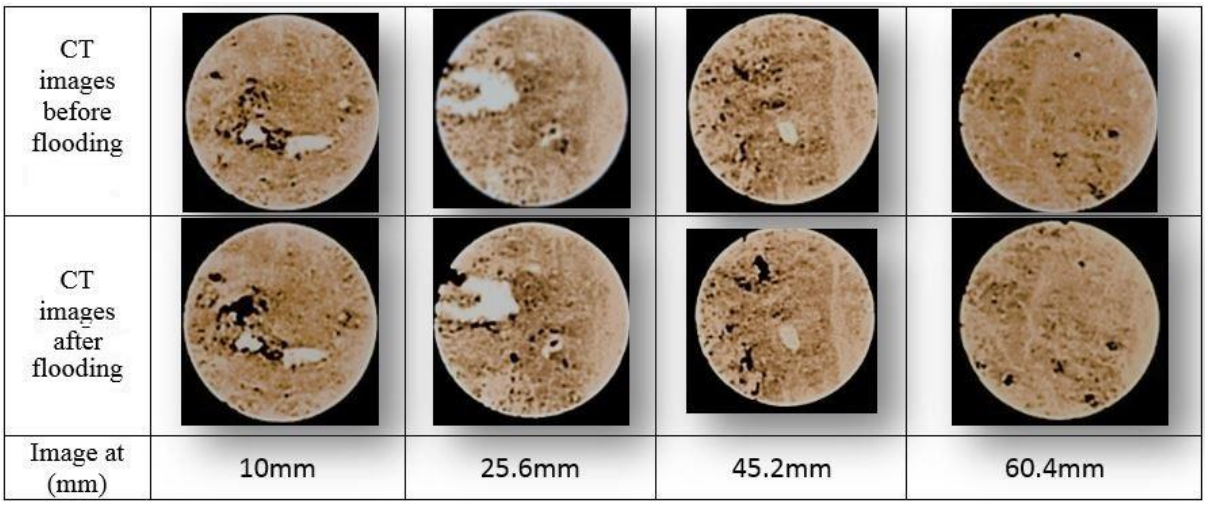

Figure 4.1. CT Value distribution and X-ray cross-sectional images for sample VS-1 before and after flooding. The CT number profiles and cross-sectional images show signs of massive mineral dissolution along the sample.

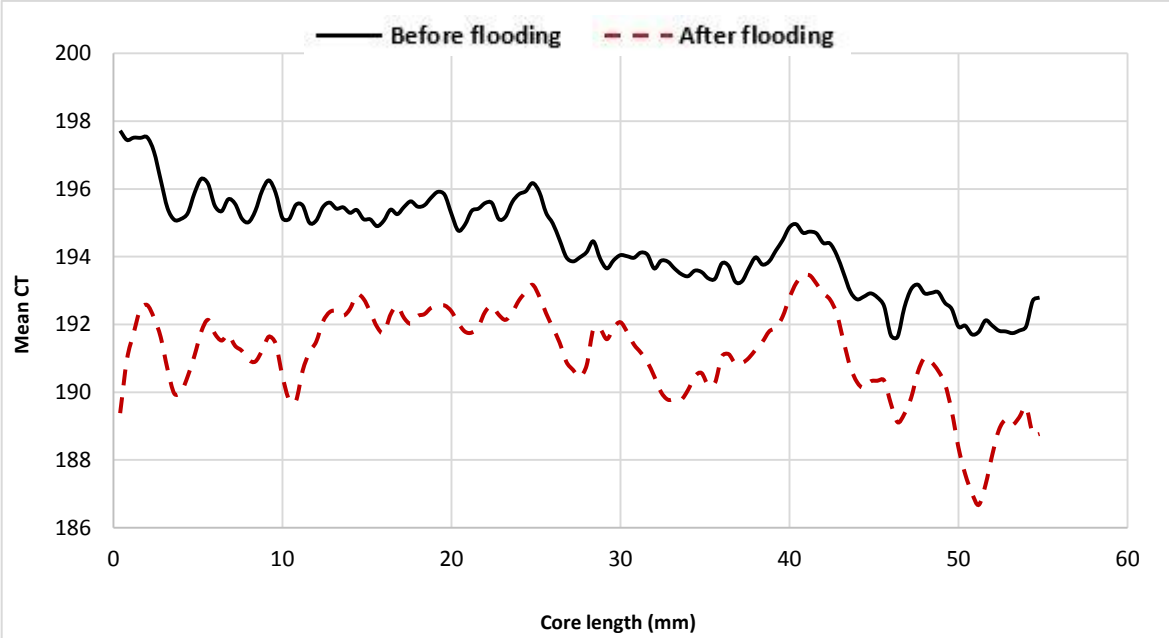

CT images before flooding	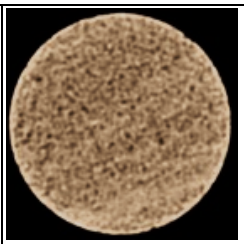	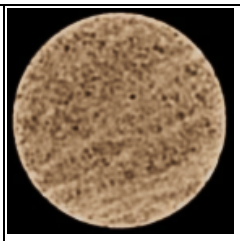	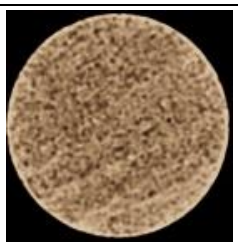	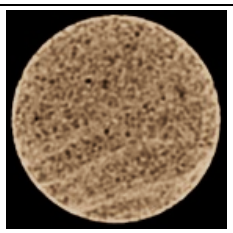
CT images after flooding	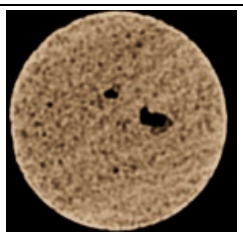	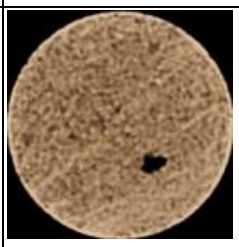	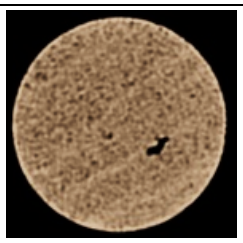	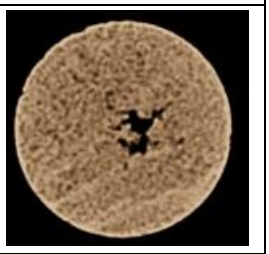
Image at (mm)	10.8 mm	25.2mm	42mm	51.2mm

Figure 4.2. CT Value distribution and X-ray cross-sectional images for sample SC-2 before and after flooding. The CT number profiles and cross-sectional images show signs of dissolution along the length of the sample. From the CT profiles, the sample seems to have become less dense due to mineral dissolution.

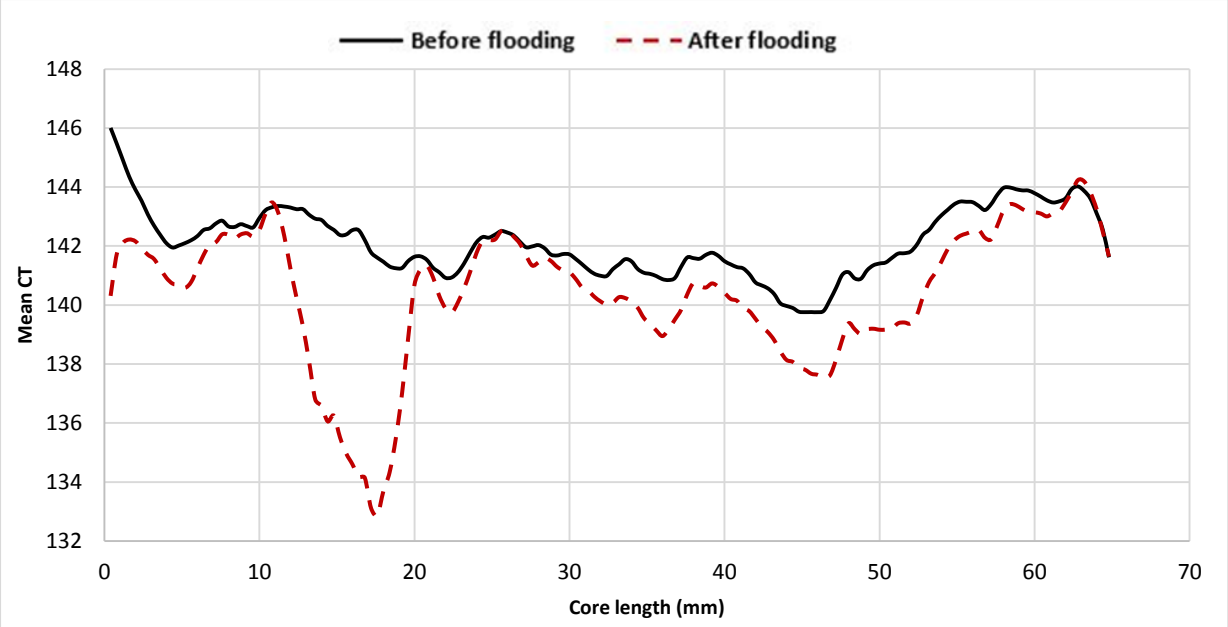

CT images before flooding	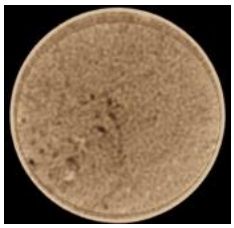	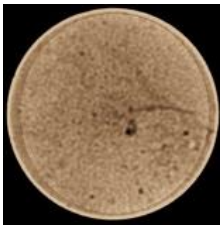	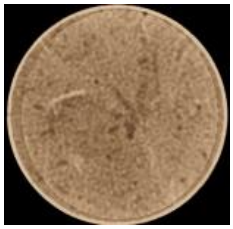	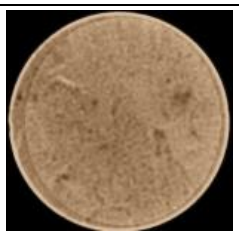
CT images after flooding	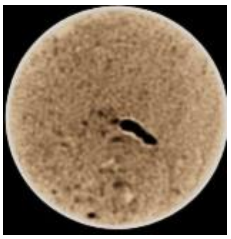	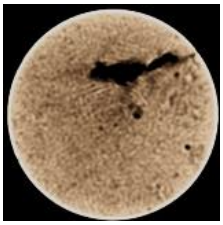	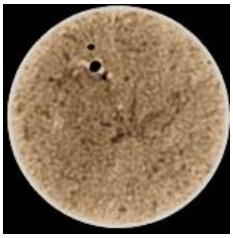	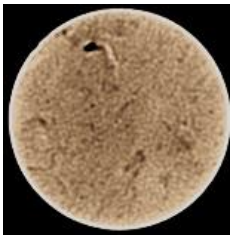
Image at (mm)	6mm	15.6mm	48.4mm	58.8mm

Figure 4.3. CT Value distribution and X-ray cross-sectional images for sample TC-2 before and after flooding. The CT number profile shows obvious signs of dissolution in the sample, where the sample becomes less dense. The dissolution is obvious at 15.6 mm from the sample inlet, possibly due to the effect of the fracture serving as a preferential flow path through which chemical reactions can occur.

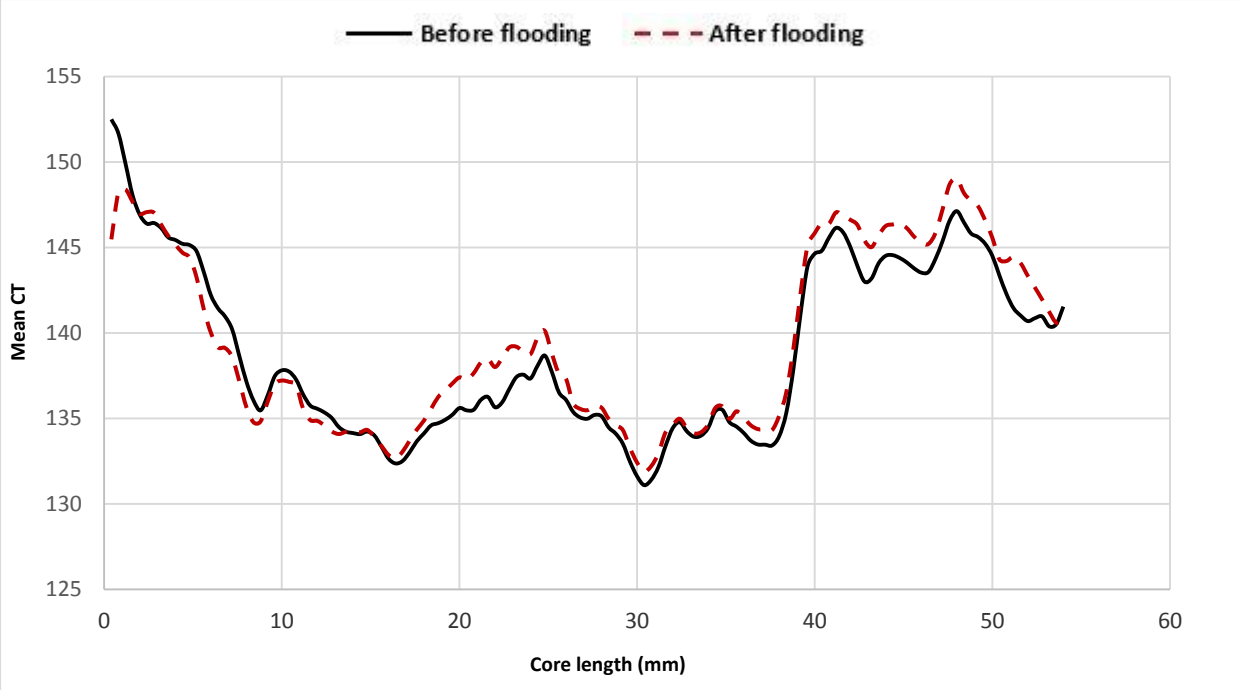

CT images before flooding	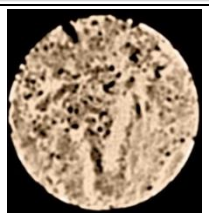	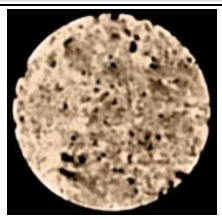	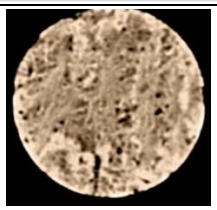
CT images after flooding	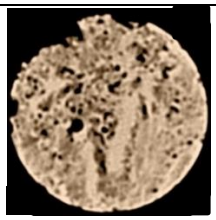	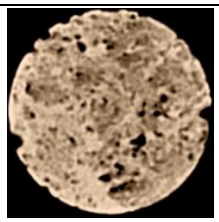	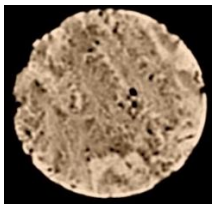
Location from inlet (mm)	4.4mm	45.6mm	54.4mm

Figure 4.4. CT Value distribution and X-ray cross-sectional images for sample VC-2 before and after flooding. The CT number profile shows an increase (mineral precipitation and compaction) and decrease (mineral dissolution) at certain locations, which is attributed to the minerals distribution within the sample.

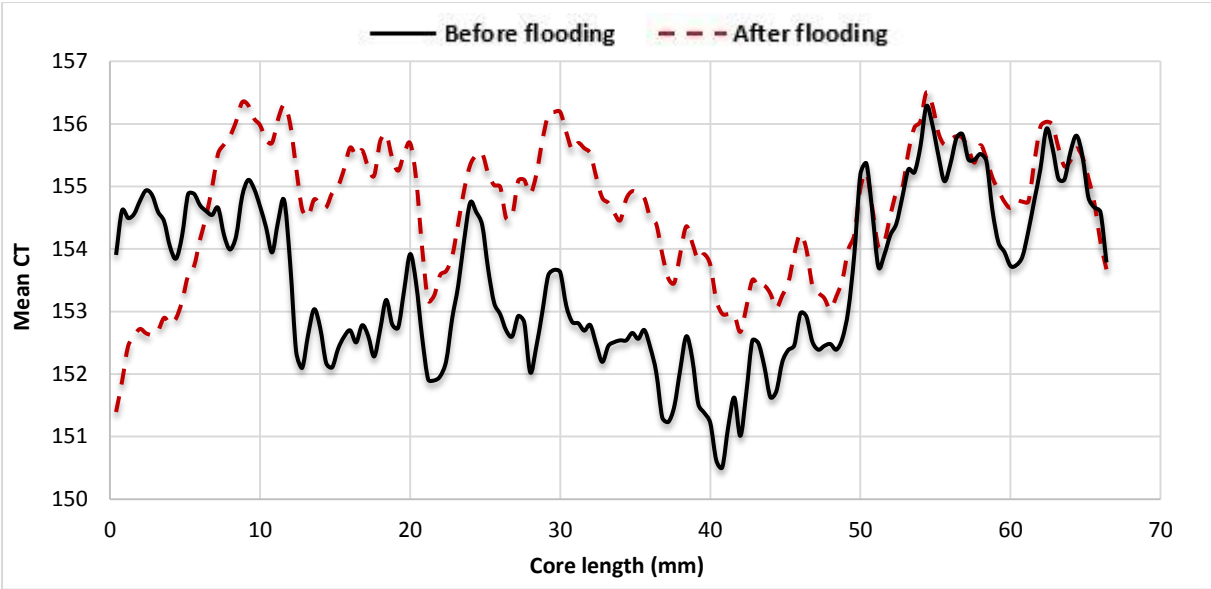

CT images before flooding			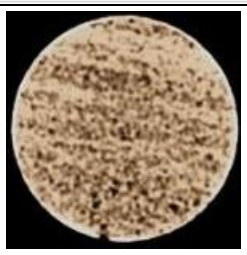	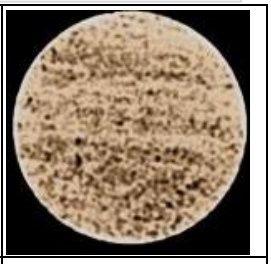
CT images after flooding	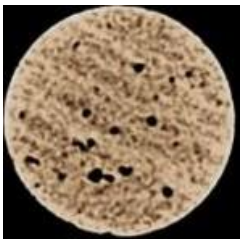	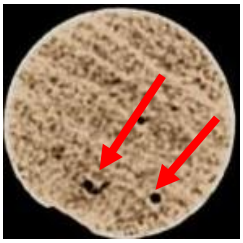	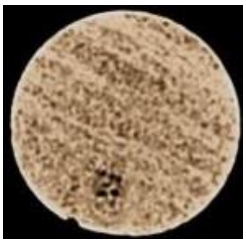	
Image at (mm)	3.6mm	14.4mm	36.8mm	60mm

Figure 4.5. CT Value distribution and X-ray cross-sectional images for sample SC-1 inlet part of the composite core before and after flooding. The CT number profiles and cross-sectional images show signs of excessive dissolution close to the inlet of the sample. Then, the CT value increased due to a combination of mineral precipitation and mechanical compaction; the compaction is obvious at 14.4 mm from the core inlet (see red arrows).

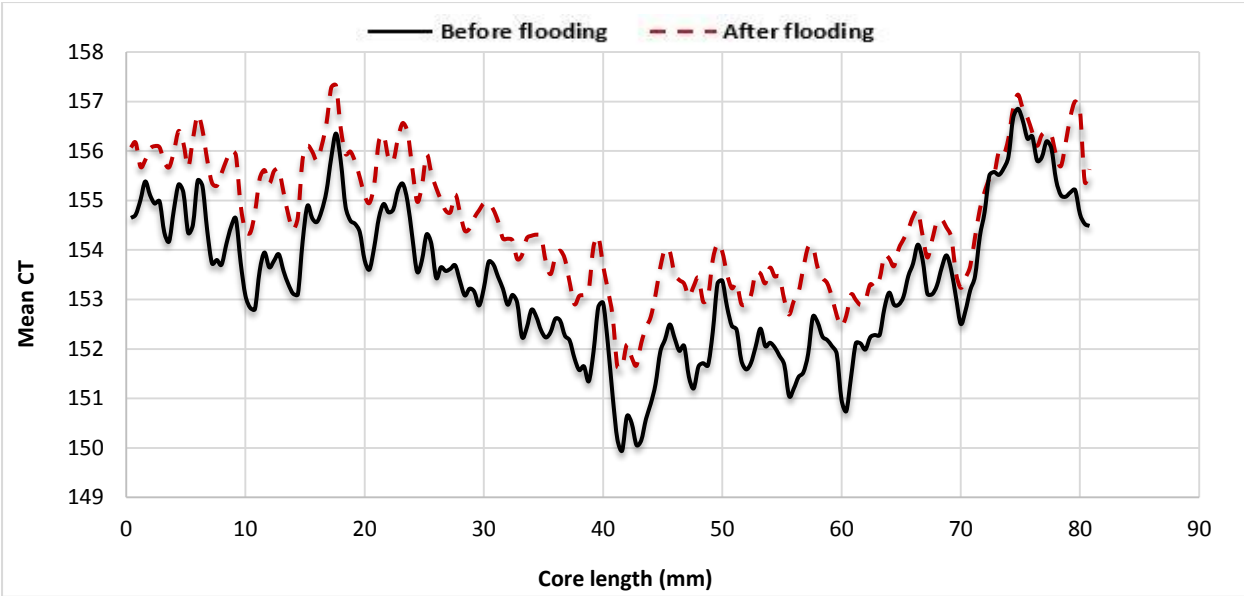

CT images before flooding	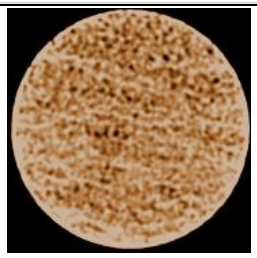	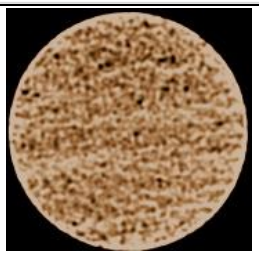	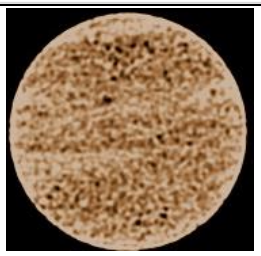	
CT images after flooding	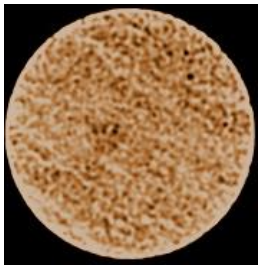	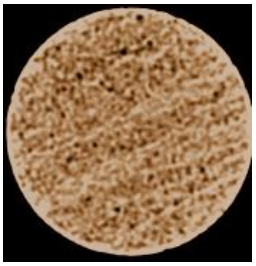		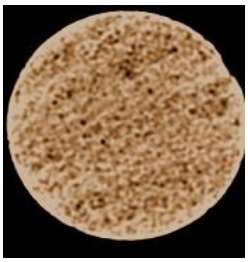
Image at (mm)	13.2mm	41.6mm	65.2mm	77.6mm

Figure 4.6. CT Value distribution and X-ray cross-sectional images for sample SC-1 outlet part of the composite core before and after flooding. The CT number profiles and cross-sectional images show signs of reduction in permeability after undergoing the flooding process. The reduction may be attributed to the mineral precipitation and mechanical compaction.

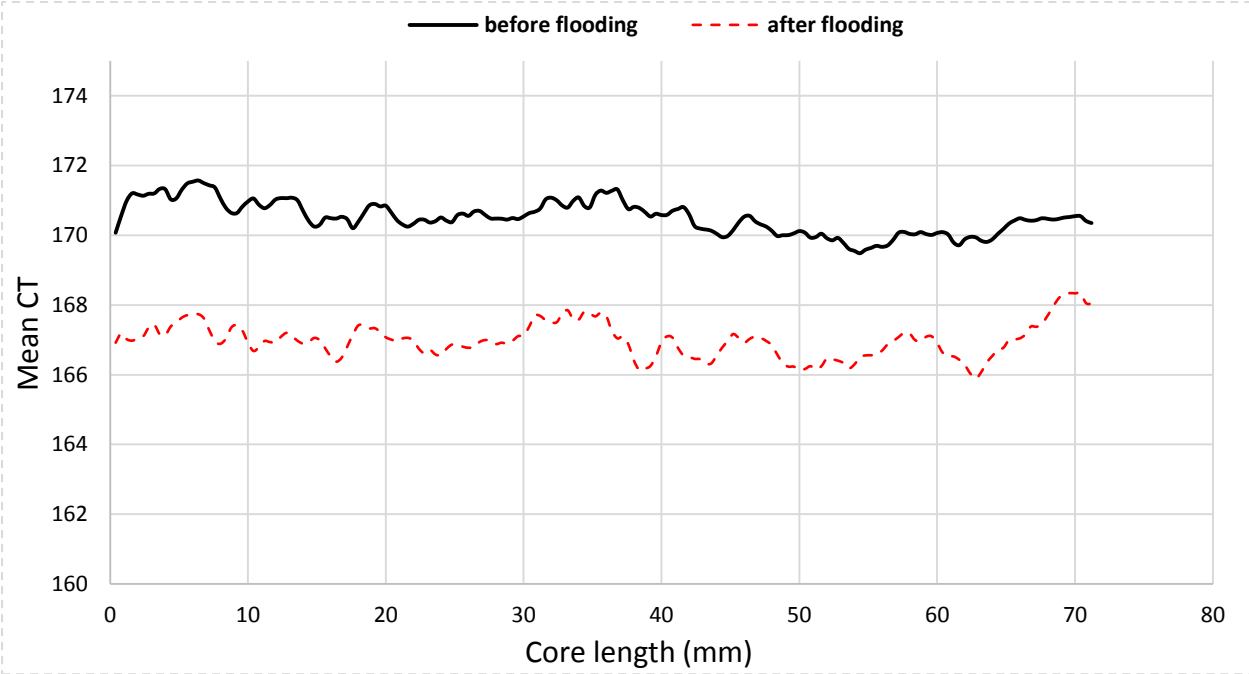

CT images before flooding	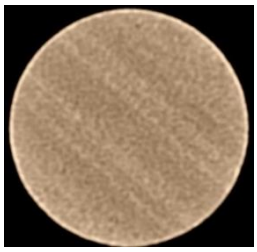	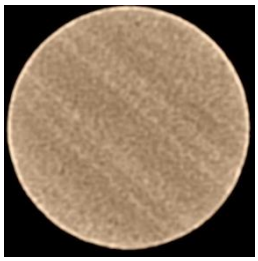	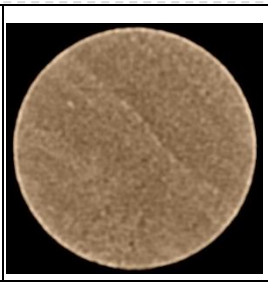	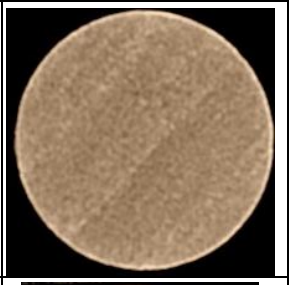
CT images after flooding	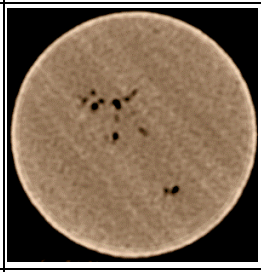	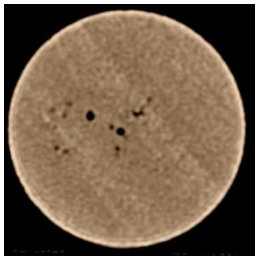	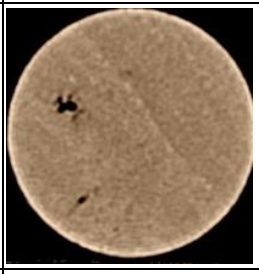	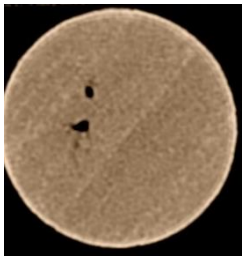
Image at (mm)	8.4mm	28.4mm	43.6mm	63.6mm

Figure 4.7. CT Value distribution and X-ray cross-sectional images for sample CH-1 inlet part of the composite core before and after flooding. The CT number profiles and cross-sectional images show signs of dissolution along the length of the sample. The sample seems to have become less dense due to mineral dissolution.

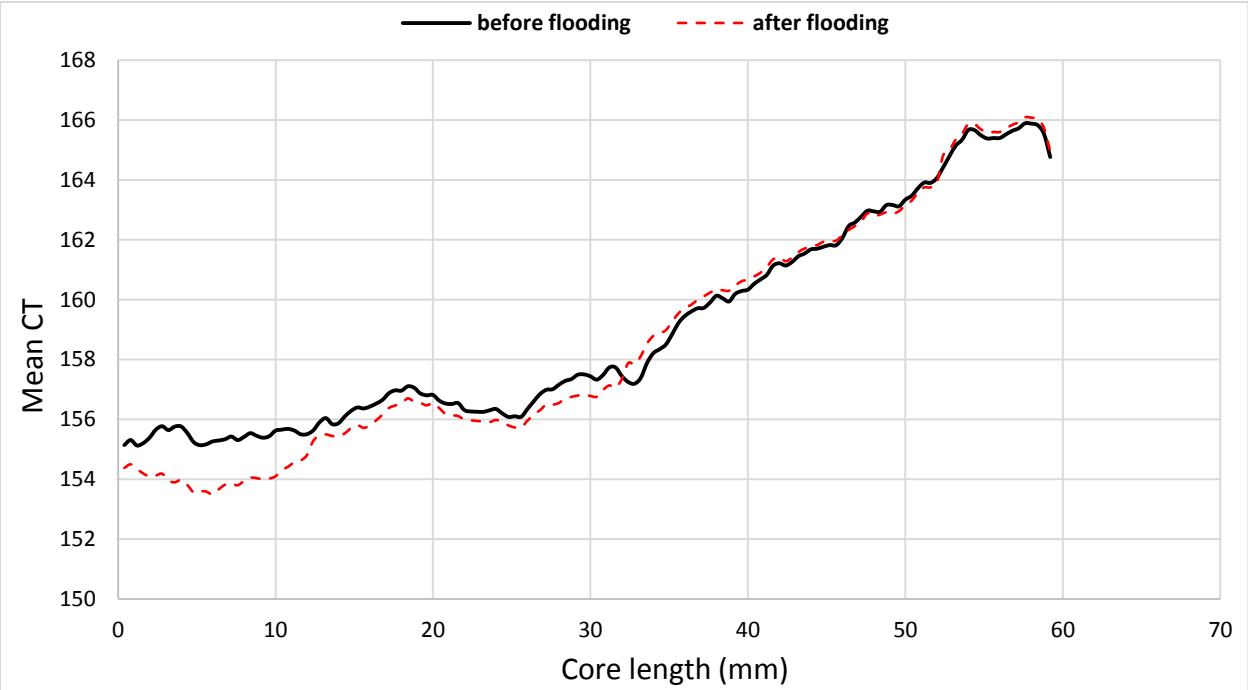

CT images before flooding	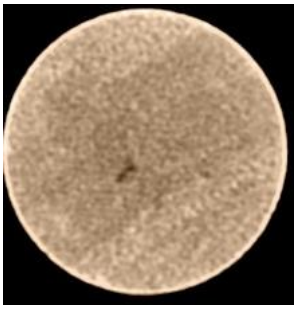	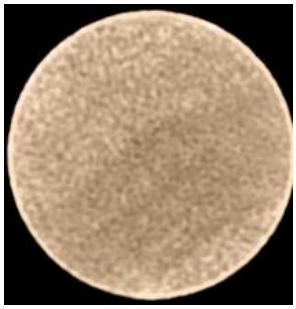	
CT images after flooding	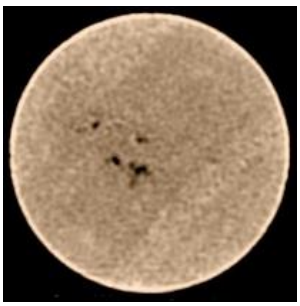	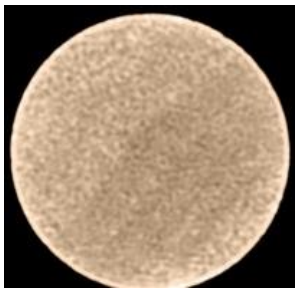	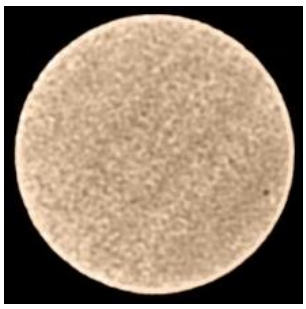
Image at (mm)	3.6mm	20.0mm	47.2mm

Figure 4.8. CT Value distribution and X-ray cross-sectional images for sample CH-1 outlet part of the composite. The CT number profiles and cross-sectional images show signs of dissolution close to the inlet after undergoing the flooding process.

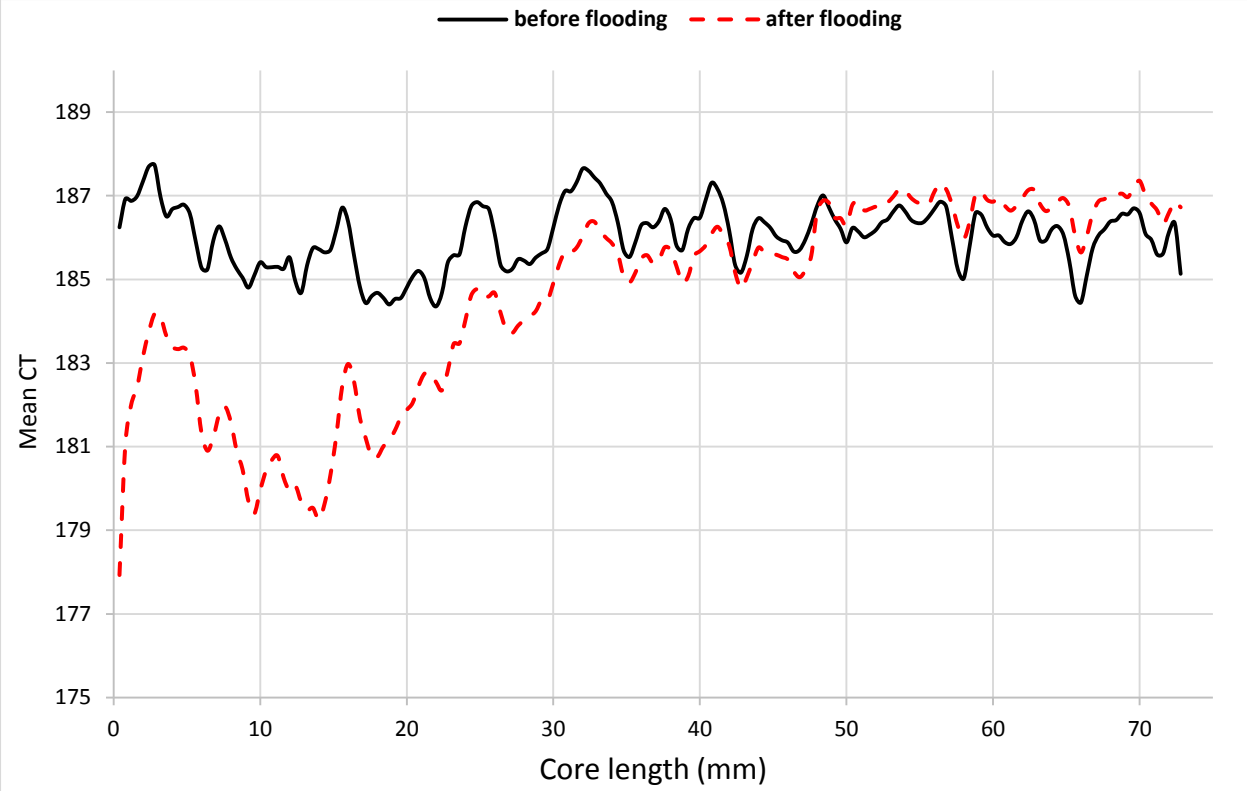

CT images before flooding	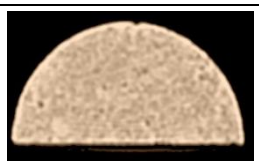		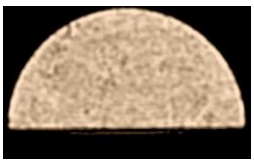	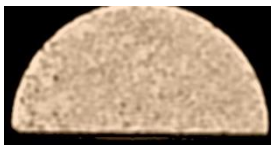
CT images after flooding			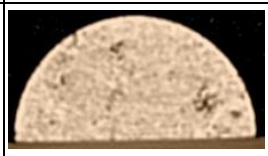	
Image at (mm)	1.2mm	14.4mm	23.2mm	55.2mm

Figure 4.9. CT Value distribution and X-ray cross-sectional images for sample IL-1 part of the composite (two halves). The CT number profiles and cross-sectional images show signs of dissolution after undergoing the flooding process.

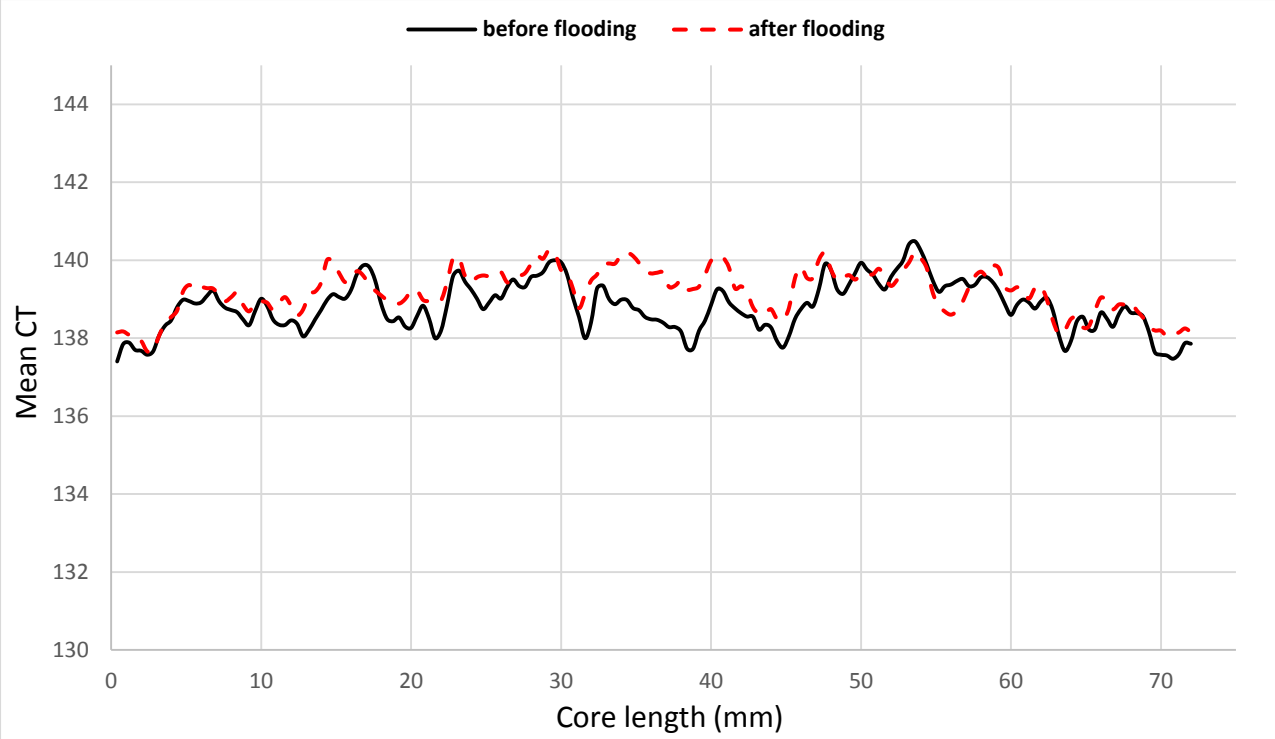

CT images before flooding	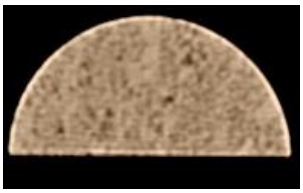	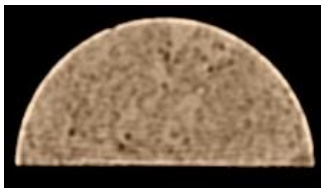	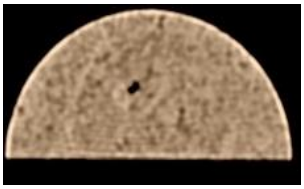
CT images after flooding	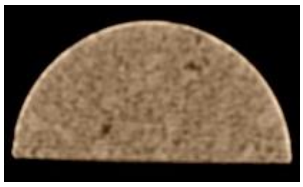	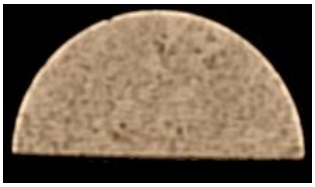	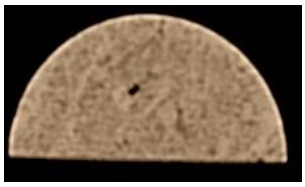
Image at (mm)	1.2mm	6.0mm	40.0mm

Figure 4.10. CT Value distribution and X-ray cross-sectional images for sample IL-2 part of the composite (two halves). The CT number profiles and cross-sectional images show almost no change after undergoing the flooding process.

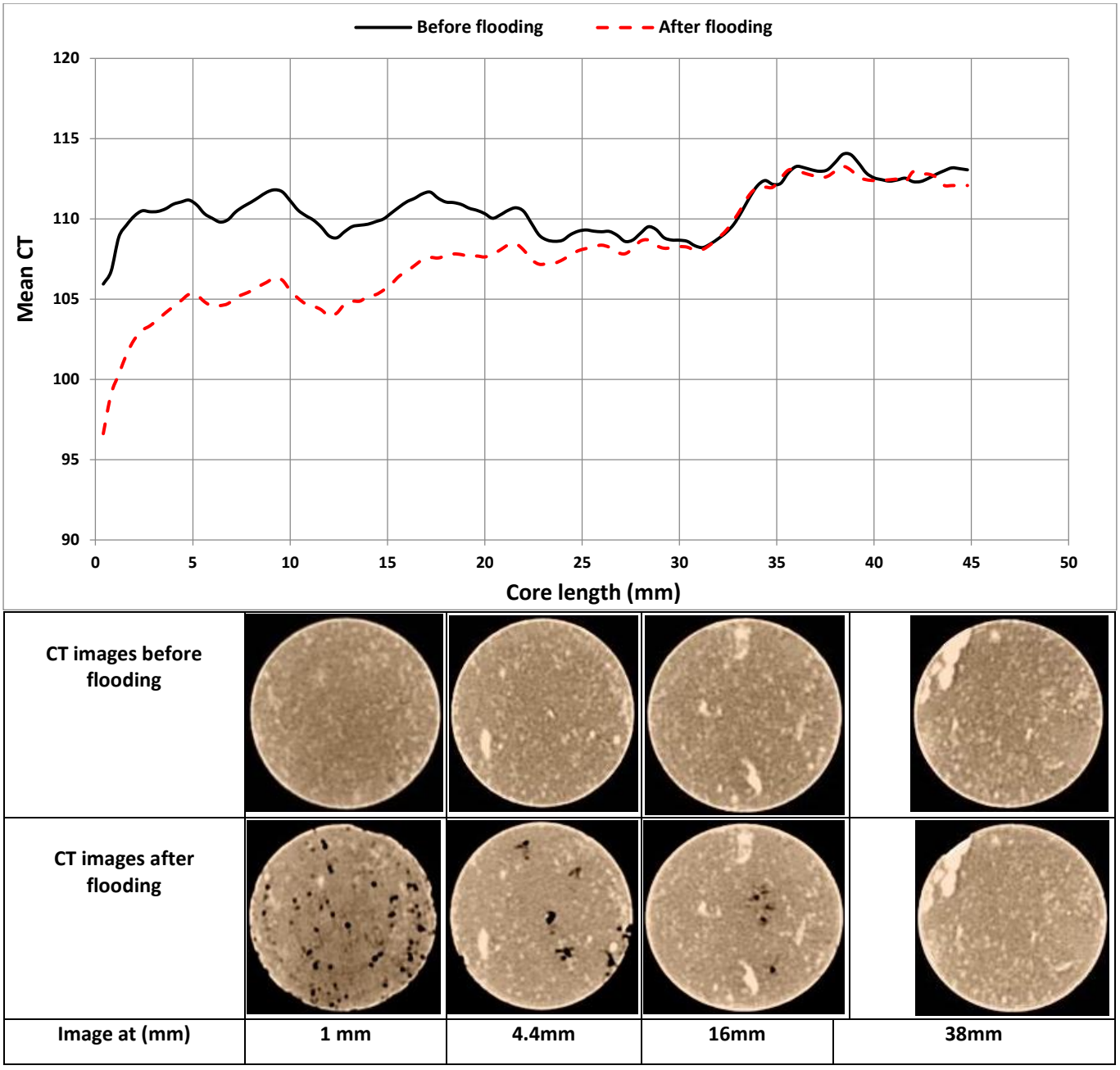

Figure 4.11. CT Value distribution and X-ray cross-sectional images for sample VS-3 before and after flooding. The CT number profiles and cross-sectional images show signs of moderate mineral dissolution close to the inlet of the sample.

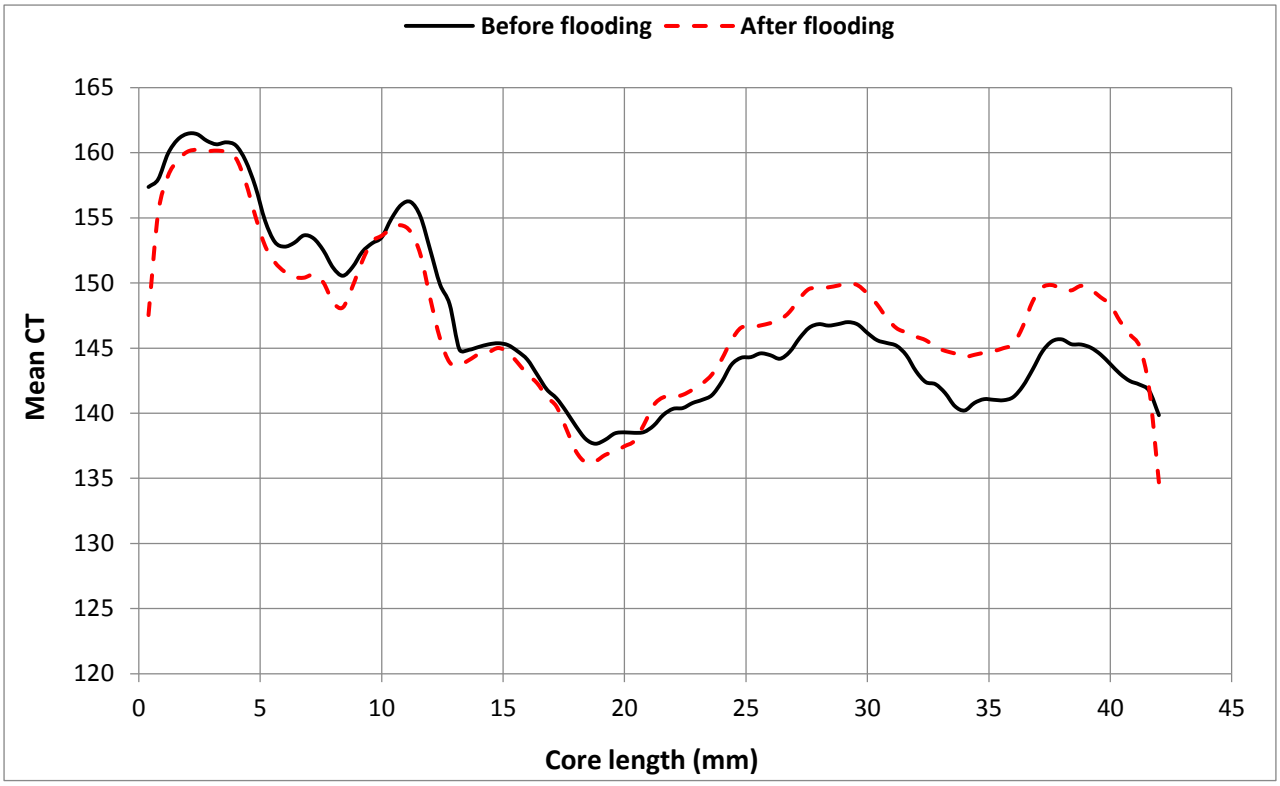

CT images before flooding			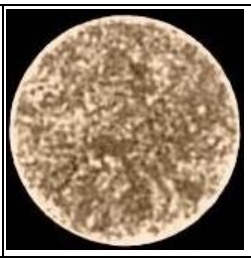	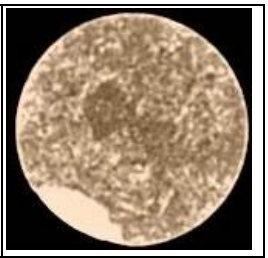
CT images after flooding	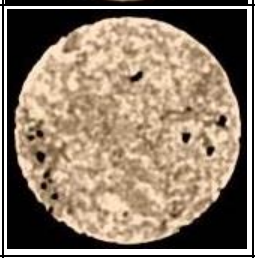	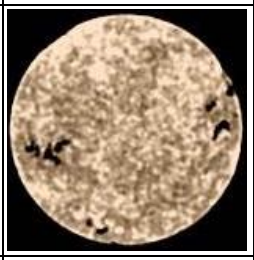	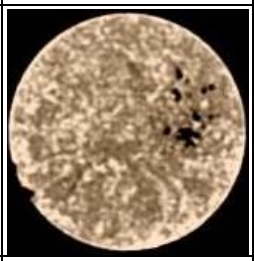	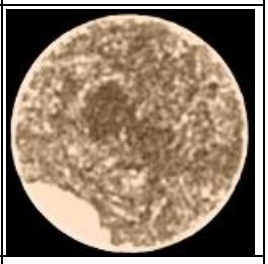
Image at (mm)	1.2 mm	11.2 mm	19.2 mm	34.4 mm

Figure 4.12. CT Value distribution and X-ray cross-sectional images for sample VS-4 before and after flooding. The CT number profiles and cross-sectional images show signs of dissolution close to the inlet of the sample. From the CT profiles, the outlet region of the sample seems to have become denser due to mineral precipitation and mechanical compaction.

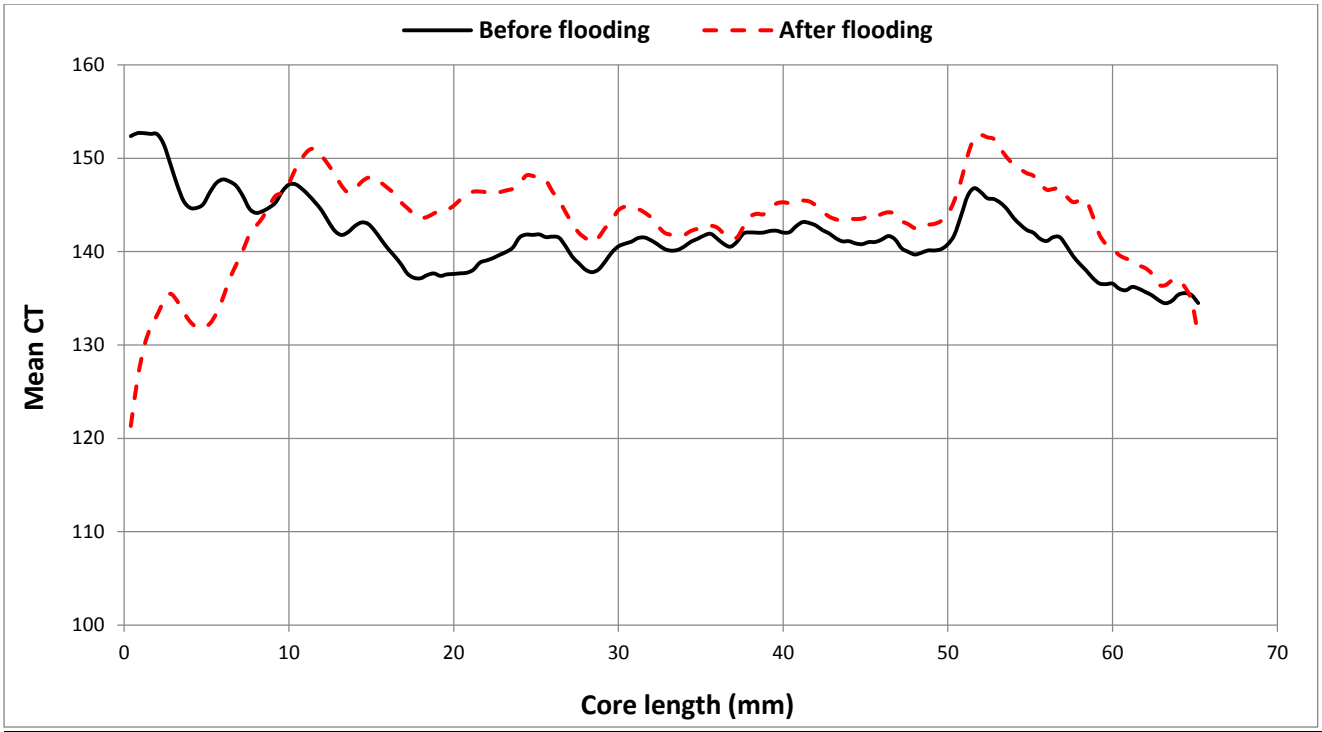

CT images before flooding	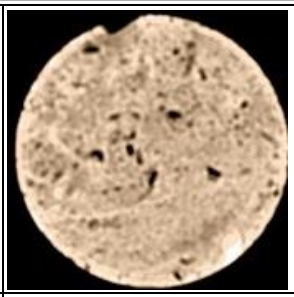	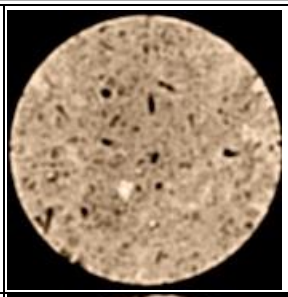	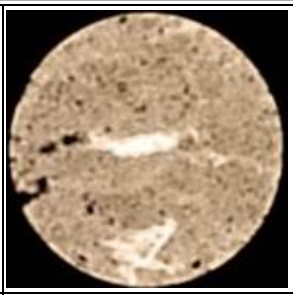
CT images after flooding	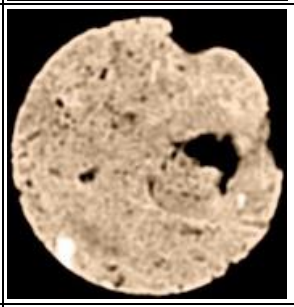	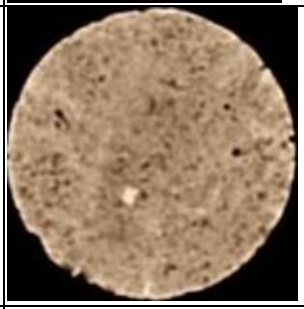	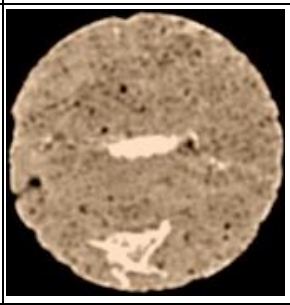
Image at (mm)	7.6 mm	21.2 mm	52.4 mm

Figure 4.13. CT Value distribution and X-ray cross-sectional images for sample VC-3 before and after flooding. The CT number profiles and cross-sectional images show signs of excessive dissolution close to the inlet of the sample. From the CT profiles, the outlet region of the sample seems to have become denser due to mineral precipitation and mechanical compaction.

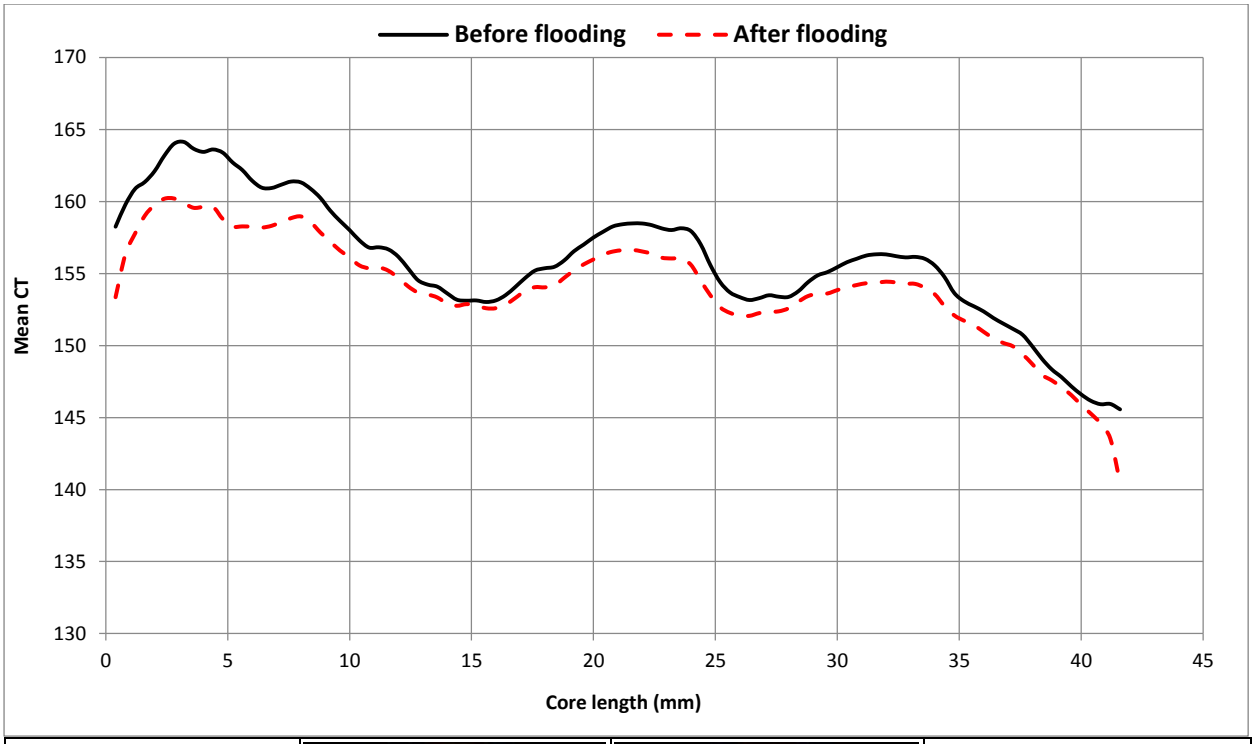

CT images before flooding		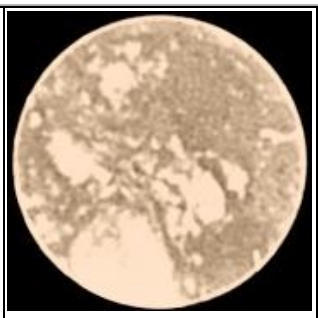	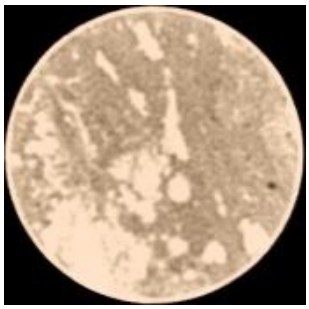
CT images after flooding	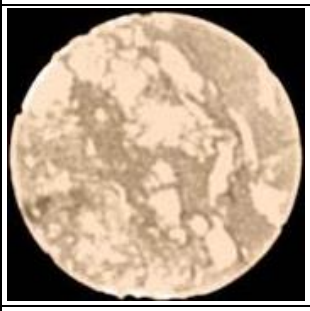	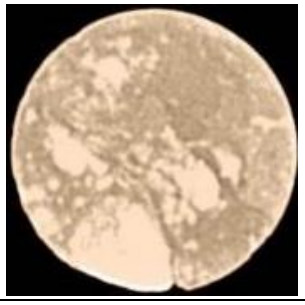	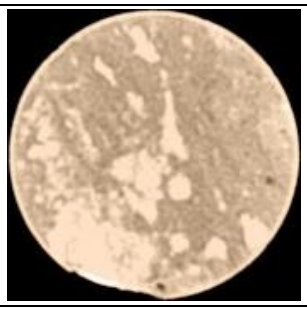
Image at (mm)	2.8 mm	22.4 mm	33.6 mm

Figure 4.14. CT Value distribution and X-ray cross-sectional images for sample TC-1 before and after flooding. The CT number profiles, in particular, show obvious signs of dissolution in the sample, with the sample becoming less dense. This change is evenly distributed throughout the sample, possibly due to the effect of the fracture serving as a preferential flow path through which chemical reactions can occur.

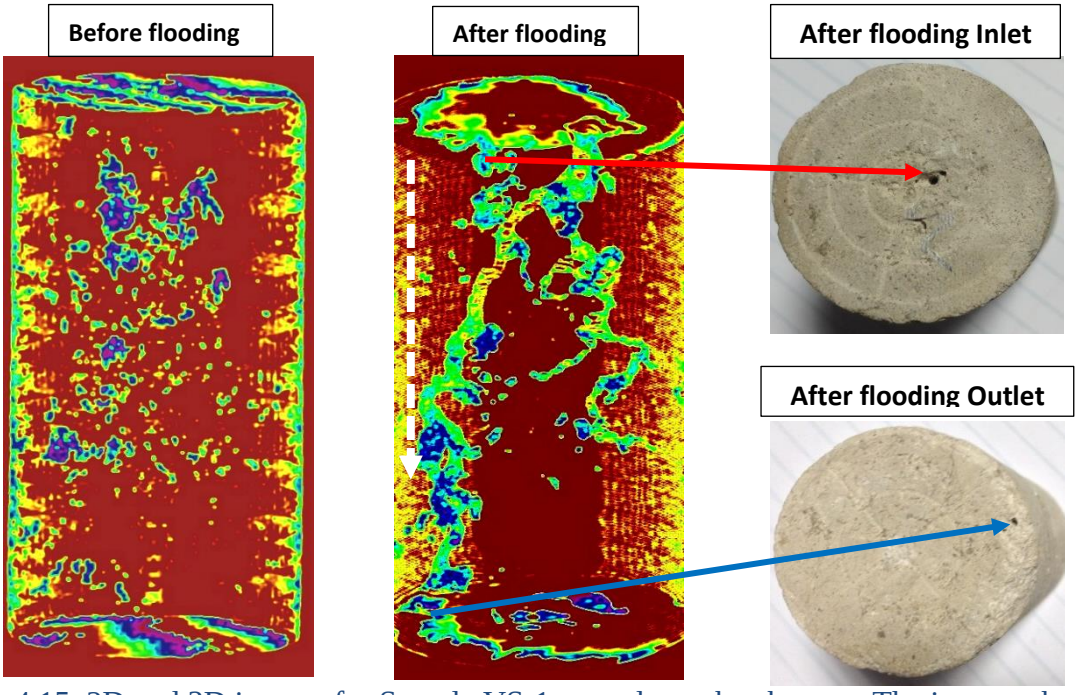

Figure 4.15. 2D and 3D images for Sample VS-1 to evaluate the changes. The images show the creation of wormholes along the length of the sample, due to the massive dissolution of calcite minerals.

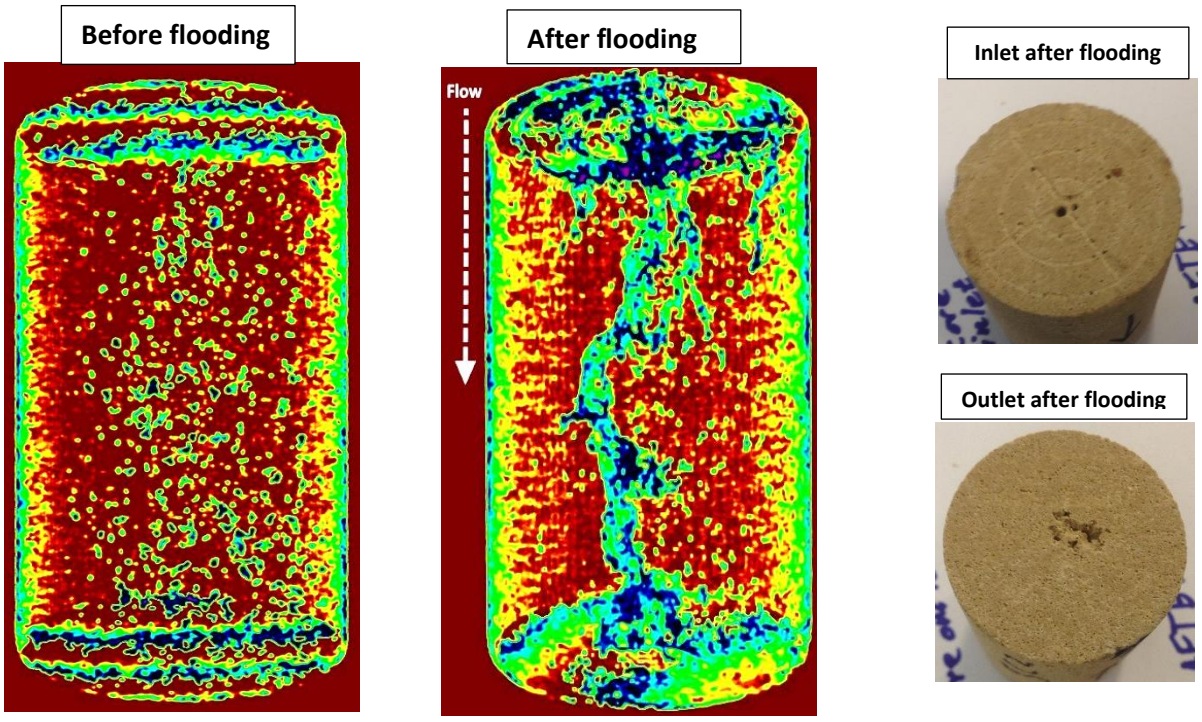

Figure 4.16. 2D and 3D images for sample SC-2 to evaluate the changes. The images show the creation of wormholes along the length of the sample, due to the massive dissolution of calcite minerals.

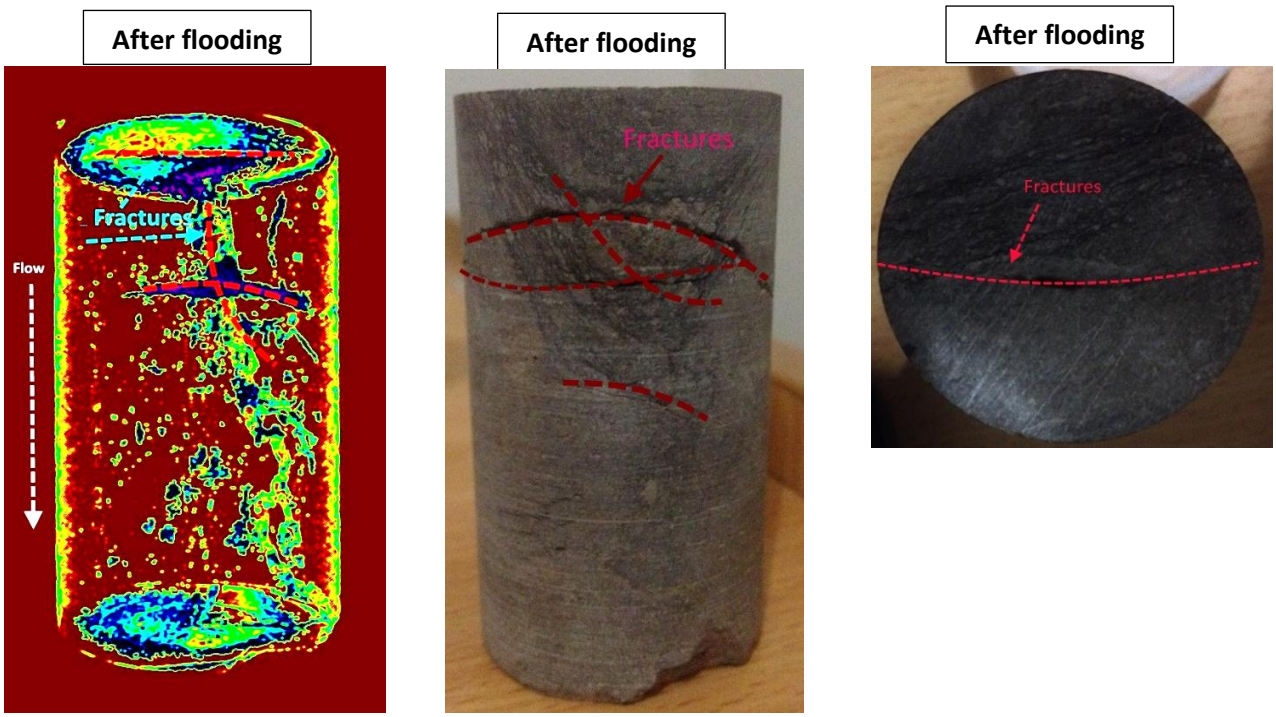

Figure 4.17. 2D and 3D images for sample TC-2 to evaluate the changes. The images show the dissolution of minerals, resulting in the formation of a wormhole, along the path of the pre-existing fracture.

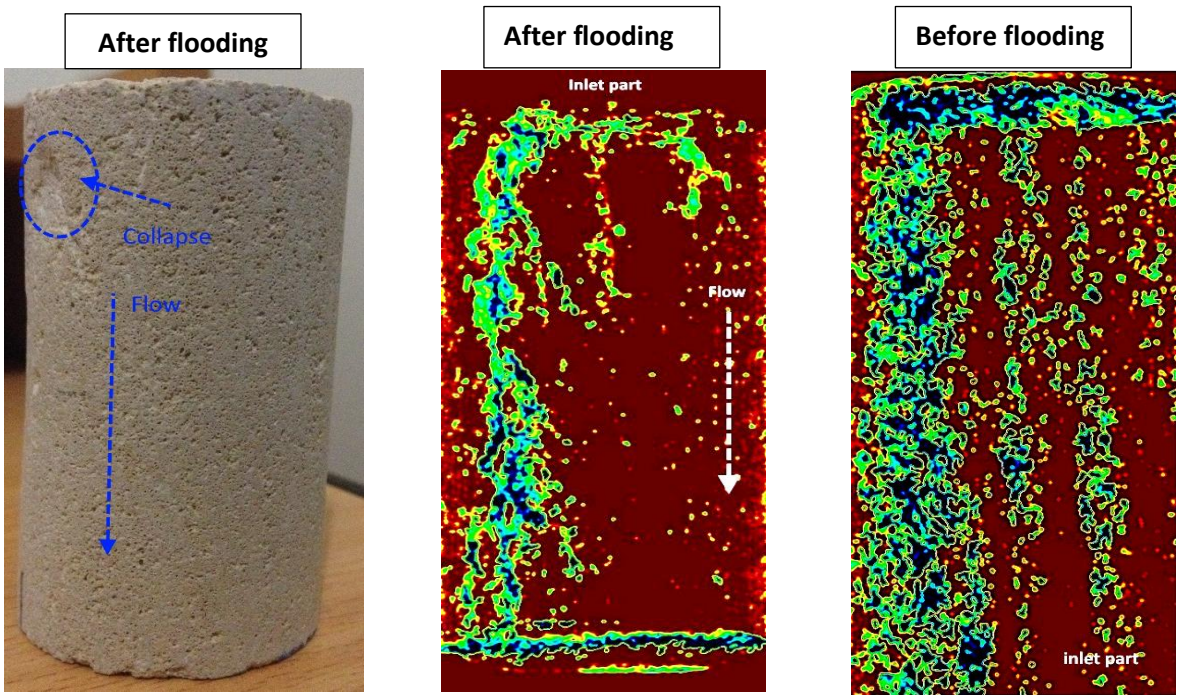

Figure 4.18. 2D and 3D images for sample SC-1 inlet part of the composite core to evaluate the changes. The images show the creation of wormholes along the length of the sample due to massive dissolution. However, the collapse of the sample under overburden pressure, which mitigated the dissolution effect, was observed from the visual image (blue circle).

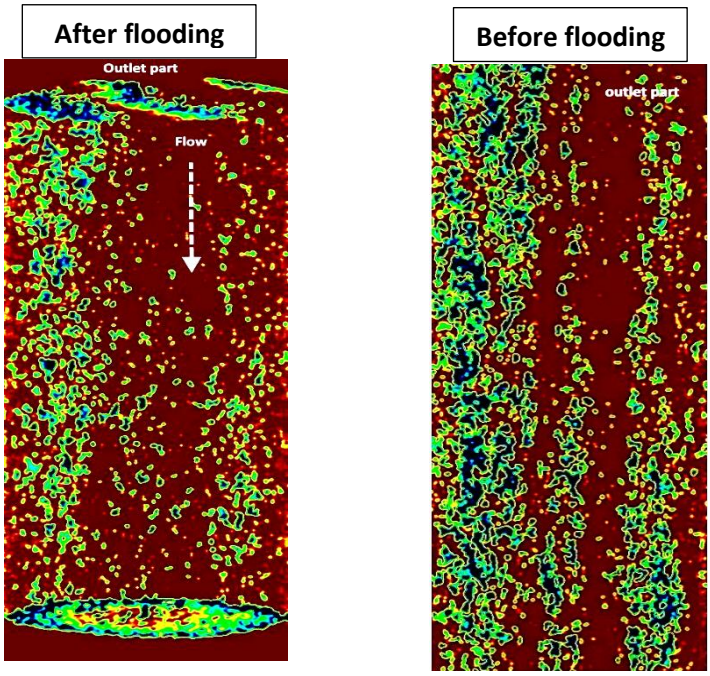

Figure 4.19. 2D and 3D images for sample SC-1 outlet part of the composite core to evaluate the changes. The images show that some pores have disappeared along the length of the sample after flooding, which causes a reduction in overall permeability. The reduction may be caused by the precipitation of minerals dissolved from the inlet plug.

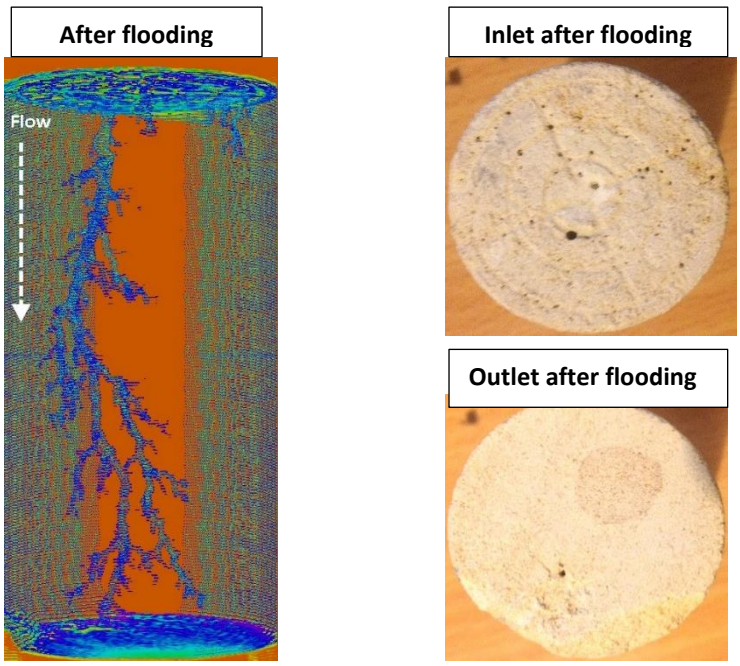

Figure 4.20. 2D and 3D images for sample CH-1 inlet part of the composite core. The images show the creation of wormholes along the length of the sample, due to massive dissolution.

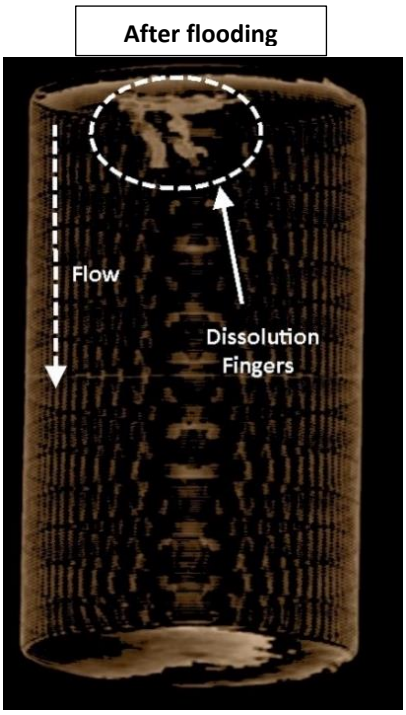

Figure 4.21. The 3D image for sample CH-1 outlet part of the composite core. The image shows dissolution fingers close to the inlet, only after undergoing the flooding process.

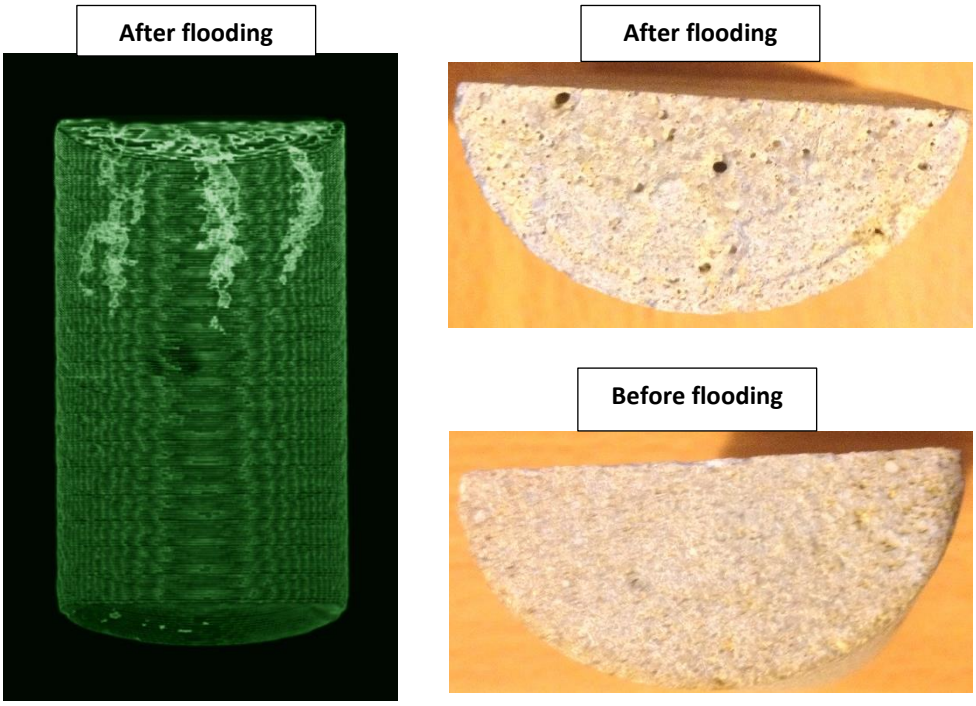

Figure 4.22. 2D and 3D images for sample IL-1 part of the composite core (two halves). The images show dissolution fingers close to the inlet, only after undergoing the flooding process.

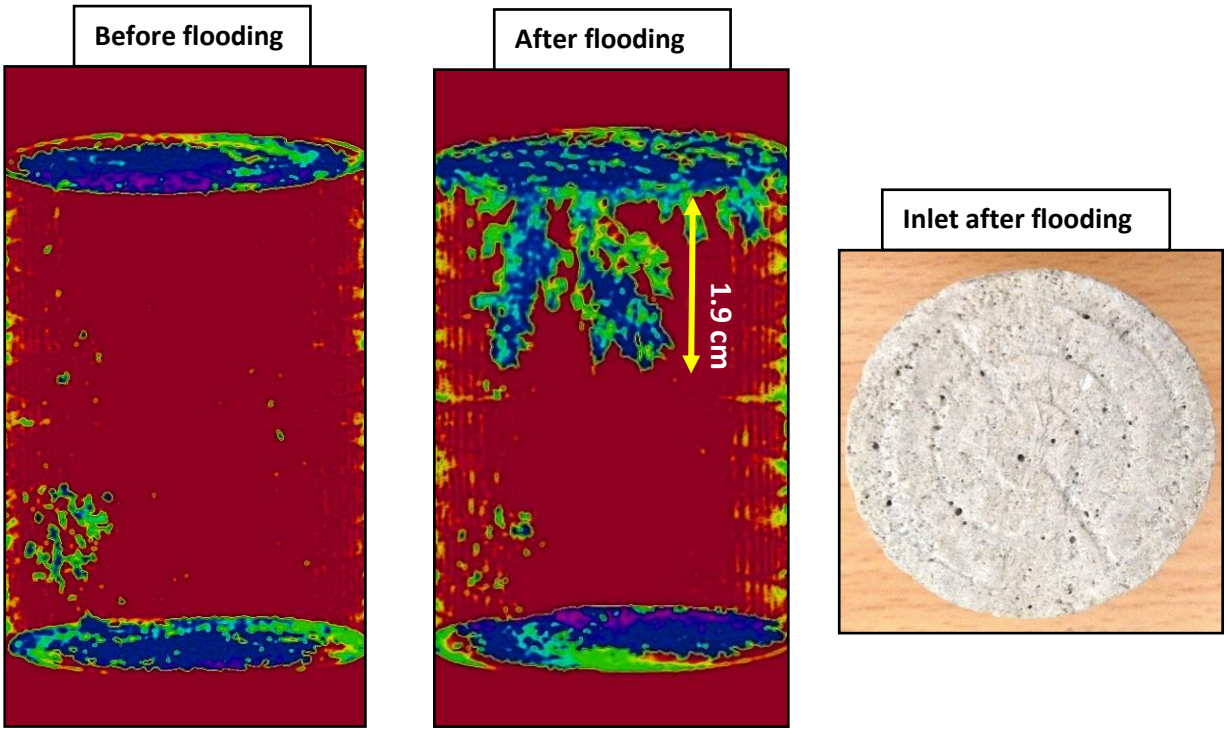

Figure 4.23. 2D view of 3D X-ray images and a photo of the inlet for sample VS-3. Both show signs of dissolution in the inlet region of the sample. Wormholes can be seen in the post-flood X-ray image.

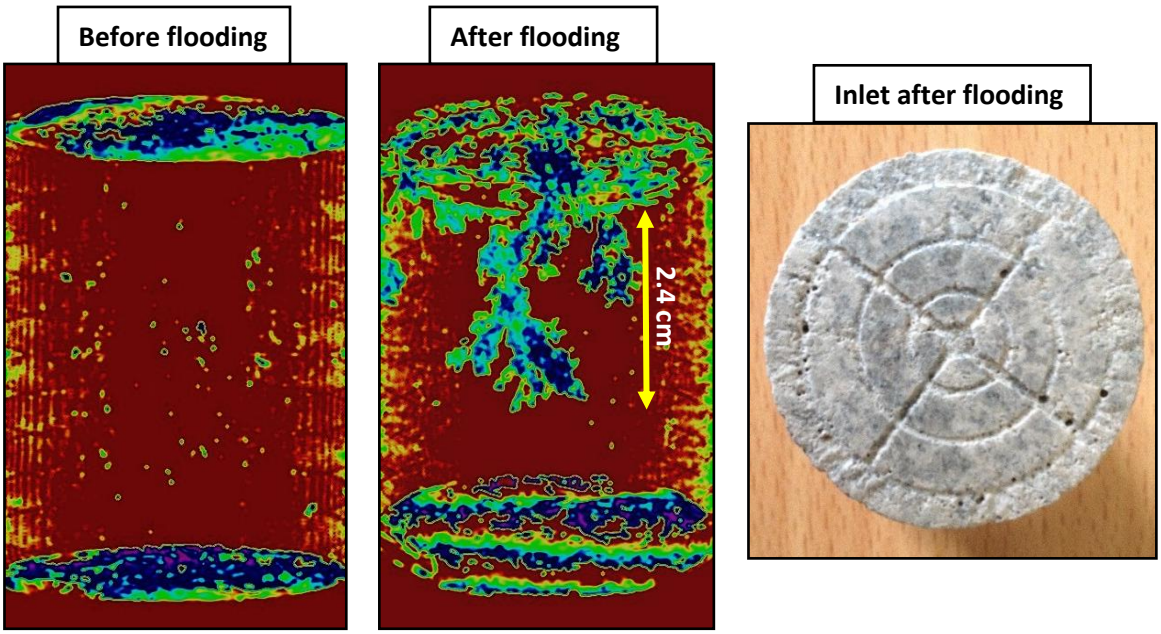

Figure 4.24. 2D view of 3D X-ray images and a photo of the inlet for sample VS-4. Signs of dissolution are apparent from both evidence. Wormholes can be seen in the post-flood X-ray image.

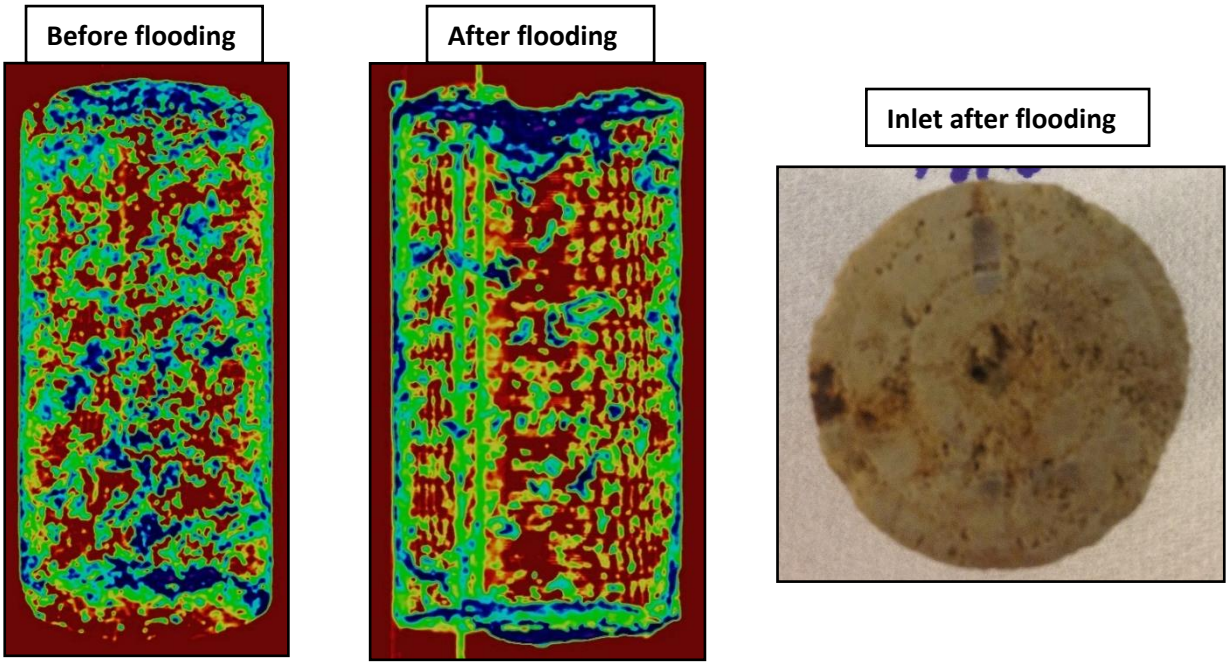

Figure 4.25. 2D view of 3D X-ray images and a photo of the inlet for sample VC-3. Both evidence show excessive dissolution in the inlet region of the sample.

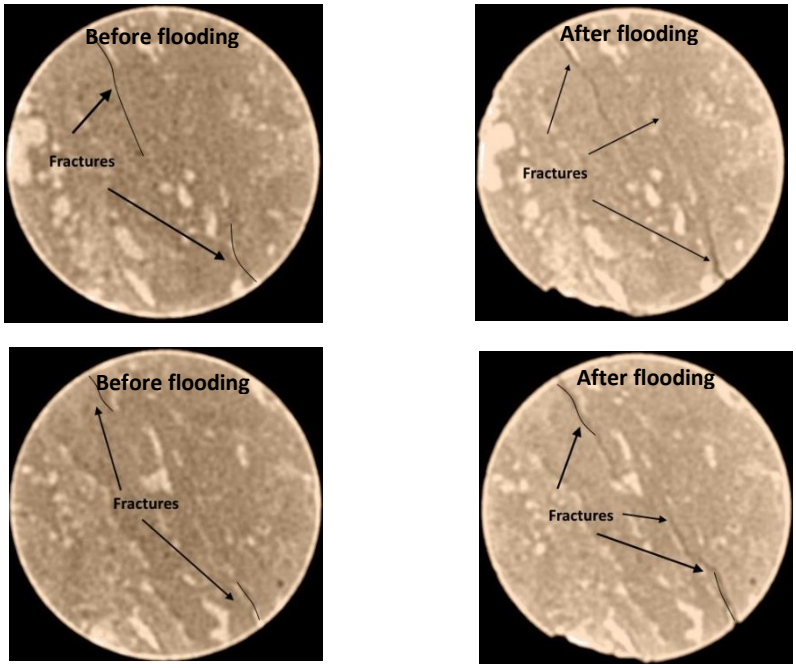

Figure 4.26. 2D X-ray images for sample TC-1, showing the location of the natural fractures before and after flooding.

4.3.2. Continuous CO_2-EOR flooding

As indicated earlier, samples SD-1, INL-2, GD-1 and INL-1 were flooded using this flooding procedure. Images and data similar to those provided earlier for flooding Scenario 1 are shown

in figures 4.27-4.34. As a preliminary observation made from the images generated for this group of samples, there is no sign of exessive dissolution apparent from them. But, as will be indicetd later, there are other meshanisms such as asphaltene and resin precipitation that may have occurred during this flooding procedure.

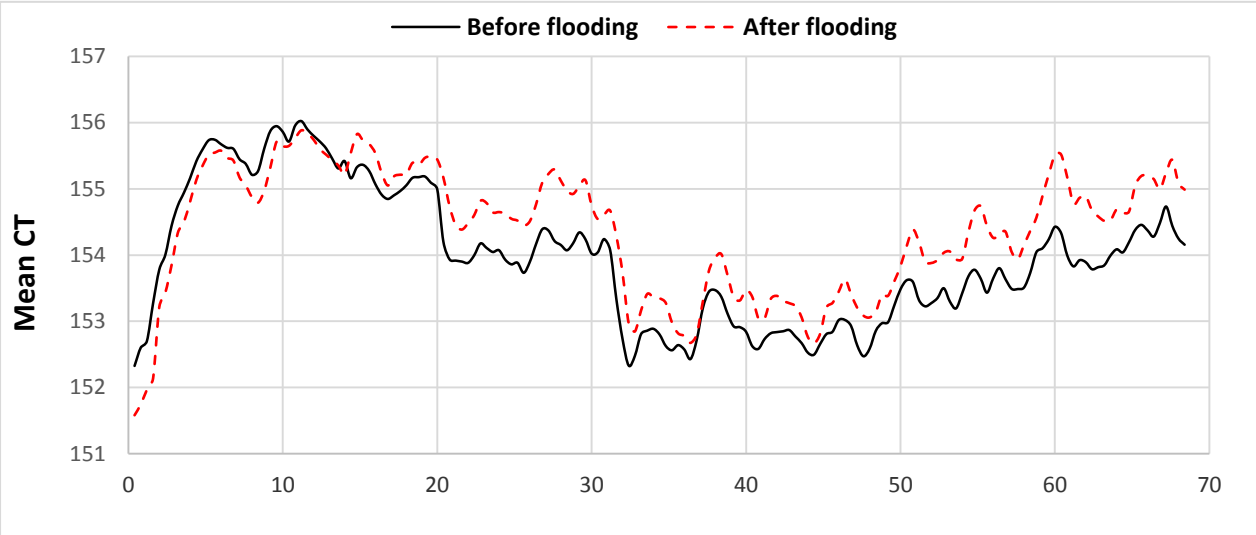

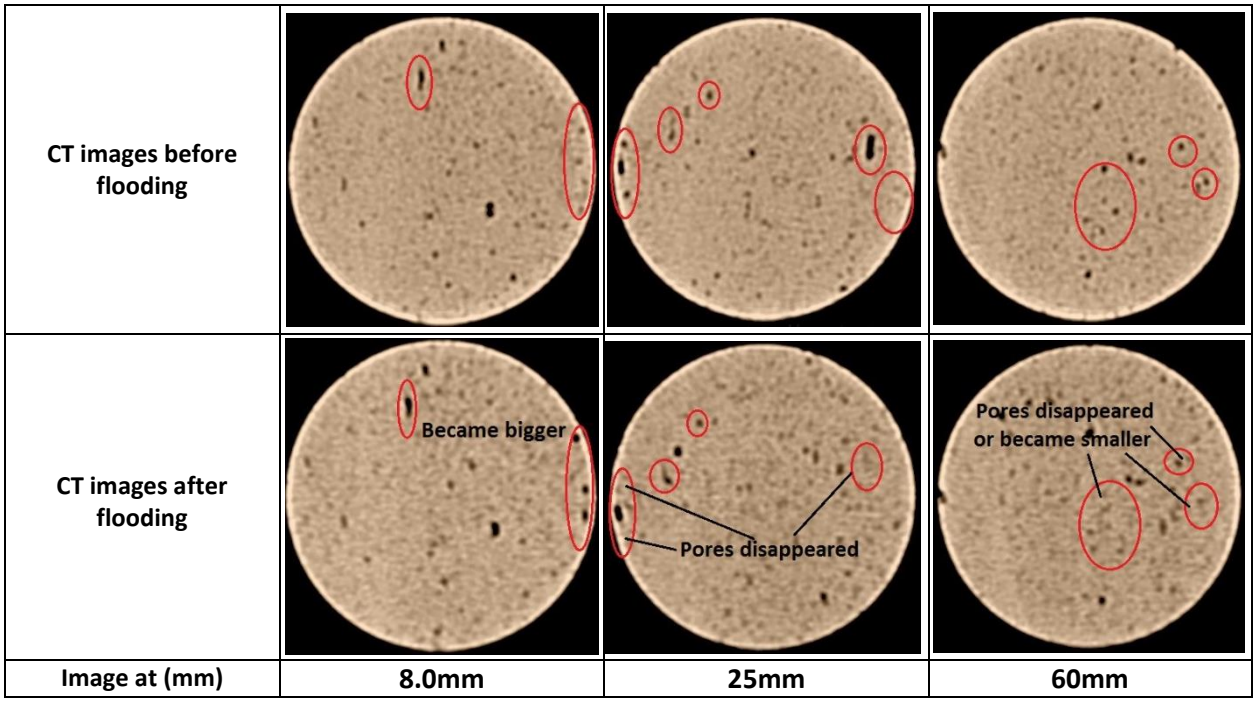

Figure 4.27. CT Value distribution and X-ray cross-sectional images for sample SD-1 inlet part of the composite core before and after flooding. The CT number profiles and cross-sectional images show signs of dissolution close to the inlet. Then, the CT profiles seem to have become denser due to asphaltene precipitation, resulting in a decrease of overall sample permeability.

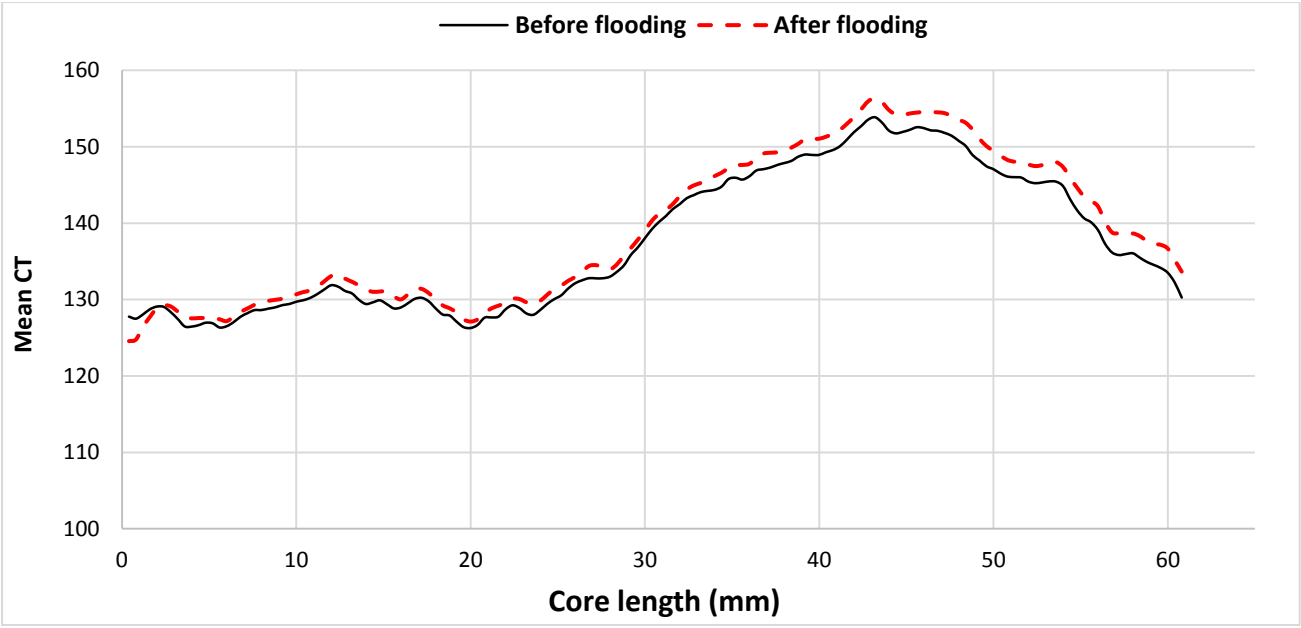

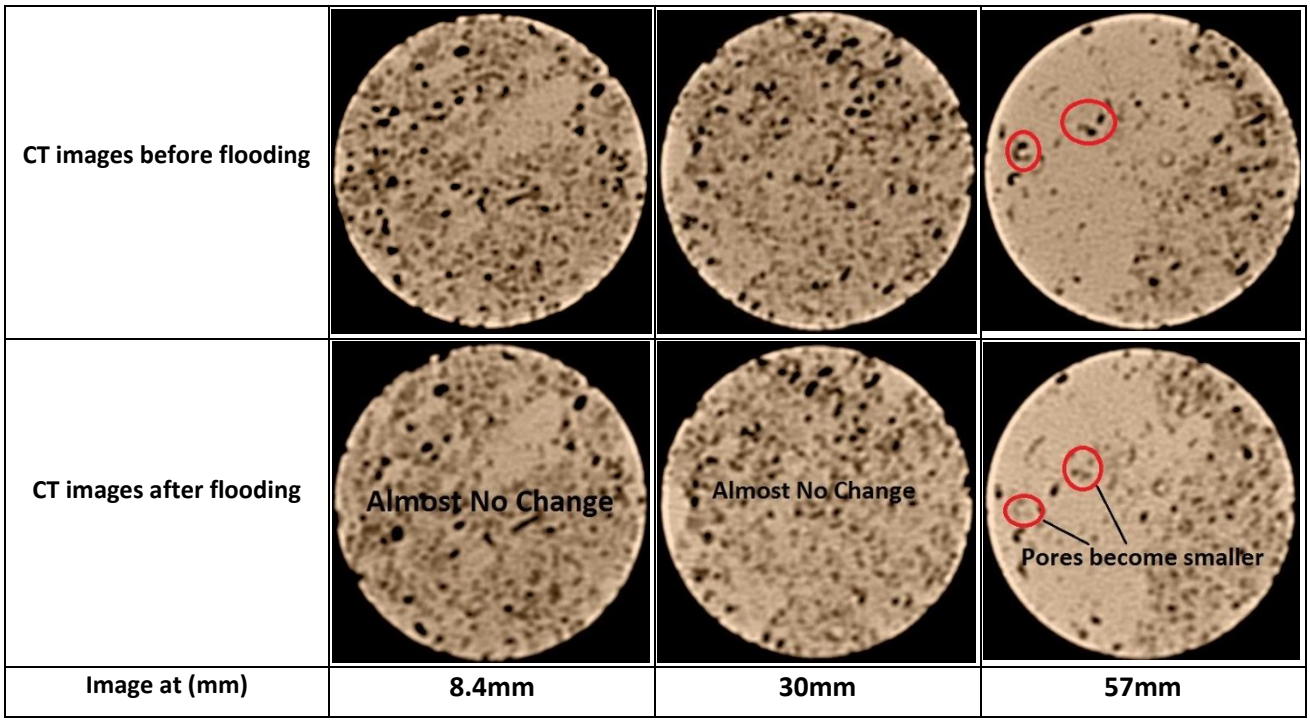

Figure 4.28. CT Value distribution and X-ray cross-sectional images for sample SD-1 outlet part of the composite core before and after flooding. The CT number profiles and cross-sectional images show almost no change in the first half of the sample. However, the CT profiles seem to have become denser at the end of the core sample. The change might be due to asphaltene and mineral precipitation, resulting in a slight decrease in sample permeability.

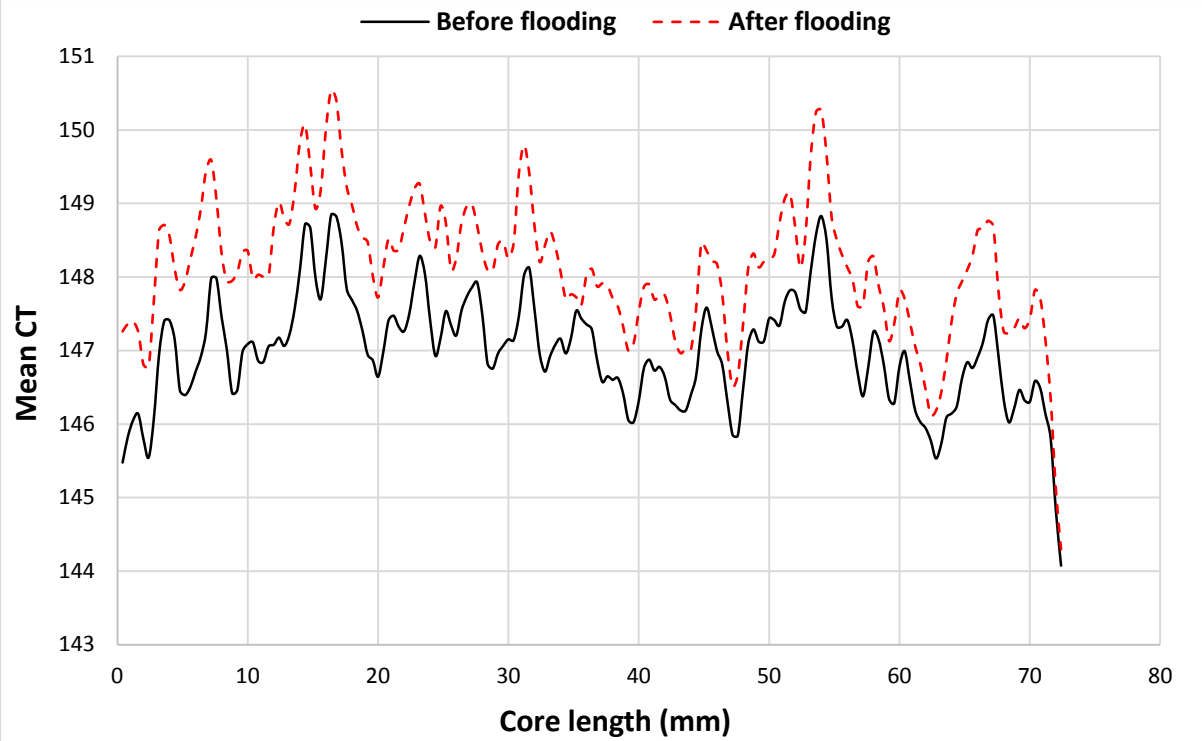

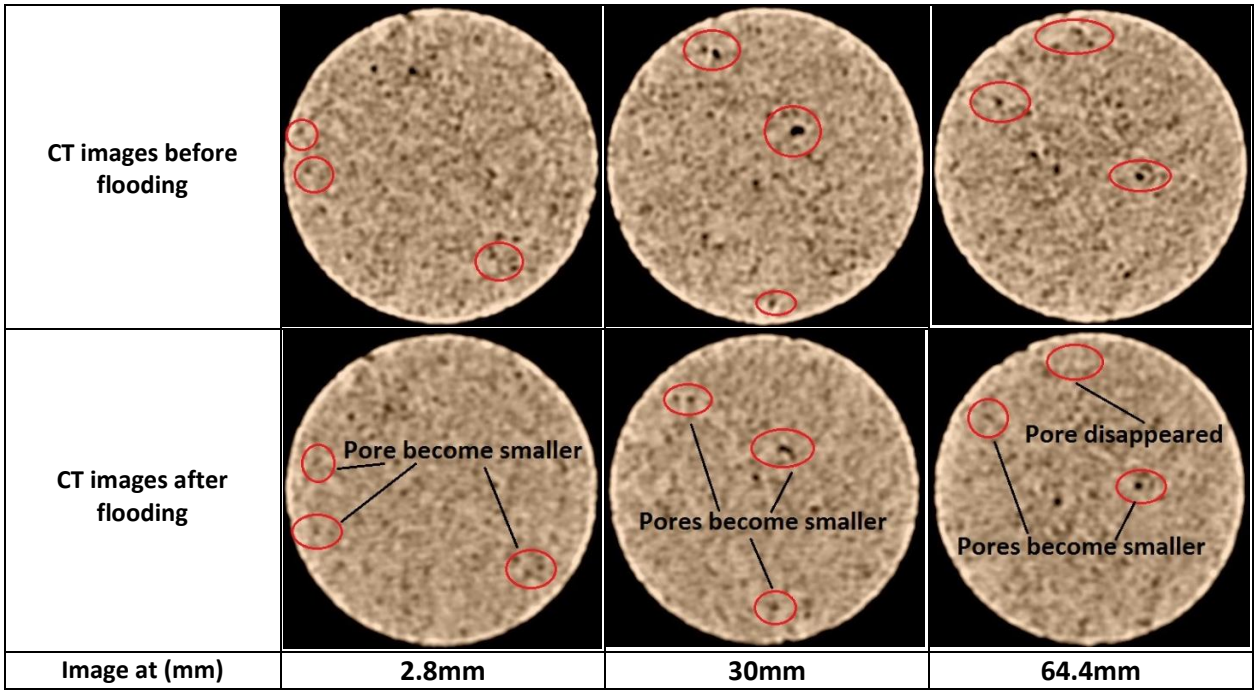

Figure 4.29. CT Value distribution and X-ray cross-sectional images for sample INL-2 inlet part of the composite core before and after flooding. The CT number profiles and cross-sectional images show signs of asphaltene precipitation along the length of the sample, as CT profiles seem to have become denser, resulting in a reduction in sample permeability.

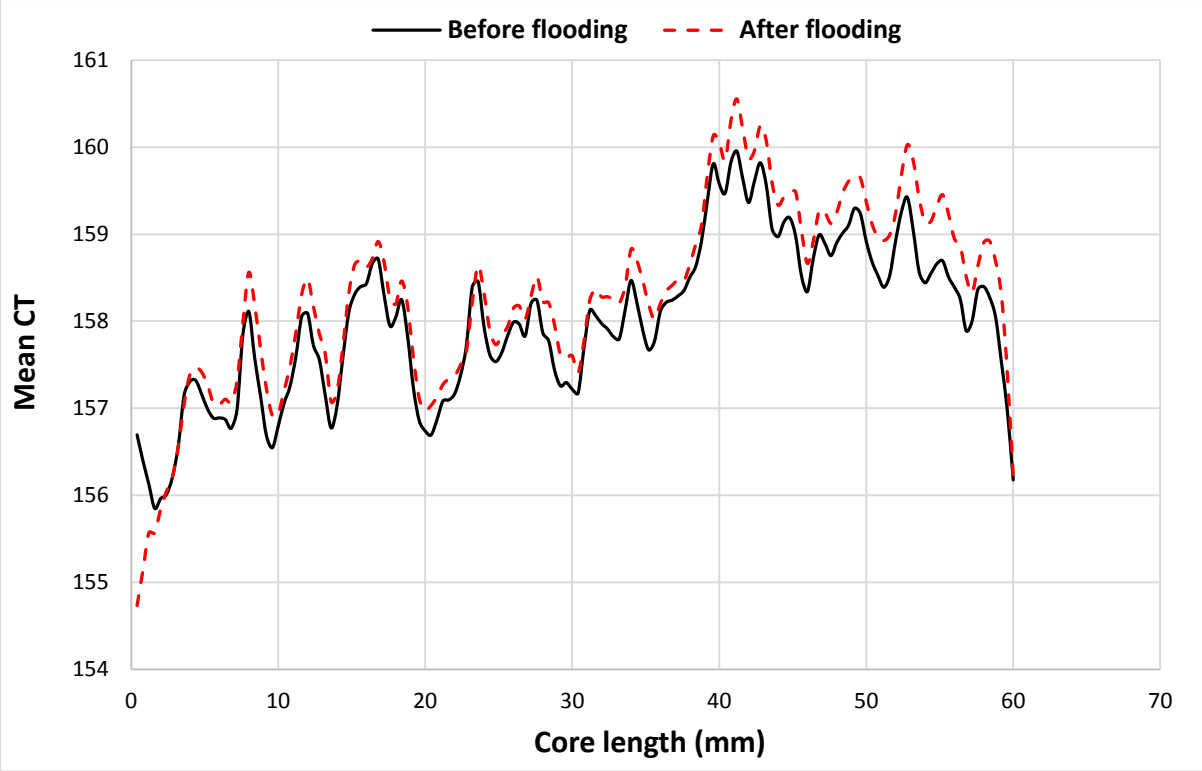

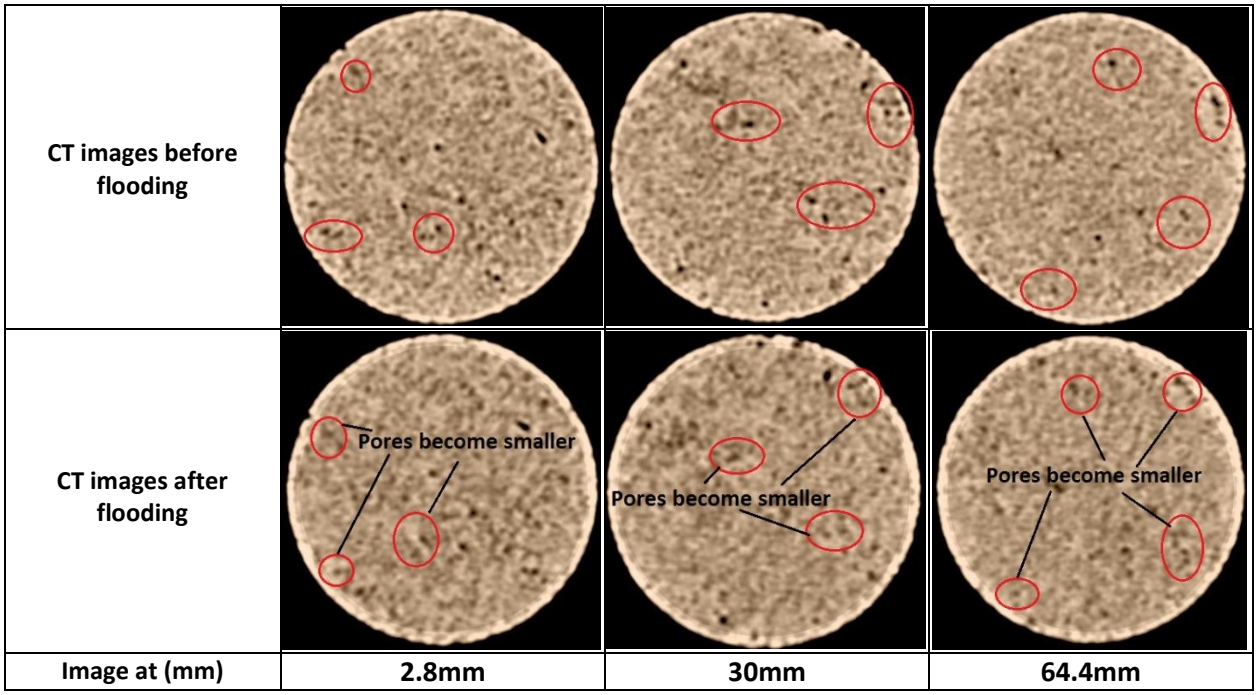

Figure 4.30. CT Value distribution and X-ray cross-sectional images for sample INL-2 outlet part of the composite core before and after flooding. The CT number profiles and cross-sectional images show signs of asphaltene precipitation along the length of the sample, as CT profiles seem to have become denser, resulting in a reduction in overall sample permeability.

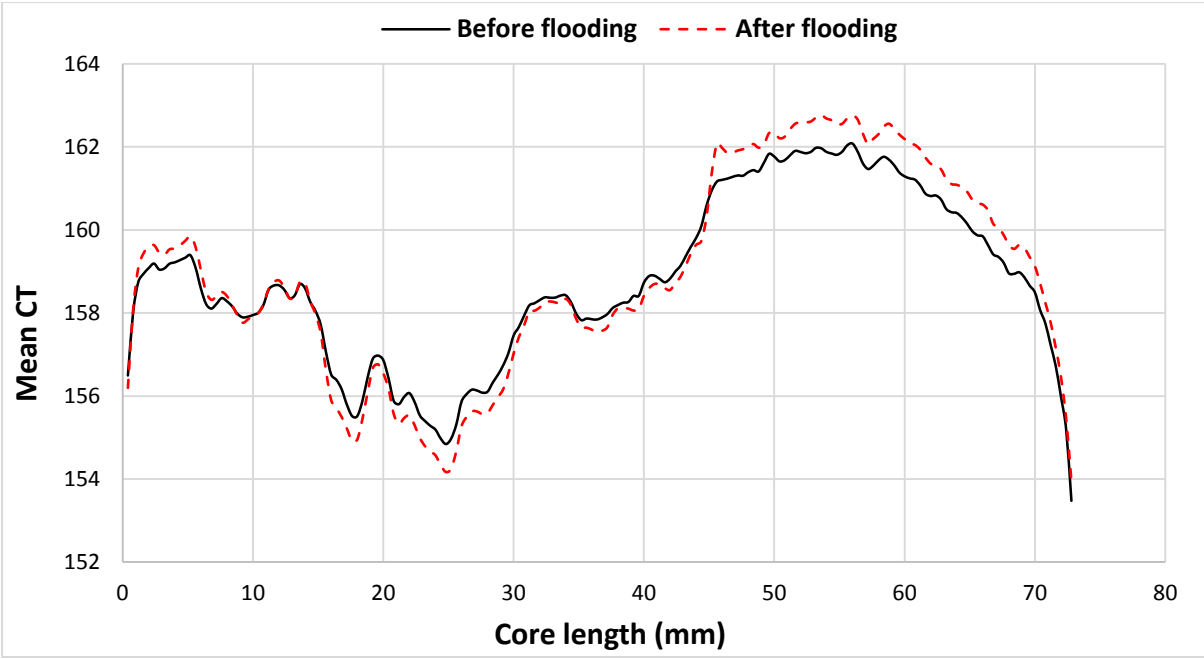

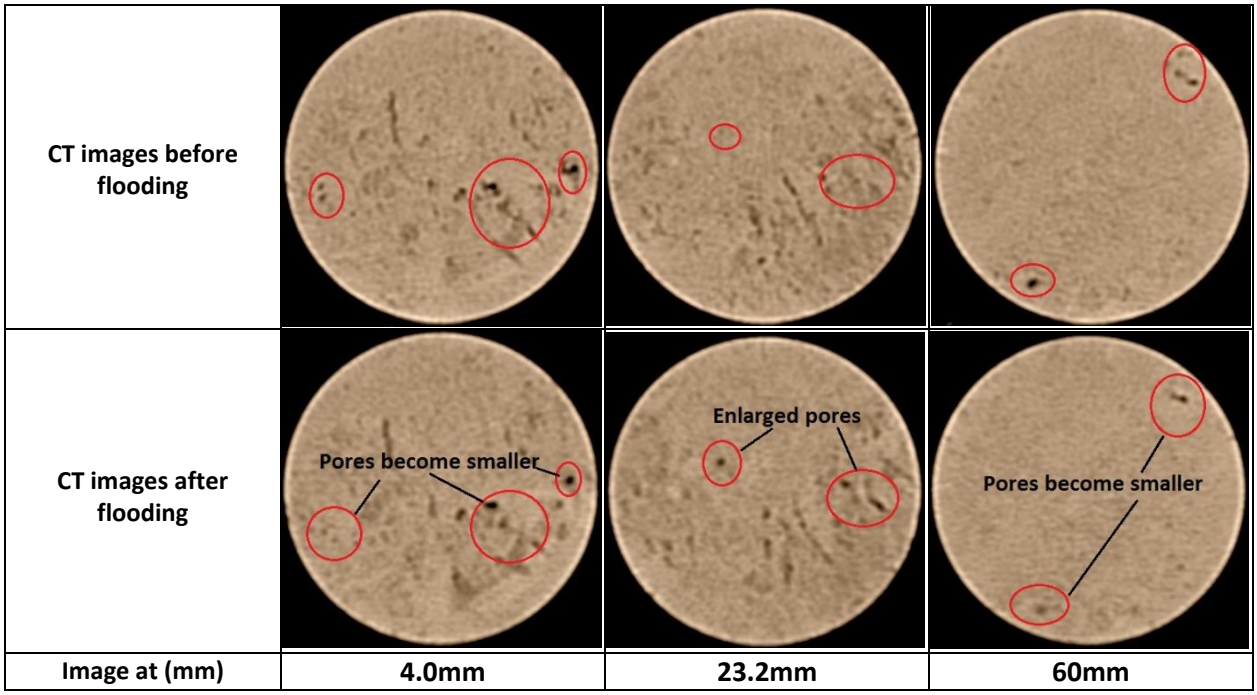

Figure 4.31. CT Value distribution and X-ray cross-sectional images for sample GD-1 before and after flooding. The CT number profile increased (asphaltene precipitation) and decreased (mineral dissolution) at certain locations. This fluctuation may be attributed to the minerals distribution within the sample.

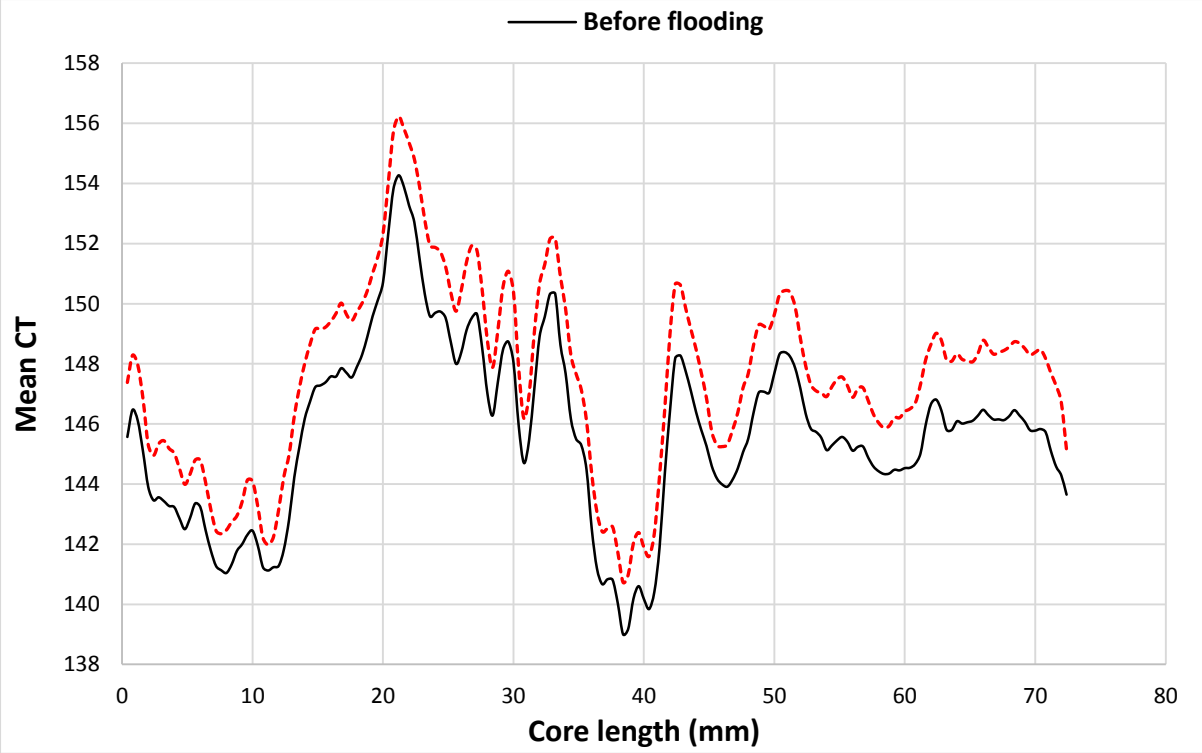

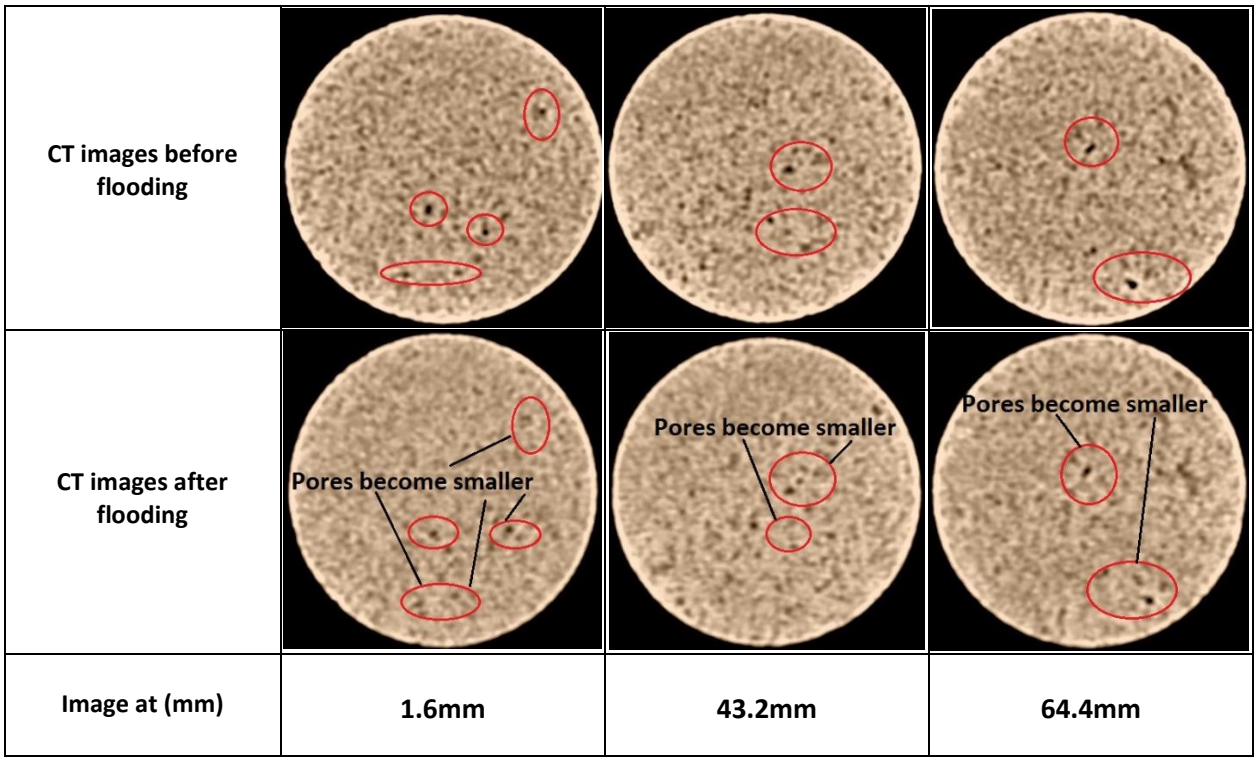

Figure 4 32. CT Value distribution and X-ray cross-sectional images for sample INL-1 before and after flooding. The CT number profiles and cross-sectional images show signs of asphaltene precipitation along the length of the sample, as CT profiles seem to have become denser, resulting in a reduction in overall sample permeability.

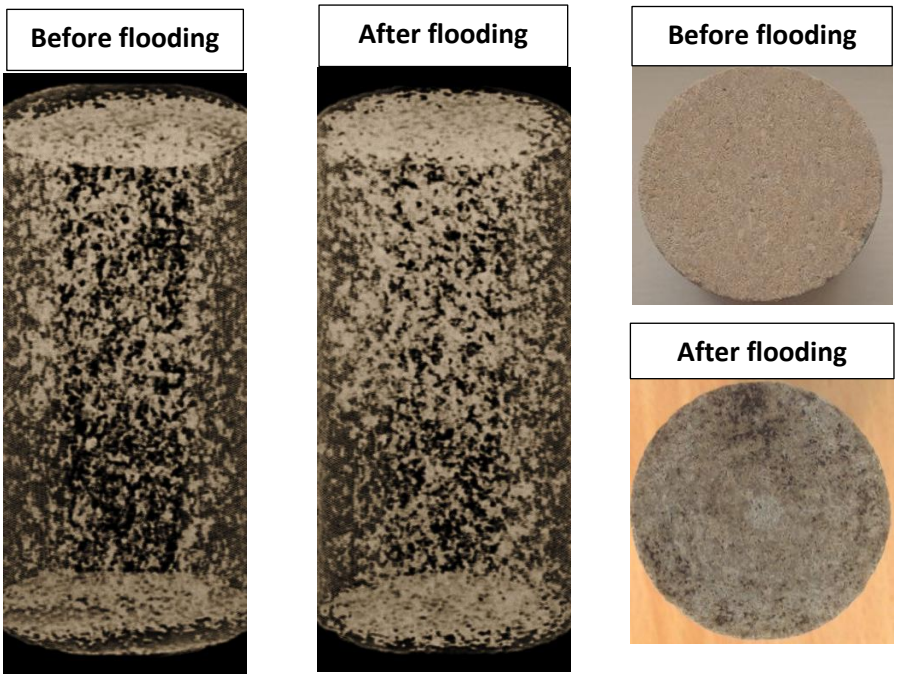

Figure 4.33. 2D and 3D images for sample INL-1 to evaluate the changes. The images show that some pores have disappeared as the image become denser showing more lighter coloured areas especially close to the sample inlet after flooding, which causes a reduction in overall permeability. The reduction may be caused by asphaltene precipitation.

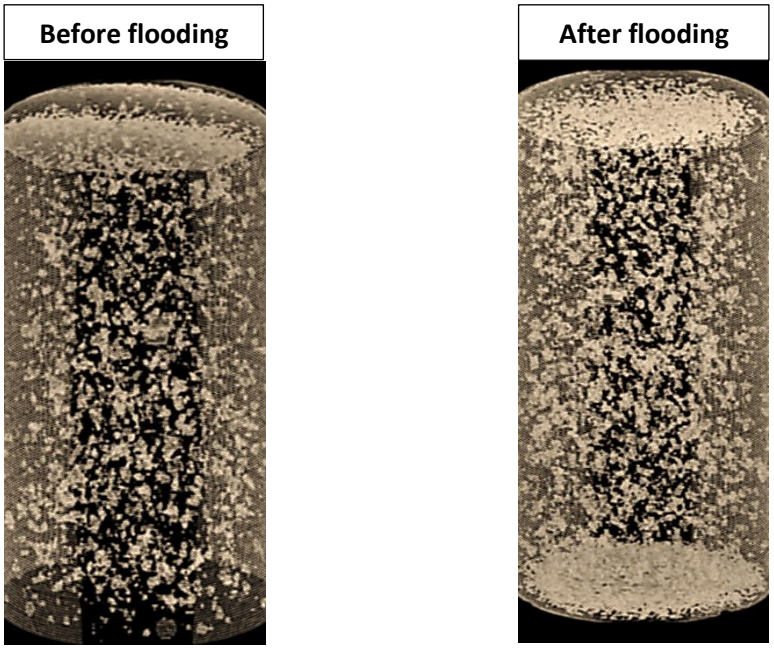

Figure 4.34. 3D images for the sample SD-1 inlet part of the composite core to evaluate the changes. The images show that some pores have disappeared along the length of the sample after flooding as the image become denser showing more lighter coloured areas, which causes a reduction in overall permeability. The reduction may be caused by asphaltene precipitation.

4.3.3. Water-Alternating-Gas (WAG) flooding

The three samples of VS-2, GD-11 and INL-11 were flooded using this flooding procedure for which similar X-ray derived data and information as those presented for the previous two flooding procedures were generated as presented in figures 4.35-4.39. As can be seen from these figures, end-results are to some extent similar to those obtained for the live brine flooding were obtained for the samples subjected to the WAG flooding.

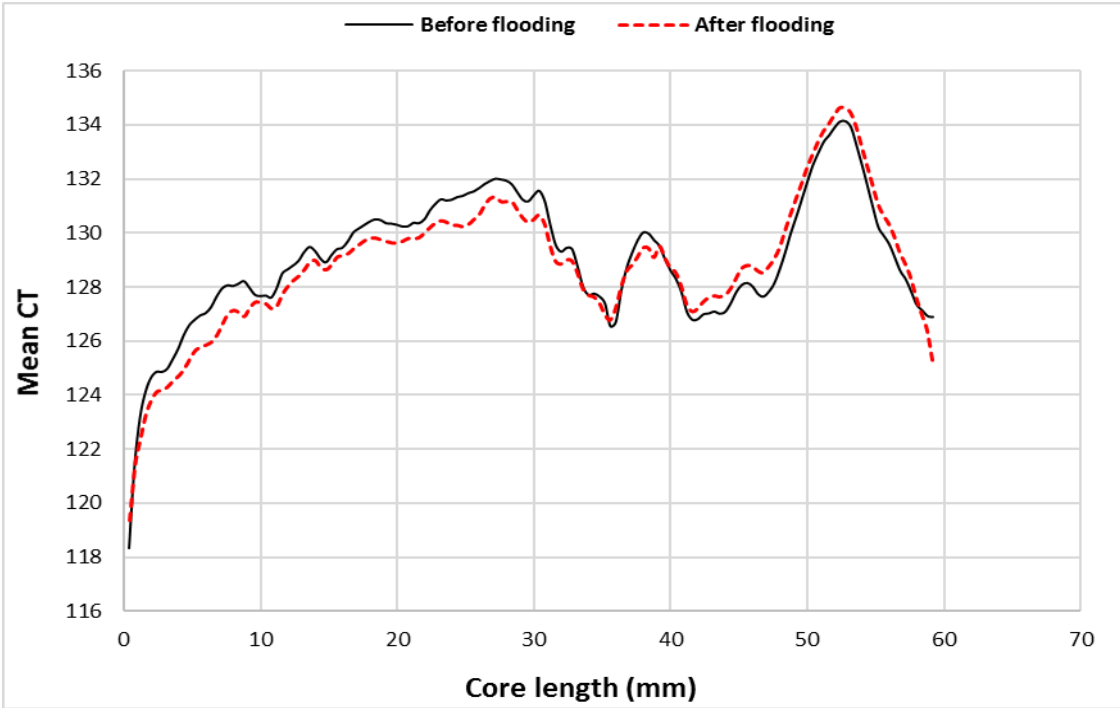

CT images before flooding			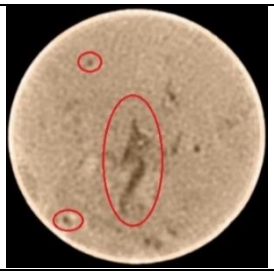
CT images after flooding		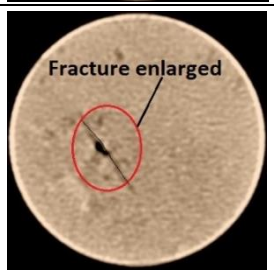	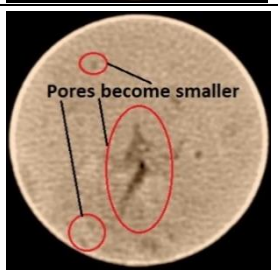
Image at (mm)	3.0mm	20.0mm	54.8mm

Figure 4.35. CT Value distribution and X-ray cross-sectional images for sample VS-2 before and after flooding. The CT number profiles and cross-sectional images show signs of dissolution in the first half of the sample. The CT profiles seem to have become denser due to asphaltene and mineral precipitation.

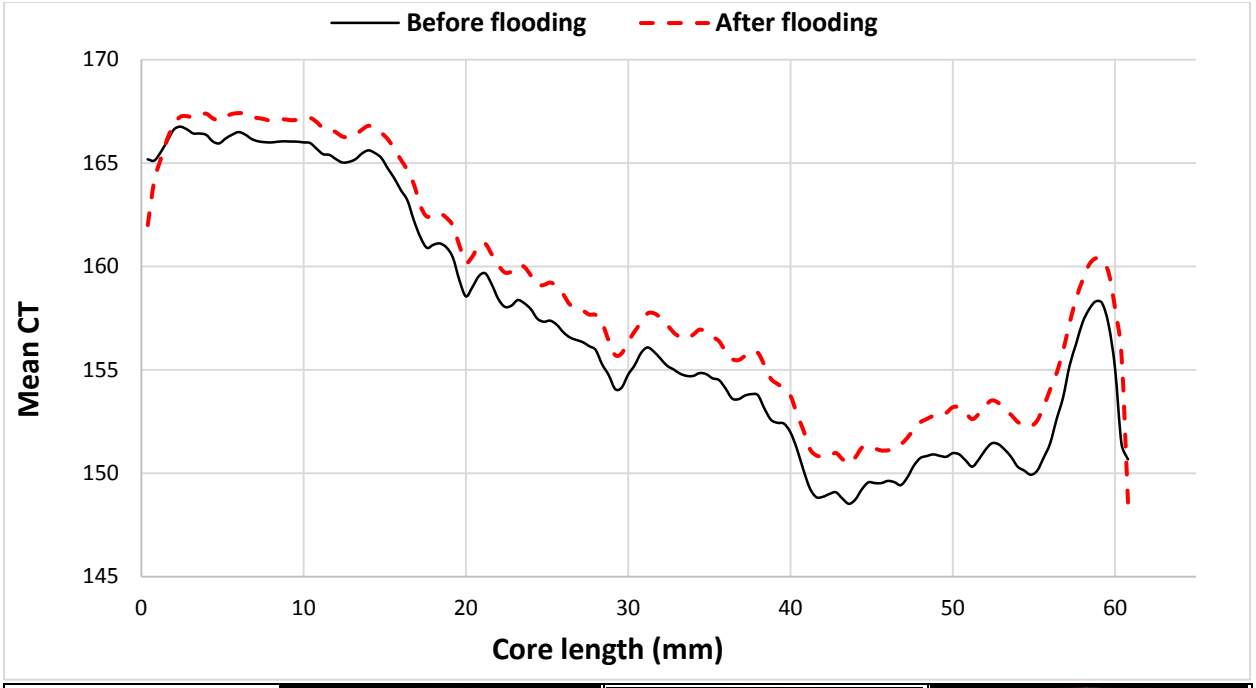

CT images before flooding		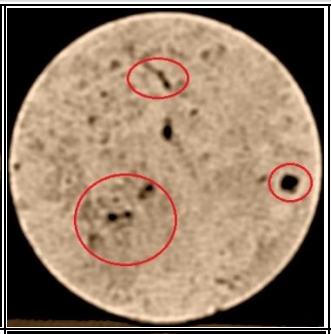	
CT images after flooding	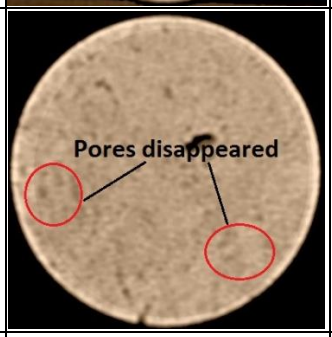	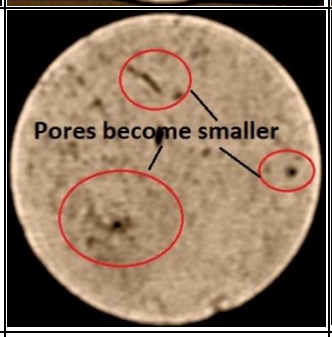	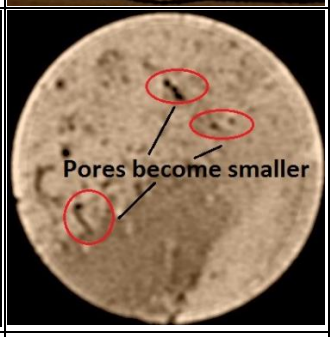
Image at (mm)	11.2mm	32.4mm	50mm

Figure 4.36. CT Value distribution and X-ray cross-sectional images for sample GD-11 before and after flooding. The CT number profiles and cross-sectional images show signs of asphaltene precipitation along the length of the sample, as the CT profiles seem to have become denser, resulting in a reduction in overall sample permeability.

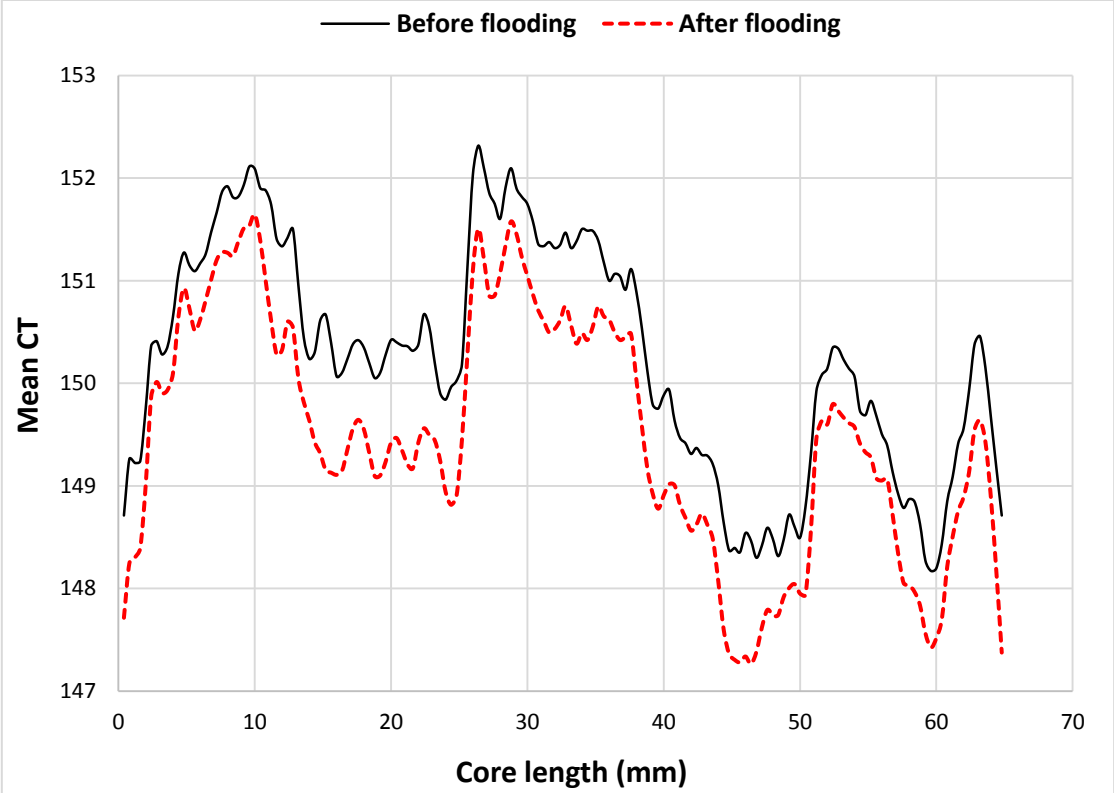

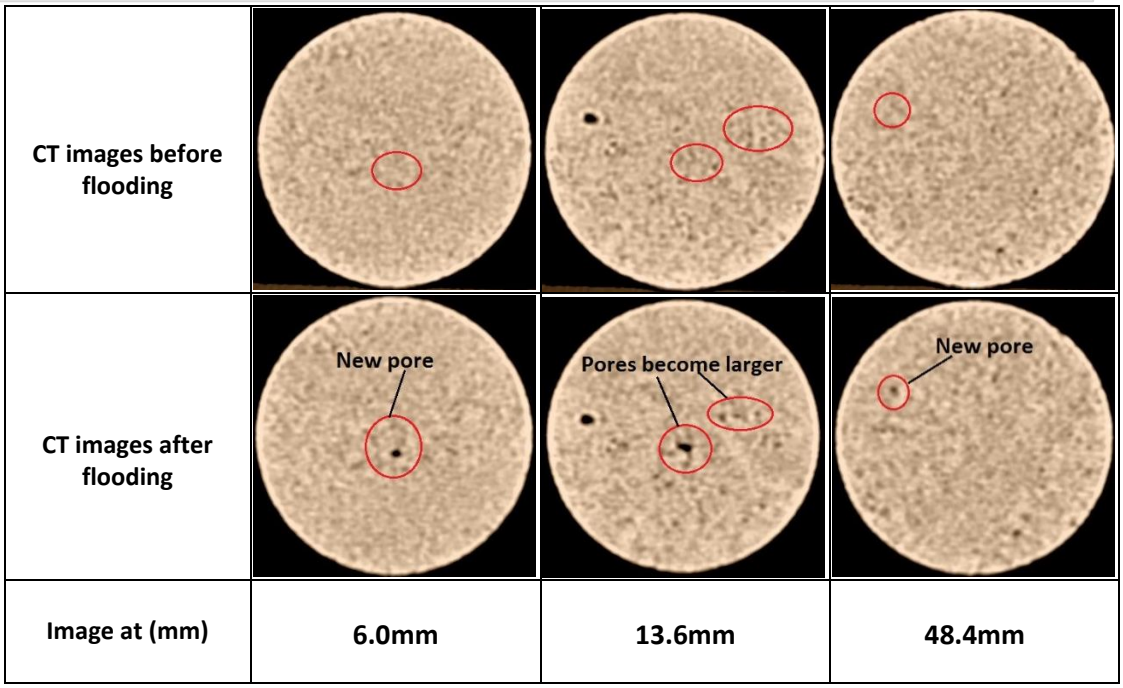

Figure 4.37. CT Value distribution and X-ray cross-sectional images for Sample INL-11 before and after flooding. The CT number profiles and cross-sectional images show signs of dissolution along the length of the sample. The CT profiles seem to have become less dense due to mineral dissolution.

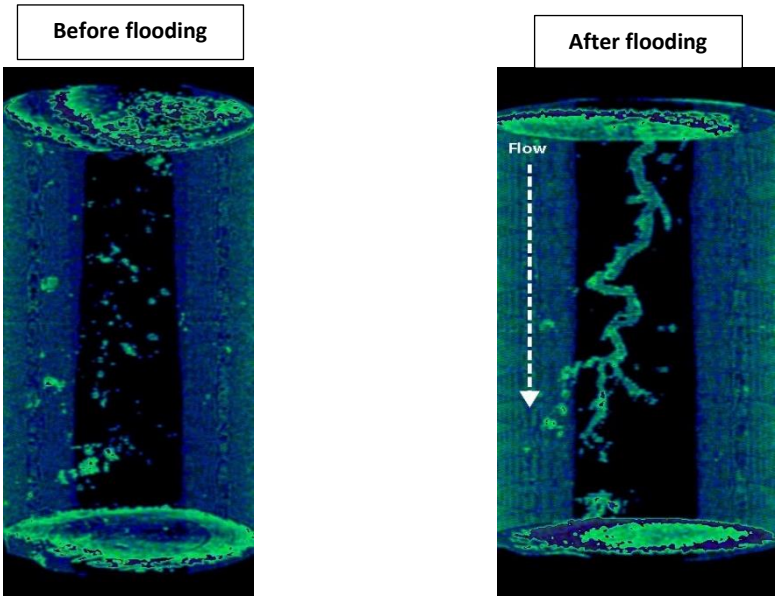

Figure 4.38. 3D images for sample VS-2 before and after flooding. The images show the creation of wormholes along the length of the sample due to the massive dissolution of carbonate minerals.

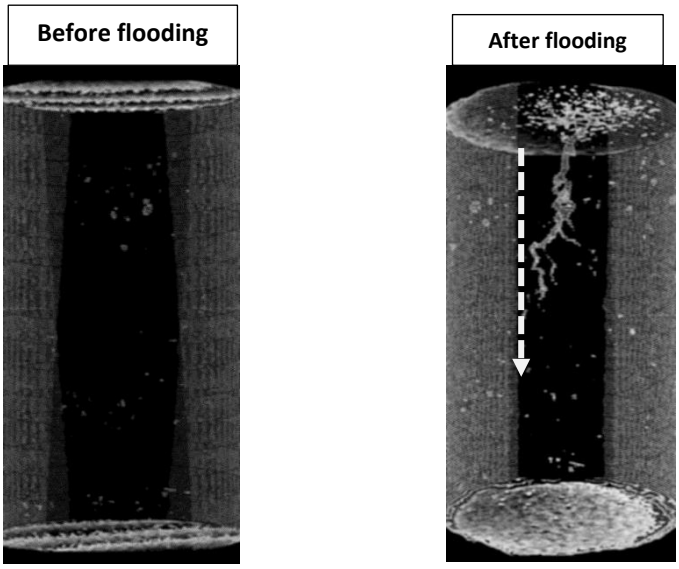

Figure 4.39. 3D images for sample INL-11 before and after flooding. The images show the creation of dissolution fingers due to mineral dissolution.

4.4. Nuclear magnetic resonance (NMR) measurements

As indicated in Chapter 3, all rock samples underwent NMR T2 measurements before and after flooding. This was to determine (qualitatively) the degree of alteration (if any) to their pore size distribution and pore network caused by the core-flood experiments.

4.4.1. Live brine flooding

For the samples flooded using this scenario, figures 4.40 - 4.53 show the NMR-derived pore size distribution (in the form T2 distributions) and cumulative NMR porosity before and after flooding. As apparent from the figures, NMR data have revealed all three cases of no apperciable change, increase and decrease in the post-flood NMR porosity of the sampels. However, for the majority of the samples, their post-flood overall pore size spectrum (i.e. NMR T2 distribution) seems to have shifted towards smaller pore sizes.

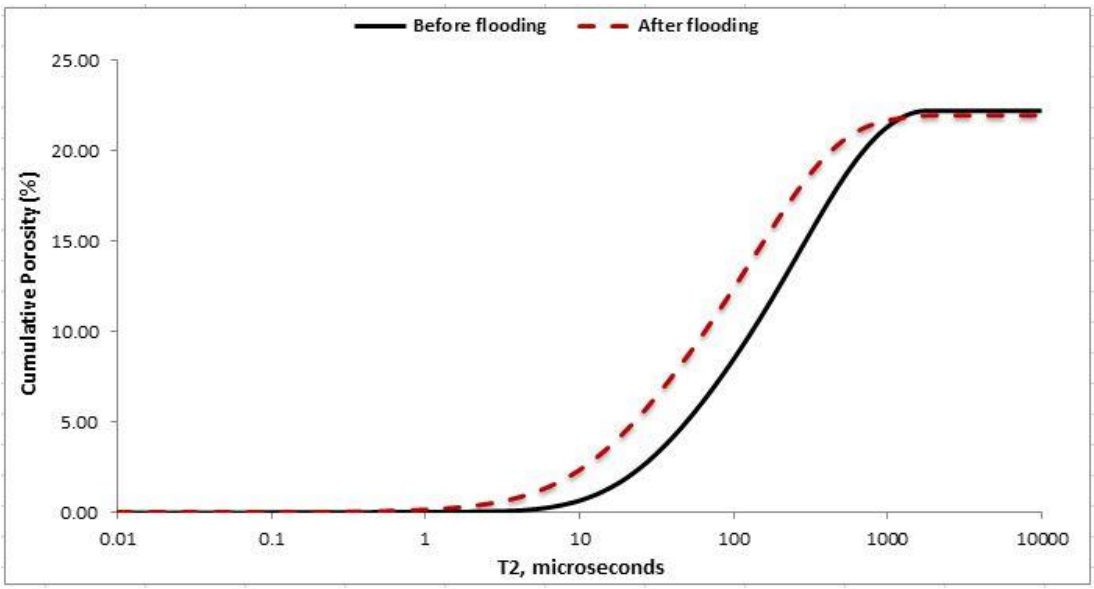

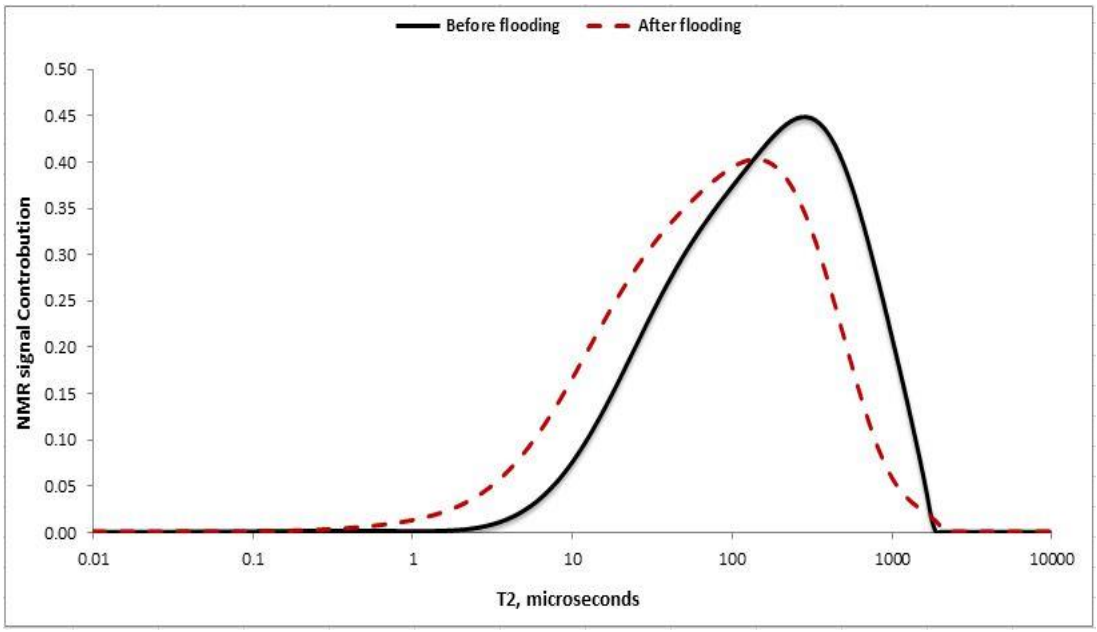

Figure 4.40. Change in the cumulative porosity (top) and incremental NMR T2 distribution (bottom) of Sample VS-1 before and after flooding. The overall NMR porosity of the sample decreased. Its NMR T2 distribution shifted to the left, indicating that the sample's pore sizes have become smaller after flooding.

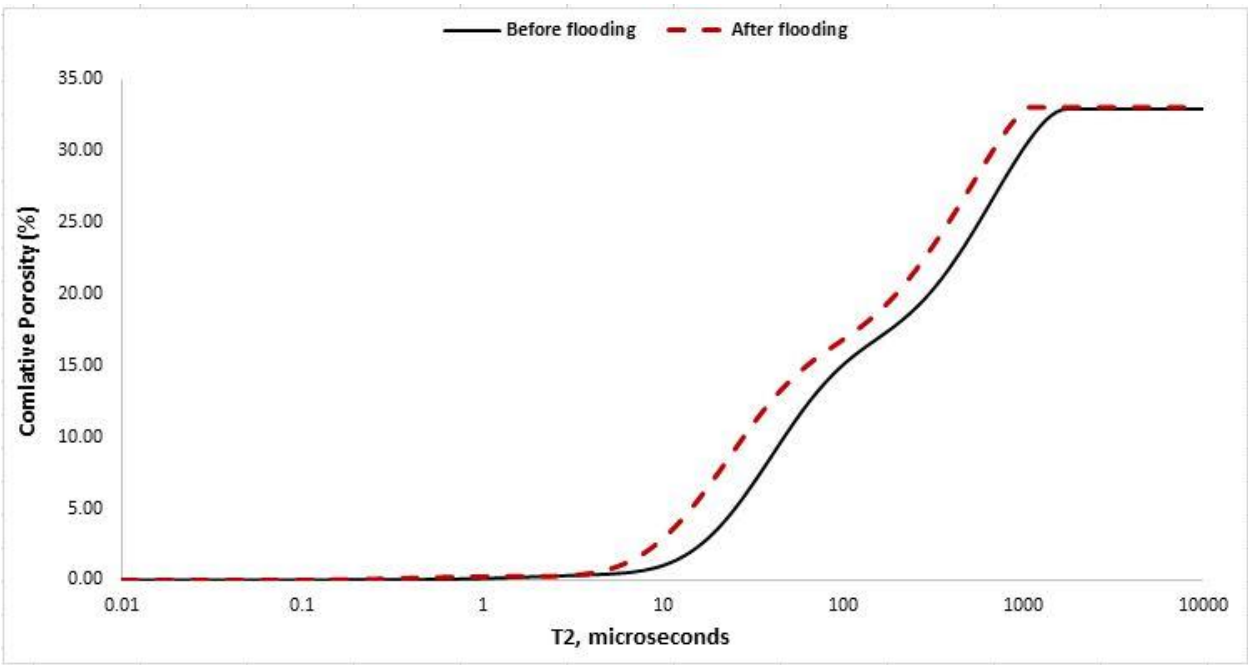

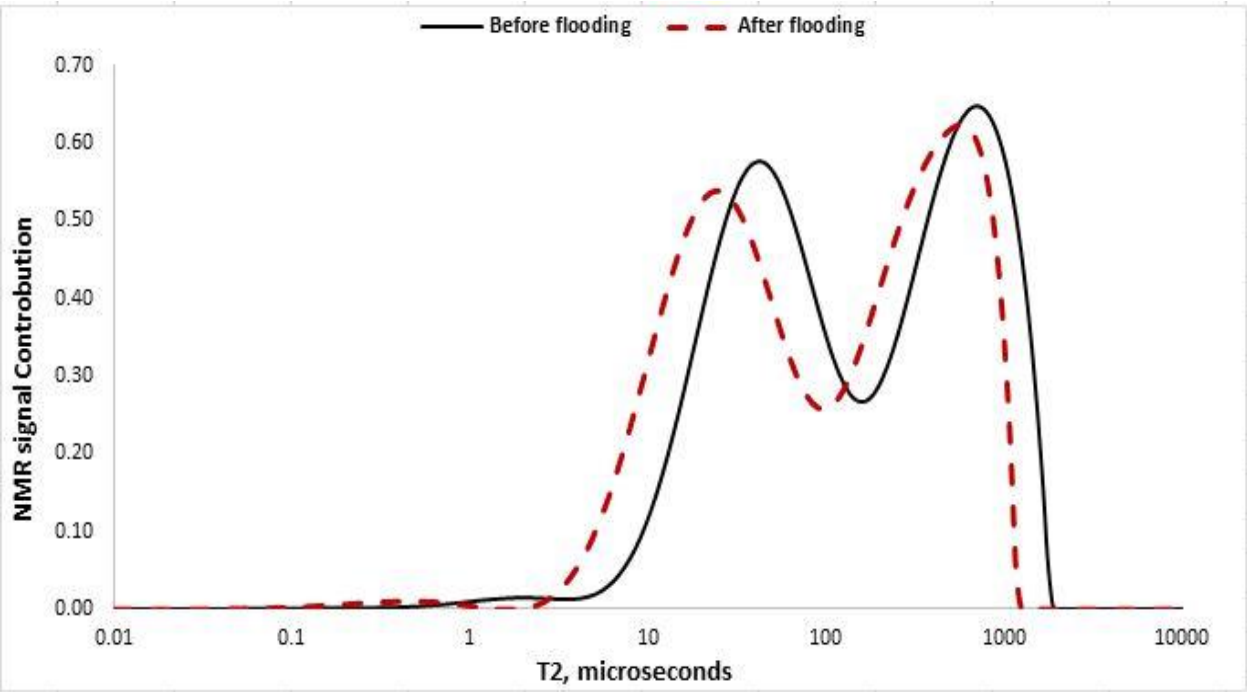

Figure 4.41. Change in the cumulative porosity (top) and incremental NMR T2 distribution (bottom) of Sample SC-2 before and after flooding. The overall NMR porosity of the sample decreased. Its NMR T2 distribution shifted to the left, indicating that the sample's pore sizes have become smaller after flooding.

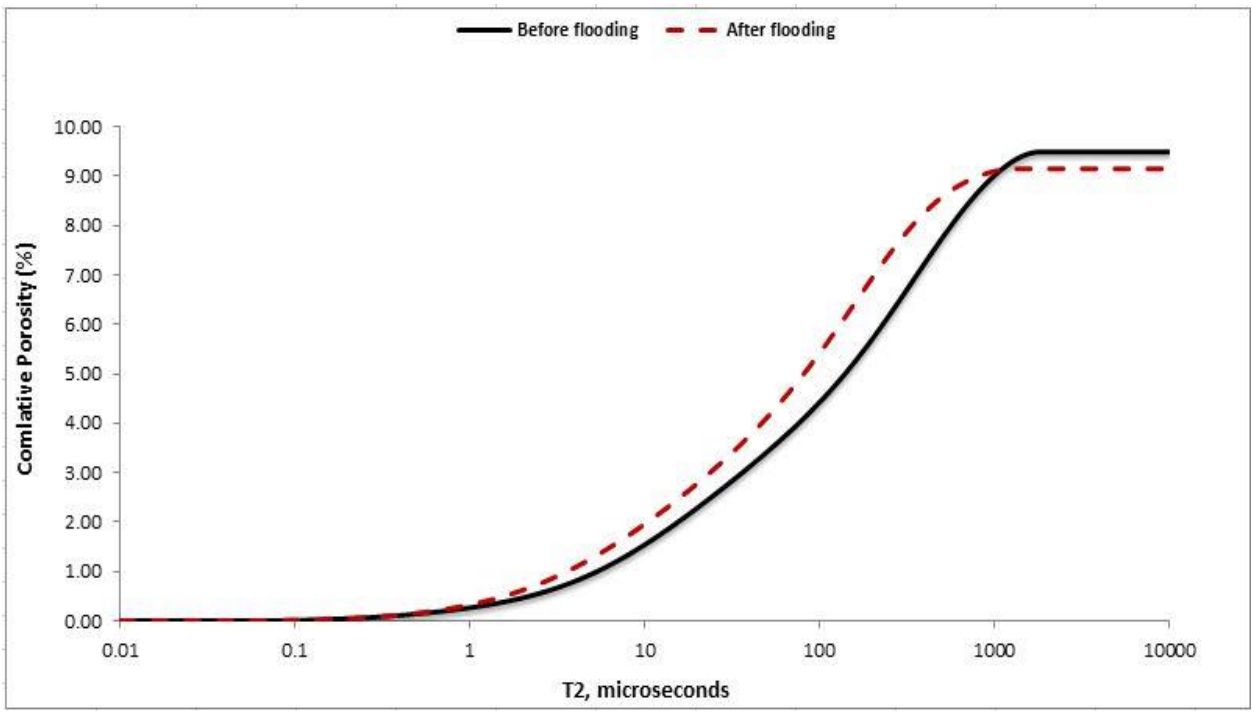

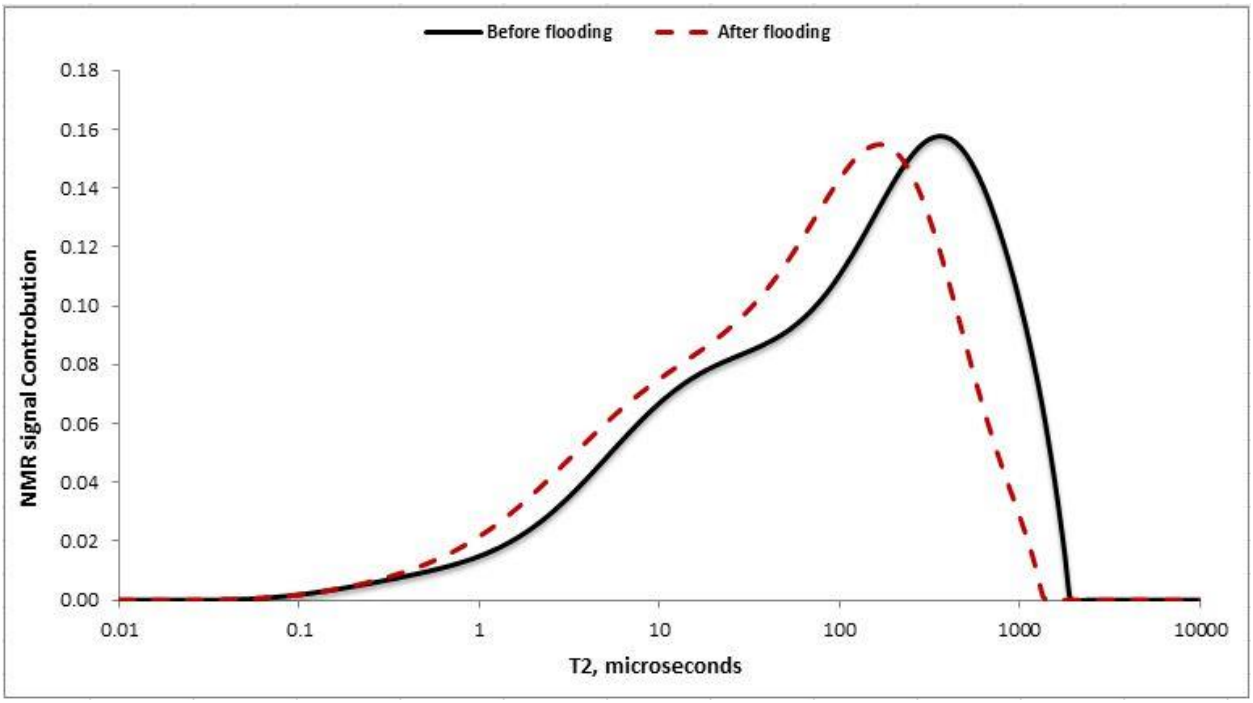

Figure 4.42. Change in the cumulative porosity (top) and incremental NMR T2 distribution (bottom) of Sample TC-2 before and after flooding. The overall NMR porosity of the sample decreased. Its NMR T2 distribution shifted to the left, indicating that the sample's pore sizes have become smaller after flooding.

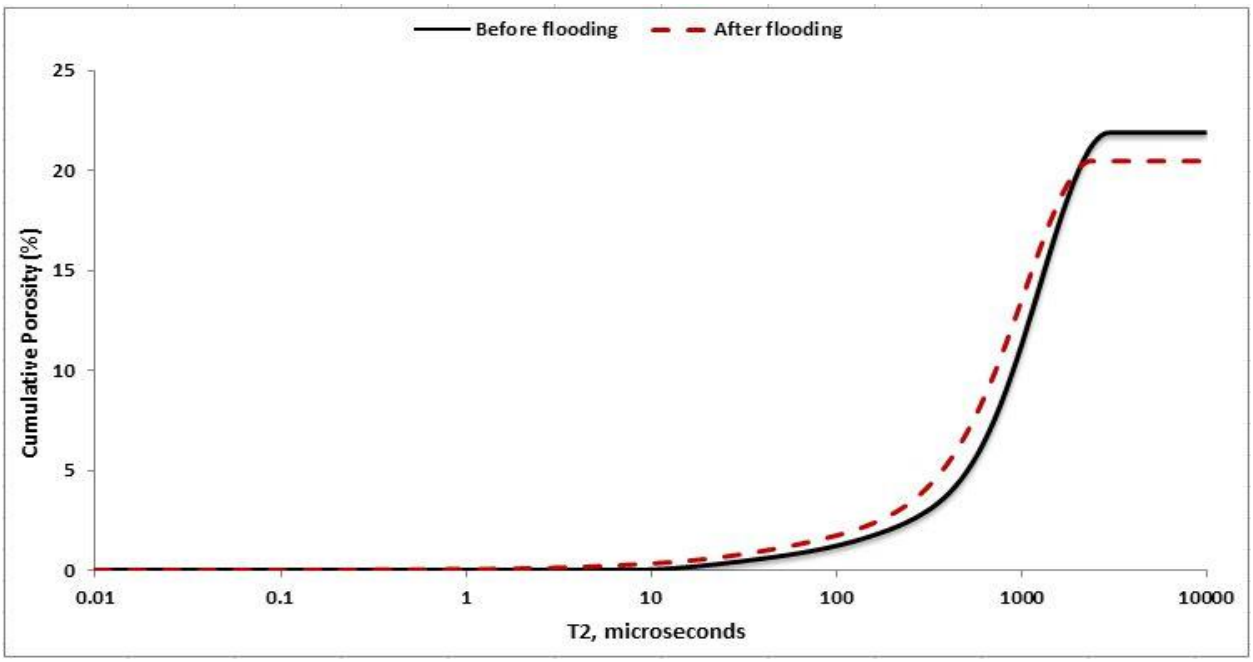

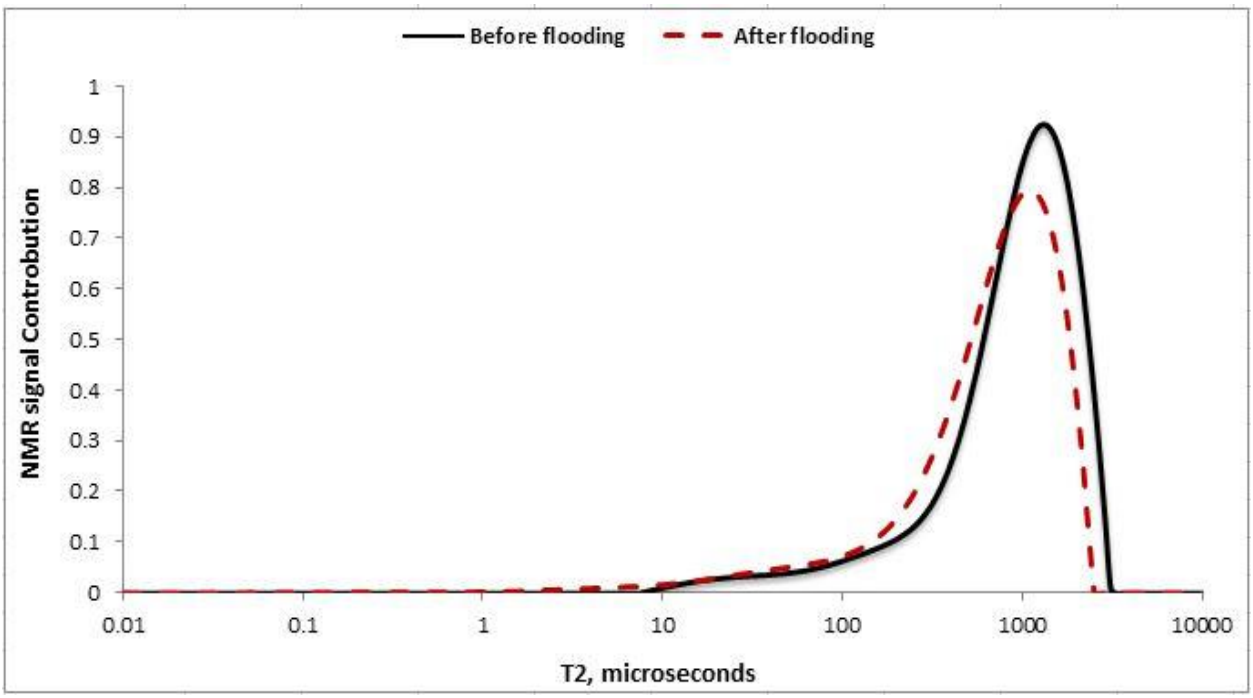

Figure 4.43. Change in the cumulative porosity (top) and incremental NMR T2 distribution (bottom) of Sample VC-2 before and after flooding. The overall NMR porosity of the sample decreased. Its NMR T2 distribution shifted to the left, indicating that the sample's pore sizes have become smaller after flooding.

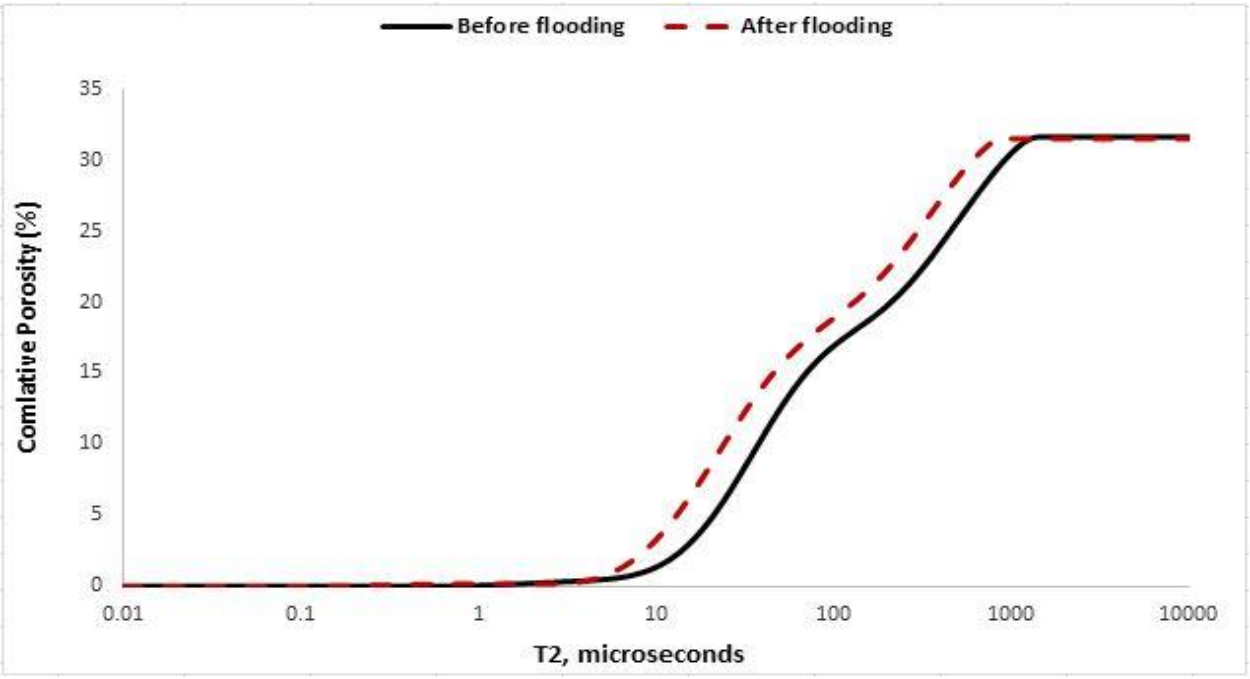

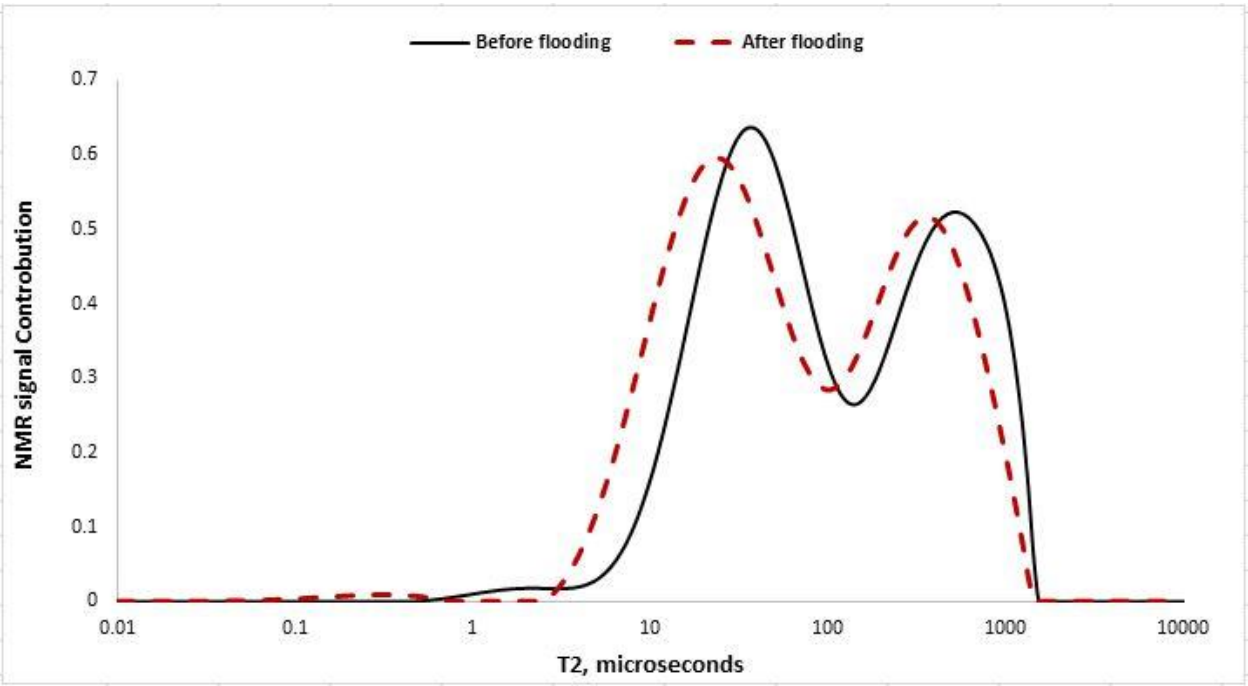

Figure 4.44. Change in the cumulative porosity (top) and incremental NMR T2 distribution (bottom) of Sample SC-1 inlet part before and after flooding. The NMR porosity of the sample decreased slightly. Its NMR T2 distribution shifted to the left, indicating that the sample's pore sizes have become smaller after flooding.

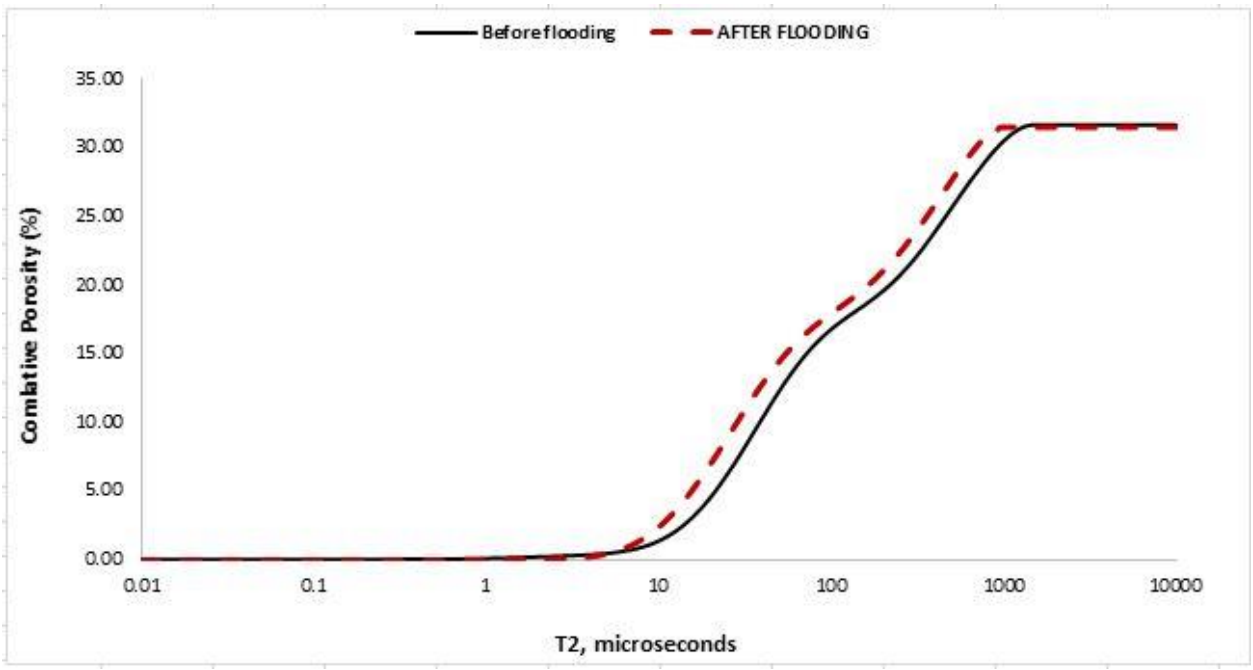

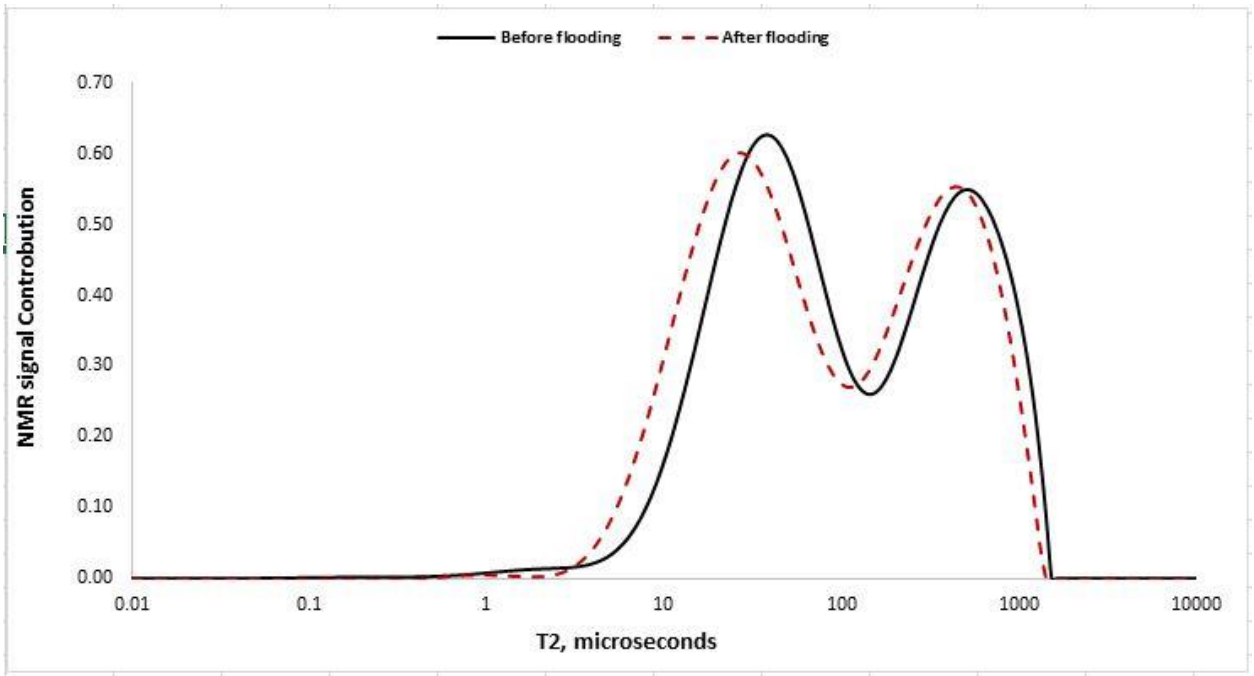

Figure 4.45. Change in the cumulative porosity (top) and incremental NMR T2 distribution (bottom) of Sample SC-1 outlet part before and after flooding. The NMR porosity of the sample decreased slightly. Its NMR T2 distribution shifted to the left, indicating that the sample's pore sizes have become smaller after flooding.

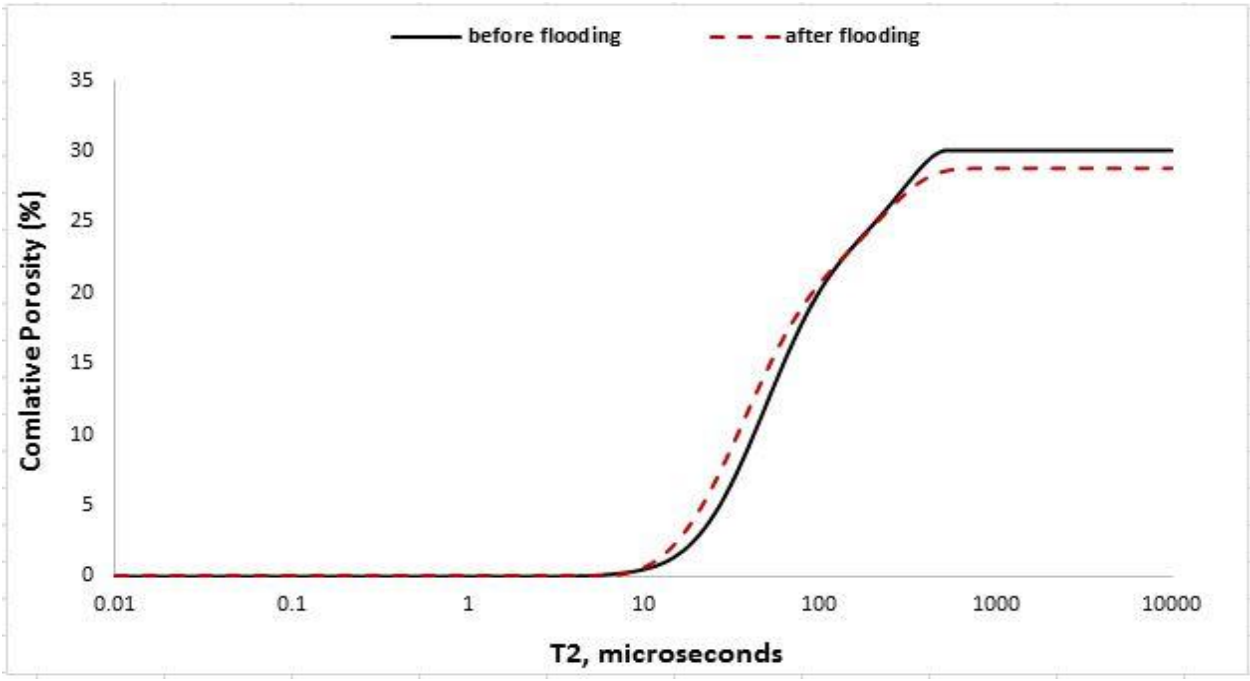

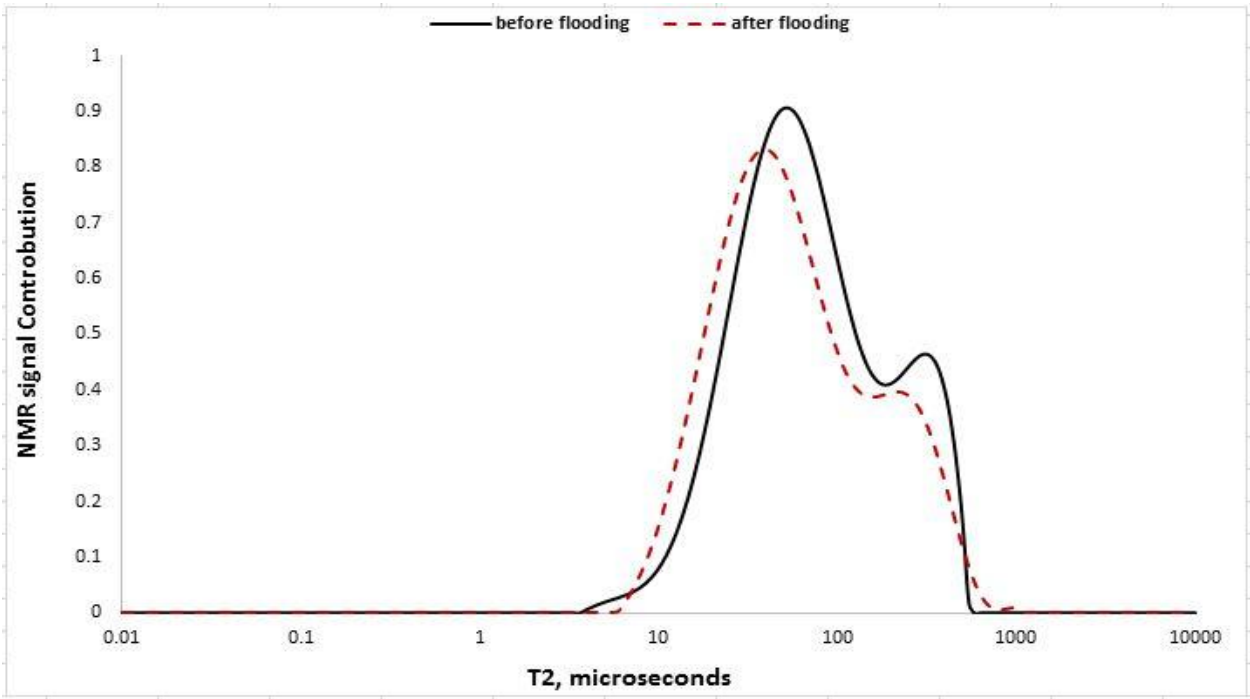

Figure 4.46. Change in the cumulative porosity (top) and incremental NMR T2 distribution (bottom) of Sample CH-1 inlet part before and after flooding. The overall NMR porosity of the sample decreased. Its NMR T2 distribution shifted to the left, indicating that the sample's pore sizes have become smaller after flooding.

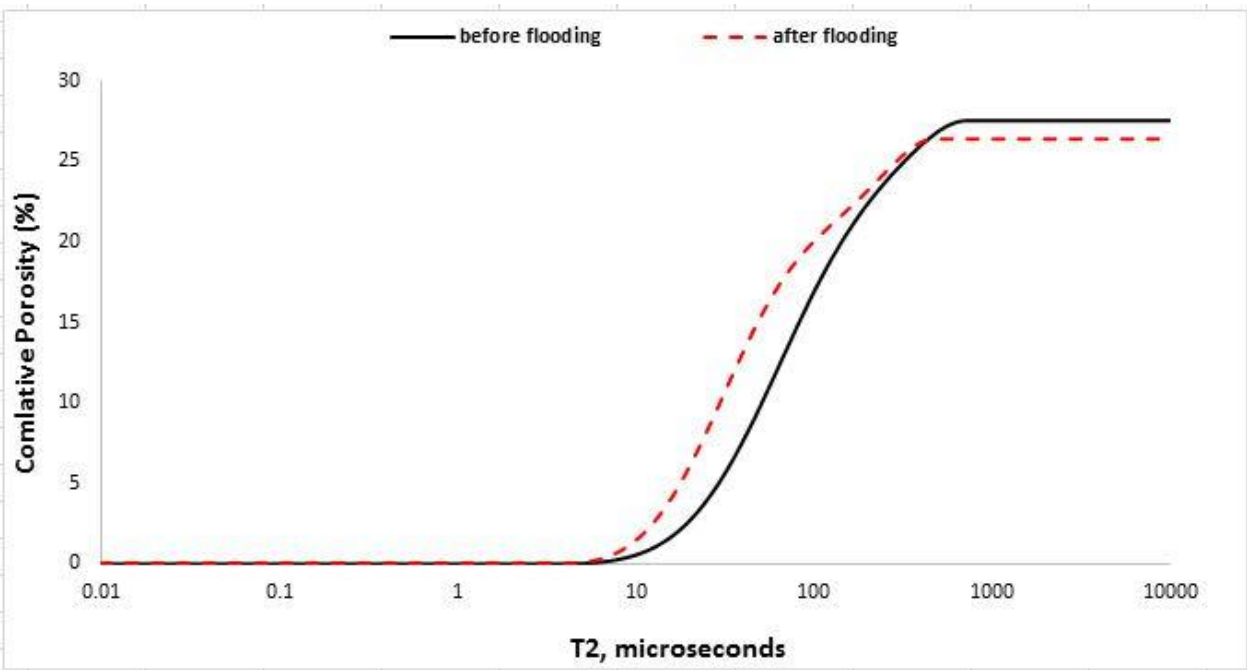

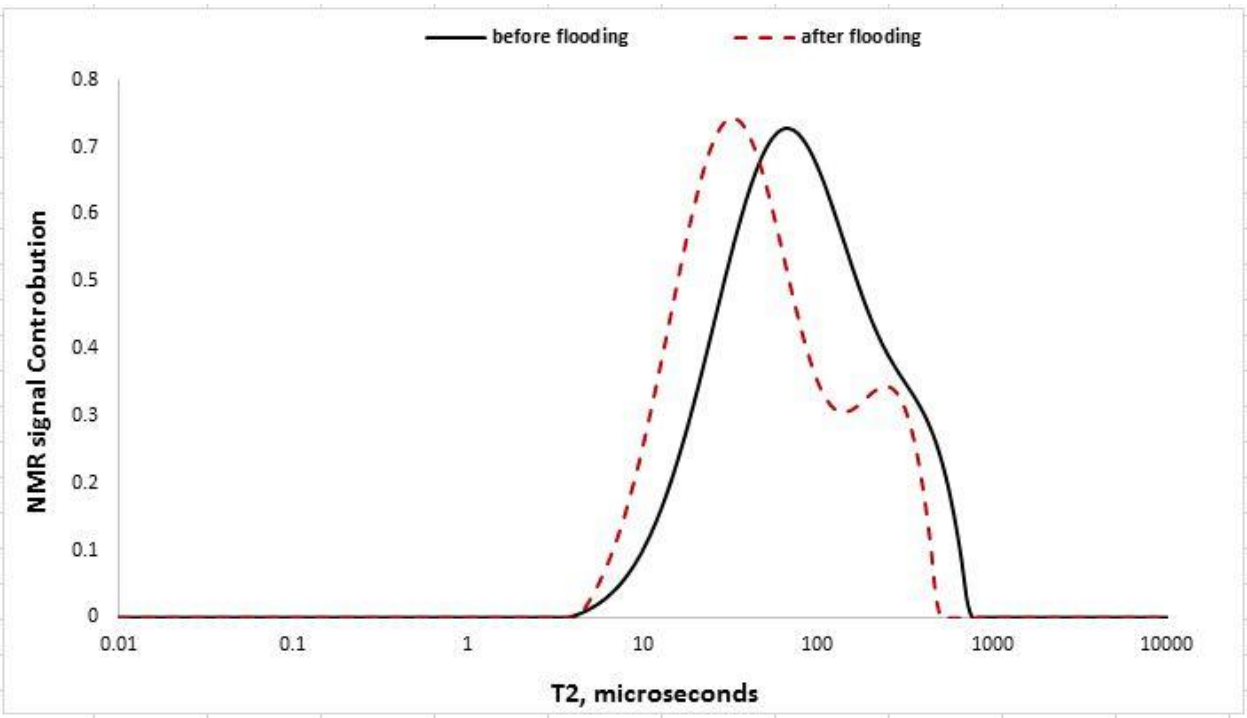

Figure 4.47. Change in the cumulative porosity (top) and incremental NMR T2 distribution (bottom) of Sample CH-1 outlet part before and after flooding. The overall NMR porosity of the sample decreased. Its NMR T2 distribution shifted to the left, indicating that the sample's pore sizes have become smaller after flooding.

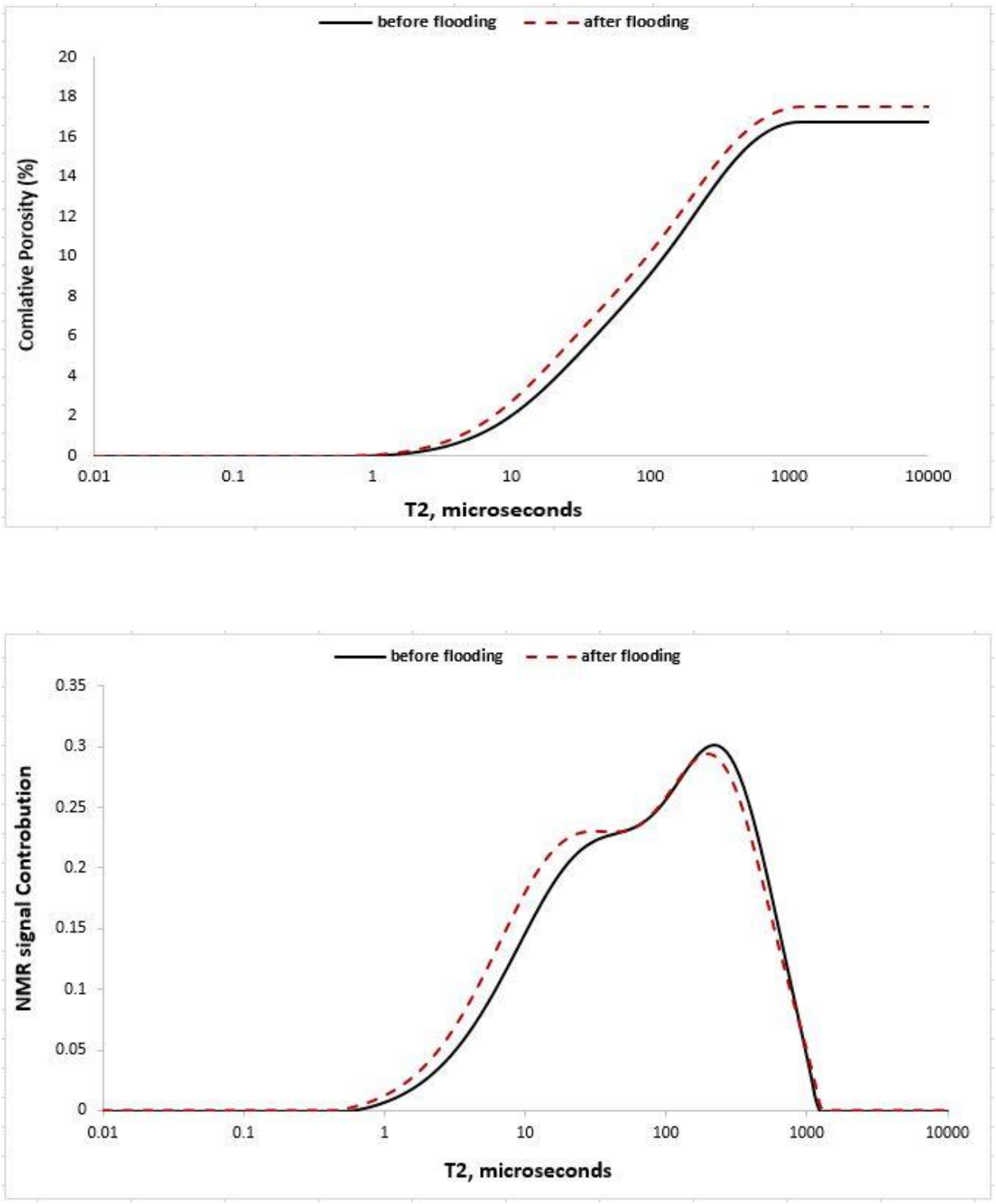

Figure 4.48. Change in the cumulative porosity (top) and incremental NMR T2 distribution (bottom) of half Sample IL-1 before and after flooding. The overall NMR porosity of the sample increased. Its NMR T2 distribution shows almost no change, indicating that the sample's pore sizes remained the same after flooding.

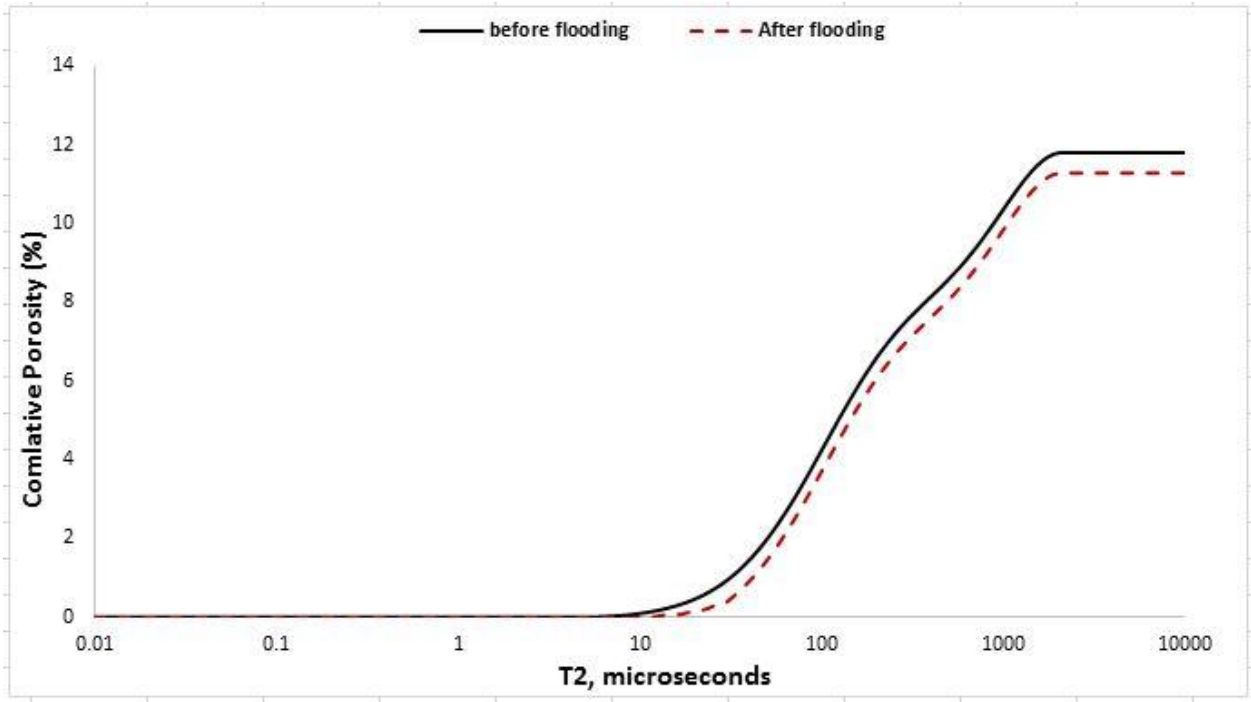

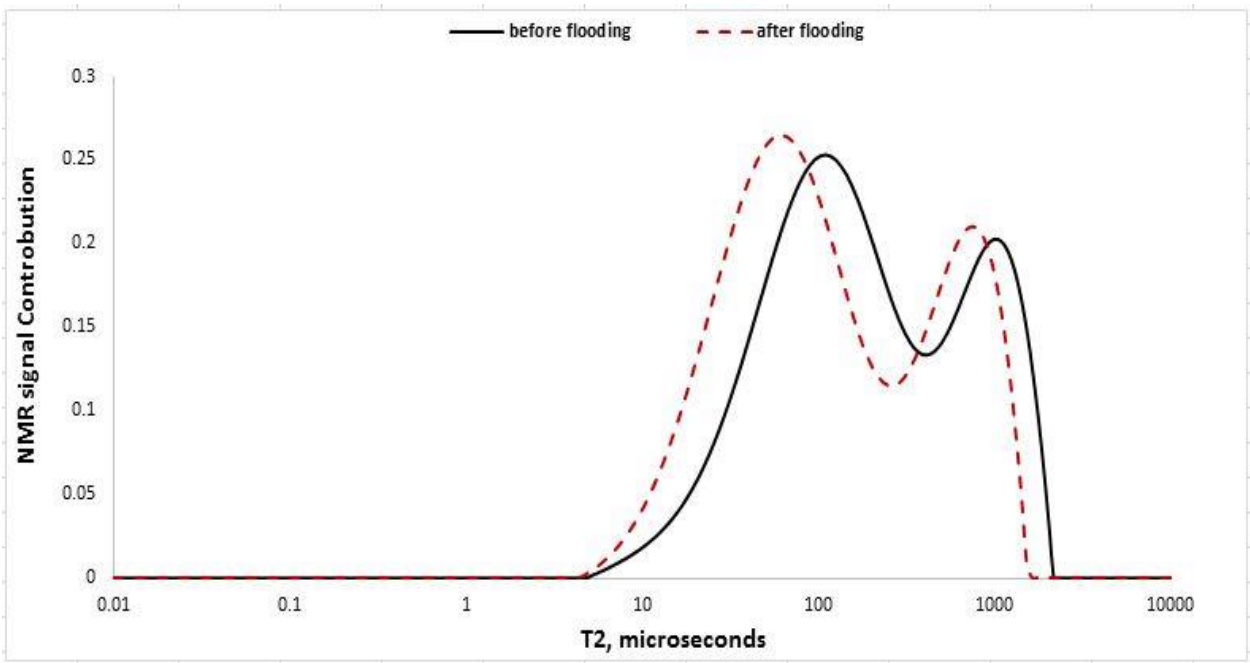

Figure 4.49. Change in the cumulative porosity (top) and incremental NMR T2 distribution (bottom) of half Sample IL-2 before and after flooding. The overall NMR porosity of the sample decreased. Its NMR T2 distribution shifted to the left, indicating that the sample's pore sizes have become smaller after flooding.

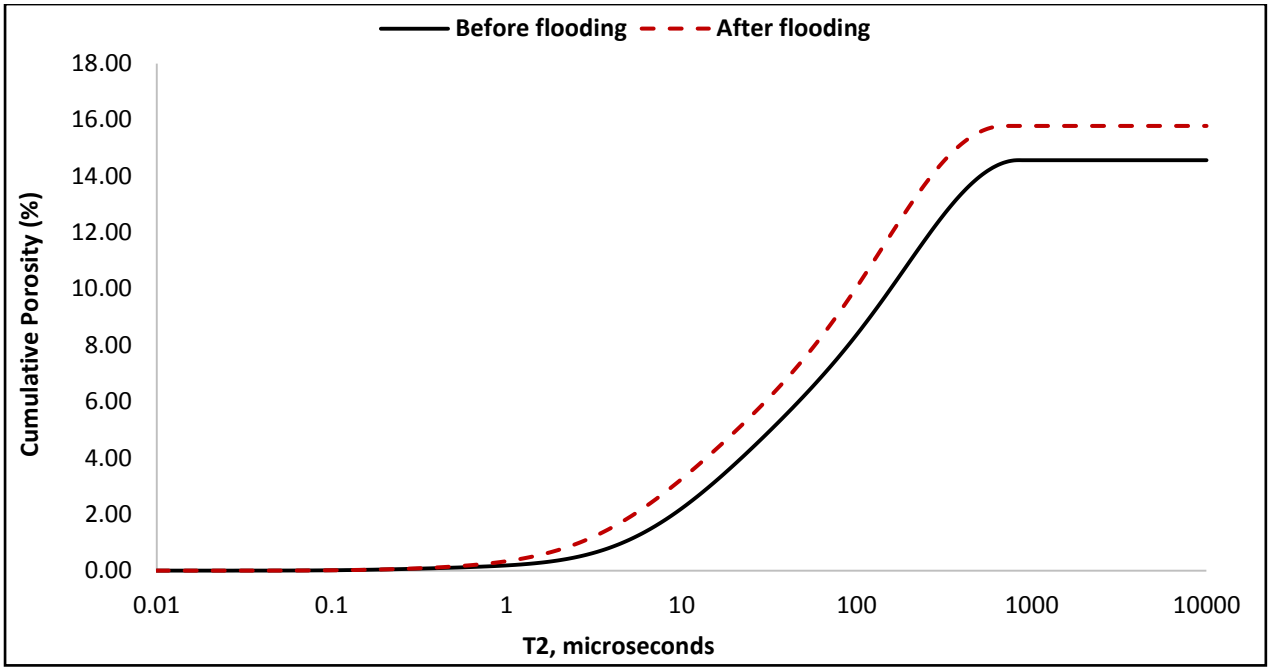

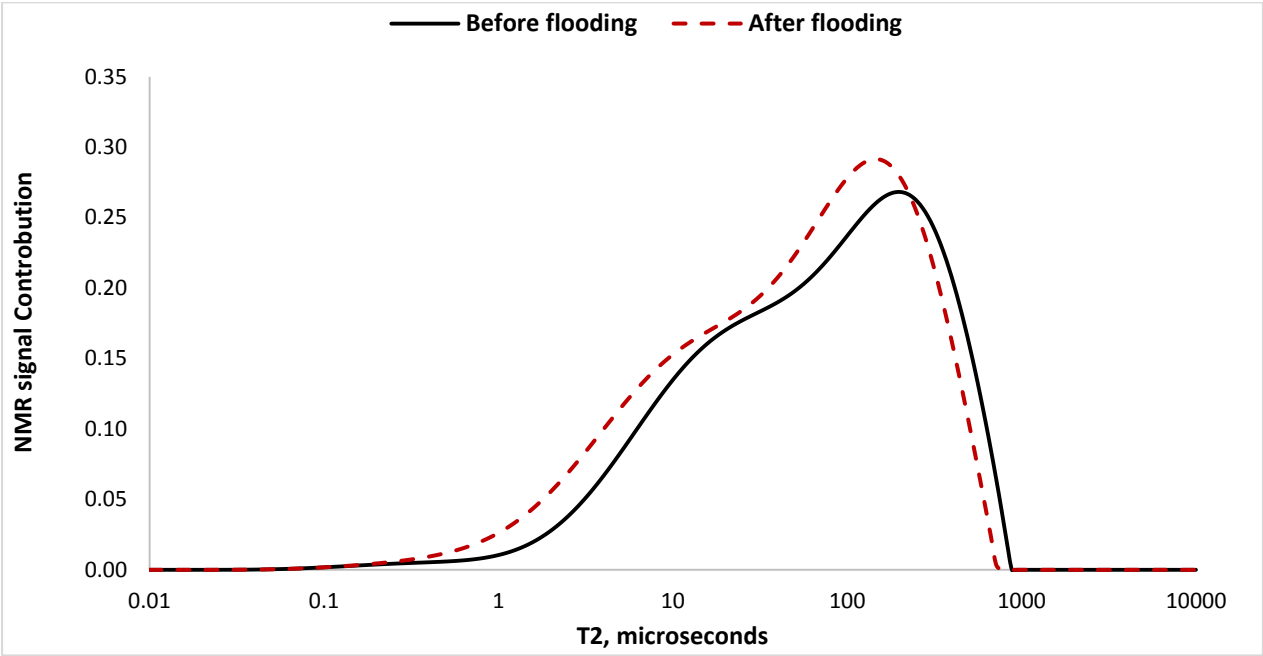

Figure 4.50. Change in the cumulative and incremental NMR T2 distribution of Sample VS-3 before and after flooding. While the overall NMR porosity of the sample increased, its NMR T2 distribution shifted to the left, indicating that the sample's pore sizes have become smaller after flooding.

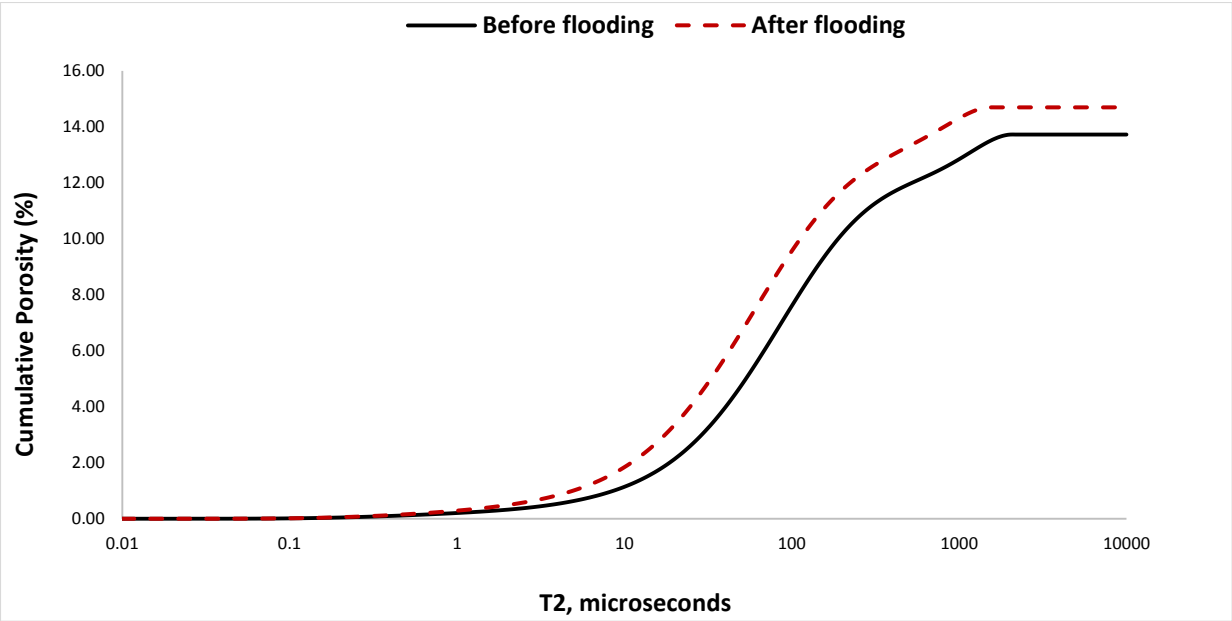

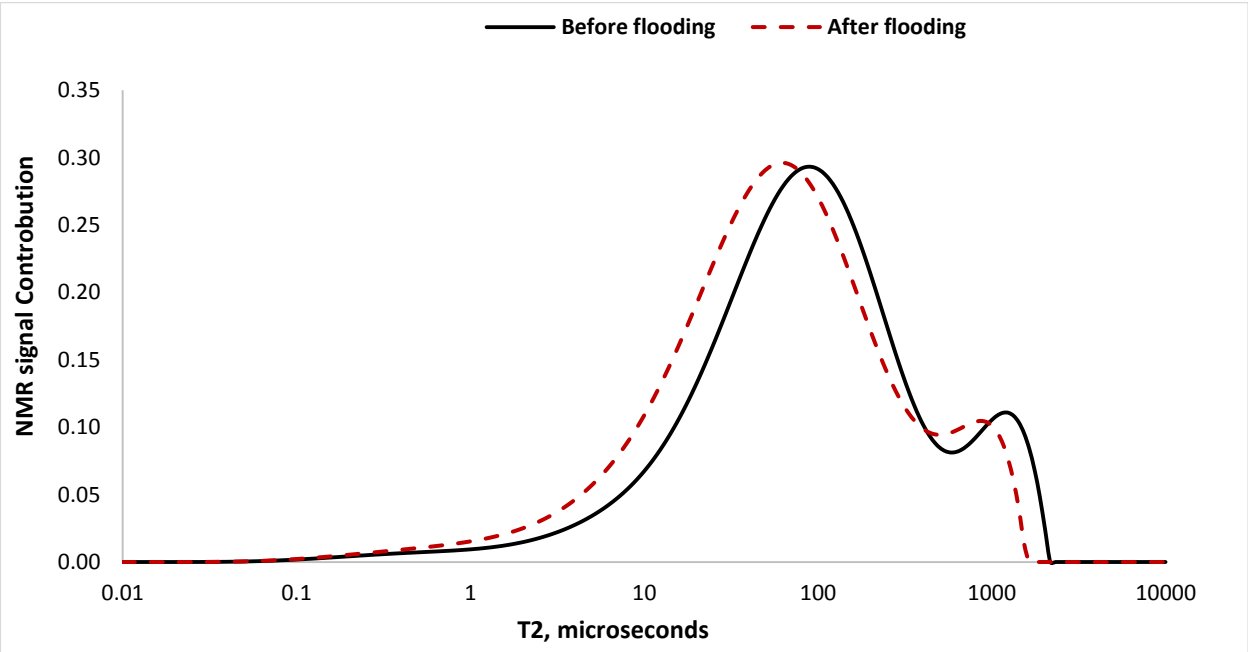

Figure 4.51. Change in the cumulative and incremental NMR T2 distribution of Sample VS-4 after flooding. While the overall NMR porosity of the sample increased, its NMR T2 distribution shifted to the left, indicating that the sample's pore sizes have become smaller after flooding.

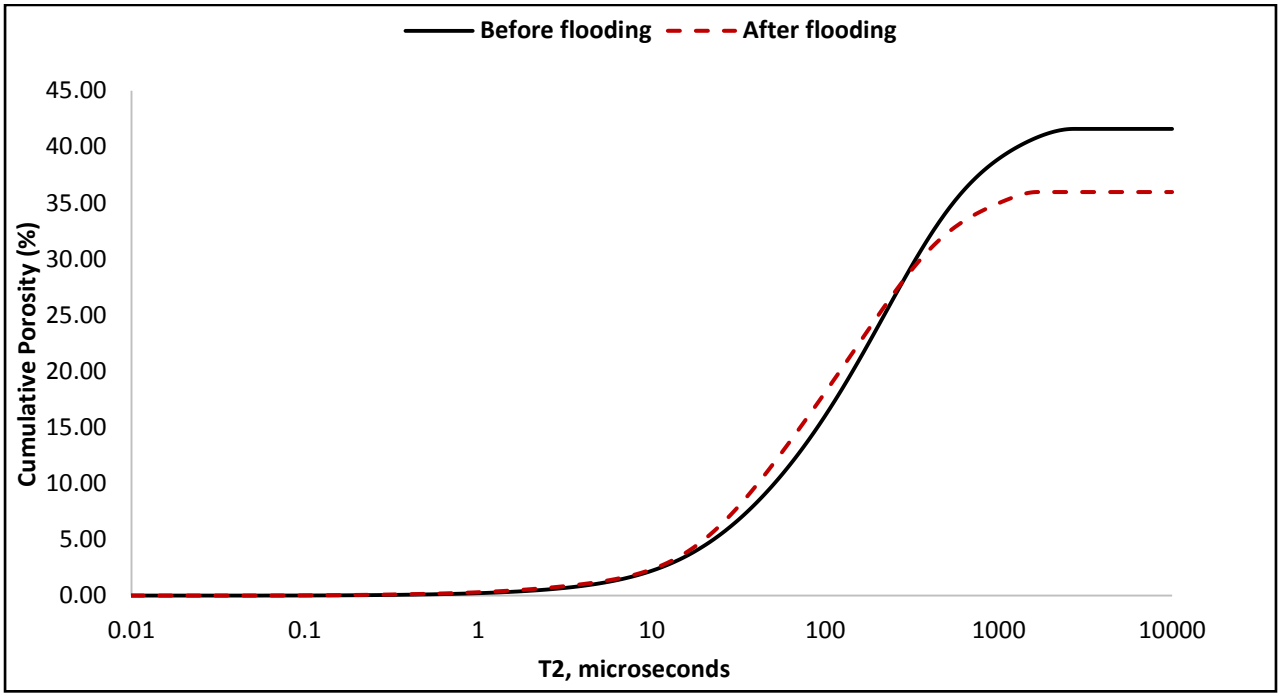

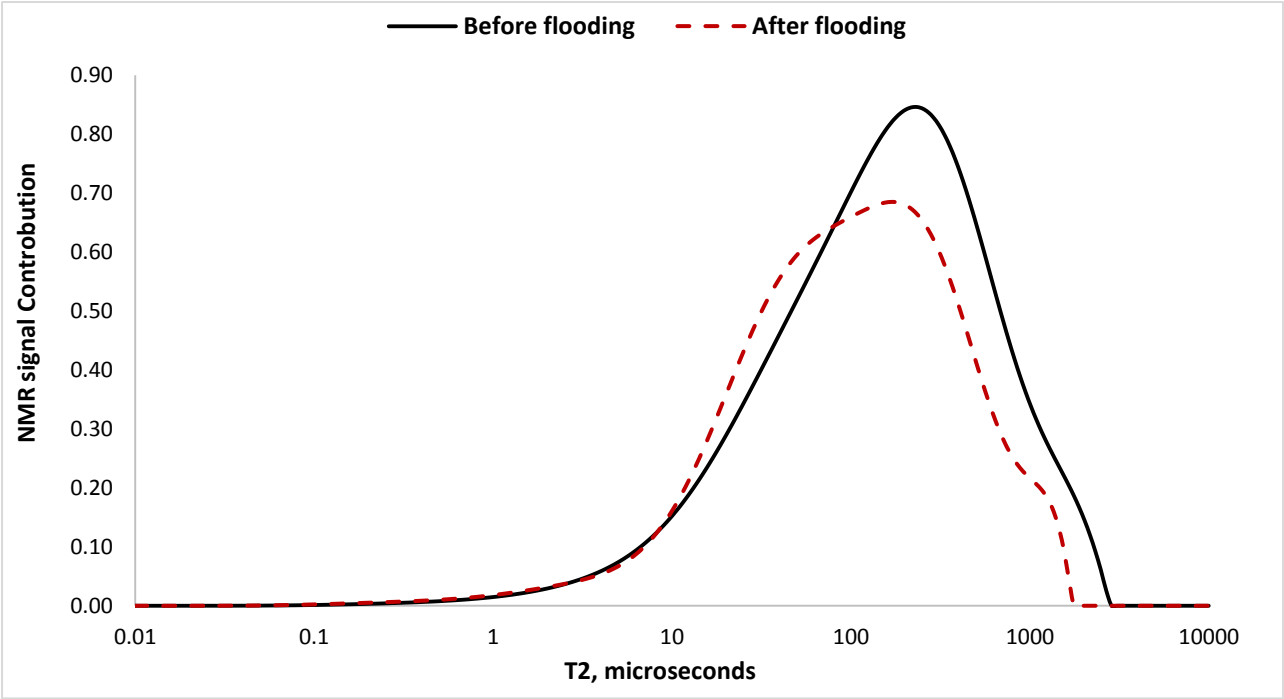

Figure 4.52. Change in the cumulative and incremental NMR T2 distribution of Sample VC-3 after flooding. The overall NMR porosity of the sample decreased. Its NMR T2 distribution showed a moderate shift to the left, indicating that the sample's pore sizes have become smaller after flooding.

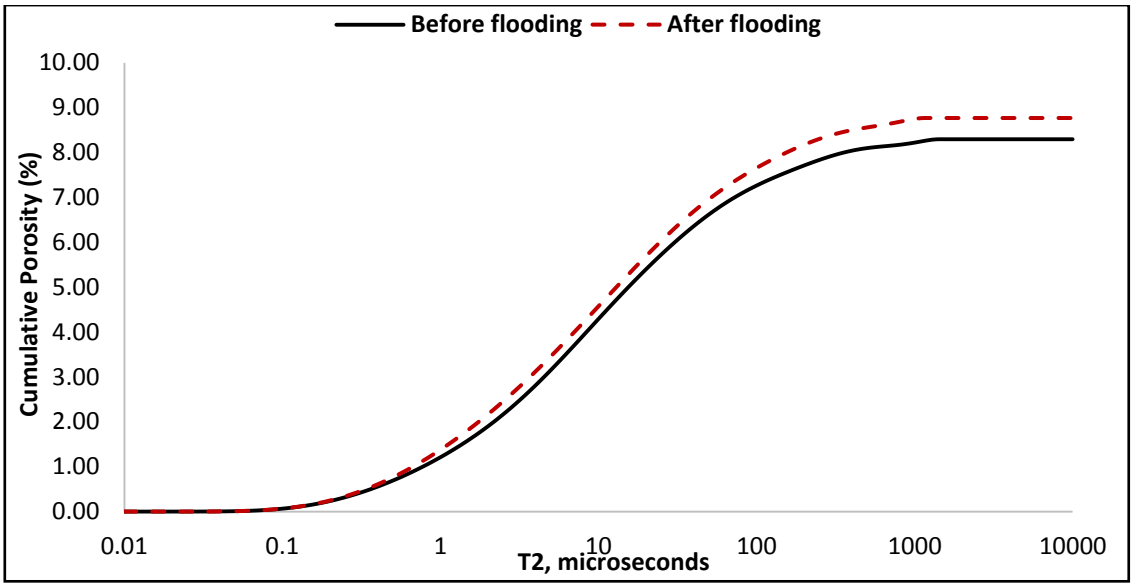

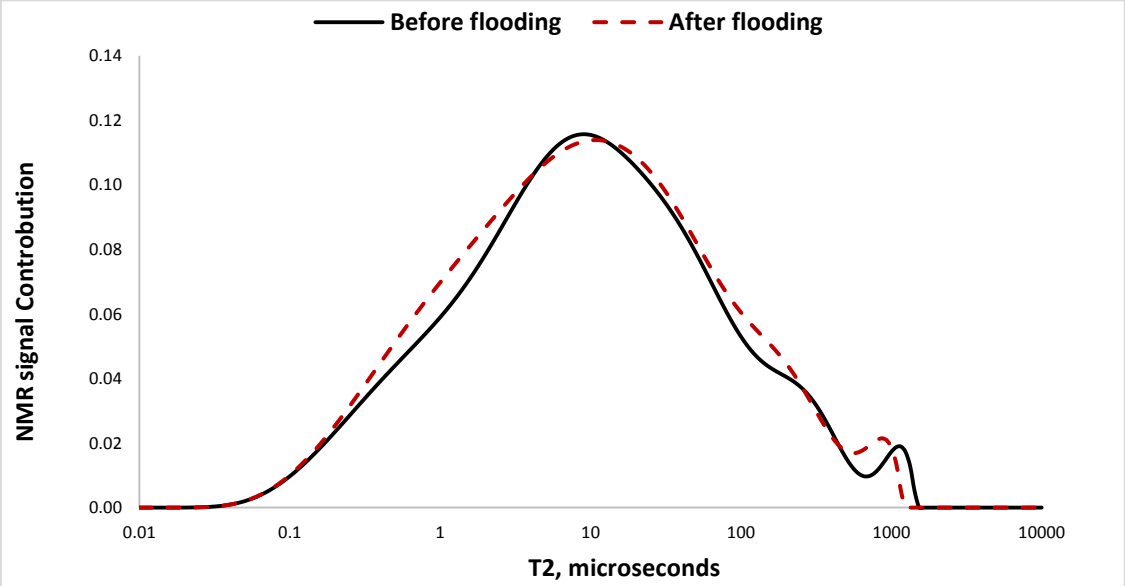

Figure 4.53. Change in the cumulative and incremental NMR T2 distribution of Sample TC-1 after flooding. While the overall NMR porosity of the sample increased, its NMR T2 distribution did not show any obvious signs of change in its pore sizes.

4.4.2. Continuous CO_2-EOR flooding

Figures 4.54-4.59 present the pre- and post-flood NMR T2 distributions and cumulative porosity plots for the samples tested as part of the continuous CO_2-EOR flooding scheme. As apparent from the figures, except for Sample INL-1, all samples show an appreciable decrese in their post-flood porosities and often a shift in their pore size spectra (represented by their NMR T2 distribution) towards smaller pore sizes.

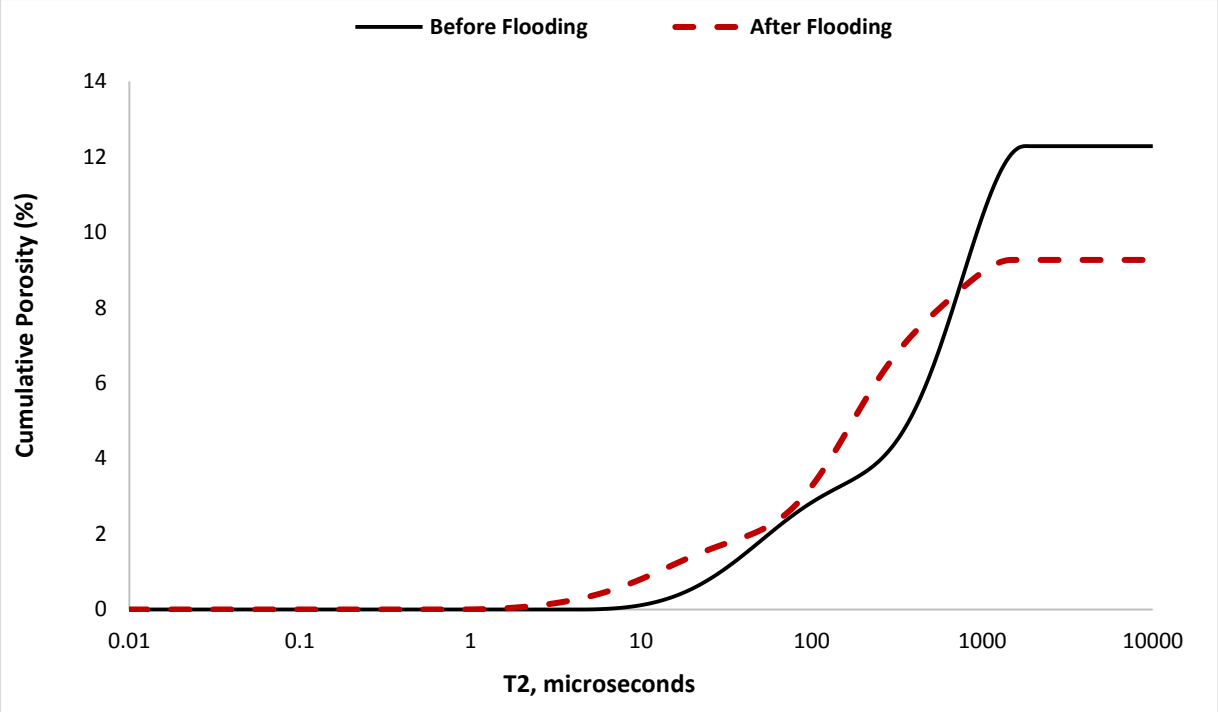

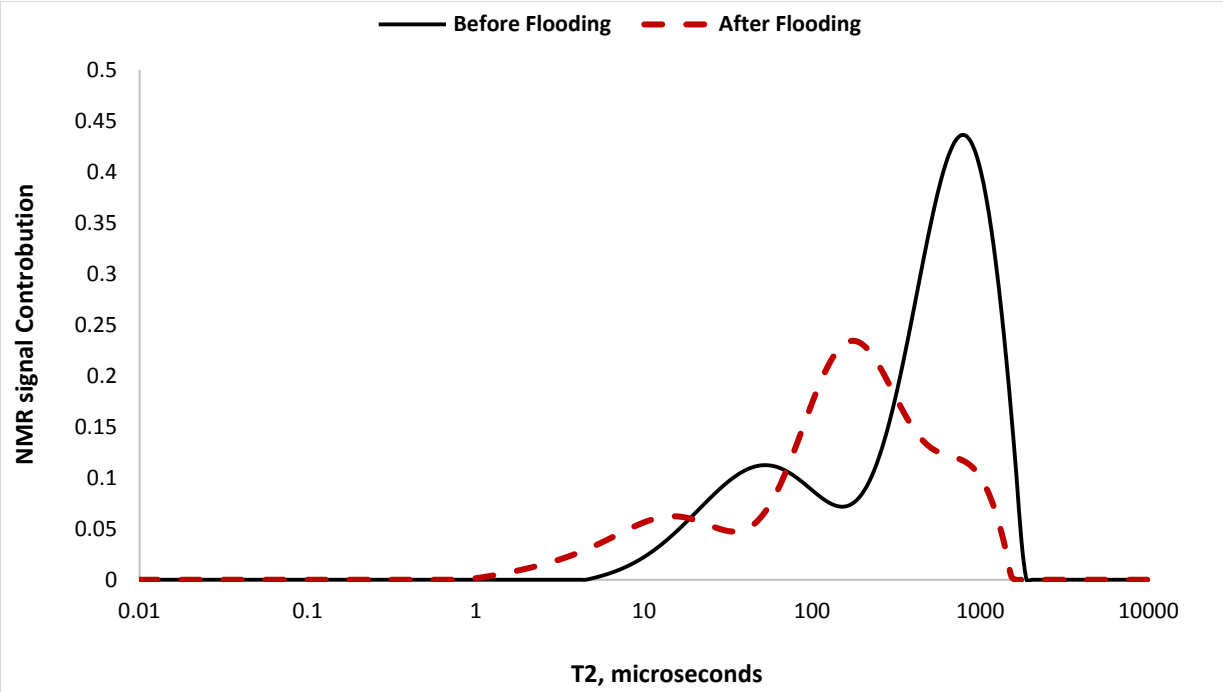

Figure 4.54. Change in the cumulative porosity (top) and incremental NMR T2 distribution (bottom) of Sample SD-1 inlet part before and after flooding. The overall NMR porosity of the sample decreased. Its NMR T2 distribution shifted to the left, indicating that the sample's pore sizes have become smaller after flooding.

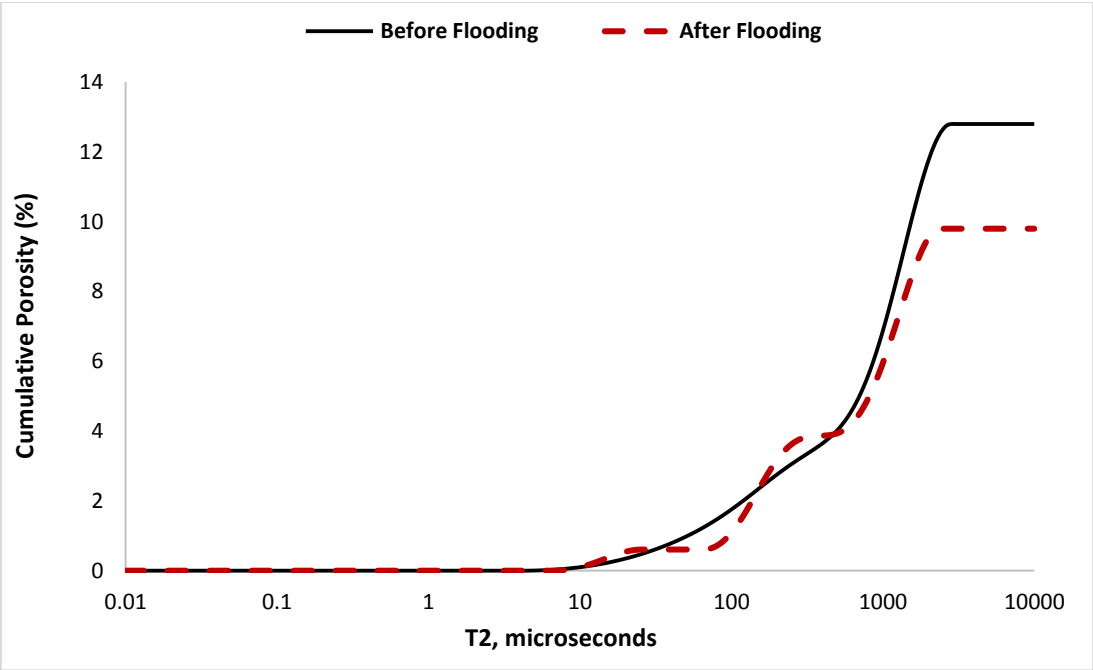

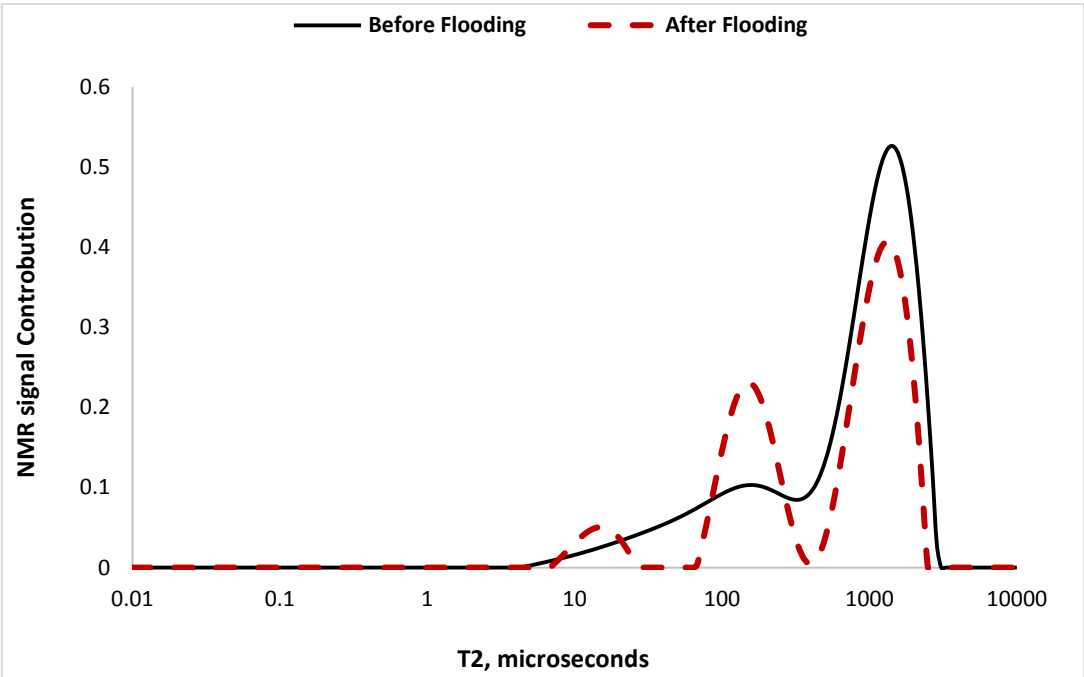

Figure 4.55. Change in the cumulative porosity (top) and incremental NMR T2 distribution (bottom) of Sample SD-1 outlet part before and after flooding. The overall NMR porosity of the sample decreased. Its NMR T2 distribution shifted to the left, indicating that the sample's pore sizes have become smaller after flooding.

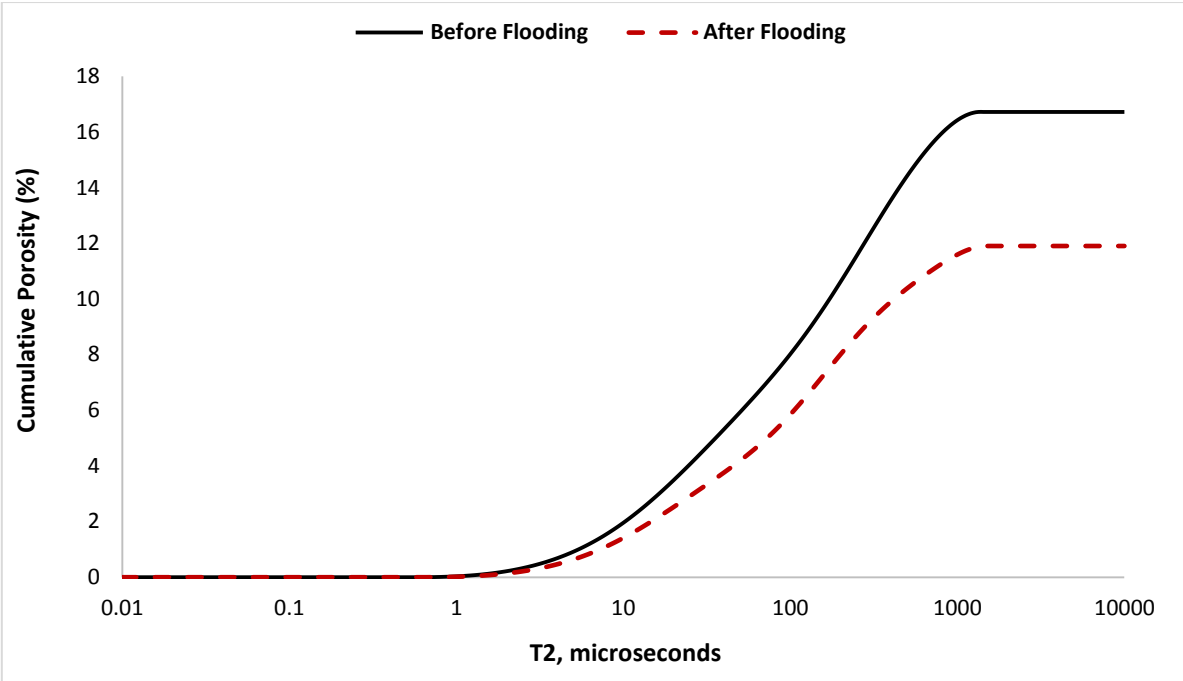

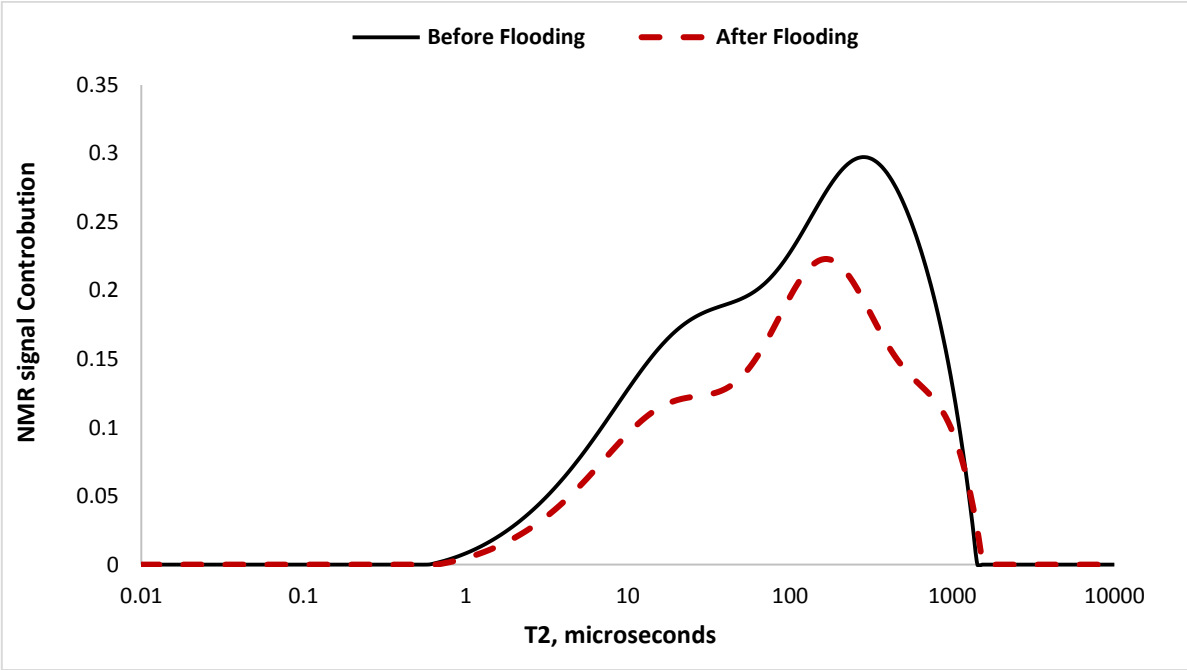

Figure 4.56. Change in the cumulative porosity (top) and incremental NMR T2 distribution (bottom) of Sample INL-2 inlet part before and after flooding. The overall NMR porosity of the sample decreased. Its NMR T2 distribution shifted to the left, indicating that the sample's pore sizes have become smaller after flooding.

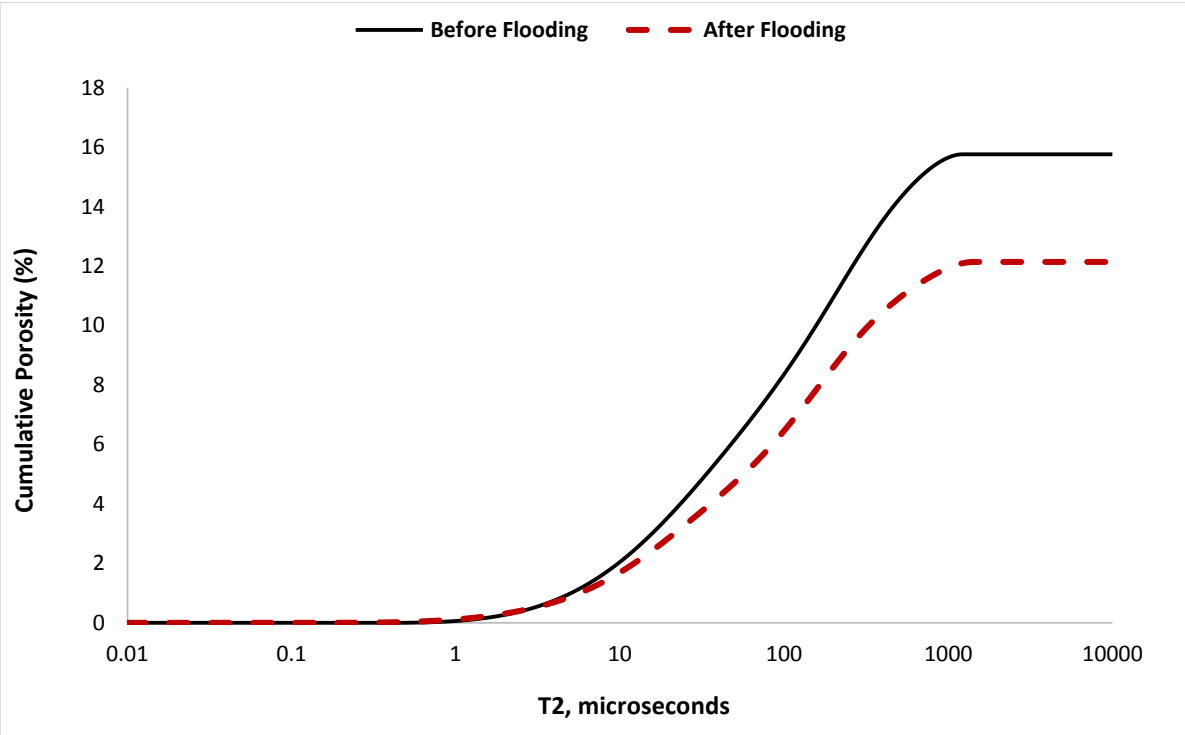

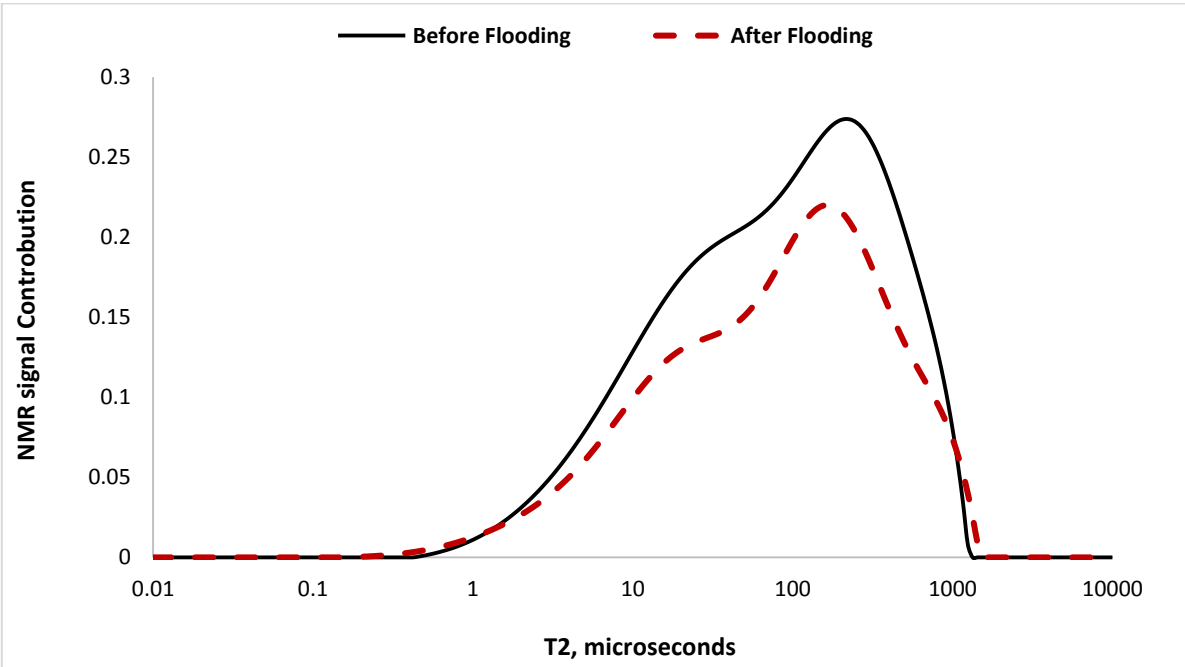

Figure 4.57. Change in the cumulative porosity (top) and incremental NMR T2 distribution (bottom) of Sample INL-2 outlet part before and after flooding. The overall NMR porosity of the sample decreased. Its NMR T2 distribution shifted to the left, indicating that the sample's pore sizes have become smaller after flooding. Due to the similarities between this sample and Sample INL-2 inlet part (e.g. same sample type, mineralogy, etc.), the NMR data show very similar initial trends and then almost identical subsequent alterations for the two samples.

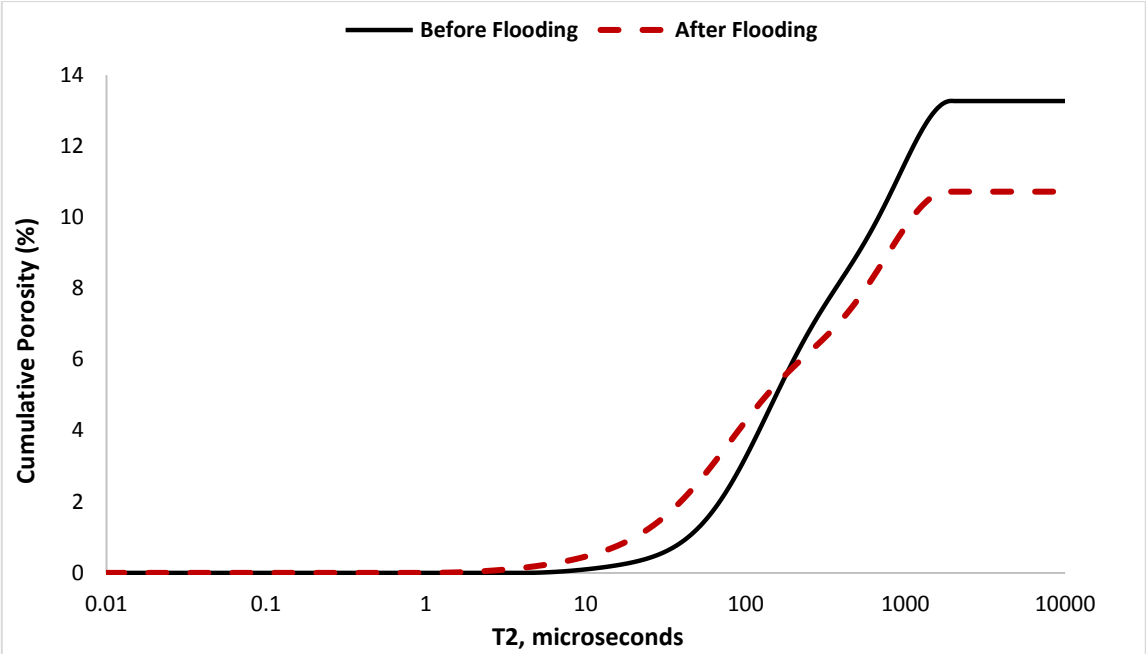

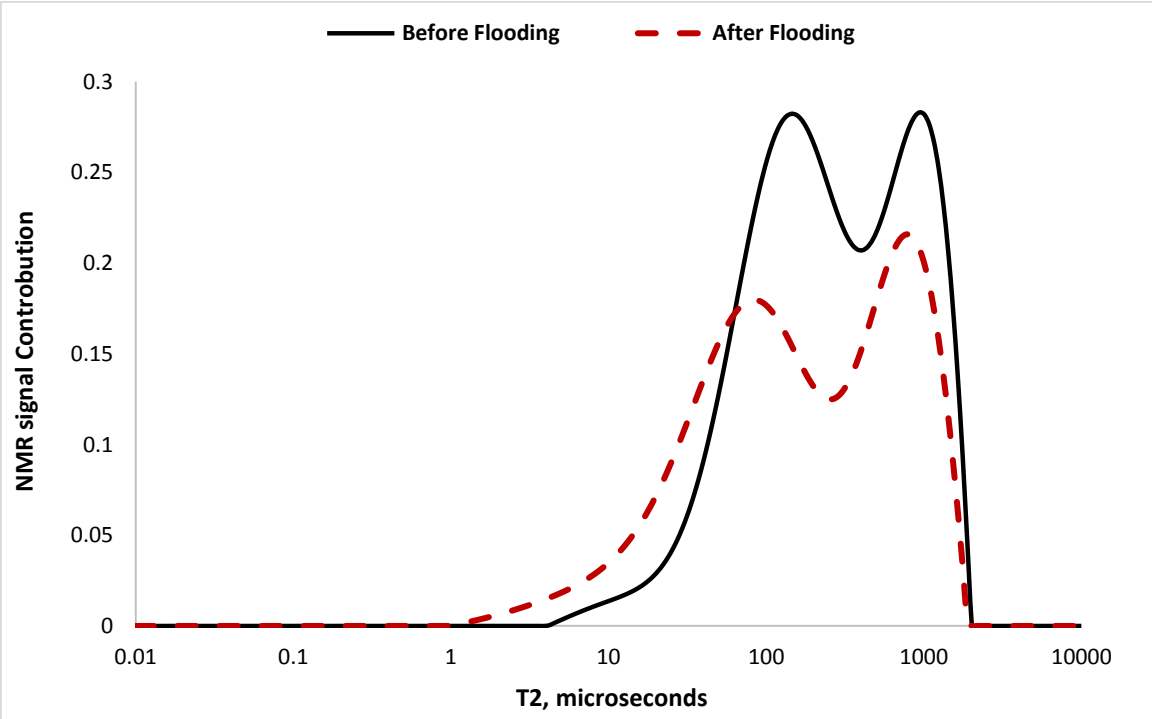

Figure 4.58. Change in the cumulative porosity (top) and incremental NMR T2 distribution (bottom) of Sample GD-1 before and after flooding. The overall NMR porosity of the sample decreased. Its NMR T2 distribution shifted to the left, indicating that the sample's pore sizes have become smaller after flooding.

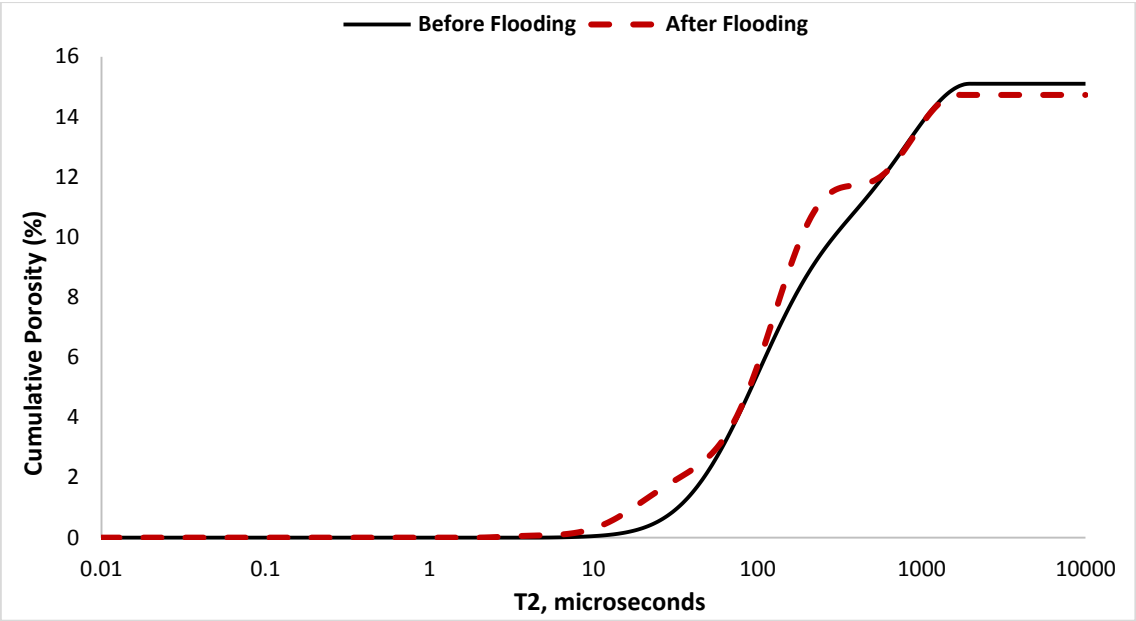

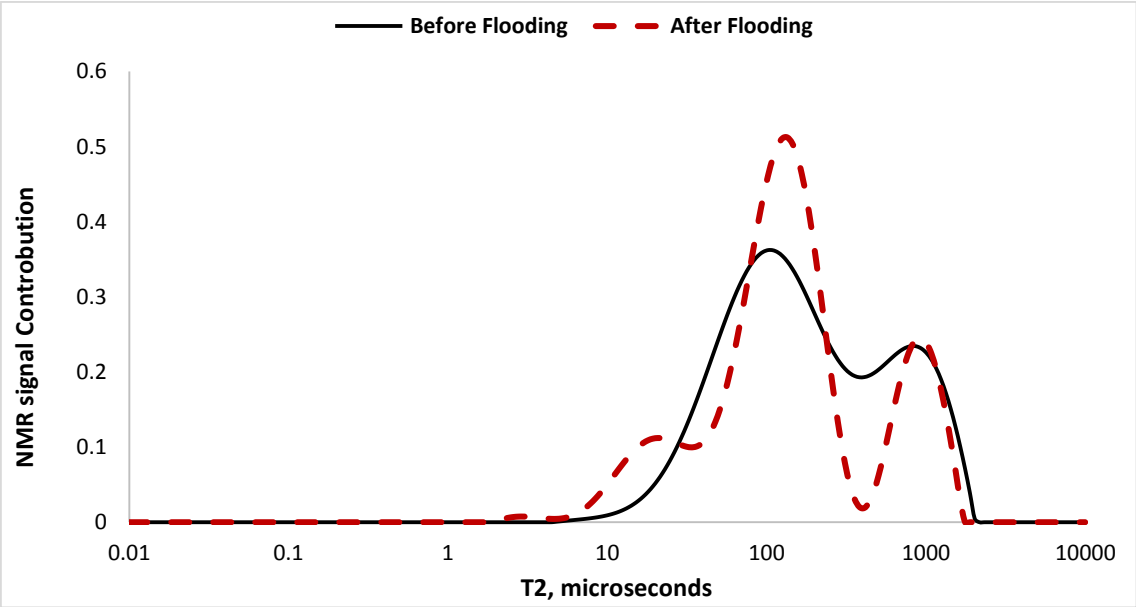

Figure 4.59. Change in the cumulative porosity (top) and incremental NMR T2 distribution (bottom) of Sample INL-1 before and after flooding. The NMR porosity of the sample decreased slightly. Its NMR T2 distribution shifted slightly to the left, indicating that the sample's pore sizes have become smaller after flooding.

4.4.3. Water-Alternating-Gas (WAG) flooding

Included in figures 4.60-4.62 are the NMR-derived pore size distribution (in the form T2 distributions) and cumulative porosity for all samples subjected to the WAG flooding at their pre- and post-flood states. For the two samples of GD-11 and VS-2, a decrease in the overall porosity is apparent. For Sample INL-11, however, the total porosity has not changed after flooding. Furthermore, a shift in the pore size distribution towards smaller pore sizes (i.e. smaller T2 values) is evident for all the post-flood samples.

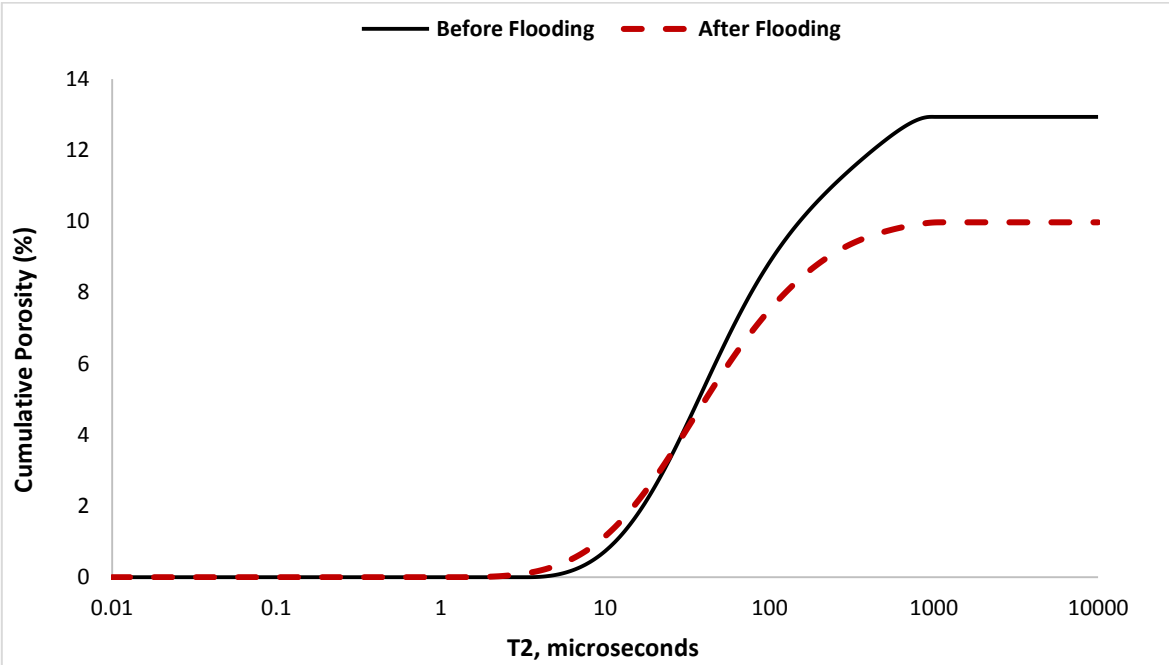

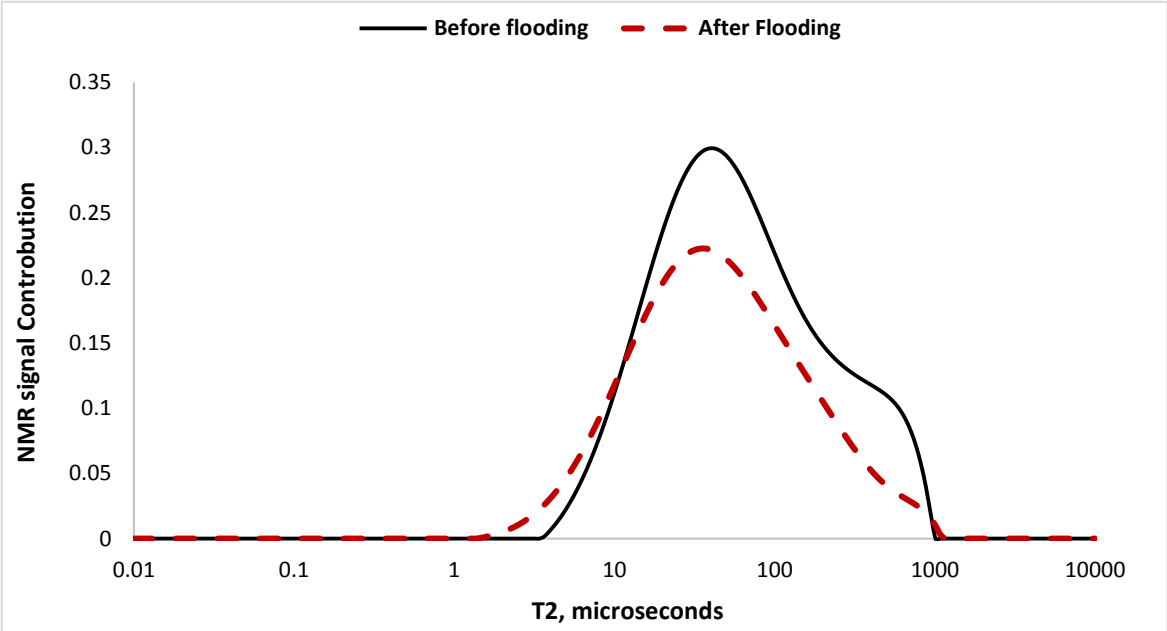

Figure 4.60. Change in the cumulative porosity (top) and incremental NMR T2 distribution (bottom) of Sample VS-2 before and after flooding. The NMR porosity of the sample decreased. Its NMR T2 distribution shifted slightly to the left, indicating that the sample's pore sizes have become smaller after flooding.

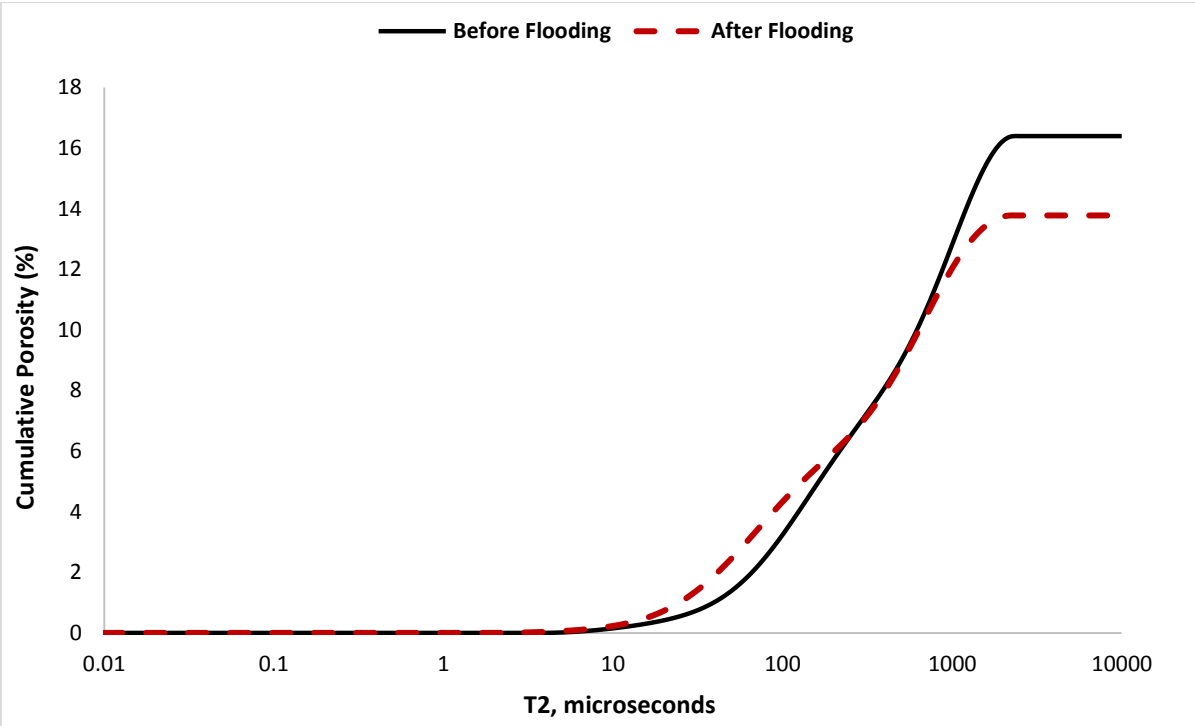

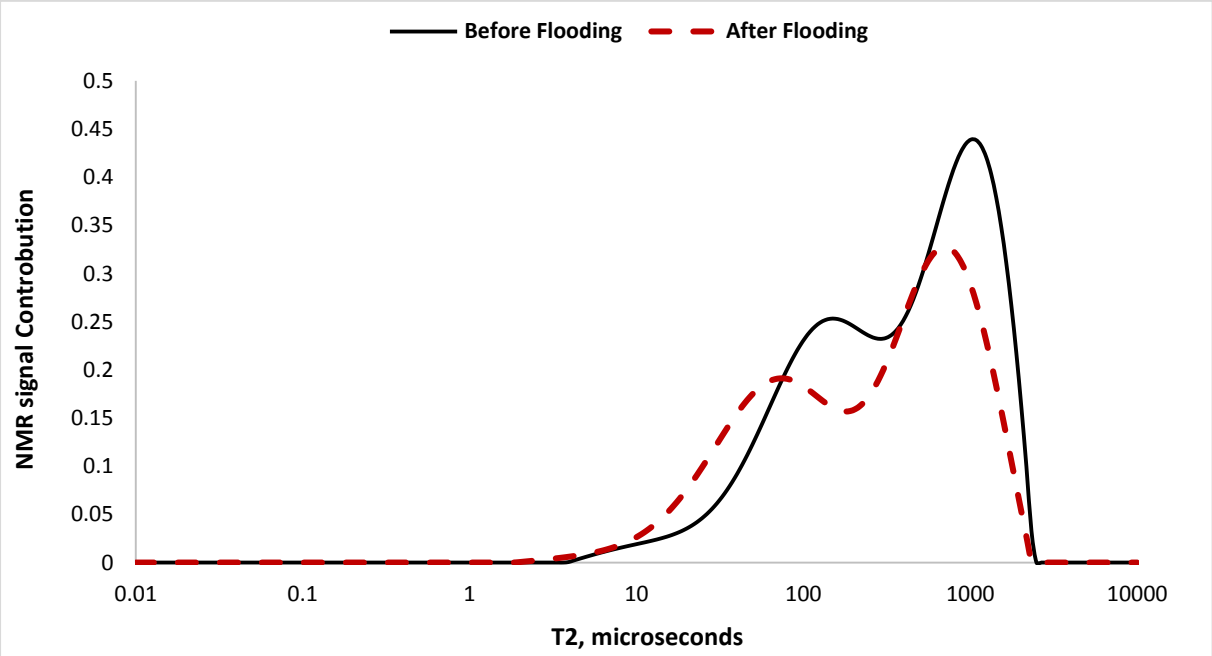

Figure 4.61. Change in the cumulative porosity (top) and incremental NMR T2 distribution (bottom) of Sample GD-11 before and after flooding. The NMR porosity of the sample decreased. Its NMR T2 distribution shifted slightly to the left, indicating that the sample's pore sizes have become smaller after flooding.

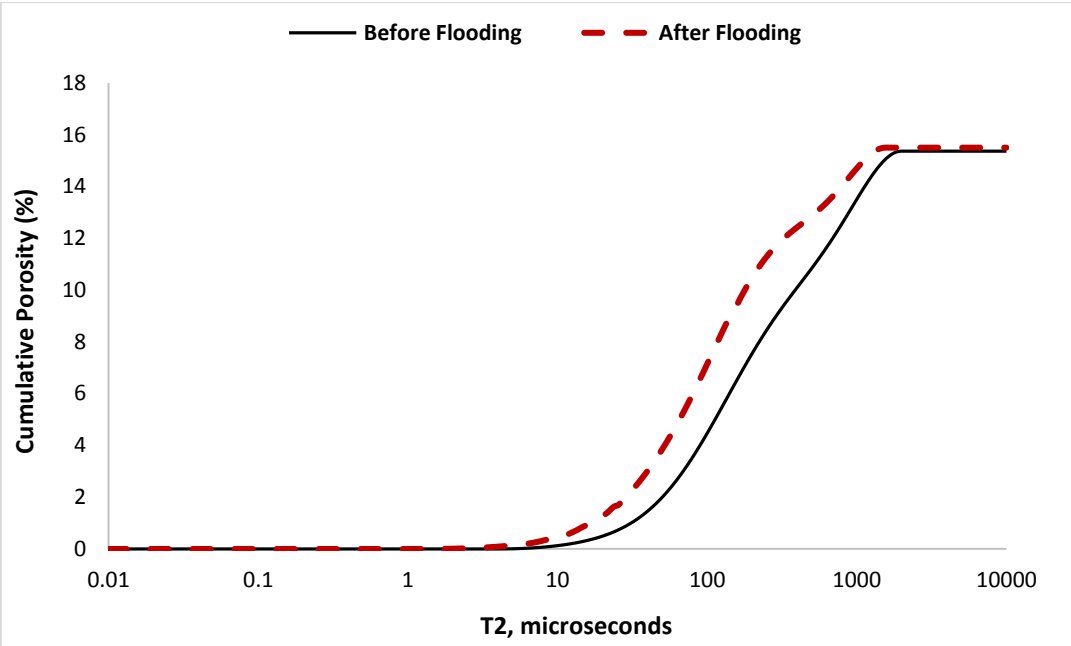

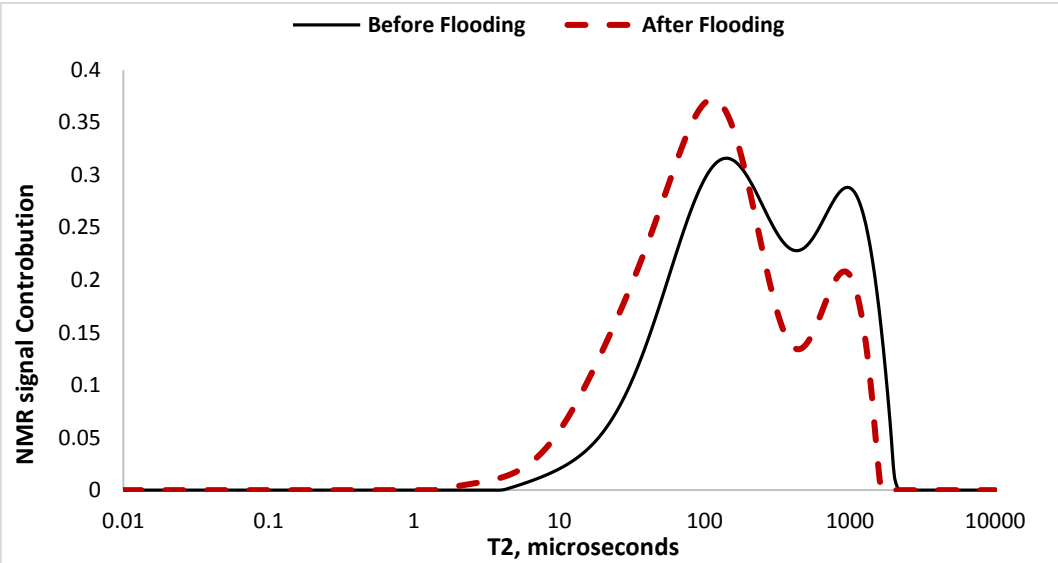

Figure 4.62. Change in the cumulative porosity (top) and incremental NMR T2 distribution (bottom) of Sample INL-11 before and after flooding. The NMR porosity of the sample showed almost no change. Its NMR T2 distribution shifted slightly to the left, indicating that the sample's pore sizes have become smaller after flooding.

4.5. Scanning Electron Microscopy (SEM)

As indicated before, SEM images were obtained for selected samples (VS-1, SC-2, SC-1, and TC-2, SD-1, CH-1 and INL-2) to evaluate any microstructural changes (mineral dissolution/precipitation, asphaltene and/or resin precipitation) that the sample may undergo during the flooding. Since full size core samples could not be accommodated by the SEM instrument, relatively thin disks (5 mm thickness, 38 mm diameter) were cut from the samples and placed in different locations along their length (i.e. in the middle, inlet or outlet of the core

samples) during flooding. For comparison purposes, the surface of the disks was imaged before flooding and then again after the flooding once they were cleaned and dried. In some experiments, cold toluene was used to clean the samples in order to remove any remaining oil and preserve any asphaltene and resin which may have precipitated. The comparison of the pre and post-flood SEM images yielded different results depending on the sample characteristics and the flooding scheme followed. Some post-flood images revealed signs of significant dissolution of carbonate minerals in the inlet or outlet regions of some samples or signs of mineral precipitation or fins migration in the middle section of a sample. From other images, asphaltene precipitation could be observed in the samples subjected to the EOR floods.

4.5.1. Live brine flooding

Figures 4.63-4.69 show the SEM images obtained for samples VS-1, SC-2, TC-2, SC-1 and CH-1. Upon close observation, the images obtained for samples VS-1 and SC-2 (Figures 4.63-4.65) clearly show the deformation resulting from the significant dissolution of carbonate minerals at the inlet and outlet of the core samples. Furthermore, the images obtained from the inlet of Sample TC-2 (Figure 4.66) reveals excessive dissolution of carbonate minerals at the location and vicinity of a pre-existing fracture. This extensive dissolution is caused by high brine flow through the fracture, thus altering its microstructural features and, in general, its entire surface. In addtion, for Sample SC-1, the SEM images generated for the disk placed in between its inlet and outlet plugs (Figures 4.67 and 4.68) reveals signs of mineral precipitation and migration of carbonate fines.

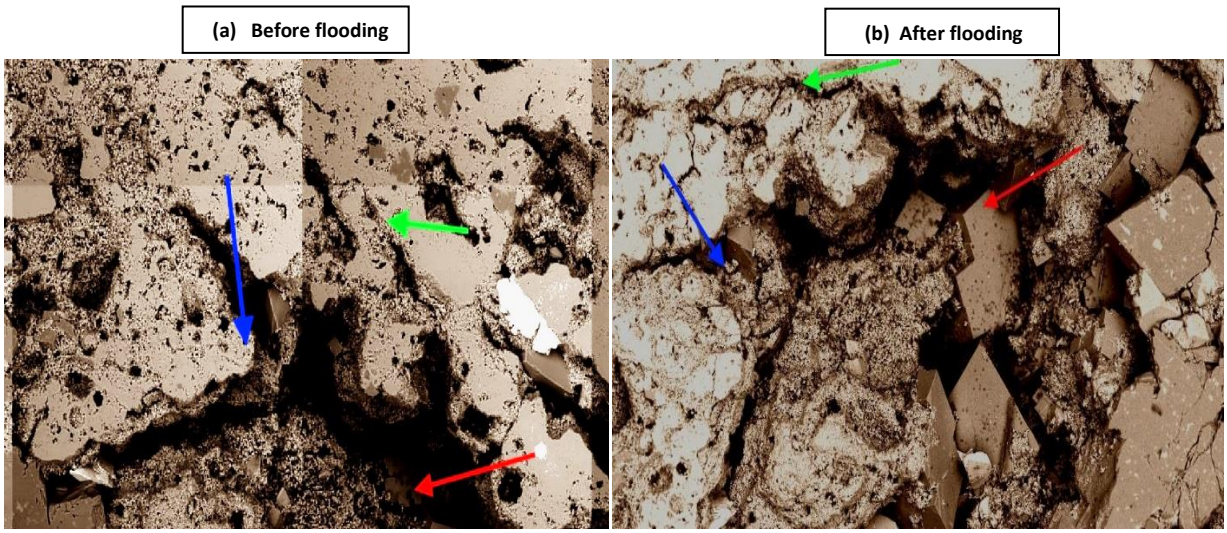

Figure 4.63. SEM images on sample VS-1 at the inlet of the core: (a) before flooding and (b) after flooding show signs of excessive dissolution of carbonate minerals, resulting in highly profound alterations to the pore structure of the the post-flood rock sample.

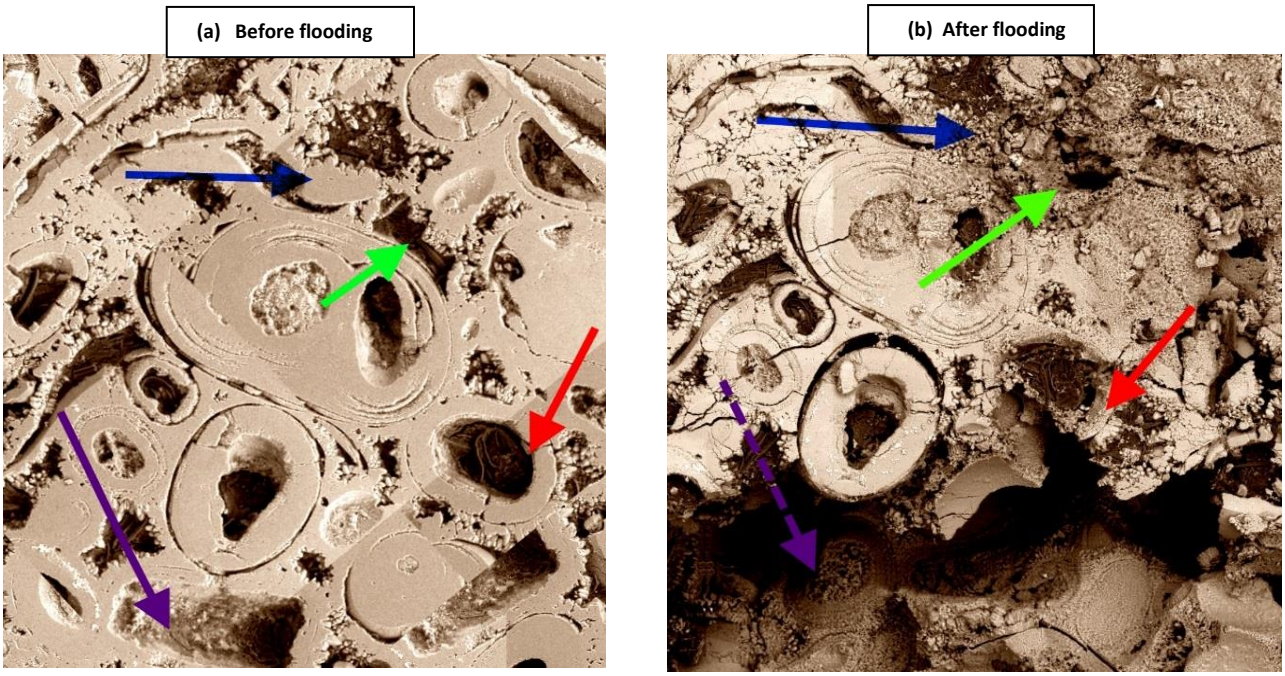

Figure 4.64. SEM images on sample SC-2 at the outlet of the core: (a) before flooding and (b) after flooding show destructive damage caused by the massive dissolution of carbonate minerals, resulting in highly profound alterations to the pore structure of the post-flooding that show signs of mineral precipitation.

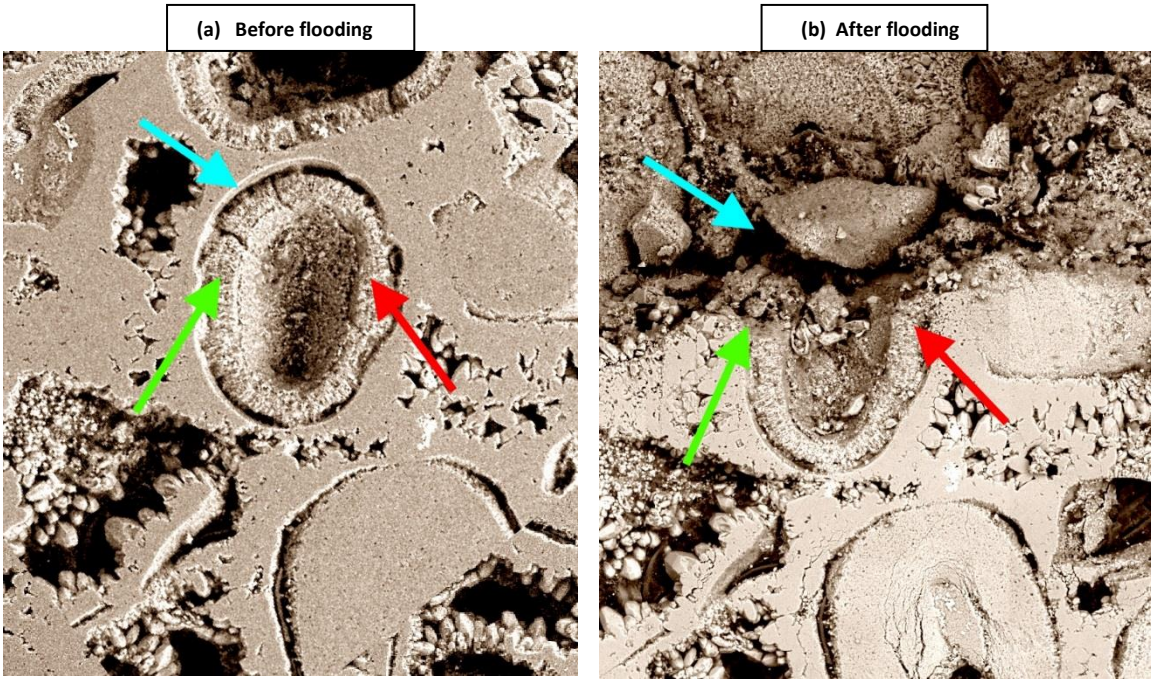

Figure 4.65. SEM images on sample SC-2 at the outlet of the core: (a) before flooding and (b) after flooding show massive dissolution of carbonate minerals, which cause changes in the pore structure of the post-flood rock sample.

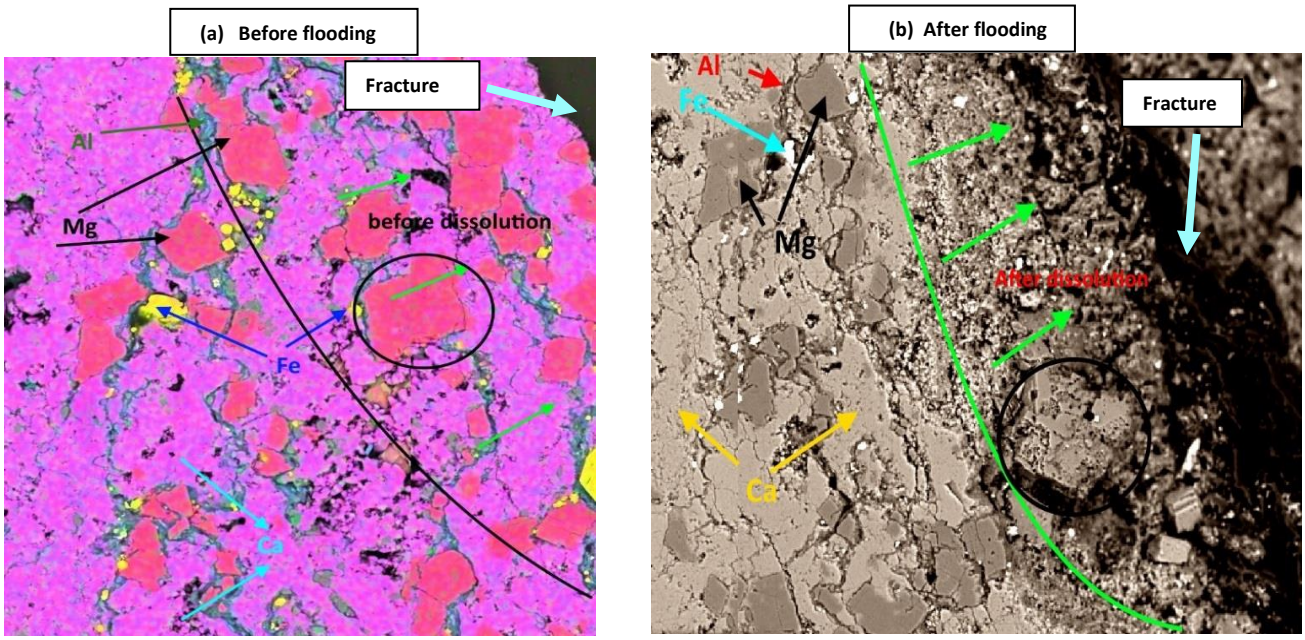

Figure 4.66. SEM images on sample TC-2 at the inlet of the core: (a) before flooding and (b) after flooding show signs of dissolution of carbonate minerals at the fracture location and its vicinity, altering the pore-scale structures and the entire surface of the fracture of the post-flood rock sample.

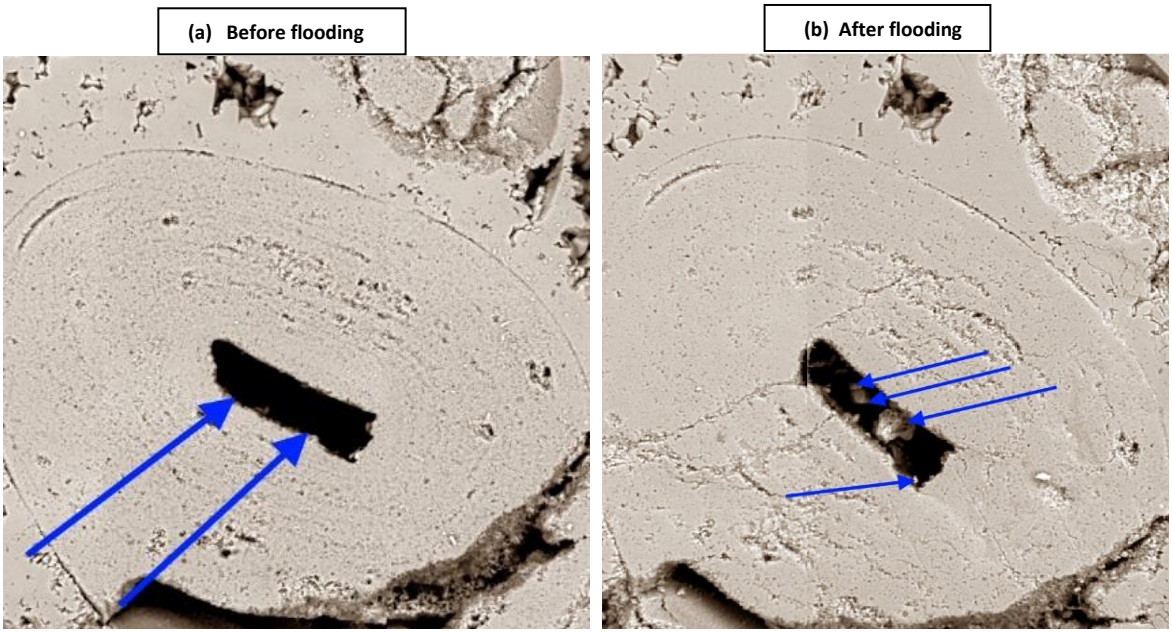

Figure 4.67. SEM images on sample SC-1 at the middle of the core: (a) before flooding and (b) after flooding show signs of mineral precipitation and possible migration of carbonate fines.

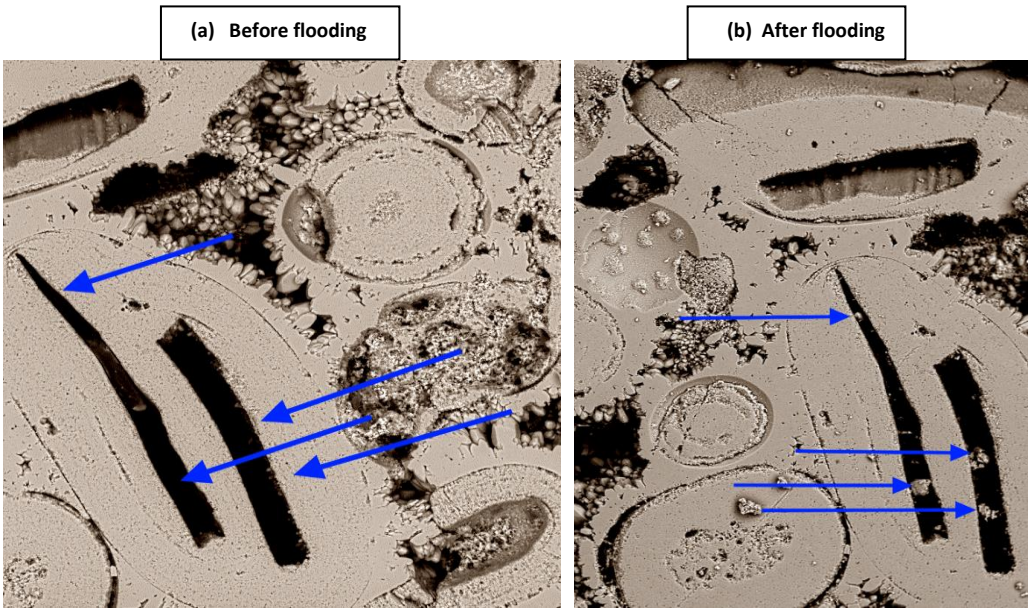

Figure 4.68. SEM images on sample SC-1 at the middle of the core: (a) before flooding and (b) after flooding show signs of mineral precipitation and possible migration of carbonate fines.

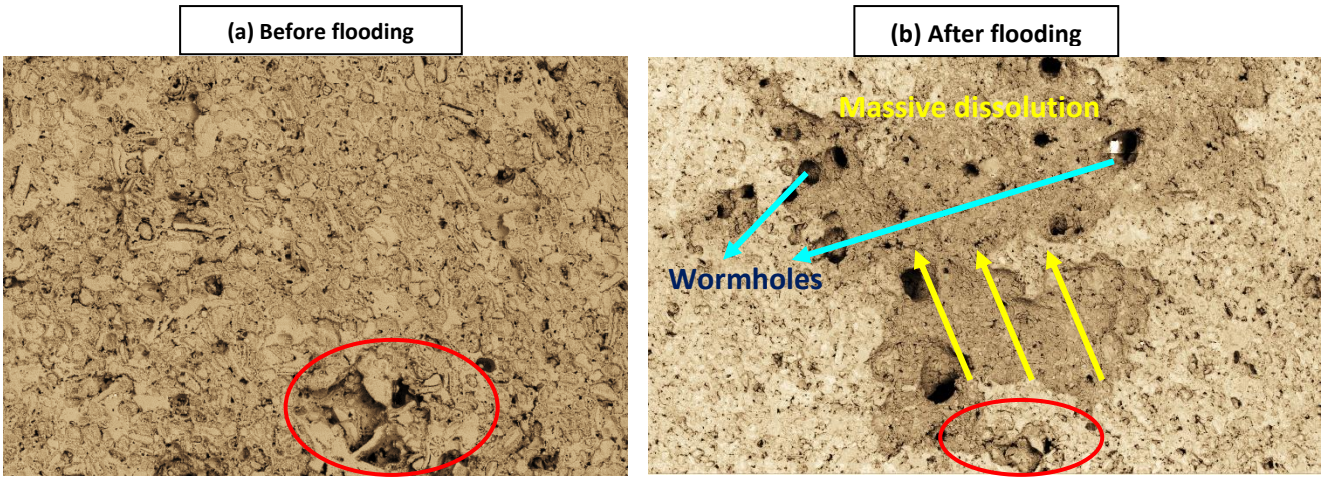

Figure 4.69. SEM images on sample CH-1 at the middle of the core: (a) before flooding and (b) after flooding show massive dissolution of carbonate minerals, which cause changes in the pore structure of the post-flood rock sample.

4.5.2. CO_2-EOR flooding

Figures 4.70 - 4.73 present the SEM images obtained for samples SD-1 and INL-2 using thin disks placed at the middle of the two samples. Upon close observation the images show signs of mineral precipitation as well as the deposition of loose mineral particles (i.e. fines migration) (Figure 4.71). Asphaltene precipitation is also evident, but no obvious signs of mineral dissolution could be found which may indicate that dissolution was not a dominant process in these samples. To confirm the presence of asphaltene precipitation, the disk belonging to Sample SD-1 was cleaned in cold toluene and then examined in the SEM. The cleaning was performed in four stages. The initial cleaning resulted in an oily residues on the surface, so the

sample was cleaned again to remove these residues. This process was repeated until no further changes were observed. The remaining dark areas, as shown in Figure 4.73, are therefore insoluble in cold toluene and expected to be asphaltene. To confirm that the deposits were indeed asphaltene, their composition was then checked with energy-dispersive x-ray spectrometry (EDS). The comparison of the EDS results from point 1, which is on a precipitate, and point 4, which is on the background dolomite, show that the precipitate is composed mostly of carbon and oxygen, with some traces of sulphur which are typical elements found in asphaltene.

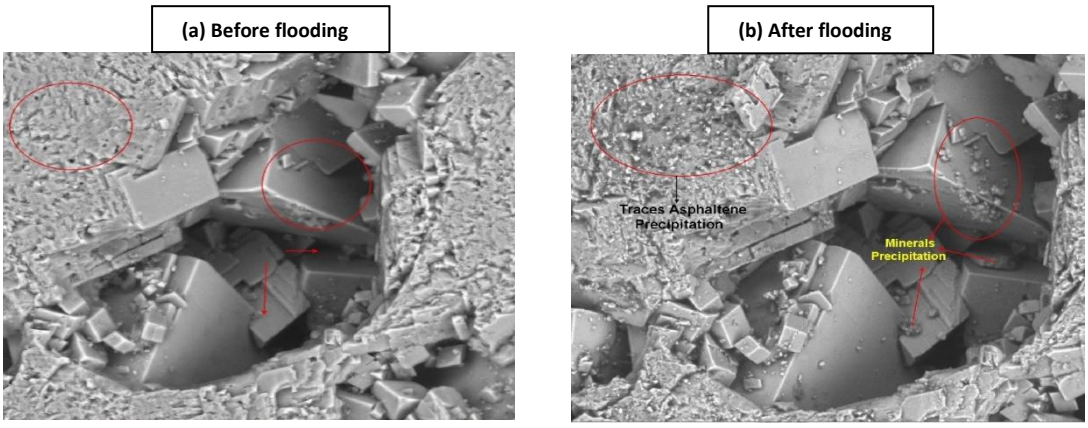

Figure 4.70. SEM images taken from a thin disk of Sample SD-1: (a) before flooding and (b) after flooding, showing evidence of mineral precipitation and traces of asphaltene deposition.

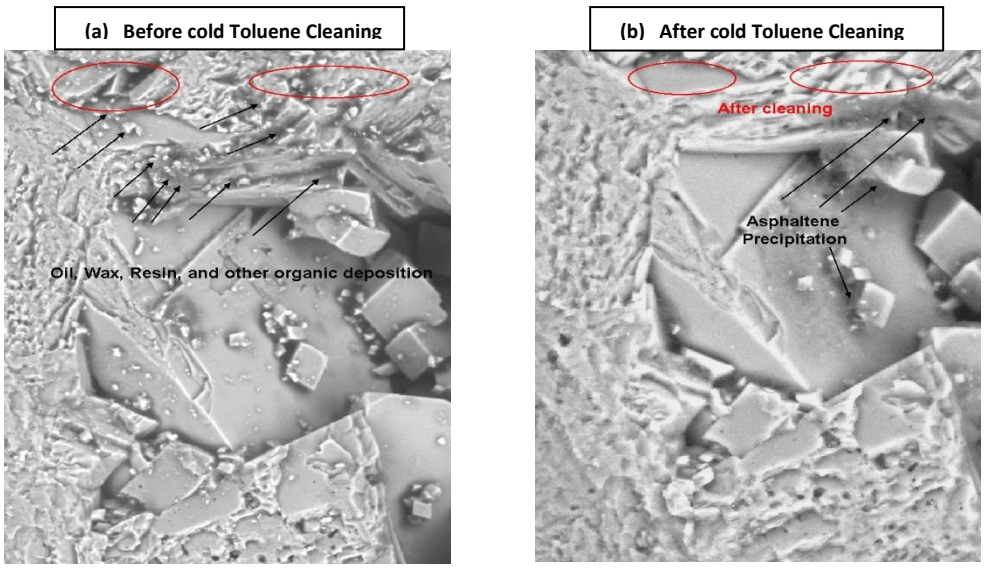

Figure 4.71. SEM images taken from a thin disk of Sample SD-1: (a) before cold toluene cleaning and (b) after cold toluene cleaning clearly showing signs of asphaltene precipitation.

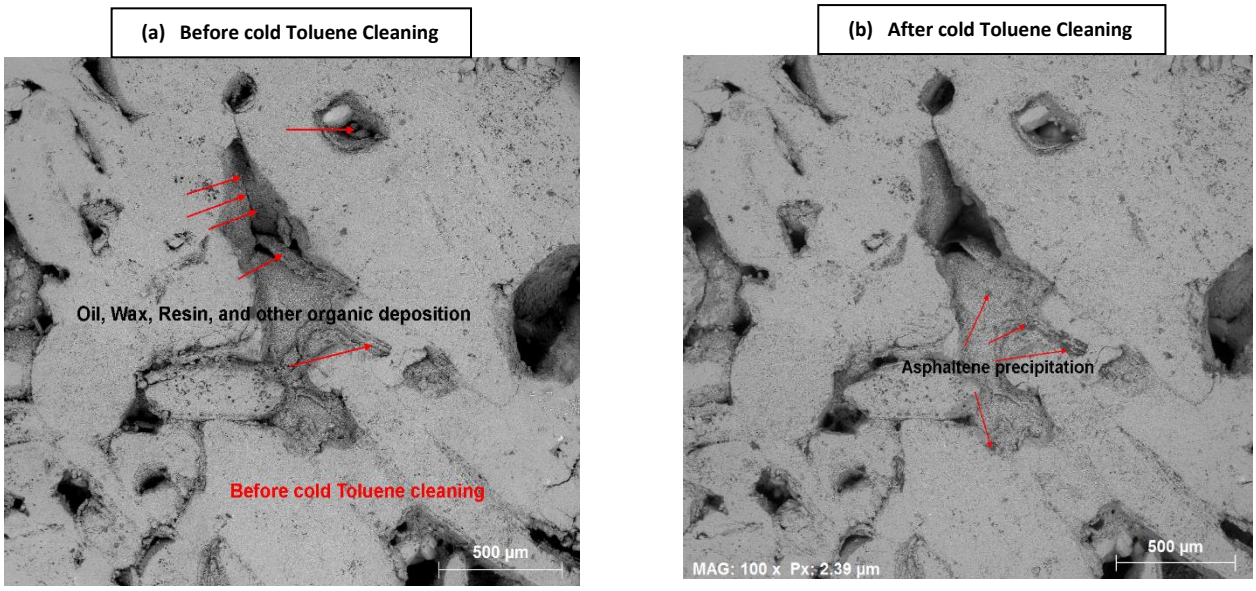

Figure 4.72. SEM images taken from a thin disk of Sample INL-2: (a) before cold toluene cleaning and (b) after cold toluene cleaning showing signs of asphaltene precipitation.

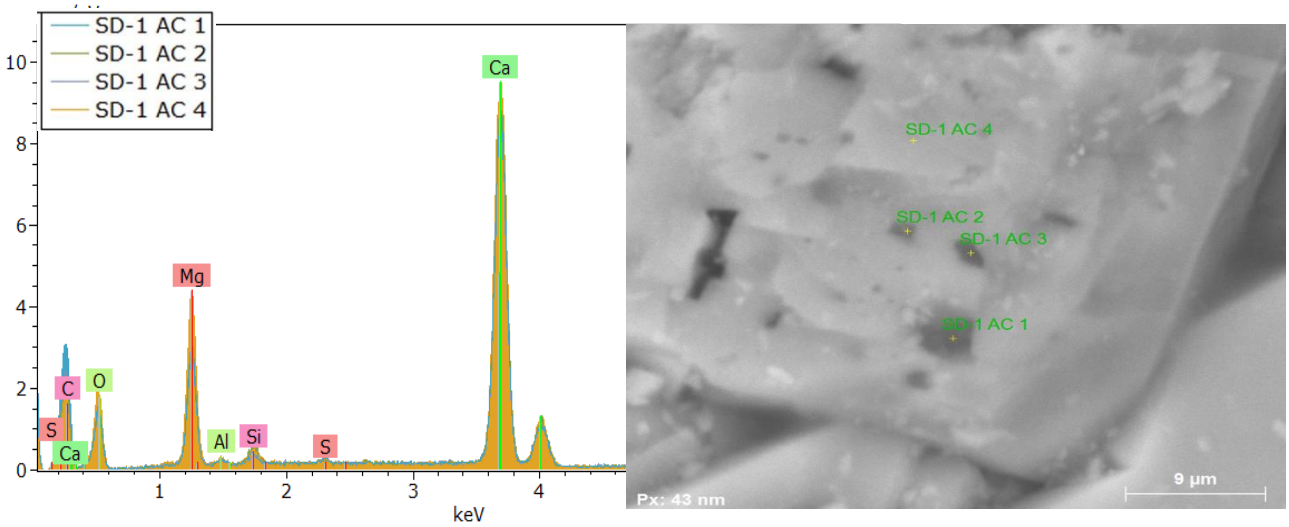

Figure 4.73. SEM images of sample SD-1 showing dark precipitates that are insoluble in cold toluene. A comparison of the EDS results obtained for these dark areas (points 1 to 3) with the background dolomite on which they sit, showing that the precipitates are mostly carbon and oxygen.

4.6. Effluent fluid chemistry analysis

To gain a better undersatnding of the results obtained from various experiments, a number of effluent fluid samples were taken during some of the core floods whose compositions were then anlysed. The fluid samples taken included both brine and crude oil samples.

4.6.1. Effluent brine samples

The effluent brine samples were taken at different times during some of the experiments. Brine analysis was conducted using Inductively Coupled Optical Emission Spectroscopy (ICP-OES) using a Varian Vista Pro axial instrument. The results of the analysis are presented in tables 4.8-4.10. As can be seen, in general, the data show an increase in the concentrations of calcium (Ca), magnesium (Mg) and sulphur (S) in the effluent brine when compared with the original brine that included 2100 mg/L of Ca and 210 mg/L of magnesium (Mg).

Table 4. 8. Results of the effluent brine analysis (Ca and Mg) collected during live brine flooding conducted on samples VS-1, SC-1 and TC-2.

Sample ID	Sampling time (mins)	Elemental composition of the brine after flooding		Net molar increase in brine after flooding		Molar ratio
		Calcium (Ca) mg/L	Magnesium (Mg) mg/L	Ca	Mg	Ca:Mg
VS.1	30	2300	240	0.00499	0.00124	4.04
VS.1	60	2100	250	0	0.00165	0.00
VS.1	90	2100	240	0	0.00124	0.00
SC-1	30	2300	250	0.00499	0.00165	3.03
SC-1	60	2400	240	0.00749	0.00124	6.06
SC-1	90	2300	240	0.00499	0.00124	4.04
TC-2	30	2300	240	0.00499	0.00124	4.04
TC-2	60	2100	230	0	0.00082	0.00
TC-2	90	2300	240	0.00499	0.00124	4.04

Table 4. 9. Results of the effluent brine analysis (Ca, Mg and S) collected during live brine flooding conducted on samples VS-3, VS-4 and TC-1.

Sample ID	Sampling time	Composition of the effluent brine		
		Calcium (Ca) mg/L	Magnesium (Mg) mg/L	Sulphur (S) mg/L
VS-3	30min	2300	420	1000
VS-3	8 hrs	2200	410	500
VS-3	15hrs	2400	420	450
VS-4	30min	2200	450	850
VS-4	8 hrs	2100	420	550
VS-4	15hrs	2200	420	450
TC-1	30min	2200	380	Not analysed
TC-1	8 hrs	1200	190	Not analysed
TC-1	15hrs	2400	310	Not analysed

Table 4. 10. Results of the effluent brine analysis (Ca and Mg) collected during WAG flooding conducted on samples VS-2, GD-11 and INL-11

Sample ID	WAG Cycle number	Composition of the effluent brine	
		Calcium (Ca) mg/L	Magnesium (Mg) mg/L
VS-2	1	2500	250
VS-2	5	2100	210
VS-2	8	2000	190
VS-2	10	2600	270
GD-11	2	2100	370
GD-11	7	2000	400
GD-11	11	2000	380
GD-11	12	2300	450
INL-11	4	2100	240
INL-11	5	2100	230
INL-11	10	2300	240
INL-11	13	1800	190
INL-11	16	2300	250
INL-11	18	2300	240

4.6.2. Crude oil samples

A modified ASTM method (D6560) was used to determine the asphaltene content in the original crude oil, as well as the effleunt oil during some of the CO_2-EOR flooding experiments. The objective of this analysis was to evaluate any possible change in the asphaltene concentration of the oil that may be caused by the precipitation of some of the asphaltene originally present in the crude oil. To analyse an oil sample it was first mixed with hexane and sonicated. This mixture was subsequently filtered through sodium sulphate and ashless floc and washed with ambient hexane to remove the oil. Hot toluene was then used to wash and remove the precipitated asphaltenes. These eluates were then dried and weighed. Table 4.11 reveals the concentration of wax, resin and asphaltene in the original and some effluent oil samples taken during some of the core flood experiments.

Table 4. 11. Wax, resin and asphaltene concentrations in original and effluent oil samples.

Sample	wax, resin, and asphaltene wt%	Asphaltene wt%
Original oil used	9.945	0.0754
Oil recovered at an early time	6.346	0.0611
Oil recovered at the middle time	4.74	0.0584
Oil recovered at a later time	3.24	0.0455

Chapter 5

5. Interpretations and Discussions

As covered in details in the previous chapters, 18 carbonate samples (Five composite cores each consisting of two core plugs and 13 individual plugs (23 plugs in total) were used in this research. The overall experimental procedure started with basic routine core analysis which was then followed by core flooding experiments conducted using three different flooding scenarios of live brine flooding, CO_2-EOR flooding using continuous CO_2 injection and CO_2 WAG flooding in which CO_2 was injected in alternation with formation water. There were also a number of critical complimentary measurements/analysis conducted (e.g. X-ray CT imaging, NMR measurements, SEM scans, etc.) whose results were believed to be helpful when analysing the outcomes of the core-flooding experiments.

The primary objective of this chapter is to present a detailed discussion and interpretation of the experimental results presented in Chapter 4. The contents of this chapter are categorised and presented at the highest level according to the three flooding scenarios referred to above. As indicated earlier in chapters 3 and 4, different groups of samples were flooded using each of the flooding scenarios. Since the results obtained, to some degree, depend on the specific properties of each sample group, the interpretation and discussion of the results obtained under each flooding scenario are further dvided and presented for each sample group separately. For each sample group also, depending on the response of a sample to the flooding process, its results are discussed on its own or together with the other alike samples.

As discussed in details in Chapter 2, during CO_2 or live brine injection into carbonate rocks, a number of geochemical interactions may occur between the fluids and/or fluid mixtures (either injected or in-situ created) and the host rock formation. Subsequently, such reactions are often followed by alterations to the petrophysical properties of the rock. During core flooding experiments involving CO_2 in particular, any observed changes in the permeability, porosity and other petrophysical properties of the post-flood samples can be largely attributed to the three mechanisms of mineral dissolution, mineral precipitation and physical compaction (Oomole et al. 1983; Izgec et al. 2006; Elkhoury et al. 2013; Smith et al. 2013; Kono et al. 2014; Luhmann et al. 2014; Tutolo et al. 2014). The occurrence and the extent of the effects of these mechanisms on a sample depend on the exact mineral composition, presence of core-scale heterogeneities and the original textural features of the sample and therefore, may vary

from one sample to the next. In other words, whether, for a particular sample, a mechanism becomes dominant or its effects become significant, depends on the nature, mineralogy and the presence of any special petrophysical features (e.g. heterogeneities, fractures) in the pre-flood sample. Much of the discussions presented in the upcoming sections of this chapter are to determine how these three mechanisms and their interplay may have caused the petrophysical alternation in the post-flood samples as revealed by the complementary measurements conduced.

It is worth noting that, as discussed in Chapter 2, two more mechanisms which can alter the properties of rock samples during flooding are fines migration and precipitation of solid particles such as asphaltenes out of the crude oil (if it is used during the flooding). The precipitation of asphaltene was indeed detected in some of the experiments conducted in this work. Furthermore, although due to the absence of susceptible minerals (i.e. clay minerals such as kaolinite), migration of clay fines was believed not to have occurred in the flooding experiments conducted in this work, carbonate fines generated and released by the mineral dissolution and mechanical deformation mechanisms were detected in some of the post-flood SEM images. Therefore, asphaltene precipitation and migration of carbonate fines are considered and discussed as two more mechanisms behind the changes observed in some of the core samples.

5.1. Live brine flooding

5.1.1. Sample group 1 (limestone cores)

5.1.1.1. Samples VS-1, SC-2 and VC-2

Samples VS-1, SC-2 and VC-2 consisted mainly of calcite, with concentrations of 93.7%, 97.4% and 96.9%, respectively, with the remainder being low concentrations of several other minerals, as presented in Table 4.1. As evident from the data presented in Table 4.2, all three post-flood cores show significant increase in their permeability and some decrease in their dry weight, which is believed to have been caused by the dissolution and removal of calcite during flooding. In support of this hypothesis, the chemical analysis of the effluent brine for Sample VS-1 (Table 4.8) indicates that the concentration of calcite in the effluent brine increased by 200 mg/L or 0.00499 mol/L in the early times of the flooding experiment.

The evolution of differential pressures across a core sample agnaist pore volume of live brine injecetd provides further insight into the changes that the core sample may undergo during the flooding process. An example of such data is plotted in Figure 5.1 for Sample VS-1. As can be seen, the differential pressure decreases significantly (from over 45 kPa to almost 0) as the live

brine is continuously injected through the sample. For this sample, the dramatic change in the differential pressure, as will be discussed in more details later, is due to the formation of a wormhole in the sample during the flood. In general, the flow of the injected live brine would initially follow any existing preferential flow path(s) through wider pore channels and more porous areas of the samples as they present the least resistance to the flow. The high brine flow rate through such flow paths would increase the dissolution rate, widening them further and eventually resulting in the formation of wormholes.

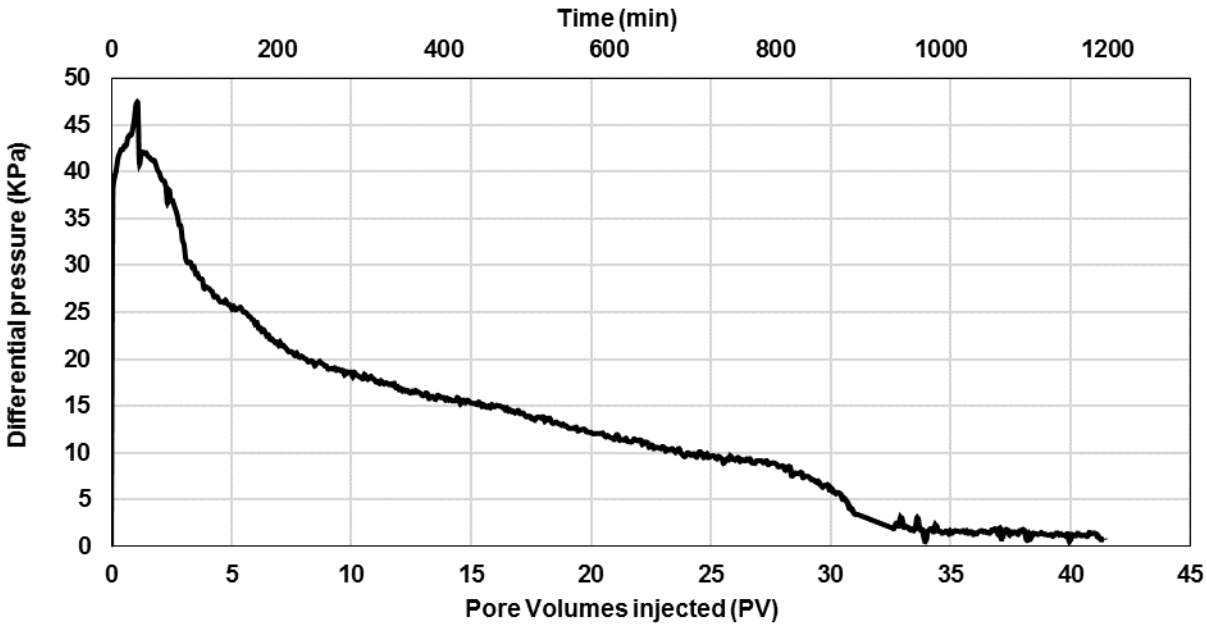

Figure 5.1. The evolution of differential pressure across Sample VS-1 during the flooding. The differential pressure decreases as the sample permeability increases under the effect of mineral dissolution.

The mineral dissolution and precipitation can be further examined by comparing the pre and post-flood SEM images generated for some of the samples. Figures 4.63, 4.64 and 4.65 present one set of such images for Sample VS-1 and two sets for Sample SC-2, respectively. In Sample VS-1, the disk used for SEM analysis was located close to its inlet, while for Sample SC-2, the disk was located close to its outlet. The images clearly reveal significant dissolution of the calcite mineral at the inlet of Sample VS-1 and outlet of Sample SC-2, resulting in highly pronounced alterations to the pore structure of the post-flood rock samples. Also, the images show that, in particular, for Sample SC-2, some micro-fractures have emerged after the core-flood experiments. Very likely, these fractures were created under overburden stress, enhanced by the weakening of the rock's strength by mineral dissolution. It is worth noting that these fractures may have also contributed towards the observed increase in the sample's permeability referred to earlier.

As mentioned in chapters 3 and 4, X-ray CT imaging was used to qualitatively evaluate any changes to the structure of the cores at the core-scale. Figure 4.15 shows a 2D view of the X-ray images generated for Sample VS-1 before and after flooding. Significant mineral dissolution and formation of wormhole features which extended from the sample's inlet to its outlet is clearly evident in these images. Similar behaviours can be observed from samples SC-2 and VC-2, as evident from figures 4.16 and 5.2. In fact, as can be seen from Figure 5.2, Sample VC-2 almost disintegrated due to excessive mineral dissolution and weakening of its structure.

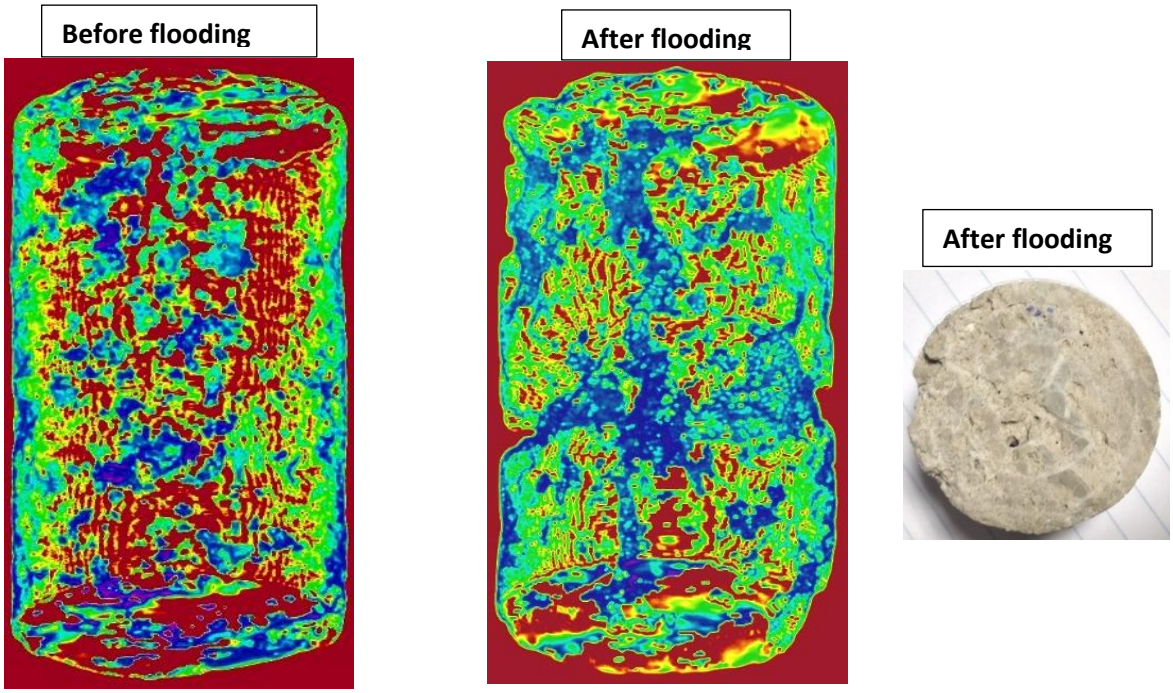

Figure 5.2. 2D view of the 3D X-ray images and a photo of the inlet face of Sample VC-2. Both show signs of significant dissolution in the sample. The overall texture of the sample seems to have been distorted in the post-flood X-ray image under the effect of dissolution and compaction mechanisms.

As indicated in earlier chapters, during the X-ray CT scanning, each sample in its dry state was divided into several hundred slices of each 0.4 mm thick. The CT values extracted from these X-ray scans were used as a means of qualitatively evaluating the average bulk density distribution along the length of the sample. Figures 4.1, 4.2 and 4.4 show a comparison between the pre and post-flood CT number distributions along the length of samples VS-1, SC-2 and VC-2, respectively. As can be seen, for samples VS-1 and SC-2, the bulk density decreased consistently at all locations along the length of the samples after their exposure to the live brine. This change can be attributed to the dissolution and removal of the carbonate minerals during the flood. Once again, the brine effluent chemistry of Sample VS-1 supports the occurrence of

this process (Table 4.8). A similar consistency is not apparent in the data provided for Sample VC-2 in Figure 4.4. Possibly, for this sample, at some locations, due to the excessive dissolution and weakening of the sample, any reductions in the bulk density caused by dissolution was counteracted and occasionally surpassed by the effect of the physical compaction. The effect of compaction is evident from a comparison between the pre and post-flood dimension measurements as provided in Table 4.2. A comparison of the pre and post-flood X-ray images, in Figures 4.15 and 4.16 in particular, confirms that the injection brine would tend to establish flow paths through wider pore channels and more porous areas of the samples and eventually, widening them further into wormholes.

One observation common across all three samples, which may be contrary to the permeability enhancements discussed earlier, is the slight reduction in the overall porosity of the samples as reported in Table 4.2. Furthermore, as can be seen from Figure 4.40, for Sample VS-1, the pore size distribution (represented by NMR T2 spectrum) of this sample after flooding is shifted towards smaller values, meaning that its overall pore sizes became smaller. In fact, the same behaviour is apparent in Figures 4.41 and 4.43 for the other two samples (SC-2 and VC-2) whose results are discussed in this section. This observation, once again, supports the physical compaction of the samples (Khather et al., 2017). For instance, as can be seen in Table 4.2, the length of sample SC-1 was reduced from 5.79 cm to 5.73 cm and its outside diameter decreased from 3.81 cm to 3.74 cm. For samples VS-1 and VC-2, similar decreases were only detected in their outside diameters.

Based on the experimental evidence, the two mechanisms of mineral dissolution and physical compaction are believed to have influenced the behaviour of samples VS-1, SC-2 and VC-2 during the flooding experiments. These two mechanisms commonly work against each other, while altering the petrophysical properties of the rock samples (Khather et al. 2017). For these three samples, mineral dissolution seems to have stronger effects on post-flood permeabilities, while the compaction seems to control the outcome with regards to the porosities and pore size distributions.

5.1.1.2. Sample TC-2

Sample TC-2 is also a limestone sample, with 9.1% porosity and 0.41 mD permeability. Upon visual inspection, as well as via the X-ray images of the core, it was found that this sample contained a few natural fractures (Figures 4.3 and 4.17). The results of the XRD analysis presented in Table 4.1 show that the sample contained 91.7% calcite, 6.0% dolomite and a low concentration of quartz. As can be seen from Table 4.2, the permeability of this sample

increased substantially after the live brine flooding and its dry weight decreased by 1.23 g, both of which could be attributed to the dissolution and removal of carbonate minerals (calcite and possibly dolomite).

The brine effluent chemistry (Table 4.8) shows increase in both Calcium (Ca) and Magnesium (Mg) concentrations with approximately 4 times more Ca dissolved than Mg. Similar to the previous samples, upon injection, the brine establishes preferential flow paths, which would be the fractures in the case of sample TC-2. As a result, the brine would flow through the fracture, leading to the dissolution and removal of carbonate minerals from both walls of the fracture, resulting in the development of a wormhole, which would naturally follow the path of the fracture. The observed permeability increase in the post-flood Sample TC-2 is contrary to what has been reported by (Polak et al. 2004), where a decrease in permeability and porosity of a fractured sample was observed after the flooding. The argument presented by these researchers is that while the dissolution through the fracture would increase the sample permeability, in their experiment this increase was counteracted by the physical compaction, due to the overburden stress, thereby reducing the aperture of the fracture (Figure 2.11) leading to overall reductions in both of the porosity and permeability of their sample. Perhaps, the dissolution of the fracture walls in the case of Sample TC-2 was not significant enough to weaken the fracture to the point where it would begin to close down under overburden stress.

The results of the chemical analysis of effluent brine for sample TC-2 indicate an increase of 200 mg/L in the concentration of Ca at the early flooding time (30 mins; Table 4.8), confirming the dissolution and removal of calcite from the sample. Figure 4.66 presents the pre- and post-flood SEM images generated for the sample disk placed at the inlet of this sample. The comparison between the images reveals the excessive dissolution of calcite at the fracture location and its vicinity caused by high brine flow through the fracture, altering the microstructural features and the entire surface of the fracture.

The post-flood X-ray CT image of Sample TC-2 (Figure 4.17) clearly shows the dissolution of minerals, resulting in the formation of a major wormhole along the path of the pre-existing major fracture along the length of the sample. Pre- and post-flood CT value profiles of this sample and selected X-ray cross-sectional images are presented in Figure 4.3. The post-flood CT value profile shows a decrease throughout the sample length, especially at the distance of 1.5 cm from its inlet, the spot where the fracture density is higher than other locations in the sample. While a significant increase in the permeability of Sample TC-2 was observed, the sample's overall porosity does not seem to have changed appreciably (Table 4.2). Figure 4.42

shows the pre- and post-flood pore size distribution (represented by NMR T2 spectrum) of this sample, as well as its cumulative porosity plot. A slight decrease in sample's oevrall porosity can be seen from this figure, as well as a minor shift in the pore size distribution towards smaller pore sizes. This may suggest that while the dissolution of minerals may have improved the sample's porosity, the physical compaction would have counteracted and even surpassed the effect of dissolution. Similar to the previous discussed three samples, in Sample TC-2, the changes in the post-flood porosity and pore size distribution seem to have been dictated by the physical compaction, while mineral dissolution seems to have had a larger control over the post-flood permeability.

5.1.1.3. Sample SC-1

Particularly important results were obtained from the experiment conducted on Sample SC-1, mainly due to the special configuration of this sample. As indicated earlier in Chapter 3, Sample SC-1 was a composite sample made up of two shorter core plugs (SC-1 inlet and SC-1 outlet), as well as a thin disk placed in between the two plugs (Figure 3.8 and Figure 5.3).

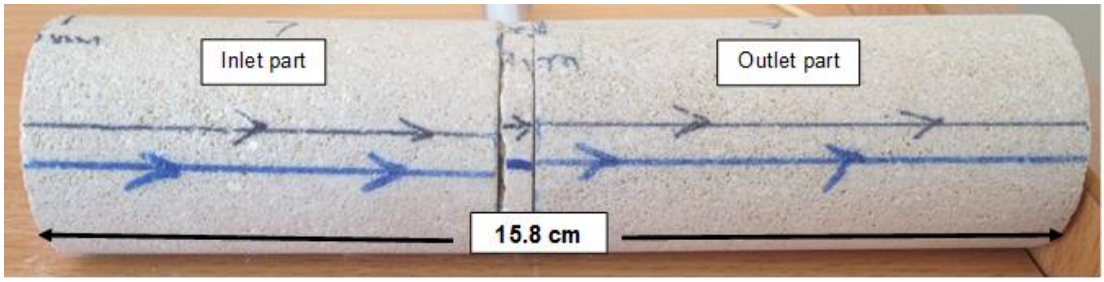

Figure 5.3. Sample SC-1 consisting of two short plugs of SC-1 (inlet part) and SC-1 (outlet part) and a thin disk.

Sample SC-1 was again a limestone sample with 97.7% calcite and 0.3% dolomite (Table 4.1). Porosity, permeability and other complementary measurements were conducted on the inlet and outlet plugs of the composite core separately, before and after flooding (Table 4.2). As will be discussed in details shortly, the collective evidence gathered for this sample indicate that the three main mechanisms of dissolution, precipitation and physical compaction as well as fines migration played their role in dictating the post-flood properties of the plugs.

A permeability increase from 46.8 mD to 71.28 mD and a dry weight decrease of 0.86 g in the inlet plug (SC-1 inlet) are attributed to the dissolution and removal of carbonate minerals. The chemical analysis of the effluent brine samples showed that Ca was dissolved at a maximum concentration of 300 mg/L or 0.00749 mol/L (Table 4.8). The cross-sectional X-ray images generated show excessive dissolution of the plug close to its inlet face (Figures 4.5 and 4.18)

causing deep dissolution fingers and wormholes through the plug. Once again, the images shown in Figure 4.18 support the previously presented argument that the brine tends to follow preferential flow paths through more porous areas and wider pore channels, leading to the creation of wormholes and improvement in permeability. On the other hand, the results of further experimental measurements (Table 4.2 and Figure 4.44) have revealed no appreciable change in the plug porosity and a slight shift in its pore size distribution towards smaller pore sizes. This observation is again a confirmation that physical compaction may have played a role in dictating some of the post-flood sample properties. A visual inspection of the plug revealed a dent on its surface, close to the injection point (Figure 4.18). This is a sign of excessive mineral dissolution and the collapse of the sample under overburden stress at this location. Furthermore, the X-ray images (Figure 4.18) show that some of the pores (mainly smaller pores) have disappeared from the post-flood plug. This observation may be attributed to effect of the physical compaction, as confirmed by the data presented in Figure 4.44.

The pre- and post-flood measurements conducted on the outlet plug of Sample SC-1 (SC-1 outlet) revealed results which were somewhat different to those achieved for the inlet plug. The permeability of the outlet plug has decreased from 37.53 mD to 32.86 mD (Table 4.2), after undergoing the flooding process. This reduction is believed to have been caused by the precipitation of minerals and the fines migration phenomenon. Both of these processes would have roots in the mineral dissoluion and physical compaction occuring in the inlet plug. It is worth noting that the total length of Sample SC-1 was almost twice that of the other samples tested in this work. The large sample length and pressure variation along the length of the sample may have enhanced the mineral precipitation (Khather et al. 2017). While the change in the porosity of this plug is negligible (Table 4.2), there is a slight shift in its pore size distribution, as depicted by Figure 4.45. The SEM images generated for a disk placed in between the two inlet and outlet plugs reveal signs of mineral precipitation and fines migration (Figure 4.67 and 4.68). Furthermore, unlike all other samples tested, where their post-flood dry weight decreased, the post-flood dry weight of plug SC-1outlet increased by 2 g (Table 4.2). This can be interpreted as a further confirmation of mineral precipitation and entrapment of fines in this plug during the brine flooding, although the brine effluent chemistry (Table 4.8) does not support the mineral precipitation observation and shows a small net molar loss of Ca and Mg. Although, it is worth noting that the number of effluent brine samples tested in this study were very limited and may be considered to be indicative only.

The post-flood CT value profile of SC-1outlet (Figure 4.6) clearly shows an increase throughout the plug length. This chnage may have been caused by a combination of mineral

precipitation and fines migration mechanisms, which may take place during the experiment. Furthermore, the cross-sectional X-ray images generated (Figure 4.6) show that some pores have disappeared along the length of the sample after flooding, which may provide another reason for the abserved reduction in the overall permeability of the plug. The disappearance of some pores may be attributed to the precipitation of minerals and fines. Once again, the comparison of the pre and post-flood 3D images shown in Figure 4.19 support the previously presented argument that a reduction in sample permeability may be attributed to mineral precipitation and fines migration, as this figure reveals once more time that some pores have disappeared from the sample after flooding.

Overall, in the case of Sample SC-1, all four mechanisms of dissolution, precipitation, compaction and fines migration seem to have been active during the flooding experiment. The way the properties of the sample have changed at various locations along its length strongly depends on the distance from the sample's inlet, with mineral dissolution controlling the sample properties close to its inlet and mineral precipitation and fines migation dictating post-flood properties near the outlet.

5.1.2. Sample group 2 (dolostone cores)

5.1.2.1. Sample VS-3

Sample VS-3 consisted of mostly dolomite (78.90 wt%) and anhydrite (9.60 wt%), with other minor accessory minerals (Table 4.1). As can be seen from Table 4.3, an increase in the permeability and porosity and a reduction in the dry weight of this sample were observed after live brine flooding. Similar to the previously discussed samples, such variations could be attributed to the effects of the mineral dissolution mechanism. This argument finds support in the results of the chemical analysis conducted on the effluent brine. As can be seen from Table 4.9, increases of 210 mg/L, 200 mg/L and 1000 mg/L in the concentrations of Mg, Ca and S, respectively, are evident during the early flooding times. These results and the molar ratios show that the main cause of permeability and porosity increase and weight decrease in this sample is the dissolution of dolomite ($CaMg(CO_3)_2$) and anhydrite ($CaSO_4$) minerals. The average molar ratio Ca:Mg is 0.6, which is greater than the other samples tested (Table 5.1) and subsequently closer to 1, as a result of increased dissolution of Ca from the aforementioned minerals. However, given the mineralogy, the Ca:Mg molar ratio should be much greater than 1. While Mg and Ca can originate from the dissolution of calcite and dolomite, the detected level of S can only be attributed to the dissolution of anhydrite. Molar ratios (Table 5.1) indicate that both dolomite and anhydrite are dissolving. However, the results show a depletion of Ca

in the solution that is indicative of a Ca-bearing mineral phase precipitating. TC-1 has an excess of Ca, but its S data are not available to assess the mass balance with the dissolution of anhydrite. TC-1 also contains more ankerite, that may produce a greater Ca:Mg ratio, with preferential dissolution of this mineral phase. Using the average molar change in the samples analysed and taking into account the following facts and assumptions: 1) all S in the solution is from anhydrite, 2) all Mg in the solution is from dolomite, 3) each sample volume is 5 mL and 4) the total experiment used 600 mL per core flood; it can be determined how much Ca was released from anhydrite and dolomite and therefore, the Ca deficit, which is the amount of calcite precipitated and an estimated net weight change (Table 5.1). Overall, the weight change calculated is approximately 1 g, which is less than the few grams of change recorded (Table 4.3). These calculations are only indicative as there are only a few measurements, but it confirms the trends observed in the other data. Calcite precipitation is approximately 1.5 g for VS-3 and VS-4 or 1% of the core mass.

Table 5. 1. The molar increase of Ca, Mg and S in the effluent brine samples related to the net dissolution of minerals and associated ratios (Ca:Mg molar ratio for dissolution of dolomite =1, Ca:S molar ratio for dissolution of anhydrite =1).

Sample	Time	Net molar increase in brine after flooding			Molar ratio		Mass balance	
		Ca	Mg	S	Ca/Mg	Ca/S	$CaCO_3$ gain (g)	Net loss (g)
VS-3	30min	0.00499	0.008642	0.031182	0.6	0.2	1.43	1.17
VS-3	8 hrs	0.002495	0.00823	0.015591	0.3	0.2		
VS-3	15hrs	0.007485	0.008642	0.014032	0.9	0.5		
VS-4	30min	0.002495	0.009877	0.026505	0.3	0.1	1.60	0.97
VS-4	8 hrs	0	0.008642	0.01715	0.0	0.0		
VS-4	15hrs	0.002495	0.008642	0.014032	0.3	0.2		
TC-1	30min	0.002495	0.006996	Not analysed	0.4	-	N/A	N/A
TC-1	8 hrs	0.001747	0.000617	Not analysed	2.8	-		
TC-1	15hrs	0.007485	0.004115	Not analysed	1.8	-		

The gradual decline in the differential pressure recorded as a function of time and pore volumes of live brine injected (Figure 5.5) is one more evidence in support of the observed increase in the permeability of this sample. Furthermore, as can be seen from the X-ray CT images presented in Figure 4.23, the mineral dissolution is highly pronounced at the inlet of the sample, where deep dissolution fingers and wormholes of lengths of up to 1.9 cm are evident. Figure 4.11 shows a decrease in the X-ray CT values (i.e. decrease in the bulk density) for the first few centimetres from the inlet of the post-flood Sample VS-3. Then, the CT values almost

match the original pre-flood values for the remainder of the sample length. This further confirms the pronounced alterations (i.e. dissolution) within the sample close to its inlet, with no or minimal changes towards its outlet. A reason for not observing any changes towards the outlet of the sample can be that any dissolution in this region was possibly masked by the precipitation of minerals and possible fines carried through from the inlet part of the sample. Another hypothesis could be that the reactive live brine became fully saturated with chemical species as it passed through the inlet part of the sample and therefore did not react with the minerals present in the outlet of the sample.

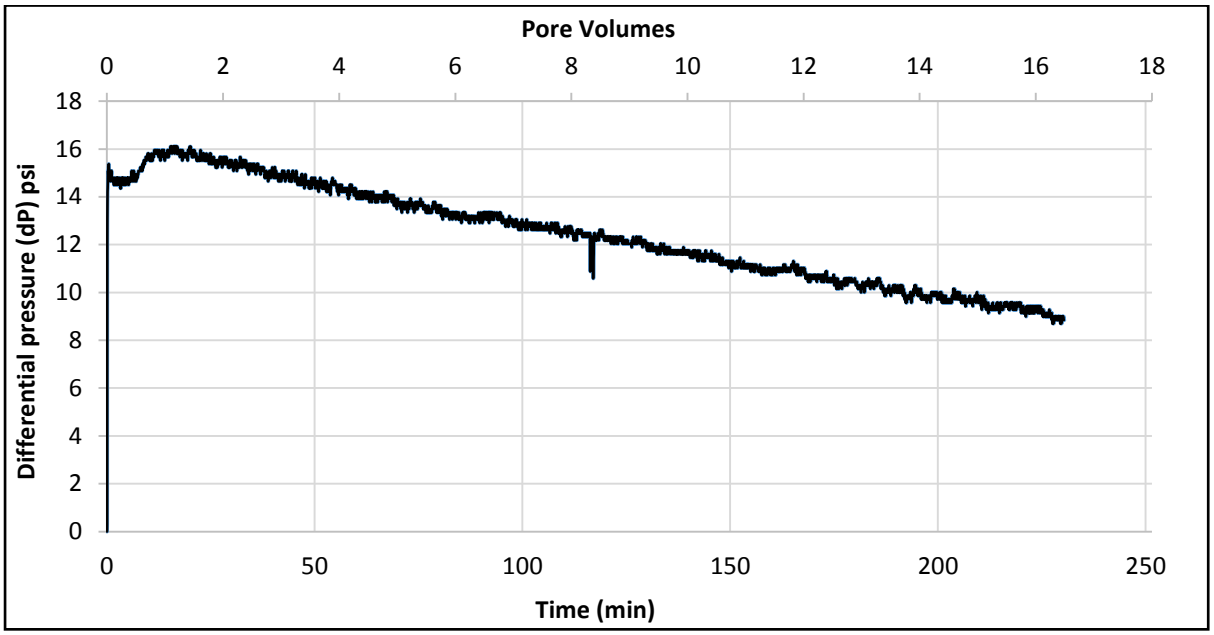

Figure 5.4. The evolution of the differential pressure across Sample VS-3 during live brine flooding. Continuous decrease in the differential pressure is a sign of minerals being dissolved from the sample resulting in improved permeability.

Similar to Sample SC-1 discussed previously, the X-ray images generated for Sample VS-3 show that the mineral dissolution has occurred predominantly close to the sample's inlet. In general, during core-flooding the dissolution begins at the injection point (inlet) of a sample. Over time, it may gradually extend, both radially and axially, within the sample leading to deeper dissolution, but the intensity of such changes remain stronger closer to the sample's inlet. Similar results have been reported by Smith et al. (2013) and Tutolo et al. (2014), where they also concluded that the majority of mineral dissolution occurred in the inlet region of their samples and dissolution fingers were created with lengths of a few millimetres from the inlet of the samples. Consequently, they have also reported increase in the porosity and bulk permeability of their samples. Furthermore, Luhmann et al. (2014) conducted similar experiments to this study and concluded that the flow rate plays a critical role in the formation

of wormhole features in the dolostone samples. Based on their findings, intermediate flow rates in particular, produce the greatest permeability enhancement and result in the development of one or more wormholes in the flooded core samples. The NMR T2 distribution presented in Figure 4.50 for Sample VS-3 indicates that for this sample as a whole, the pore sizes became smaller, possibly caused by the dissolution and transportation of minerals from smaller pores and pore throats and their precipitation in larger pores. Mechanical compaction is an unlikely mechanism in the case of this sample, as its physical dimensions show no change between its pre- and post-flood states (Table 4.3).

For sample VS-3, all evidence suggest that the mineral dissolution mechanism is the primary cause of the observed changes in its post-flood properties such as the detected enhancements to the sample porosity and permeability, as well as the decrease in its dry weight.

5.1.2.2. Samples VS-4 and VC-3

To some extent, different results were obtained from the measurements conducted on the pre and post-flood states of samples VS-4 and VC-3, as compared with those obtained for sample VS-3. The two main constituents of Sample VS-4 were dolomite at 57.90 wt% and anhydrite at 38 wt%. The concentration of anhydrite in Sample VS-4 is significantly greater than Sample VC-3, which consists mainly of dolomite at 98.80 wt% (Table 4.1). As can be seen from Table 4.3, unlike Sample VS-3, reductions of 3.5% and 57.4% were observed in the post-flood permeability of samples of VS-4 and VC-3, respectively.

The dissolution of dolomite and anhydrite was confirmed by the chemical analysis of the effluent brine for Sample VS-4, where the results indicate increases of 240 mg/L, 100 mg/L and 850 mg/L in the concentrations of Mg, Ca and S, respectively, at the early flooding times (Table 4.9). While the observed S shows some anhydrite dissolution, like VS-3 or VS-4, molar ratios show a marked depletion of Ca and do not reflect the expected increased dissolution of anhydrite and resulting Ca:Mg > 1. The depletion of Ca can be attributed to the precipitation of calcite from a mass balance approach (~1.6 g; Table 5.1), although this is unconfirmed in the core mineralogy. Also, the number of fluid samples analysed is limited. Further fluid sampling and analysis may be required if a detailed geochemistry study is required and should incorporate the analysis of HCO_3, pH and the direct determination of SO_4, instead of S. However, conducting such analysis and measurements do not fall within the objective set for this study.

Deep dissolution fingers with lengths of up to 2.4 cm can be observed in the X-ray CT images generated for this sample (Figure 4.24). Considering the evident excessive mineral dissolution,

the contradictory observed reduction in the permeability of samples VC-3 and VS-4 can be attributed to the mechanisms of mineral precipitation, fines migration and mechanical compaction. Very likely, the minerals dissolved and fines dislodged were transported from the inlet region and precipitated close to their outlet. The signs of mechanical compaction are more obvious from the results obtained for Sample VC-3, where the core length was reduced from 6.95 cm to 6.84 cm and its outside diameter decreased from 3.76 cm to 3.71 cm. That is probably the reason behind the reduction of 5% in the porosity of this sample (Table 4.3).

Figures 4.12 and 4.13 reveal similar behaviours for samples VS-4 and VC-3 after undergoing the flooding process. For both samples, a decrease in the CT values is evident close to their inlets after undergoing the flooding process, which indicates a decrease in average bulk density of the post-flood samples in that area, pointing towards the occurrence of dissolution and removal of minerals. On the other hand, the same figures show an increase in the CT values for the remainder of the post-flood samples, as compared with the original pre-flood values. This indicates an increase in the average bulk density close to the samples' outlets. Such changes again confirm the occurrence of the possible mechanisms of mineral precipitation, physical compaction and fines migration in the outlet region of the samples. The 2D representation of the 3D X-ray images generated for samples VS-4 and VC-3 are provided in Figures 4.24 and 4.25, both of which show not only dissolutions close to the inlet of the samples, but also the fact that some pores have become smaller or even disappeared from the images after flooding. Once again, the latter changes can be tied to the effects of the two possible mechanisms of mineral precipitation, physical compaction and fines migration. Figures 4.51 and 4.52 present the NMR T2 spectra and cumulative NMR porosities for samples VS-4 and VC-3, respectively, in their pre- and post-flood states. It is evident from these figures that the T2 distributions are shifted towards lower values meaning that, overall, the pore sizes have become smaller in both post-flood samples.

While the two samples of VS-4 and VC-3 behaved similarly in certain aspects, there have also been differences in the way they responded to the flooding process. For example, unlike Sample VC-3, the porosity of Sample VS-4 increased by 1%. Also, as evident from the dimension measurements, Sample VS-4 did not undergo the same degree of mechanical compaction as Sample VC-3 (Table 4.3). The permeability of this sample also did not decrease as much as Sample VC-3. Such differences in behaviour can be explained considering the differences in the textural features and petrophysical properties of the two samples in their pre-flood states. As presented in Table 3.5, Sample VC-3 is classified as a vuggy dolostone,

whereas VS-4 is a tight dolostone. Therefore, the pre-flood Sample VC-3 is considered structurally weak, making it highly susceptible to mechanical compaction and furthermore, it would become even weaker during the flooding due to the effects of the mineral dissolution. In comparison, Sample VS-4, as a well-cemented tight dolostone, would be structurally stronger and subsequently less influenced by possible mechanical compaction. Similar results were obtained by Smith et al. (2013) whose vuggy dolomite samples showed a rapid dissolution of calcite cement, due to flooding, leaving behind a very weak skeleton of large dolomite crystals. Subsequently, under the effect of confining pressure, both the porosity and permeability of their samples decreased.

Another observation of Sample VS-4 was that it lost the greatest mass amongst the three samples included in this sample group whose pre and post-flood dry weights were measured. Sample VS-4 lost 4.81 g compared to TC-1, 3.4 g and VS-3, 2.9 g (Table 4.3). This mass loss may be tied to the mineralogy of the samples, as presented in Table 4.1. Anhydrite has a very high reaction rate and a greater solubility in the live brine, compared with the other minerals present in the composition of these samples. Therefore, it is believed that Sample VS-4, having the highest percentage of anhydrite, lost the highest weight due to the dissolution mechanism, followed by samples TC-1 and VS-3, which had the second highest and lowest percentages of anhydrite, respectively. However, it is worth noting that this was not evident in the S analysis performed on the very limited effluent brine samples collected.

Overall, considering the alterations that occurred in the post-flood samples of VC-3 and VS-4, it may be assumed that the effects of mineral dissolution and mechanical compaction were dominant for both samples.

5.1.2.3. Sample TC-1

Sample TC-1 was a fractured dolostone with 6.45% porosity and 0.11mD permeability in its original state (Table 4.3). The results obtained from the XRD analysis (Table 4.1) revealed that this sample contained 75.70 wt% dolomite, 20.70 wt% anhydrite and minor accessory minerals of quartz and ankerite. The pre and post-flood measurements show an increase in the post-flood sample permeability of 0.57 mD or an increase of more than 5 times, which may be attributed to the dissolution and removal of carbonate minerals from the sample (Table 4.3). As discussed in details in Chapter 2 and early on in this chapter, in a fractured sample such as TC-1, the injection fluid tends to flow through the fractures as preferential flow paths, leading to the dissolution of minerals from the walls of the fractures, resulting in a possible increase in sample permeability. Due to the presence of the fractures and their role as preferential flow paths, the

live brine's interaction with the matrix of the rock away from the fractures may become limited. Chemical analysis of the effluent brine for Sample TC-1 indicates increases in the concentrations of Mg by 170 mg/L and Ca by 100mg/L at the early times of the experiment (Table 4.9). The S concentration data of the effluent brine was not available for this sample, but given its anhydrite content, the concentration of this element in the brine could have also been high. Such data may confirm that the main cause of permeability and porosity increase in this sample is the dissolution and removal of dolomite and anhydrite, as present in the mineralogy of the sample. Furthermore, the CT number profiles and X-ray CT images presented collectively in figures 4.14 and 4.26 confirm that mineral dissolution indeed occurred along the length of the fracture. As can be seen, Figure 4.14 shows an almost even decrease in the CT values along the entire length of this post-flood sample, likely due to the even mineral dissolution and subsequent increase in the sample permeability along the length of the fracture. The porosity of this sample also increased by approximately 1.1%. No change in the pore size distribution of this sample was observed as presented in the form of the NMR T2 distribution in Figure 4.53.

5.1.3. Sample group 3 (chalk cores)

As mentioned in chapters 3 and 4, Group 3 included two chalk core plugs (Figure 3.10 and Table 4.4) sourced from the Middle East. These two core plugs were then stacked together in series to construct a composite rock sample (i.e. CH-1) to use for live brine flooding. As shown in Table 4.1, Sample CH-1 consisted mainly of calcite (98.9%) and low concentrations of dolomite and quartz (0.7 and 0.4%, respectively). As evident from the data presented in Table 4.4, the post-flood inlet plug showed a substantial increase in its permeability (38.49 mD to 6408.52 mD) after the live brine flooding, and its dry weight decreased by 1.076 g, which very likely was caused by the dissolution and removal of calcite mineral during flooding. The post-flood X-ray CT images generated for this plug and the photo taken from its inlet (Figure 4.20) clearly show the excessive dissolution of minerals close to its inlet face and along its length, resulting in the formation of a major wormhole along the inlet plug. The pre- and post-flood X-ray CT value profiles presented in Figure 4.7 for the inlet plug clearly show a decrease in the CT values (i.e. decrease in the bulk density) along the length of the sample after undergoing the live brine flooding. The above decrease in the sample's bulk density is caused by the previously explained mineral dissolution within the core sample. The mineral dissolution can be further examined by comparing the pre- and post-flood SEM images generated for a thin disk placed in between the inlet and outlet plugs of Sample CH-1 (Figure 4.69). The images

clearly reveal significant dissolution of the calcite, resulting in highly pronounced alterations to the pore structure of the post-flood sample.

On the other hand, the results obtained from the commulative and incremental NMR T2 distributions plotted for the inlet plug (Figure 4.46) revealed a negligible decraese in the plug's overall porosity and a slight shift in its pore size distribution towards smaller pore sizes. The results of the pre- and post-flood gas porosity measurements also conform with the results of the NMR measurements. Given the highly pronounced chnages obsevred for this samples as discussed in the previous paragraph, the very subtle change to its porosity and pore size distribution could be attributed to the effects of the physical compaction mechanism caused by the overburden pressure applied during the experiment. The physical compaction phenomenon also finds support in the pre- and post-flood dimension measurements (Table 4.4) which revealed that the inlet plug became shorter by 1 mm after flooding.

Madland et al. (2006) conducted similar experiments on chalk cores which were weakened significantly after exposure to carbonated water, as a result of mineral dissolution and formation of a major wormhole. As discussed by the above researchers, this weakening then influenced the stability of their samples and gave rise to physical compaction under overburden pressure (Madland et al. 2006). Other similar research work whose resulted are reported in the literature (Korsnes et al. 2008; Liteanu et al. 2013), have similarly concluded that CO_2 injection into chalk rocks can significantly affect their petrophysical properties.

The results of the pre- and post-flood measurements conducted on the outlet plug of sample CH-1 (CH-1 outlet) were somewhat different to those achieved for the inlet plug. The permeability of the outlet plug decreased slightly from 29.77 mD to 28.67 mD (Table 4.4) after flooding. This reduction is believed to have been caused by the possible precipitation of dissolved minerals and fines carried through from the inlet core plug. The relatively large length of Sample CH-1 ($\sim 14.5\ cm$) and the associated pressure variations in the direction of flood could have enhanced the mineral precipitation. Furthermore, as another evidence in support of possible mineral precipitation and fines migration, the post-flood dry weight of the outlet plug increased by ~ 1 g (Table 4.4). No sign of compaction was observed for this plug as there was almost no change in its post-flood dimensions. While the change in the porosity of this plug is negligible (Table 4.4), there is a slight shift in its pore size distribution, as depicted by Figure 4.47.

A comparison between the outlet plug's pre- and post-flood X-ray CT value profiles (Figure 4.8) reveal a slight decrease in the bulk density for the first few centimetres of the plug. Then,

the CT values almost match the original pre-flood values for the remainder of the sample. Furthermore, as can be seen from the X-ray CT images presented in Figure 4.21, mineral dissolution seems to be pronounced only in the first a few millimetres of the outlet plug as evident from small dissolution fingers formed at its inlet.

Overall, the pronounced changes in the properties of the inlet plug of Sample CH-1 seem to have been cause by the mineral dissolution and mechanical compaction mechanisms. The subtle changes observed in the outlet plug on the other hand indicated that the effect of these two mechanisms would have been negligible in this plug whose properties seems to have been slightly changed by possible mineral precipitation and fines migration.

5.1.4. Sample group 4 (manufactured hetergeneous Indiana Limestone sample)

As stated earlier, during the core-flooding experiments the injected carbonated water tends to, at least initially, follow any existing preferential flow paths (e.g. a fracture) in the rock sample as they present the least resistance to the flow. The high brine flow rate going through an established flow path may then increase the dissolution rate, widening the flow path further increasing the reactive surface area even further. Eventually, this would result in the formation of obvious dissolution patterns (e.g. wormholes) along the length of the core sample, and thus leading to the alteration of sample permeability and porosity.

Although some of the experiments discussed so far have shown the above to be the case, in order to obtain a more solid evidence, a flooding experiment was performed on an especially manufactured heterogeneous sample made up of two half plugs prepared by axially splitting two initially intact limestone core plugs (IL-1 and IL-2) into two halves (Figure 3.11). The sample preparation has already been discussed in Chapter 3. In addition to polishing the contact surfaces of the half plugs, a few layers of a special lint-free tissue paper were placed between them to make sure a perfect match was obtained between their contact surfaces and any possible flow through the joint between them would be eliminated. Since there was high permeability and porosity contrasts between the two half plugs (Table 4.5), this sample assembly would be helpful in investigating the effect of preferential flow of the injected brine through a particular region of a rock sample and how this phenomenon may control any variations in the petrophysical of various sections of the sample. On the other hand, both half plugs had similar mineral compositions with 97% of calcite and minor traces of dolomite and quartz (Table 4.1).

As expected, every half plug underwent a different levels of variations to their petrophysical properties after undergoing the flooding procedure. The post-flood X-ray CT images of the high permeability IL-1 sample (Figures 4.9 and 4.22) clearly show signs of mineral dissolution

and formation of wormholes (dissolution fingers) close to its inlet. However, similar images for the low permeability IL-2 sample (Figure 4.10) show no visible signs of dissolution. A comparison between the X-ray CT value profiles presented in figures 4.9 and 4.10 for samples IL-1 and IL-2, respectively, reveals that although there is a substantial difference between the pre- and post-flood profiles for Sample IL-1, there is almost no appreciable difference between the profiles belonging to Sample IL-2. The above results clearly confirm the fact that the injected live brine would have flown through preferential flow paths leaving the rest of a sample almost intact. In addition, a detailed comparison between some of the pre- and post-flood X-ray CT images generated for Sample IL-1 (Figure 5.9) clearly show that for this sample on its own the injected live brine has followed more porous areas of the sample (yellow circles) making them wider turning them into wormholes. It is worth noting that a comparison between the pre- and post-flood porosity and permeability values of the two half plugs could not be done because it was not possible to do these measurements on the half plugs.

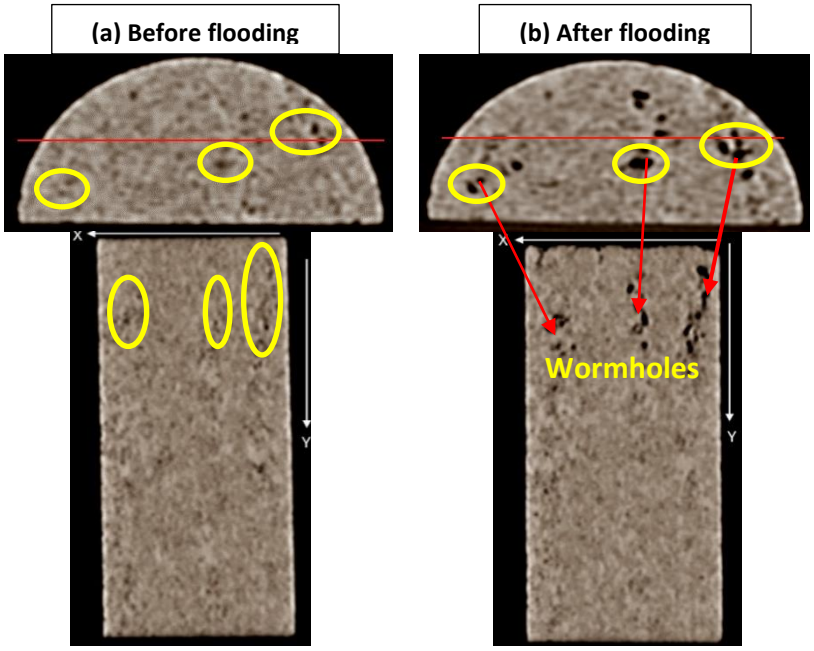

Figure 5.5. X-ray CT scan vertical and horizontal section images of sample IL-1: (a) before flooding and (b) after flooding. The images clearly show that the live brine tends to follow the large pores and establish new paths.

5.2. Continuous CO_2-EOR flooding

As indicated in Chapter 4 and earlier in this chapter, four flooding experiments were conducted on different carbonate samples (Table 4.6) using a CO_2-EOR flooding procedure. In these experiments several PV's of CO_2 were injected continuously as an attempt to recover the residual oil left behind by the initial water flood. One primary objective of these experiments

was to investigate the occurrence of the mechanisms of mineral dissolution, mineral precipitation, fines migration and physical compaction during this flooding scenario. Furthermore, a number of complementray measurements were provsioned in the experimental plan so the occurrence of asphaltene precipitation (as the fifth mechanism mentioend in Chapter 2) which was suspect to take place during the CO_2 injection could be detected.

As indicated in Chapter 3, four carbonate core plugs (two composite cores and two individuals (six samples in total)) (Table 3.8) were used for the continuous CO_2-EOR flooding to assemble four individual core samples. In other words, four out of the six plugs were used to construct two compoiste cores while the other two were used individually on their own (Table 3.8). The composite samples each included a thin sample disk placed in between the two longer plugs (Figure 3.12) which would be used to pinpoint any microstructural changes that the samples may undergo during flooding.

As can be seen from figures 5.10 to 5.13, the continous CO_2 flooding resulted in a considerable incremental oil recovery (29.2-51.2%) across all four samples proving that CO_2 flooding may be considered as an effective EOR technique under the conditions applied in these experiments. The pre- and post-flood petrophysical measurements (Table 4.6) indicate that all samples have undergone a moderate to significant reduction in their gas permeability (13-58%). The same measurements also reveal a very subtle reduction in the posoity of majority of the samples. Such alterations may indicate the occurrence of fines migration, mineral and/or asphaltene precipitation and possible physical compaction during the flooding process. Given the fact that the X-ray CT images presented in figures 4.27 to 4.34, only reveal very limited signs of mineral dissolution, it is beieved that asphaltene precipitation is the main mechanism to blame for the above chnages in the posoity and permeability of the samples. The mesaured increase in the dry weights of all the post-flood samples (Table 4.6) may be considered as an another evidence in support of the occurrence of asphaltene precipitation. Similar outcomes have been attributed by other researchers to asphaltene precipitated in their samples due to CO_2 flooding (Srivastava et al. 1997).

As discussed in details in Chapter 2, the role of CO_2 injection in causing asphaltene precipitation has been largely recognised in the literature such those published by Srivastava, Huang and Dong (1999) and Takahashi et al. (2003) as two examples. Srivastava, Huang and Dong (1999) have reported that the CO_2 concentration in a susceptible crude oil plays a significant role in causing asphaltene deposition. These resaerchers indicate that after the onset point, asphaltene precipitation would increase as the CO_2 concentration increases. A similar

discussion has been presented by Takahashi et al. (2003) where they indicate that in a reservoir asphaltene precipitation could lead to formation damage and reduction in the formation rock permeability.

The dominance of asphaltene precipitation over other mechanisms in the experiments conducted here may be recognised further by analysing the results obtained for the two composite samples tested in this part of the study. As observed and discussed in details previously for the composite samples tested using live brine flooding, in the case of occurrence and dominance of mineral dissolution and precipitation and fines migration, the inlet and outlet plugs of a composite sample would react completely different to the flooding process. That is, normally an increase in permeability would be evident in the inlet plug and opposite pobservation would be made for the outlet plug. The X-ray CT images also would normally show different results for the two plugs. For the case the two composite samples tested using the continuous CO_2-EOR flooding scheme however, in general, the inlet and outlet plugs of the composite cores react similarly to the flooding. Such a behaviour can also be seen in the CT number profiles plotted in figures 4.27 to 4.30. As can be seen, all plots show an increase in the CT numbers for almost the whole length of the inlet and outlet plugs. The limited or no contribution of the mineral dissolution/precipitation and fines migration may be attributed to the fact that the highly reactive live brine was not used to flood the samples tested using the continuous CO_2-EOR flooding scheme. In these experiments, for any chemical recation to occure between the rock and fluids, the CO_2 has to first dissolve in the brine present in the samples whose amount is limited and much of it would be displaced out of the samples by CO_2 ahead of the CO_2 flood front.

The results of the pre- and post-flood microstructural analysis perfomred on samples SD-1 and ILN-2 using SEM were presented in Chapter 4 in figures 4.70 to 4.73. As apparent from these figures, asphaltene particles can be clearly seen to have been deposited on the pore surfaces of the samples. A comparison between the asphaltene and resin content of an original crude oil sample and those of some effluent crude oil samples collected during some of the experiments (Table 4.9) may be used as another sign of occurrence of asphaltene precipitation. The data presented in Table 4.11 show a reduction in the asphaltene and resin concentration in the produced crude oil, as CO_2 flooding proceeds.

The results of the NMR measurements presented in figures 4.54 to 4.59 can be used as one last piece of evidence in support of the dominance of asphaletene precipitation in the samples tested using the continuous CO_2-EOR flooding scenario. As can be seen, almost all NMR T2

distribution plots have shifted towards smaller values indicating an overall reduction in the pore sizes of the samples leading to a reduction their porosities as revealed by the cumulative porosity plots figures 4.54 to 4.59. The pre- and post-flood NMR porosity values provided in Table 4.6 show a similar behaviour. It is worth noting that the inconsistency between the amount of the porosity reductions detected from gas porosity and NMR porosity measurement technqiues (i.e. significantly more reduction is revealed by NMR measurements) may be attributed to wettability alterations that are expected to have been caused by asphaltene precipitation. Such change in the wettability are expected to have influneced the NMR results but would have no effect on the gas porosity measuremnets.

Furthermore, the result revealed the asphaltene participation to decrease from the inlet to the outlet along the length of the cores flooded. A similar observation has been made by Srivastava, Huang, and Dong (1999), who concluded that asphaltene precipitation would be more pronounced near the inlet region of the cores subjected to CO_2 flooding.

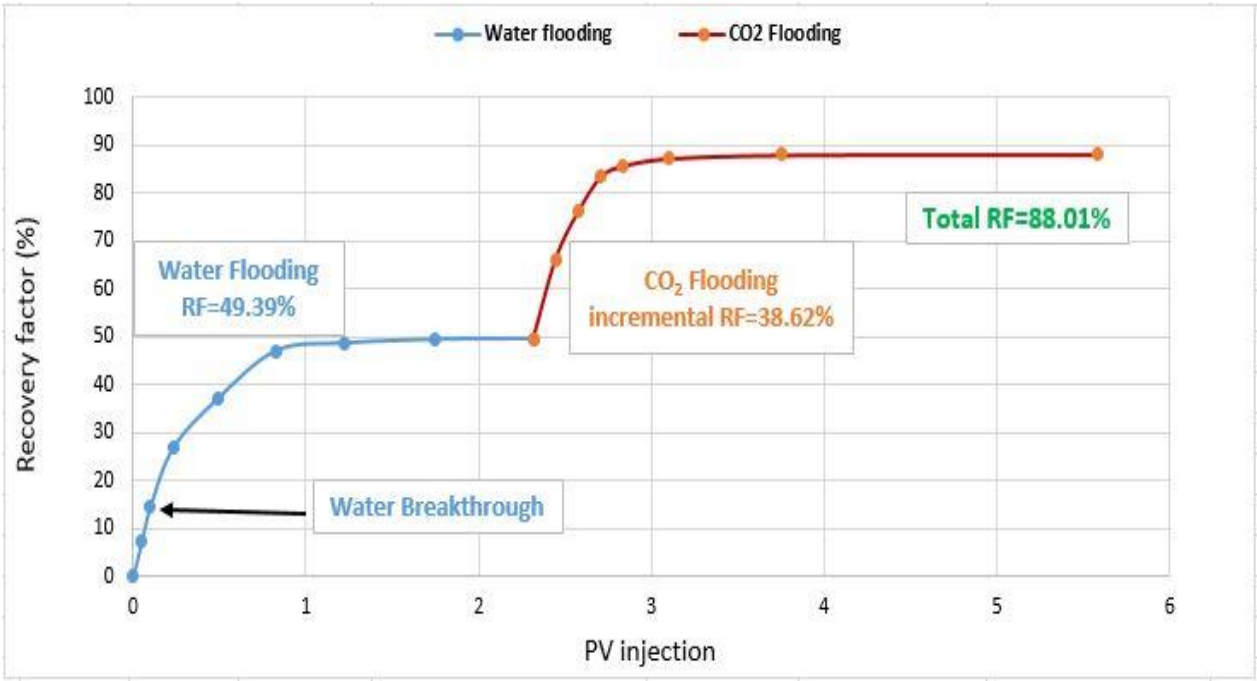

Figure 5.6. Oil recovery versus pore volume injected (PVI) for Sample SD-1.

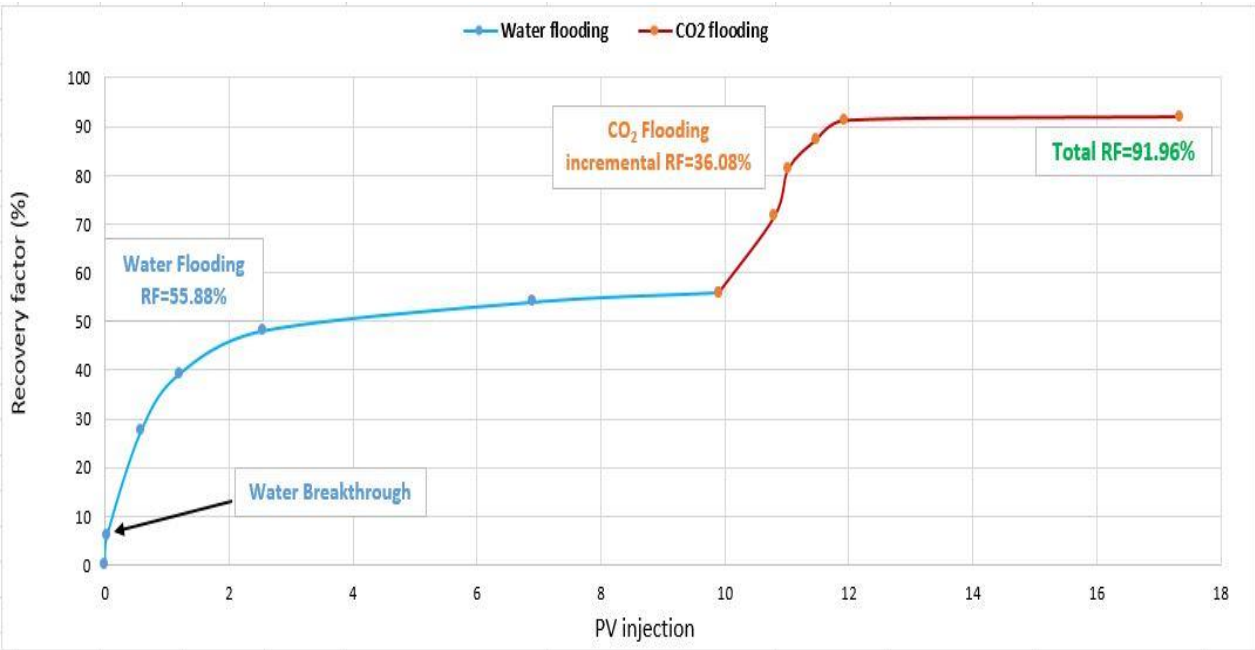

Figure 5.7. Oil recovery versus pore volume injected (PVI) for Sample GD-1.

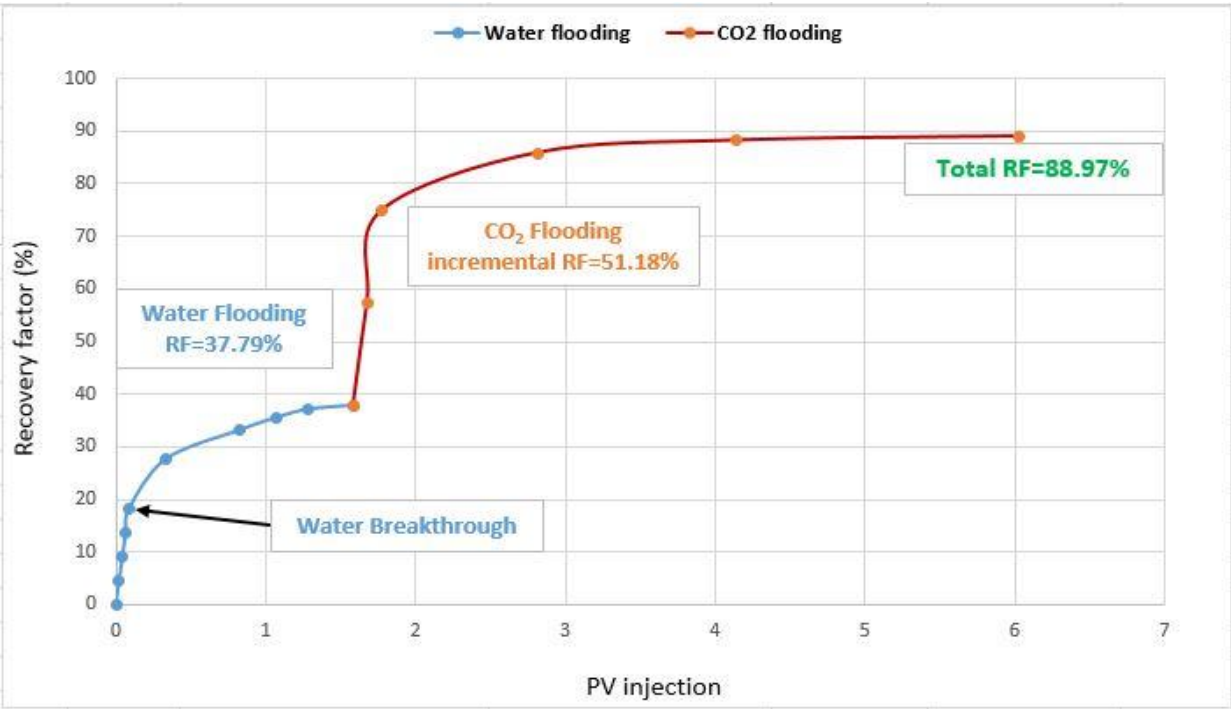

Figure 5.8. Oil recovery versus pore volume injected (PVI) for Sample INL-2.

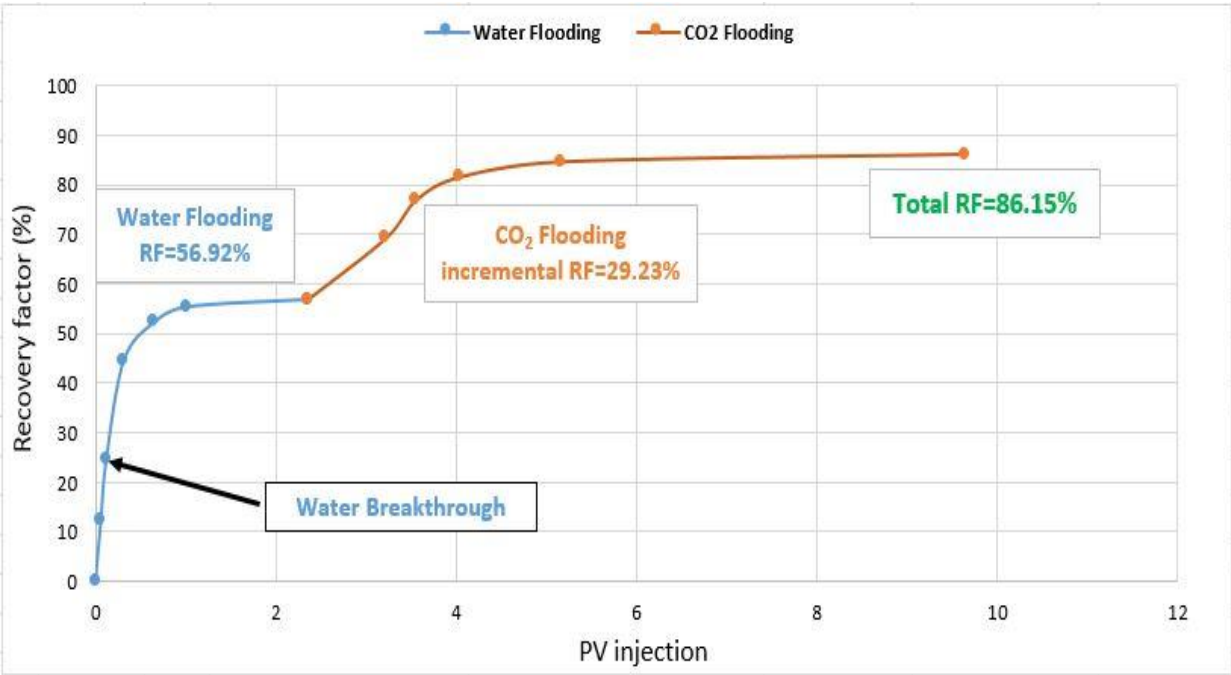

Figure 5.9. Oil recovery versus pore volume injected (PVI) for Sample INL-1.

5.3. Water-Alternating-Gas (WAG) flooding

Three core flooding experiments were conducted using a water-alternating-gas (WAG) flooding scheme in which formation water was injected in alternation with CO_2 into three carbonate samples (two limestone and one dolostone). As discussed earlier for the four samples tested using the CO_2-EOR flooding (i.e. continuous CO_2 injection), other than the asphaltene precipitation, the effect of the other mechanisms (i.e. mineral dissolution, precipitation, fines migration and physical compaction) identified to influence sample properties during the live brine flooding, was found to be minimal or non-existence. Therefore, the main objective of the WAG experiments was to evaluate if this flooding scheme would make any differences with regards to the effect of the above mechanisms.

As can be seen from figures 5.14 to 5.16, the WAG flooding resulted in ultimate recoveries close to those achieved using the continuous CO_2 flooding although the incremental volumes of oil produced by WAG flooding seem to be have been mobilised and recovered more gradually.

5.3.1. Samples VS-2 and INL-11 (limestone)

Samples VS-2 and INL -11 consist mainly of calcite, with concentrations of 82.20% and 99.30% respectively, with the balance being low concentrations of other minerals, as presented in Table 4.1. A major difference between the results obtained for the WAG and continuous CO_2 flooding is revealed upon comparing the differences between pre- and post-flood sample

permeabilities resulted from the two flooding schemes. As can be seen from Table 4.7, both of the limestone samples (VS-2 and INL-11) show significant improvement to their post-flood permeability. If the results obtained for the live brine flooding are used as a guide, such a change can be attributed to the effect of the mineral dissolution mechanism. This hypothesis finds strong support in the results of the chemical analysis performed on the effluents brine samples collected during WAG flooding (Table 4.10) as well as the X-ray CT images and CT number plots included in Figure 4.35 and figures 4.37 to 4.39. In particular, the formation of dissolution fingers/wormholes is easily visible in the images presented in figures 4.38 and 4.39.

The different dissolution patterns resulted for the two samples discussed here are believed to have influenced the recovery factors obtained for these two samples. The X-ray images clearly show that mineral dissolution and the formation of wormholes extend almost to the end of Sample VS-2 (Figure 4.38), where only limited dissolution fingers (~1.5 cm) are formed in Sample INL-11 (Figure 4.39). It is believed that the significant dissolution within Sample VS-2 caused the injected fluids to follow the wormholes created bypassing many parts of the sample. Therefore, a large amount of oil would be left behind resulting in lower oil recovery in this sample. On the other hand, the less sever dissolution in Sample INL-11 might not affect the displacement efficiency in this sample significantly resulting in a higher oil recovery factor.

Similar to the case of continuous CO_2 flooding, the asphaltene precipitation is expected to have occurred during the WAG flooding process however, its negative effect on the sample permeabilities would have been masked and surpassed by the effect of mineral dissolution mechanism.

Similar to the CO_2-EOR flooding scheme, the non-reactive dead brine was used during the WAG injections, however the alternating injection of CO_2 and brine seems to have managed to give rise to the dissolution mechanism something that did not take place during the continuous CO_2 injection of the CO_2-EOR scheme. The dissolution power of a WAG flood may stem from the fact that it brings CO_2 and brine in contact several times within the rock sample and flow-lines of the flooding apparatus facilitating the generation of the reactive carbonated brine.

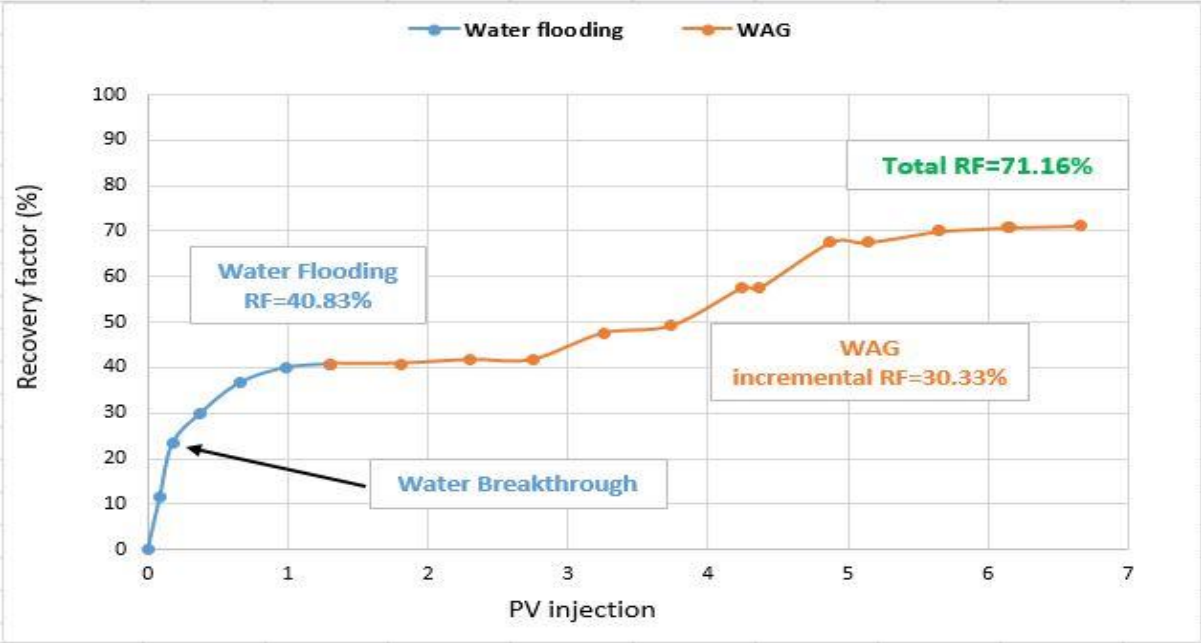

Figure 5.10. Oil recovery versus pore volume injected (PVI) for Sample VS-2.

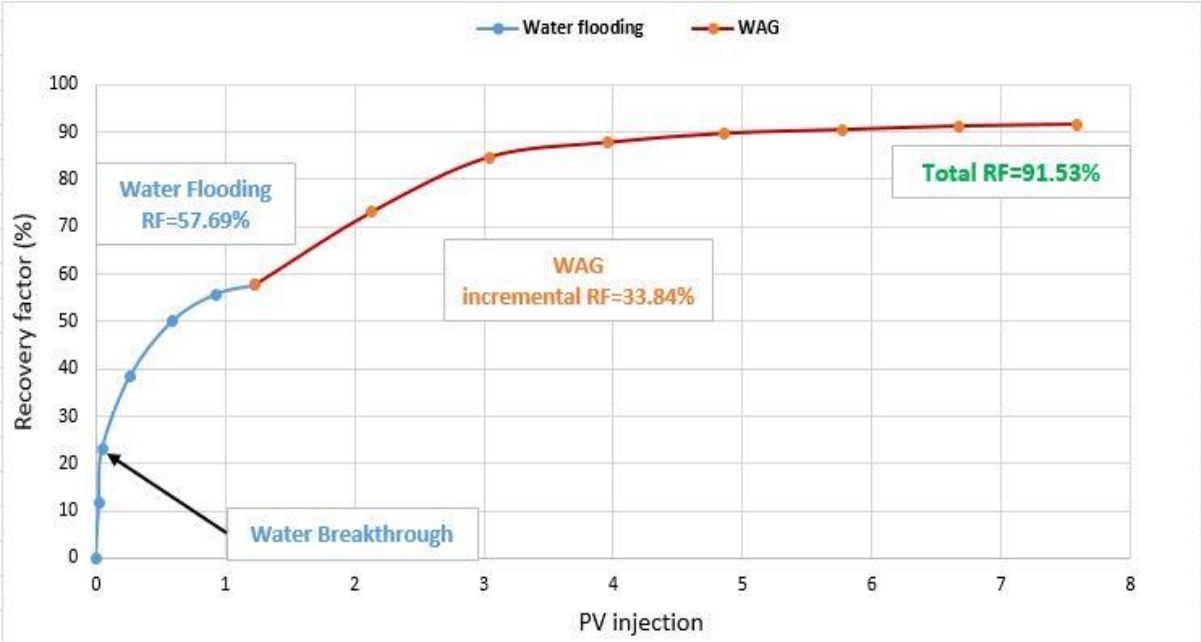

Figure 5.11. Oil recovery versus pore volume injected (PVI) for sample INL-11.

Similar to many of the samples tested using the live brine and continuous CO_2-EOR flooding schemes, the porosity of samples VS-1 and INL-11 decreased slightly as shown by the data presented in Table 4.7. The measured NMR T2 spectra of these two samples also shifted towards smaller values, meaning that their overall pore sizes became smaller (Figures 4.60 and 4.62). Such a behaviour may have been caused by physical compaction of the samples and possible asphaltene precipitation. For instance, as can be seen in Table 4.7, the length of Sample VS-1 shows a dectrease of 0.07 cm.

Overall, for these two limestone samples, the evidence at hand support the dominance of the mineral dissolution mechanism and possible occurrence of asphletene precipitation and mechnical compaction.

5.3.2. Sample GD-11 (dolostone)

This sample consists of mostly dolomite (98.2 wt%) and very small fractions of quartz and albite (Table 4.1). Based on the data presented in Table 4.7, the samples underwent a significant reduction in its permeability (46%) and a slight reduction in its porosity. As can be seen from Figure 4.61, the pore size distribution (represented by the NMR T2 spectrum) of this sample after flooding is also shifted towards smaller values. Furthermore, the X-ray CT images and CT number profile presented for this sample in Figure 4.36 do not show strong signs of mineral dissolution. These results are mostly in line with those obtained for the samples tested using the continuous CO_2 flooding (i.e. CO_2-EOR scheme). Therefore, it may be concluded that in the absence of considerable fluid-rock geochemical interactions, asphaltene precipitation may be held responsible for the changes detected in the petrophysical properties of this sample.

Although all three samples of VS-2, ILN-11 and GD-11 were tested using identical flooding procedures and the same injection fluids, the post-flood samples VS-2 and INL-11 show strong signs of mineral dissolution while a similar behaviour cannot be seen from Sample GD-11. The reason behind this apparent discrepancy can be found in the mineral composition of the samples. As indicated above, Sample GD-11 consists mainly of dolomite which, as discussed earlier, is much less reactive with the injection fluids compared with calcite which was the main constituent of samples VS-2 and INL-11.

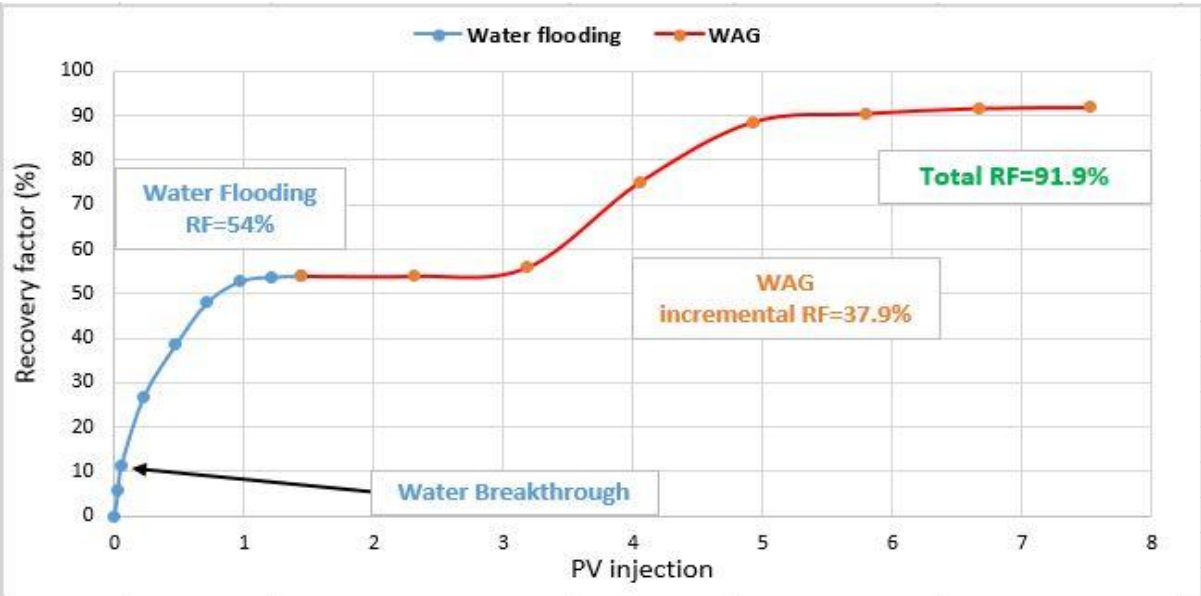

Figure 5.12. Oil recovery versus pore volume injected (PVI) for sample GD-11.

Chapter 6

6. Summary, conclusions and recommendations

6.1. Summary

Carbon dioxide may be injected in various forms (e.g. a single continuous phase, in alternation with water/brine, as carbonated water/brine, etc.) into a deep subsurface geological setting for the purpose of EOR, mere disposal and storage or both. Regardless of the injection purpose and the CO_2 method of delivery, such operations would result in the injected or in-situ formed reactive fluids to come in contact with the host rock formation triggering a series of possible geochemical reactions. Subsequently, such reactions may alter the formation's petrophysical properties (e.g. permeability, pore size distribution, porosity, mechanical strength, etc.). It is imperative that the operator of an injection site, among other important aspects of the injection process, would need to initially paint a clear picture of the significance and consequences of the aforementioned reactions. The chemistry of such reactions have already been well-defined in the relevant literature however, one may expect that the extent to which they may alter the characteristics of the host rock would greatly depend on a number of formation-specific factors such as its mineral composition, presence of heterogeneities and rock's structural and textural features. Therefore, first the possibility of occurrence of geochemical reactions and, if the occur, their possible end-effects would require a detailed evaluation on a case-by-case basis.

In general, there are three main mechanisms of mineral dissolution, mineral precipitation, mechanical compaction have been introduced in the literature as the driving force behind the earlier mentioned petrophysical alterations. In fact, it is the occurrence, extent of the effects and the interplay between these mechanisms that may be case dependent. There are two more mechanisms namely asphaltene precipitation and carbonate fines migration whose occurrence may be associated with the injection of CO_2 and subsequent in-situ thermophysical and/or geochemical reactions. The CO_2 induced asphaltene precipitation is again a well characterised phenomenon covered extensively in the literature however, the generation and release of carbonate fines by the mineral dissolution and physical compaction mechanisms has not received the attention it may deserve by the researchers in the field.

As the primary objective of the current study, the occurrence of the above mentioned five mechanisms and the extent of the effects that may have on the petrophysical properties of a wide range of carbonate core samples have been investigated. For the purpose of this

investigation, limestone, dolostone and chalk core plugs collected from various sources have been subjected to continuous live brine flooding, continuous CO_2-EOR flooding or CO_2 WAG flooding under elevated pressure and temperature. The laboratory-scale flooding experiments have been complemented by a number of diagnostic techniques such as porosity, permeability and NMR measurements, X-ray CT and SEM imaging, XRD analysis and finally chemical analysis of the effluent brine and crude oil (if used). Many of the above rock characterisation techniques were conducted on rock samples in their pre- and post-flood state. As some of the important aspects of this research, these auxiliary measurements, when combined with innovative sample preparation and data analysis techniques, not only were able to pinpoint the occurrence of the above mentioned rock-altering mechanisms but also to determine and explain their detailed interplay. Furthermore, the specially designed research work made it possible to establish and discuss specific relationships between the occurrence of such mechanisms, their end-effects and the rock-specific structural, mineralogical and textural features.

This dissertation, from Chapter 1 to Chapter 5, provides a full picture of the research work carried out by initially defining the problem at hand and the objectives set for this study. Subsequently, it presents a detailed introduction and background to the earlier mentioned mechanisms including how they may occur and their subsequent effects and implications. Then, it provides a full description of the experimental program devised for this study along with the rationale behind provisioned techniques. Finally, it lays out the detailed presentation of the results obtained along with their comprehensive interpretation and discussion.

6.2. Conclusions

Presented below are the main conclusions that can be drawn from the interpretation and discussions presented on the data and information gathered organised according to the earlier mentioned flooding scenarios utilised.

6.2.1. Live brine flooding

The permeability of the majority of core samples tested under this scenario increased, while their dry weight decreased after undergoing the flooding. These changes are believed to have been caused by the dissolution and removal of carbonate minerals from the samples. Due to their specific mineral composition, the above alterations in the dolomite samples is attributed to the dissolution and removal of the dolomite and anhydrite minerals, while in the limestone samples they are believed to have been caused by the dissolution and removal of calcite. The dissolution of minerals could be easily detected in some samples using a comparison between their pre- and post-flood states through visual inspection or the X-ray and SEM images

generated for the samples. During the flooding experiments, the brine flow was seen to follow the more porous areas, wider pore channels or pre-exiting fractures focusing the work of the mineral dissolution mechanism in these preferential flow paths, leading to the formation of wormholes along the length of the core samples. The effect of preferential flow paths on the eventual alterations that a sample may undergo was demonstrated by using a specially manufactured heterogeneous layered sample. For this flooding scenario, the dominance of the dissolution mechanism also resulted in a slight increase in the post-flood porosity of a few samples. The effects of this mechanism was found to be of greater importance in the limestone samples compared with the dolostones. This is attributed to the higher reactivity potential of the calcite as the main constituent of limestone compared with that of dolomite found at a high proportion in dolostone samples. Slight reductions in the porosity and pore sizes were observed in some of the core samples. A reduction in the permeability was also seen for one core plug which was placed at the outlet end of a relatively long composite sample. The above mentioned alterations are believed to have been caused by one or a combination of several of the mineral precipitation, carbonate fines migration and mechanical compaction mechanisms dominating over mineral dissolution.

The pre- and post-flood dry weight measurements, X-ray CT number profiles and SEM and X-ray CT images were found insightful in pinpointing the effect of the suspect mechanisms towards the above mentioned petrophysical changes. Overall, the changes in the porosity and pore size distribution of the post-flood samples seem to have been dictated by the compaction mechanism, while the dissolution mechanism seems to have had a stronger control over their post-flood permeabilities. The variability in the response of the samples to flooding seems to be a function of not only their mineralogy but also their pre-flood specific characteristics, such as the presence of core and micro-scale heterogeneities and special structural and textural features.

6.2.2. Continuous CO_2 and WAG flooding

Both of the continuous and WAG flooding schemes resulted in substantial additional oil recovery proving both to be effective EOR techniques under the experimental conditions explored in this work. In the samples tested under both flooding scenarios, asphaltene precipitation was found to be an active mechanism contributing and, at times, being dominant towards shaping the final post-flood petrophysical properties of the rock samples. The SEM images captured and the analysis of the original and effluent crude oil samples provided adequate evidence in support of the occurrence of asphaltene precipitation. The effect of this

mechanism was found to vary along the length of the samples, as revealed by the X-ray CT number profiles generated and the permeability measurements conducted, with having more pronounced effects closer to their inlet (i.e. injection point).

The continuous CO_2 flooding failed to promote the occurrence of mineral dissolution mechanism due to the lack of exposure of rock samples to adequate quantity of the reactive fluids (mainly carbonated brine) for long enough time. Since the occurrence of mechanical compaction, mineral precipitation and carbonate fines migration would depend on the mineral dissolution mechanism to take place initially, in continuous CO_2 flooding, the effect of these three mechanisms on the post-flood sample properties are believed to have been minimal. Due to the absolute dominance of the asphaltene precipitation, a considerable decrease in the post-flood permeability was seen across all samples tested using this flooding scenario. These samples also underwent subtle decreases to their porosity and pore sizes. On the other hand, the CO_2 WAG flooding resulted in the post-flood alternations that were to some extent similar to those observed for the case of live brine flooding. This behaviour is attributed to the adequate exposure of the samples tested under this scenario to relatively abundant volume of the reactive brine over long enough time. As a result, increase in the post-flood permeability was observed for some samples. The presence of dissolution fingers and wormholes was also detected in some of the post-flood X-ray images generated for some samples whose formation seem to have negatively impacted on the incremental oil recovery achieved from the WAG flooding.

6.3. Recommendations

Any further research in the area explored by this research work may benefit from the following recommendations:

- The experiments were carried out in this work under constant flow rate (0.5 cc/min). Since the flow rate influences the mineral dissolution rates considerably, further experiments are required to evaluate the effect of this factor on the post-flood petrophysical properties in details.

- Conducting experiments similar to those included in this work with regular real-time X-ray imaging may provide further insights into how various mechanisms may contribute versus flooding time towards shaping the post-flood characteristics of various samples.

- More detailed effluent fluid sampling during flooding experiments may provide greater insights into the occurrence of fluid-rock interactions versus experimental timeframe and their effects.
- Different crude oils with different asphaltene content may be used in order to have a better understanding of the effect of asphaltene precipitation during EOR processes.
- The effect of the core-scale heterogeneity on the precipitation of asphaltene is in need of further investigation.
- In general, any further research would benefit from numerical simulation and reactive transport modelling studies at various scales. These can lead to a better understanding of the fluid-rock interactions and their effects at smaller core and wellbore scales as well as their implications for the larger field-scale.

Nomenclature

CO_2	Carbon dioxide
2D:	2 dimensional
3D:	3 dimensional
A:	Area
API:	American Petroleum Institute (Unit of gravity)
BPR:	Back pressure regulator
BT:	Breakthrough
cc:	Cubic centimetre
CCS:	Carbon capture and storage
CO2CRC:	Cooperative Research Centre for Greenhouse gas Technologies
CO_2-EOR:	Enhanced oil recovery using CO2 injection
cP:	Centipoise
d:	Diameter
EOR:	Enhanced oil recovery
ft:	Foot/Feet
gr:	Gram
Gt:	Giga tonnes
hr:	Hour
IFT:	Interfacial tension
k:	Permeability
L:	Length
m:	Meter
mD:	Milli-Darcy
mg:	Milligrams
min:	Minute
mm:	Millimetre
Mol:	Mole

MPa:	Megapascal
NMR:	Nuclear Magnetic Resonance
P:	Pressure
PID:	Proportional–Integral–Derivative controller
Ppm:	Parts per million
Psi:	Pound per square inch
Psig:	psi-gauge
P-T:	Pressure-temperature
PV:	Pore volume
PVT:	Pressure-volume-temperature
q:	Volumetric flow-rate
S:	Saturation
Sec:	Second
SEM:	Scanning Electron Microscopy
SS:	Steady-state
T:	Temperature
USS:	Unsteady-state
WAG:	Water-alternating-gas
μ:	Viscosity
Ø:	Porosity
ρ:	Density
Θ:	Contact angle
Δp:	Differential pressure
σ:	Interfacial tension
ASTM:	Asphaltene Standard Test Method
MMP:	Minimum Miscibility Pressure
EGR:	Enhance natural Gas Recovery
RF:	Recovery Factor

Kr: Relative permeability

XRD: X-ray powder diffraction

kV: Kilovolt

CT: Medical X-ray CT

EDX Energy-Dispersive X-ray

01/10/2018 Rightslink® by Copyright Clearance Center

Copyright Clearance Center RightsLink®

Home Account Info Help

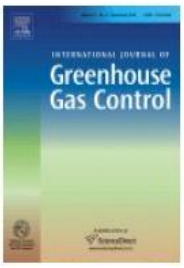

Title: Experimental investigation of changes in petrophysical properties during CO2 injection into dolomite-rich rocks

Author: Mohamed Khather,Ali Saeedi,Reza Rezaee,Ryan R.P. Noble,David Gray

Publication: International Journal of Greenhouse Gas Control

Publisher: Elsevier

Date: April 2017

© 2017 Elsevier Ltd. All rights reserved.

Logged in as:
Mohamed Khather
Curtin university

LOGOUT

Please note that, as the author of this Elsevier article, you retain the right to include it in a thesis or dissertation, provided it is not published commercially. Permission is not required, but please ensure that you reference the journal as the original source. For more information on this and on your other retained rights, please visit: https://www.elsevier.com/about/our-business/policies/copyright#Author-rights

BACK CLOSE WINDOW

Copyright © 2018 Copyright Clearance Center, Inc. All Rights Reserved. Privacy statement. Terms and Conditions.
Comments? We would like to hear from you. E-mail us at customercare@copyright.com

Copyright Clearance Center RightsLink®

Home Account Info Help

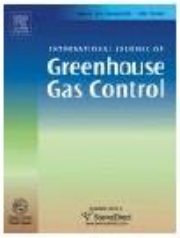

Title: Experimental evaluation of carbonated brine-limestone interactions under reservoir conditions-emphasis on the effect of core scale heterogeneities

Author: Mohamed Khather,Ali Saeedi,Reza Rezaee,Ryan R.P. Noble

Publication: International Journal of Greenhouse Gas Control

Publisher: Elsevier

Date: January 2018

© 2017 Elsevier Ltd. All rights reserved.

Logged in as:
Mohamed Khather
Curtin university
LOGOUT

Please note that, as the author of this Elsevier article, you retain the right to include it in a thesis or dissertation, provided it is not published commercially. Permission is not required, but please ensure that you reference the journal as the original source. For more information on this and on your other retained rights, please visit: https://www.elsevier.com/about/our-business/policies/copyright#Author-rights

BACK CLOSE WINDOW

Copyright © 2018 Copyright Clearance Center, Inc. All Rights Reserved. Privacy statement. Terms and Conditions.
Comments? We would like to hear from you. E-mail us at customercare@copyright.com

Copyright Clearance Center RightsLink®

Home Account Info Help

Title: An experimental study for carbonate reservoirs on the impact of CO2-EOR on petrophysics and oil recovery

Author: Mohamed Khather,Ali Saeedi,Matthew B. Myers,Michael Verrall

Publication: Fuel

Publisher: Elsevier

Date: 1 January 2019

© 2018 Elsevier Ltd. All rights reserved.

Logged in as:
Mohamed Khather
Curtin university
LOGOUT

Please note that, as the author of this Elsevier article, you retain the right to include it in a thesis or dissertation, provided it is not published commercially. Permission is not required, but please ensure that you reference the journal as the original source. For more information on this and on your other retained rights, please visit: https://www.elsevier.com/about/our-business/policies/copyright#Author-rights

BACK CLOSE WINDOW

Copyright © 2018 Copyright Clearance Center, Inc. All Rights Reserved. Privacy statement. Terms and Conditions.
Comments? We would like to hear from you. E-mail us at customercare@copyright.com

Attribution table

1. First paper

   Experimental Investigation of Changes in Petrophysical Properties during CO_2 Injection into Dolomite-Rich Rocks.

   Journal of International Journal of Greenhouse Gas Control 59: 74-90.

	Conception and design	**Acquisition of data & method**	**Data conditioning & manipulation**	**Analysis & statistical method**	**Interpretation & discussion**	**Final approval**
Dr. Ali Saeedi	x		x	x	x	x
I acknowledge that these represent my contribution to the above research output. Signed.						
Dr. Reza Rezaee		x				
I acknowledge that these represent my contribution to the above research output. Signed.						
Dr. Ryan Noble					x	
I acknowledge that these represent my contribution to the above research output. Signed.						
Dr. David Gray						x
I acknowledge that these represent my contribution to the above research output. Signed. As Mohamed's supervisor, I am signing on behalf of this co-author as he has resigned from his position in CSIRO and Mohamed is not able to locate him.						

Attribution table

2. Second paper

Experimental evaluation of carbonated brine-limestone interactions under reservoir conditions-emphasis on the effect of core scale heterogeneities.

Journal of International Journal of Greenhouse Gas Control, 68: 128-145

	Conception and design	**Acquisition of data & method**	**Data conditioning & manipulation**	**Analysis & statistical method**	**Interpretation & discussion**	**Final approval**
Dr. Ali Saeedi	x		x	x	x	x
I acknowledge that these represent my contribution to the above research output. Signed.						
Dr. Reza Rezaee		x				
I acknowledge that these represent my contribution to the above research output. Signed.						
Dr. Ryan Noble					x	
I acknowledge that these represent my contribution to the above research output. Signed.						

Attribution table

1. Third paper

   Experimental Study for Carbonate Reservoirs on the Impact of CO_2-EOR on Petrophysics and Oil Recovery

   Journal of Fuel 235: 1019-1038. doi: https://doi.org/10.1016/j.fuel.2018.08.094.

	Conception and design	**Acquisition of data & method**	**Data conditioning & manipulation**	**Analysis & statistical method**	**Interpretation & discussion**	**Final approval**
Dr. Ali Saeedi			x	x	x	x
I acknowledge that these represent my contribution to the above research output. Signed.						
Dr. Matthew Myers				x	x	x
I acknowledge that these represent my contribution to the above research output. Signed.						
Dr. Michael Verrall		x			x	
I acknowledge that these represent my contribution to the above research output. Signed.						

References

Abdallah, Wael, Jill S Buckley, Andrew Carnegie, John Edwards, Bernd Herold, Edmund Fordham, Arne Graue, Tarek Habashy, Nikita Seleznev, and Claude Signer. 2007. "Fundamentals of Wettability." *Technology* 38 (1125-1144): 268.

Agar, Susan M, and Gary J Hampson. 2014. "Fundamental Controls on Flow in Carbonates: An Introduction." *Petroleum Geoscience* 20 (1): 3-5.

Al-Quraishi, Abdulrahman, and M. Khairy. 2005. "Pore Pressure Versus Confining Pressure and Their Effect on Oil–Water Relative Permeability Curves." *Journal of Petroleum Science and Engineering* 48 (1–2): 120-126. doi: http://dx.doi.org/10.1016/j.petrol.2005.04.006.

Ancheyta, Jorgetrejo Fernandotrana Mohan Singh. 2010. *Asphaltenes, Chemical Transformation During Hydroprocessing of Heavy Oils*.

Anderson, WG. 1986. "1987, Wettability Literature Survey–Part 1 to Part 6." *J. Pet. Technol*: 1125-1144.

Asghari, Koorosh, and Adal Al-Dliwe. 2004. "Optimization of Carbon Dioxide Sequestration and Improved Oil Recovery in Oil Reservoirs." *GHGT7 Proceedings, Vancouver, BC, Canada*.

Babadagli, T. 2006. "Optimization of CO_2 Injection for Sequestration / Enhanced Oil Recovery and Current Status in Canada." In *Advances in the Geological Storage of Carbon Dioxide: International Approaches to Reduce Anthropogenic Greenhouse Gas Emissions*, eds S. Lombardi, L. K. Altunina and S. E. Beaubien, 261-270. Dordrecht: Springer Netherlands.

Bachu, Stefan. 2008a. " CO_2 Storage in Geological Media: Role, Means, Status and Barriers to Deployment." *Progress in Energy and Combustion Science* 34 (2): 254-273. doi: http://dx.doi.org/10.1016/j.pecs.2007.10.001.

———. 2008b. " CO_2 Storage in Geological Media: Role, Means, Status and Barriers to Deployment." *Progress in Energy and Combustion Science* 34 (2): 254-273.

Bachu, Stefan, W. D. Gunter, and E. H. Perkins. 1994. "Aquifer Disposal of CO_2: Hydrodynamic and Mineral Trapping." *Energy Conversion and Management* 35 (4): 269-279. doi: http://dx.doi.org/10.1016/0196-8904(94)90060-4.

Bagheri, MB, R Kharrat, and C Ghotby. 2011. "Experimental Investigation of the Asphaltene Deposition Process During Different Production Schemes." *Oil & Gas Science and Technology–Revue d'IFP Energies nouvelles* 66 (3): 507-519.

Bennion, Brant, and Stefan Bachu. 2005. "Relative Permeability Characteristics for Supercritical CO_2 Displacing Water in a Variety of Potential Sequestration Zones." 2005/1/1/. SPE: Society of Petroleum Engineers. doi: 10.2118/95547-MS.

Bennion, D.B., Scott, JA. and Bennion, D.W. 1992. "Detailed Laboratory Studies of Chemically and Biologically Induced Formation Damage in the East Wilmington Field." *Petroleum Society of CIM*.

Benson, Sally M. 2004. "Carbon Dioxide Capture and Storage in Underground Geologic Formations"

Benson, Sally M, and David R Cole. 2008. " CO_2 Sequestration in Deep Sedimentary Formations." *Elements* 4 (5): 325-331.

Berryman, James G. 1992. "Effective Stress for Transport Properties of Inhomogeneous Porous Rock." *Journal of Geophysical Research: Solid Earth* 97 (B12): 17409-17424. doi: 10.1029/92JB01593.

Burrowes, G, and C Gilboy. 2001. "Investigating Sequestration Potential of Carbonate Rocks During Tertiary Recovery from a Billion Barrel Oil Field, Weyburn, Saskatchewan: The Geoscience Framework (Iea Weyburn CO_2 Monitoring and Storage Project)" *Proceedings of the First National Conference on Carbon Sequestration. US Department of Energy, National Energy Technology Laboratory (NETL)*: Citeseer.

Cârcoană, Aurel. 1992. "Applied Enhanced Oil Recovery ".

Chalbaud, C, M Robin, S Bekri, and P Egermann. 2007. "Wettability Impact on CO_2 Storage in Aquifers: Visualisation and Quantification Using Micromodel Tests, Pore Network Model and Reservoir Simulations" *International symposium of the society of core analysts, Calgary, Canada*,

Chung, Frank, Partha Sarathi, and Ray Jones. 1991. *Modeling of Asphaltene and Wax Precipitation*.

Class, Holger, Anozie Ebigbo, Rainer Helmig, Helge K. Dahle, Jan M. Nordbotten, Michael A. Celia, Pascal Audigane et al. 2009. "A Benchmark Study on Problems Related to CO_2 Storage in Geologic Formations." *Computational Geosciences* 13 (4): 409-434. doi: 10.1007/s10596-009-9146-x.

Coates, George R, Lizhi Xiao, and Manfred G Prammer. 1999. *Nmr Logging: Principles and Applications*: Gulf Professional Publishing.

Demirbas, Ayhan. 2016. "Deposition and Flocculation of Asphaltenes from Crude Oils." *Petroleum Science and Technology* 34 (1): 6-11.

Detwiler, Russell L. 2008. "Experimental Observations of Deformation Caused by Mineral Dissolution in Variable-Aperture Fractures." *Journal of Geophysical Research: Solid Earth (1978–2012)* 113 (B8).

Detwiler, Russell L, and Harihar Rajaram. 2007. "Predicting Dissolution Patterns in Variable Aperture Fractures: Evaluation of an Enhanced Depth-Averaged Computational Model." *Water resources research* 43 (4).

Donaldson, Erle C. 2008. *Wettability / Erle C. Donaldson and Waqi Alam*. Edited by Waqi Alam. Houston, Tex.: Houston, Tex. : Gulf Pub. Co.

Dunn, K-J, David J Bergman, and Gerald A LaTorraca. 2002. *Nuclear Magnetic Resonance: Petrophysical and Logging Applications*. Vol. 32: Elsevier.

Egermann, Patrick, Brigitte Bazin, and Olga Vizika. 2005. "An Experimental Investigation of Reaction-Transport Phenomena During CO_2 Injection" *SPE Middle East Oil and Gas Show and Conference*: Society of Petroleum Engineers.

Elkhoury, Jean E, Pasha Ameli, and Russell L Detwiler. 2013. "Dissolution and Deformation in Fractured Carbonates Caused by Flow of CO_2-Rich Brine under Reservoir Conditions." *International Journal of Greenhouse Gas Control* 16: S203-S215.

Emera, M. K., and H. K. Sarma. 2006. "A Genetic Algorithm-Based Model to Predict Co-Oil Physical Properties for Dead and Live Oil." 2006/1/1/. PETSOC: Petroleum Society of Canada. doi: 10.2118/2006-197.

Enick, Robertm, and Scottm Klara. 1990. " CO_2 Solubility in Water and Brine under Reservoir Conditions." *Chemical Engineering Communications* 90 (1): 23-33. doi: 10.1080/00986449008940574.

Farokhpoor, Raheleh, Bård J. A. Bjørkvik, Erik Lindeberg, and Ole Torsæter. 2013. " CO_2 Wettability Behavior During CO_2 Sequestration in Saline Aquifer -an Experimental Study on Minerals Representing Sandstone and Carbonate." *Energy Procedia* 37: 5339-5351. doi: http://dx.doi.org/10.1016/j.egypro.2013.06.452.

Forchheimer, P. 1901. " Wasserbewegung Durch Boden. Zeitschrift Des Vereines Deutscher Ingenieure " 45(50), 1781–8.

Gale, John, Chris Hendriks, Wim Turkenberg, Michael Godec, Vello Kuuskraa, Tyler Van Leeuwen, L. Stephen Melzer, and Neil Wildgust. 2011. "10th International Conference on Greenhouse Gas Control Technologies CO_2 Storage in Depleted Oil Fields: The Worldwide Potential for Carbon Dioxide Enhanced Oil Recovery." *Energy Procedia* 4: 2162-2169. doi: http://dx.doi.org/10.1016/j.egypro.2011.02.102.

Gaus, Irina. 2010. "Role and Impact of CO_2–Rock Interactions During CO_2 Storage in Sedimentary Rocks." *International Journal of Greenhouse Gas Control* 4 (1): 73-89. doi: http://dx.doi.org/10.1016/j.ijggc.2009.09.015.

Gunter, William D., Ernest H. Perkins, and Tom J. McCann. 1993. "Aquifer Disposal of CO_2-Rich Gases: Reaction Design for Added Capacity." *Energy Conversion and Management* 34 (9–11): 941-948. doi: http://dx.doi.org/10.1016/0196-8904(93)90040H.

Halmann, Martin M, and Meyer Steinberg. 1998a. *Greenhouse Gas Carbon Dioxide Mitigation: Science and Technology*: CRC press.

Halmann, Martin M. , and Meyer Steinberg. 1998b. *Greenhouse Gas Carbon Dioxide Mitigation: Science and Technology*: Lewis Publishers- CRC Press.

Hangx, S. 2005. "Subsurface Mineralisation. Rate of CO_2 Mineralisation and Geomechanical Effects on Host and Seal Formations. Behaviour of the CO_2-H_2O System and Preliminary Mineralisation Model and Experiments."

Hawez, H, and Z Ahmed. 2014. "Enhanced Oil Recovery by CO_2 Injection in Carbonate Reservoirs." *WIT Transactions on Ecology and the Environment* 186: 547-558.

Hirschberg, Ade, LNJ DeJong, BA Schipper, and JG Meijer. 1984. "Influence of Temperature and Pressure on Asphaltene Flocculation." *Society of Petroleum Engineers Journal* 24 (03): 283-293.

Holm, L. W., and V. A. Josendal. 1974. "Mechanisms of Oil Displacement by Carbon Dioxide." doi: 10.2118/4736-PA.

IEA. 2008. *Geologic Storage of Carbon Dioxide Staying Safety Underground*. USA.

IPCC. 2005. *Carbon Dioxide Capture and Storage*. United States of America.

Izgec, Omer, Birol Demiral, Henri Bertin, and Serhat Akin. 2008. " CO_2 Injection into Saline Carbonate Aquifer Formations Ii: Comparison of Numerical Simulations to Experiments." *Transport in Porous Media* 73 (1): 57-74.

Izgec, Omer, Birol Demiral, Henri Jacques Bertin, and Serhat Akin. 2005. " CO_2 Injection in Carbonates" *SPE Western Regional Meeting*: Society of Petroleum Engineers.

———. 2006. "Experimental and Numerical Modeling of Direct Injection of CO_2 into Carbonate Formations" *SPE Annual Technical Conference and Exhibition*: Society of Petroleum Engineers.

Jafari Behbahani, Taraneh, Cyrus Ghotbi, Vahid Taghikhani, and Abbas Shahrabadi. 2012. "Investigation on Asphaltene Deposition Mechanisms During CO_2 Flooding Processes in Porous Media: A Novel Experimental Study and a Modified Model Based on

Multilayer Theory for Asphaltene Adsorption." *Energy & Fuels* 26 (8): 5080-5091. doi: 10.1021/ef300647f.

Jha, K. N. N. 1986. "A Laboratory Study of Heavy Oil Recovery with Carbon Dioxide." doi: 10.2118/86-02-03.

Jiang, Haifeng, Lily Nuryaningsih, and Hertanto Adidharma. 2010. "The Effect of Salinity of Injection Brine on Water Alternating Gas Performance in Tertiary Miscible Carbon Dioxide Flooding: Experimental Study." 2010/1/1/. SPE: Society of Petroleum Engineers. doi: 10.2118/132369-MS.

Jindrová, Tereza, and Jirı Mikyška. 2015. "Phase Equilibria Calculation of CO_2-H_2O System at Given Volume, Temperature, and Moles in CO_2 Sequestration." *IAENG Journal of Applied Mathematics* 45 (3): 183-192.

Jonoud, Sima, Ole Petter Wennberg, Alex Larsen, and Giulio Casini. 2013. "Capturing the Effect of Fracture Heterogeneity on Multiphase Flow During Fluid Injection." *SPE Reservoir Evaluation & Engineering* 16 (02): 194-208.

Kadhim, Fadhil Sarhan, Ariffin Samsuri, and Ahmad Kamal Idris. 2014. "Calculation of Petrophysical Properties for Mishrif Carbonate Reservoir." *AIP Conference Proceedings* 1621 (1): 756-762. doi: doi:http://dx.doi.org/10.1063/1.4898552.

Khather, Mohamed, Ali Saeedi, Reza Rezaee, Ryan RP Noble, and David Gray. 2017. "Experimental Investigation of Changes in Petrophysical Properties During CO_2 Injection into Dolomite-Rich Rocks." *International Journal of Greenhouse Gas Control* 59: 74-90.

Kono, Fumio, Ayato Kato, Mai Shimokawara, and Kazuki Tsushima. 2014. "Laboratory Measurements on Changes in Carbonate Rock Properties Due to CO_2-Saturated Water Injection" *Abu Dhabi International Petroleum Exhibition and Conference*: Society of Petroleum Engineers.

Korsnes, RI, MV Madland, KAN Vorland, T Hildebrand-Habel, TG Kristiansen, and A Hiorth. 2008. "Enhanced Chemical Weakening of Chalk Due to Injection of CO_2 Enriched Water" *International Symposium of the Society of Core Analysts, Abu Dhabi, United Arab Emirates*,

Lemon, Phillip Edward, Abbas Zeinijahromi, Pavel G. Bedrikovetsky, and Ibrahim Shahin. 2011. "Effects of Injected Water Chemistry on Waterflood Sweep Efficiency Via Induced Fines Migration." In *SPE International Symposium on Oilfield Chemistry, The Woodlands, Texas, USA*, 2011/1/1/. 17. SPE: Society of Petroleum Engineers. doi: 10.2118/140141-MS.

Li, Huazhou. 2013. "Phase Behaviour and Mass Transfer of Solvent (S)-CO_2-Heavy Oil Systems under Reservoir Conditions." Faculty of Graduate Studies and Research, University of Regina.

Liteanu, Emilia, CJ Spiers, and JHP De Bresser. 2013. "The Influence of Water and Supercritical CO_2 on the Failure Behavior of Chalk." *Tectonophysics* 599: 157-169.

Lucia, F Jerry. 2007. *Carbonate Reservoir Characterization: An Integrated Approach*: Springer Science & Business Media.

Luhmann, Andrew J, Xiang-Zhao Kong, Benjamin M Tutolo, Nagasree Garapati, Brian C Bagley, Martin O Saar, and William E Seyfried. 2014. "Experimental Dissolution of Dolomite by CO_2-Charged Brine at 100 C and 150bar: Evolution of Porosity, Permeability, and Reactive Surface Area." *Chemical Geology* 380: 145-160.

Luquot, Linda, and Philippe Gouze. 2009. "Experimental Determination of Porosity and Permeability Changes Induced by Injection of CO_2 into Carbonate Rocks." *Chemical Geology* 265 (1): 148-159.

Madland, Merete V, Anne Finsnes, Ali Alkafadgi, Rasmus Risnes, and Tor Austad. 2006. "The Influence of CO_2 Gas and Carbonate Water on the Mechanical Stability of Chalk." *Journal of Petroleum Science and Engineering* 51 (3): 149-168.

Mangalsingh, D., and T. Jagai. 1996. "A Laboratory Investigation of the Carbon Dioxide Immiscible Process." 1996/1/1/. SPE: Society of Petroleum Engineers. doi: 10.2118/36134-MS.

Mazzullo, SJ. 2004. "Overview of Porosity Evolution in Carbonate Reservoirs." *Kansas Geological Society Bulletin* 79 (1/2): 20-28.

Moghadasi, J, H Müller-Steinhagen, M Jamialahmadi, and A Sharif. 2004. "Model Study on the Kinetics of Oil Field Formation Damage Due to Salt Precipitation from Injection." *Journal of Petroleum Science and Engineering* 43 (3): 201-217.

Mohamed, Ibrahim Mohamed, Jia He, Mohamed Mahmoud, and Hisham A Nasr-El-Din. 2010. "Effects of Pressure, CO_2 Volume, and the CO_2 to Water Volumetric Ratio on Permeability Change During CO_2 Sequestration" *Abu Dhabi International Petroleum Exhibition and Conference*: Society of Petroleum Engineers.

Mosavat, Nader, Ali Abedini, and Farshid Torabi. 2014. "Phase Behaviour of CO_2–Brine and CO_2–Oil Systems for CO_2 Storage and Enhanced Oil Recovery: Experimental Studies." *Energy Procedia* 63: 5631-5645.

Müller, Nadja. 2011. "Supercritical CO_2-Brine Relative Permeability Experiments in Reservoir Rocks—Literature Review and Recommendations." *Transport in porous media* 87 (2): 367-383.

Nguele, Ronald, Mohammad R Ghulami, Kyuro Sasaki, Hikmat Said-Al Salim, Arif Widiatmojo, Yuichi Sugai, and Masanori Nakano. 2016. "Asphaltene Aggregation in Crude Oils During Supercritical Gas Injection." *Energy & Fuels* 30 (2): 1266-1278.

Niu, Ben, Ali Al-Menhali, and Sam Krevor. 2014. "A Study of Residual Carbon Dioxide Trapping in Sandstone." *Energy Procedia* 63: 5522-5529. doi: http://dx.doi.org/10.1016/j.egypro.2014.11.585.

Oelkers, Eric H, Sigurdur R Gislason, and Juerg Matter. 2008. "Mineral Carbonation of CO_2." *Elements* 4 (5): 333-337.

Oldenburg, CM, and Christine Doughty. 2011. "Injection, Flow, and Mixing of CO_2 in Porous Media with Residual Gas." *Transport in porous media* 90 (1): 201-218.

Oomole, O, and JS Osoba. 1983. "Carbon Dioxide-Dolomite Rock Interaction During CO_2 Flooding Process" *Annual Technical Meeting*: Petroleum Society of Canada.

Otani, J. 2004. "State of the Art Report on Geotechnical X-Ray Ct Research at Kumamoto University" *Proceeding of the 1st international workshop on X-ray CT for geomaterials (GeoX2003),*

Polak, Amir, Derek Elsworth, Jishan Liu, and Abraham S Grader. 2004. "Spontaneous Switching of Permeability Changes in a Limestone Fracture with Net Dissolution." *Water Resources Research* 40 (3).

Priisholm, S., B. L. Nielsen, and O. Haslund. 1987. "Fines Migration, Blocking, and Clay Swelling of Potential Geothermal Sandstone Reservoirs, Denmark." *SPE Formation Evaluation* 2 (02): 168-178. doi: 10.2118/15199-PA.

Pruess, Karsten, Tianfu Xu, John Apps, and Julio Garcia. 2001. "Numerical Modeling of Aquifer Disposal of CO_2." 2001/1/1/. SPE: Society of Petroleum Engineers. doi: 10.2118/66537-MS.

Saeedi, Ali. 2012. *Experimental Study of Multiphase Flow in Porous Media During CO_2 Geo-Sequestration Processes*: Springer Science & Business Media.

Saeedi, Ali, and Reza Rezaee. 2012. "Effect of Residual Natural Gas Saturation on Multiphase Flow Behaviour During CO_2 Geo-Sequestration in Depleted Natural Gas Reservoirs." *Journal of Petroleum Science and Engineering* 82: 17-26.

Saeedi, Ali, Reza Rezaee, Brian Evans, and Ben Clennell. 2011. "Multiphase Flow Behaviour During CO_2 Geo-Sequestration: Emphasis on the Effect of Cyclic CO_2–Brine

Flooding." *Journal of Petroleum Science and Engineering* 79 (3–4): 65-85. doi: http://dx.doi.org/10.1016/j.petrol.2011.07.007.

Salem, Adel M, and Shedid A Shedid. 2013. "Variation of Petrophysical Properties Due to Carbon Dioxide (CO_2) Storage in Carbonate Reservoirs." *Journal of Petroleum and Gas* 4 (4): 91-102.

Sally Benson, Peter Cook. 2011. "Underground Geological Storage."

Scripps Institution of Oceanography. 2015. "Mauna Loa Observatory, Hawaii.".

Seo, J. G., and D. D. Mamora. 2003. "Experimental and Simulation Studies of Sequestration of Supercritical Carbon Dioxide in Depleted Gas Reservoirs." 2003/1/1/. SPE: Society of Petroleum Engineers. doi: 10.2118/81200-MS.

Shafiee, ME, and A Kantzas. 2009. "Investigation on the Effect of Overburden Pressure on Vuggy Carbonate Oil Reservoir Core Properties" *Canadian International Petroleum Conference*: Petroleum Society of Canada.

Simon, R., and D. J. Graue. 1965. "Generalized Correlations for Predicting Solubility, Swelling and Viscosity Behavior of CO_2-Crude Oil Systems." doi: 10.2118/917-PA.

Smith, Megan M, Yelena Sholokhova, Yue Hao, and Susan A Carroll. 2013. "CO_2-Induced Dissolution of Low Permeability Carbonates. Part I: Characterization and Experiments." *Advances in Water Resources* 62: 370-387.

Span, Roland, and Wolfgang Wagner. 1996. "A New Equation of State for Carbon Dioxide Covering the Fluid Region from the Triple-Point Temperature to 1100 K at Pressures up to 800 Mpa." *Journal of Physical and Chemical Reference Data* 25 (6): 1509-1596. doi: doi:http://dx.doi.org/10.1063/1.555991.

Srivastava, Raj K, and Sam S Huang. 1997. "Asphaltene Deposition During CO_2 Flooding: A Laboratory Assessment" *SPE Production Operations Symposium*: Society of Petroleum Engineers.

Stumm, Werner. 1992. "Chemistry of the Solid-Water Interface: Processes at the Mineral-Water and Particle-Water Interface in Natural Systems."

Sun, Chang-Yu, and Guang-Jin Chen. 2005. "Measurement of Interfacial Tension for the CO_2 Injected Crude Oil+ Reservoir Water System." *Journal of Chemical & Engineering Data* 50 (3): 936-938.

Takahashi, Satoru, Yoshihisa Hayashi, Shunya Takahashi, Nintoku Yazawa, and Hemanta Sarma. 2003. "Characteristics and Impact of Asphaltene Precipitation During CO_2 Injection in Sandstone and Carbonate Cores: An Investigative Analysis through

Laboratory Tests and Compositional Simulation." 2003/1/1/. SPE: Society of Petroleum Engineers. doi: 10.2118/84895-MS.

Tiab, D, and EC Donaldson. 2004. "Petrophysics: Burlington, Massachusetts." Gulf Professional Publishing, Elsevier.

Tutolo, Benjamin M, Andrew J Luhmann, Xiang-Zhao Kong, Martin O Saar, and William E Seyfried Jr. 2014. "Experimental Observation of Permeability Changes in Dolomite at CO_2 Sequestration Conditions." *Environmental science & technology* 48 (4): 2445-2452.

UNFCCC. 2002. *Information Kit Climate Change*. United Nations Framework Convention on Climate Change.

USCSC. 2009. *Greenhouse Gases, Global Warming & Ccs*. The U.S. Carbon Sequestration Counci.

Wagner, Wolfgang, and A. Pruss. 1993. "International Equations for the Saturation Properties of Ordinary Water Substance. Revised According to the International Temperature Scale of 1990. Addendum to J. Phys. Chem. Ref. Data 16, 893 (1987)." *Journal of Physical and Chemical Reference Data* 22 (3): 783-787. doi: doi:http://dx.doi.org/10.1063/1.555926.

Wellman, Tristan P, Reid B Grigg, Brian J McPherson, Robert K Svec, and Peter C Lichtner. 2003. "Evaluation of CO_2-Brine-Reservoir Rock Interaction with Laboratory Flow Tests and Reactive Transport Modeling" *International symposium on oilfield chemistry*: Society of Petroleum Engineers.

Whitaker, Stephen. 1986. "Flow in Porous Media I: A Theoretical Derivation of Darcy's Law." *Transport in Porous Media* 1 (1): 3-25. doi: 10.1007/bf01036523.

Wilson, M. J., L. Wilson, and I. Patey. 2014. "The Influence of Individual Clay Minerals on Formation Damage of Reservoir Sandstones: A Critical Review with Some New Insights." In *Clay Minerals*.

Wright, Iain Washington, Philip Sefton Ringrose, Allan S. Mathieson, and Ola Eiken. 2009. "An Overview of Active Large-Scale CO_2 Storage Projects." 2009/1/1/. SPE: Society of Petroleum Engineers. doi: 10.2118/127096-MS.

Xu, Tianfu, John A Apps, and Karsten Pruess. 2001. "Analysis of Mineral Trapping for CO_2 Disposal in Deep Aquifers." *Lawrence Berkeley National Laboratory*.

Yang, Daoyong, Yongan Gu, and Paitoon Tontiwachwuthikul. 2008. "Wettability Determination of the Reservoir Brine-Reservoir Rock System with Dissolution of CO_2

(Sub 2) at High Pressures and Elevated Temperatures." *Energy & Fuels* 22 (1): 504-509. doi: 10.1021/ef700383x.

Zekri, Abdul Razag Y, Shedid A Shedid, and Reyadh A Almehaideb. 2013. "Experimental Investigations of Variations in Petrophysical Rock Properties Due to Carbon Dioxide Flooding in Oil Heterogeneous Low Permeability Carbonate Reservoirs." *Journal of Petroleum Exploration and Production Technology* 3 (4): 265-277.

Zekri, Abdulrazag Y, Shedid A Shedid, and Reyadh A Almehaideb. 2009. "Investigation of Supercritical Carbon Dioxide, Asphelteni c Crude Oil, and Formation Brine Interactions in Carbonate Formations." *Journal of Petroleum Science and Engineering* 69 (1): 63-70.